Modelling storm-time TEC changes using linear and non-linear techniques

A thesis submitted in fulfillment of the requirements
for the degree of

DOCTOR OF PHILOSOPHY

of

Rhodes University

by

Jean Claude Uwamahoro

March 2019

Abstract

Statistical models based on empirical orthogonal functions (EOF) analysis and non-linear regression analysis (NLRA) were developed for the purpose of estimating the ionospheric total electron content (TEC) during geomagnetic storms. The well-known least squares method (LSM) and Metropolis-Hastings algorithm (MHA) were used as optimization techniques to determine the unknown coefficients of the developed analytical expressions. Artificial Neural Networks (ANNs), the International Reference Ionosphere (IRI) model, and the Multi-Instrument Data Analysis System (MIDAS) tomographic inversion algorithm were also applied to storm-time TEC modelling/reconstruction for various latitudes of the African sector and surrounding areas. This work presents some of the first statistical modeling of the mid-latitude and low-latitude ionosphere during geomagnetic storms that includes solar, geomagnetic and neutral wind drivers. Development and validation of the empirical models were based on storm-time TEC data derived from the global positioning system (GPS) measurements over ground receivers within Africa and surrounding areas. The storm criterion applied was $Dst \leqslant -50$ nT and/or $K_p \geqslant 4$. The performance evaluation of MIDAS compared with ANNs to reconstruct storm-time TEC over the African low- and mid-latitude regions showed that MIDAS and ANNs provide comparable results. Their respective mean absolute error (MAE) values were 4.81 and 4.18 TECU. The ANN model was, however, found to perform 24.37 % better than MIDAS at estimating storm-time TEC for low latitudes, while MIDAS is 13.44 % more accurate than ANN for the mid-latitudes. When their performances are compared with the IRI model, both MIDAS and ANN model were found to provide more accurate storm-time TEC reconstructions for the African low- and mid-latitude regions. A comparative study of the performances of EOF, NLRA, ANN, and IRI models to estimate TEC during geomagnetic storm conditions over various latitudes showed that the ANN model is about 10 %, 26 %, and 58 % more accurate than EOF, NLRA, and IRI models, respectively, while EOF was found to perform 15 %, and 44 % better than NLRA and IRI, respectively. It was further found that the NLRA model is 25 % more accurate than the IRI model. We have also investigated for the first time, the role of meridional neutral winds (from the Horizontal Wind Model) to storm-time TEC modelling in the low latitude, northern and southern hemisphere mid-latitude regions of the African sector, based on ANN models. Statistics have shown that the inclusion of the meridional wind velocity in TEC modelling during geomagnetic storms leads to percentage improvements of about 5 % for the low latitude, 10 % and 5 % for the northern and southern hemisphere mid-latitude regions, respectively. High-latitude storm-induced winds and the inter-hemispheric blows of the meridional winds from summer to winter hemisphere have been suggested to be associated with these improvements.

Publications from this thesis

1. Uwamahoro, J. C., Giday, N. M., Habarulema, J. B., Katamzi-Joseph, Z. T., & Seemala, G. K. (2018). Reconstruction of storm-time total electron content using ionospheric tomography and artificial neural networks: A comparative study over the African region. Radio Science, 53, 118. https://doi.org/10.1029/2017RS006499. The outcome from this publication forms a part of chapter 4.

2. Uwamahoro, J.C., Habarulema, J.B. & Burešová, D. (2019). Highlights about the performances of storm-time TEC modelling techniques for low/equatorial and mid-latitude locations. Advances in Space Research, https://doi.org/10.1016/j.asr.2019.01.027. Chapter 5 presents the content of this paper.

3. Uwamahoro, J. C., Habarulema, J. B., & Okouma, P. M. (2018). Storm time total electron content modeling over African low-latitude and midlatitude regions. Journal of Geophysical Research: Space Physics, 123. https://doi.org/10.1029/2018JA025455. Results from this publication are summarized in chapter 6.

Acknowledgement

I would like to express my sincere gratitude to my supervisor, Dr John Bosco Habarulema, for his advice and support that helped me to achieve my goals. His research professionalism and work ethic are encouraging and have stimulated my own growth in the research environment. I am also thankful to the South African National Research Foundation (NRF) and South African National Space Agency (SANSA) for the PhD bursary, and all the support during the past six years, from honours to PhD level.

I received wonderful support from fellow students and SANSA researchers, for which I am grateful. They made the research environment enjoyable and fruitful and are the reason for my research progress during my stay at SANSA. A special thank-you to Alessio Pignalberi, Laura Wentworth, and Michael Heyns for their assistance with python programming. It was such a blessing to have met all of them during my studies.

Special thanks to my wife, Claudine Uwineza, my children, Claudette Umugwaneza and Claudia Ujeneza, and my family in general for their encouragement, support, and being with me during my studies.

Sincere gratitude goes to my late parents Florence Nizeyemariya and Jean Bosco Twagirimana. Their confidence in my ability to succeed in academia has been a great source of inspiration. It is for this reason that this milestone has been accomplished.

My heartfelt gratitude extends to all who contributed directly or indirectly to the realization of this work and to my growth and journey over the years.

My God, thank you for everything you provided and for protecting my life during my studies.

Dedication

This thesis is dedicated to my loving wife, Claudine Uwineza, and my daughters, Claudette Umugwaneza and Claudia Ujeneza.

Contents

Abstract

List of Figures

List of Tables

Chapter 1

Introduction

The ionospheric electron density varies due to a mixture of complex mechanisms that modify temporal and spatial distributions of ionized particles, such as changes in solar radiation intensity, interaction of interplanetary and geomagnetic fields, as well as the atmospheric dynamics (Mitchell & Spencer, 2003). The state of the ionosphere becomes more complicated during geomagnetic storms since the ionospheric electron density is redistributed due to electric field perturbations and induced currents in the ionosphere (Tsurutani *et al.*, 2004, 2006a), and other mechanisms such as neutral winds (Fesen *et al.*, 1989), expansion of the equatorial ionisation anomaly (Tsurutani *et al.*, 2004), large-scale travelling ionospheric disturbances (TIDs) (Borries *et al.*, 2009), and neutral composition changes (Prölss, 1980). Among several disturbances that highly affect the ionospheric variability, geomagnetic storms are listed at the first place to have more and disadvantageous societal impacts. This is due to their long duration (one to several days), and their extension to low and middle latitudes which are the most populated regions (Davies, 1990). For satellite navigational systems, total electron content (TEC) is known to be a good descriptive parameter of the ionospheric dynamic (Hofmann-Wellenhof *et al.*, 1992). TEC is defined as the total number of electrons within a column with a cross-section of 1 m^2 centered on ray path between satellite and receiver (Hofmann-Wellenhof *et al.*, 1992; Misra & Enge, 2006). During geomagnetic and ionospheric storms, ionospheric electron density/TEC may be enhanced or depleted relative to the days that precede or follow the storm, and the effect is termed as positive or negative storm effect, respectively (Prölss, 1980; Volland, 1995). A non-significant storm effect corresponds to the case where there is no change in electron density/TEC during the storm day compared to regular state (Vijaya Lekshmi *et al.*, 2011; Matamba *et al.*, 2015).

Understanding the mechanisms responsible for ionospheric responses during storm conditions is of utmost importance for accurate storm-time prediction of the ionospheric dynamics. Electron density/TEC variations due to geomagnetic and ionospheric storms have adverse impacts on ground-based and space-based technologies. Typical examples of the deleterious effects that severe storms and solar flares which occurred between October - November 2003 had on technological systems are listed in Doherty *et al.* (2004). For the benefits of the society, the safety of ground-based and space-borne technologies is required. Thus, products that are able to nowcast and forecast storm-time ionospheric behaviour are important for space weather community in order to mitigate detrimental effects that may impact directly or indirectly on human life. This study focused on the development of mathematical equations based on the constructed storm-time TEC databases, for estimating TEC during geomagnetic storms. On a latitudinal scale, the performances of existing models/techniques for reconstructing TEC during storm conditions were evaluated with respect to established models. The models/techniques that were considered are the International Reference Ionosphere (IRI), which is a standard empirical model of the ionosphere (Rawer *et al.*, 1978; Bilitza, 2001), and the Multi-Instrument Data Analysis System (MIDAS), an inversion algorithm for ionospheric tomography (Mitchell & Spencer, 2003). Observational TEC data used in this study were derived from Global Navigation Satellite System (GNSS) measurements, specifically, the Global Positioning System (GPS) records from a network of ground-based receivers within the African sector and surrounding areas.

The ionosphere-thermosphere reaction due to magnetic storms can be understood via Physics-based models and simulation studies. Empirical or data-based models of the ionosphere have the advantage that, they do not depend on the evolving theoretical understanding of the physical processes that govern the ionospheric dynamics (Bilitza *et al.*, 2014). However, the evaluation of the contribution of an included input in empirical models to storm-time ionospheric modelling, can provide the information on whether a given physical process represented by that input influences the ionospheric variability or not. In this perspective, the current study focuses on the development of empirical models and not on Physics-based models.

There exists a number of physics-based models (based on first principles) that can provide electron density/TEC. Typical examples include the Thermosphere Ionosphere Electrodynamics General Circulation Model (TIEGCM) (Richmond *et al.*, 1992), Coupled Thermosphere Ionosphere Plasmasphere Electrodynamics (CTIPe) model (Fuller-Rowell & Rees, 1980; Codrescu *et al.*, 2008), Global Ionosphere Thermosphere Model (GITM) (Ridley *et al.*, 2006), and SAMI3 (Sami3 is Also a Model of the Ionosphere) (Huba *et al.*, 2000). Empirical (data-based) standard models of the ionosphere such as the IRI, Bent ionospheric model, and NeQuick are also available (Llewellyn & Bent, 1973; Bilitza *et al.*, 1988; Radicella, 2009). Other empirical models of ionospheric TEC or critical frequency of the F2 layer ($foF2$) have been extensively developed based on mathematical approaches such as data assimilation techniques (Kalman filtering and Kriging method) (e.g., Hajj *et al.*, 2004; Fuller-Rowell *et al.*, 2006; Ercha *et al.*, 2015; Pignalberi *et al.*, 2017), empirical orthogonal functions (EOF) analysis (e.g., Ercha *et al.*, 2012; Uwamahoro & Habarulema, 2015; Dabbakuti *et al.*, 2016), regression analysis (e.g., Kakinami *et al.*, 2009; Mukhtarov *et al.*, 2013a,b; Hajra *et al.*, 2016), and theory of splines (e.g., Schmidt *et al.*, 2011; Erdogan *et al.*, 2017). Artificial neural networks (ANNs) have more often been applied to TEC and $foF2$ modelling during geomagnetically quiet and storm conditions (e.g., Hernandez-Pajares *et al.*, 1997; Cander, 1998; Poole & McKinnell, 2000; McKinnell & Poole, 2004; Tulunay *et al.*, 2004; Oyeyemi *et al.*, 2006; Tulunay *et al.*, 2006; Habarulema *et al.*, 2007; Leandro & Santos, 2007; Maruyama, 2007; Habarulema *et al.*, 2009a,b, 2010; Acharya *et al.*, 2011; Habarulema *et al.*, 2011; Habarulema & McKinnell, 2012; Ratnam *et al.*, 2012; Watthanasangmechai *et al.*, 2012; Huang & Yuan, 2014; Sur *et al.*, 2015; Uwamahoro & Habarulema, 2015; Okoh *et al.*, 2016; Tshisaphungo *et al.*, 2018). Studies have shown that ionospheric modelling is more difficult during storms compared to quiet conditions (e.g., Ratnam *et al.*, 2011; Ercha *et al.*, 2012; Kumar *et al.*, 2014; Cander, 2015). A number of challenges related to storm-time ionospheric modelling/reconstruction have been raised. For example, the inaccuracy/failure of empirical models to capture positive or negative ionospheric responses during storm conditions has been reported (e.g., Fuller-Rowell *et al.*, 2000; Habarulema *et al.*, 2010, 2011; Watthanasangmechai *et al.*, 2012; Mukhtarov *et al.*, 2013a; Uwamahoro & Habarulema, 2015). Difficulty in storm-time modelling of the low/equatorial ionosphere, normally characterized by complex electrodynamic changes and consequential high TEC gradients compared to middle latitude has also been reported (Materassi & Mitchell, 2005; Adewale *et al.*, 2011; Kenpankho *et al.*, 2011; Chartier *et al.*, 2014; Panda *et al.*, 2015; Giday & Katamzi-Joseph, 2018; Uwamahoro *et al.*, 2018b). Incomplete knowledge of the main drivers of storms and the lack of/insufficient representation of all mechanisms that are involved in storm processes, are likely the main reasons for inaccurate storm-time ionospheric modelling. Another common reason for inaccuracy in empirical models such as IRI in some regions (e.g., low/equatorial and auroral latitudes) is the lack of or sparse data sources (Bilitza & Reinisch, 2008).

Although much effort has been put into the improvement of ionospheric modelling, further improvements are still required in order to accurately predict the storm impact (e.g., Habarulema *et al.*, 2011; Watthanasangmechai *et al.*, 2012; Mukhtarov *et al.*, 2013a; Uwamahoro & Habarulema, 2015). For example, empirical models of the ionosphere such as IRI and NeQuick have been and are still being improved as new data and more accurate models become available (Bilitza, 2003; Radicella, 2009). In the same framework, the current work is an effort towards improving TEC modelling during geomagnetic storms by investigating new modelling inputs and evaluating their contributions. Thus, there are a number of particularities of this work when compared with existing works. The first is that, in addition to the standard modelling inputs that represent diurnal and seasonal variations of TEC, solar and geomagnetic activities, the meridional wind velocity has been introduced for the first time in storm-time TEC modelling and its contribution to modelling results has been evaluated statistically. The second particularity concerns the databases used for the implementation of models. While previous empirical models were based on a mixture of TEC data for both quiet and disturbed conditions, the present work relies on storm-time TEC databases only, built based on the storm criterion of $Dst \leqslant -50$ nT and/or $K_p \geqslant 4$. On this point, the hypothesis is that one of the sources of inaccuracy of previous storm-time models may have resided in the use of databases dominated by quiet-time data.

1.1 Motivation and importance of the project

Propagation of ground-to-satellite and over-the-horizon radio signals depends on the structure of the ionosphere. Geomagnetic and ionospheric storms significantly alter the properties of the ionosphere. Thus, TEC perturbations due to geomagnetic storms have a significant impact on radio communication over the entire radio spectrum, i.e. from extremely low frequency (< 3 kHz) to super high frequency (3000 - 30 000 MHz), and to satellite applications such as navigation, space weather forecasting, GPS surveying, and remote sensing systems, which rely on electromagnetic signals that pass through the ionosphere (Hofmann-Wellenhof *et al.*, 1992; Moldwin, 2008; Gleason & Gebre-Egziabher, 2009; Ercha *et al.*, 2015). For instance, TEC encountered along the signal path between satellite and a receiver is one of the main sources of error for positioning applications (Rama Rao *et al.*, 2006; Ciraolo *et al.*, 2007). Time-varying currents induced in the ionosphere by large geomagnetic storms may in turn generate electrical currents in ground-based infrastructures such as electric power lines, telephone lines, and pipelines. The resulting adverse impacts such as disruption or complete damage of the equipment could lead to enormous socioeconomic losses (Doherty *et al.*, 2004; Moldwin, 2008). Another point of motivation is that existing storm-time TEC models need further improvements especially in predicting positive and negative storm phases. Accurate storm-time models may provide warnings to space weather community, so as to offer an opportunity to plan appropriately and at the right time referring to what is likely to happen some time ahead.

1.2 Project objectives

The main objectives of this project are to:

- Build storm-time TEC databases for selected GPS stations within Africa and surrounding areas.
- Develop mathematical equations to estimate TEC during geomagnetic storms.
- Explore and evaluate the performances of different storm-time TEC techniques.
- Investigate new modelling inputs and evaluate their contributions to storm-time TEC modelling.

1.3 Thesis outline

This thesis consists of 7 chapters.

Chapter one discusses work done in the field of ionospheric modelling and the potential contribution of the current work towards the improvement of storm-time TEC modelling. The project motivation and objectives, and thesis structure are also presented.

Background theory on the Earth's atmosphere, ionosphere and magnetosphere, as well as a description of TEC, geomagnetic and ionospheric storms, is provided in Chapter 2.

The data sources exploited for this study, data processing steps, and modelling inputs, are briefly presented in Chapter 3. Climatological models (IRI and Horizontal Wind Model (HWM)) used in this work, and the MIDAS algorithm are also described. Background theory on empirical storm-time TEC modelling techniques considered (artificial neural networks (ANNs), Non-linear regression analysis (NLRA), the Metropolis-Hastings Algorithm (MHA), and empirical orthogonal functions (EOF) analysis) is also provided.

Chapter 4 covers the evaluation of the contribution of different solar activity modelling inputs (sunspot number (SSN), solar flux index ($F10.7$), and its derivative ($F10.7p$)) to TEC modelling during geomagnetic storms and the results are compared with NLRA model predictions complemented with MHA. This chapter also presents the results about the performance evaluation of ANNs and MIDAS over equatorial/low and mid-latitudes of the African sector.

Statistical results and highlights about different storm-time TEC models developed for low/equatorial and middle latitudes, compared to IRI predictions over the locations considered, are presented in Chapter 5.

Chapter 6 presents the results about the contribution of meridional neutral winds (represented by meridional neutral wind velocity in modelling) on TEC modelling during storm conditions.

Conclusions and suggestions for future work are provided in Chapter 7.

Chapter 2

Theoretical background

In this chapter, a brief description of the Earth's atmosphere is provided and particular attention is paid to the ionosphere, which is the most important layer for radio communication. Basic theory of the ionospheric total electron content (TEC), as a descriptive parameter of the state of the ionosphere, is provided. An introduction to Earth's magnetosphere and its coupling to the solar wind is also presented, as well as a brief summary on the mechanisms that drive the ionospheric responses during geomagnetic storms.

2.1 Earth's atmosphere

The atmosphere is a layer of mixed gases that surrounds the Earth. Its major components are Nitrogen (N_2, 78.11 %), Oxygen (O_2, 20.95 %), Argon (Ar, 0.93 %), Neon (Ne, 18.18×10^{-4} %), and Helium (He, 5.24×10^{-4} %). Other important constituents are water (H_2O, 0 - 7 %), Carbon dioxide (CO_2, 0.01 - 0.1 %), and Ozone (O_3, 0 - 0.00001 %) (Zolesi & Cander, 2014). The Earth's atmosphere is important for life since it protects us from solar and extragalactic cosmic rays, contains Oxygen we use to breath and Carbon dioxide necessary for plants. The main source of atmosphere's heat is the Sun and pressure gradients originating from temperature differences between two points are the main drivers of atmospheric winds. Terrestrial weather is also a direct result of temperature changes (heating and cooling) in the lower atmosphere (White, 1970). The vertical structure of the Earth's atmosphere is described by studying the behaviour of temperature with altitude. Based on temperature variation with respect to height, the Earth atmosphere is subdivided into several regions: troposphere, stratosphere, mesosphere, thermosphere, and exosphere (Rishbeth & Garriott, 1969; White, 1970; Davies, 1990; Zolesi & Cander, 2014).

The troposphere extends from the Earth's surface up to an altitude of about 15 km above the equator, and 10 km above the geographical poles (Zolesi & Cander, 2014). Within this region, the temperature decreases from about 290 K at the Earth's surface to 220 K at the tropopause, the upper boundary of the troposphere (White, 1970). The average temperature decrease is 6.5 K per km and convective movement of the air is the main reason for the decrease in temperature within the troposphere. Warmer air masses in contact with the

Earth's surface cool down as they move upward in an adiabatic process (Zolesi & Cander, 2014). Above the troposphere is the stratosphere which extends up to an altitude of about 50 km, i.e. at the stratopause. The temperature increases with increasing altitude, from 220 K to about 270 K because of the existence of the ozone layer (tri-atomic Oxygen atom) which absorbs ultraviolet (UV) radiation from the Sun (Rishbeth & Garriott, 1969; Kelley, 2009; Zolesi & Cander, 2014). The temperature increase in the stratosphere is not only from absorption of UV by 0_3, but also the absorption by 0_2 and N_2 is important. The mesosphere lies within the altitude range of 50 km (stratopause) to about 85 km, i.e. the upper boundary of the mesosphere, called the mesopause (Rishbeth & Garriott, 1969; Davies, 1990). The temperature varies from about 270 K to 180 K at the mesopause (White, 1970). Above the mesosphere is the thermosphere with its upper limit, the thermopause, at an altitude of about 500 km. However, it is important to note that the exact altitude of the thermopause varies with time of the day, solar flux, season, and location of solar energy inputs. The thermosphere is named as such because of the rapid increase in temperature with height from 180 K to 1500 K at a height of about 300 km (White, 1970). The increase in temperature within the thermosphere is due to the absorption of UV radiation by Oxygen and Nitrogen atoms at greater heights (Rishbeth & Garriott, 1969; Kelley, 2009; Zolesi & Cander, 2014). The UV radiation, and to some extend also X-rays, dissociate Oxygen and Nitrogen molecules and a large fraction of the heat liberated in the thermosphere is removed by downward conduction in such a way that the temperature increases upward (Rishbeth & Garriott, 1969). The outermost layer of the Earth's atmosphere is called the exosphere and extends from the thermopause to higher altitudes. The exosphere is characterized by a temperature which is nearly constant and low atmospheric density, so that collisions between neutral molecules are negligible (Rishbeth & Garriott, 1969; White, 1970). The lower boundary of the exosphere is called the exobase and the upper boundary corresponds to the line of separation between the Earth's atmosphere and the interplanetary medium (Visconti, 2001; Zolesi & Cander, 2014). An illustrative sketch of the atmospheric temperature variation with respect to altitude is shown in Figure 2.1 (a).

The Large number of ionized particles found in thermosphere and exosphere results from extreme UV (EUV) radiation and X-rays. These two regions overlap with the Earth's ionosphere, which is a portion of the Earth's upper atmosphere composed of charged particles (free electrons and positive ions) under the control of gravity and the Earth's magnetic field (Zolesi & Cander, 2014). Free electrons and positive ions within the ionosphere are approximately in equal number and the ionospheric medium is assumed to be electrically neutral (Davies, 1990).

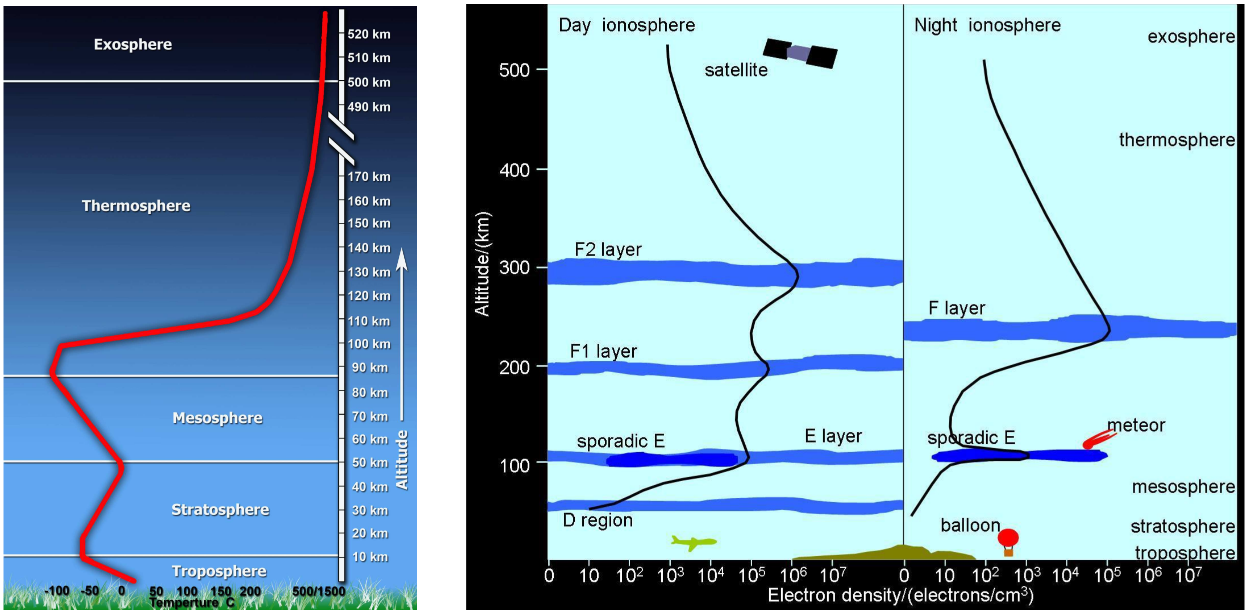

(a) Average temperature profile through the atmosphere.

(b) Schematic representation of daytime and nighttime ionospheric structures.

Figure 2.1: A schematic illustration of (a) Average temperature profile of the Earth's atmosphere (`http://www.ces.fau.edu/nasa/module-2/atmosphere/earth.php`) and (b) Daytime and nighttime electron density profiles (`http://www.sws.bom.gov.au/Educational`).

2.2 Ionosphere

The region of the Earth's atmosphere mostly composed of ions, extending from about 50 km to 1000 km is called ionosphere (Misra & Enge, 2006). The ionosphere covers the mesosphere, thermosphere, and the exosphere (Zolesi & Cander, 2014). The ozone layer (ozonosphere) which extends roughly from 10 km to 80 km with a peak of concentration at about 25 km, overlaps with the lower ionosphere from the altitude of about 50 km (Rishbeth & Garriott, 1969). Ions are formed through a process called photoionization. When EUV photons hit neutral atoms (referred here as A) such as Oxygen atoms in the Earth's atmosphere, some electrons (e^-) are detached from neutrals and move freely, causing neutral atoms to become positive ions (A^+) as follows (McNamara, 1991; Kelley, 2009):

$$A \longrightarrow A^+ + e^- .$$

Only free electrons are responsible for reflection of radio waves in the ionosphere because they are much lighter than positive ions and thus, respond fast to rapid oscillations of radio waves (McNamara, 1991). Through a reverse process of photoionization, namely recombination, electrons are lost in the upper ionosphere when they combine with positive ions to form neutral atoms (Rishbeth & Garriott, 1969; McNamara, 1991; Kelley, 2009). In the lower ionosphere, free electrons are mostly lost through a process called attachment. During the attachment process, electrons are attached to neutral atoms which thus become negative ions (Rishbeth & Garriott, 1969; McNamara, 1991). Similar to positive ions, negative ions are much heavier than electrons and are thus incapable of responding to rapid oscillations of radio waves (McNamara, 1991).

There exists two types of recombination: radiative recombination (combination of atomic ion with electron) and dissociative recombination (combination of molecular ion with electron) (Rishbeth & Garriott, 1969; McNamara, 1991). In the former, free electrons combine directly with positive ions X^+ to produce neutral atom A as follows:

$$\mathrm{X^+ + e^- \longrightarrow A +\ Radiative\ energy}$$

In dissociative recombination, ions are lost through a two-stage process. In the first stage (charge exchange), positive ions (X^+) produced by photoionization combine with neutral molecules, A_2 (e.g., Oxygen or Nitrogen molecules) to produce positive molecular ions where one atom in the primary molecule has been substituted.

$$\mathrm{X^+ + A_2 \longrightarrow AX^+ + A}$$

In the second stage, the positive molecular ions (AX^+) resulting from the charge exchange process combine with free electrons to produce neutral atoms A and X:

$$\mathrm{AX^+ + e^- \longrightarrow A + X}$$

An important point to note is that radiative recombination is less important than dissociative recombination, which is more efficient. It should also be noted that photoionization occurs only during daytime when the Sun is above the horizon, while recombination and attachment are always happening, and take place at all ionospheric heights (McNamara, 1991).

It is well known that the neutral atmosphere is composed of a variety of atoms and molecules (e.g., Oxygen, Nitrogen, Nitric oxide) which can be photoionized. Their densities decrease with increasing altitude while the EUV radiation intensity responsible for photoionization reduces towards lower altitudes due to sunlight absorption/attenuation. A consequential result of these two opposing effects is the formation of a layer of electrons characterized by unequal electron densities at different altitudes. The maximum electron density is observed at a certain height while below and above this particular point, electron densities are lower (McNamara, 1991; Kelley, 2009). The structure of the ionosphere can be explained based on electron density variation with respect to altitude (electron density profile). The ionosphere is subdivided into different layers named D, E, and F, which cover the altitude ranges of about 50 - 85 km, 85 - 140 km, and 140 - 600 km. The high ionosphere extends from 600 km to the altitudes above (White, 1970). During daytime, F layer splits into two different layers F1 (140 - 200 km) and F2 (200 - 600 km). After sunset, photoionization ceases and recombination is the dominant mechanism. As a consequence, the D, E, and F1 layers almost disappear during nighttime while the F2 layer persists. This makes the F2 to be more appropriate for high frequency (HF) communication (McNamara, 1991). A schematic representation of daytime and nighttime structures of the ionosphere are shown in Figure 2.1 (b).

During solar quiet conditions, cosmic rays are the main source of photoionization in D layer, specifically at altitudes below 70 km, because they have sufficient energy to deeper penetrate the lower ionosphere. Above 70 km, in D and E layers, X rays and Lyaman-α UV radiation are responsible for photoionization (Rishbeth & Garriott, 1969; White, 1970). The D layer is absent during the night and typical value of the maximum electron density at noon is about 1.5×10^{10} m^{-3} in the mid-latitude, while it is 1.5×10^{11} m^{-3} in the E region, but reduces up to $<10^{10}$ m^{-3} during the night as the E layer tends to vanish completely (McNamara, 1991). For F layer, EUV radiation is the primary source of photoionization and maximum electron densities are about 2.5×10^{11} m^{-3} and 10^{12} m^{-3} at noon time for F1 and F2 layers, respectively. At midnight the F2 layer density reduces to 10^{11} m^{-3} while the F1 layer is absent at night (White, 1970; McNamara, 1991).

The electron density of a specific layer gives an idea about the frequency for HF communication. The ionospheric plasma is considered as a cold weakly ionized gas composed of electrons (lighter species) and positive ions (heavy species) in equal number (Davies, 1990; Baumjohann *et al.*, 1997). When electron gas within a slab of plasma is displaced by a small distance x from the gas of positive ions, the force acting on an electron is

$$F = m\ddot{x} = eE \tag{2.1}$$

where $m = 9.1091 \times 10^{-31}$ kg, $e = 1.6021 \times 10^{-19}$ C, and $\ddot{x}$ are the electron mass, charge, and acceleration, respectively, and E is the electric field induced by polarization of the slab of electrically neutral plasma. Given that the expression of the surface charge density is $\sigma = Q/S = (n/V)ex = Nex$, where $Q = ne$ and n are the total charge and total number of electrons within the slab, S and $V = S \times x$ are the slab surface and volume, $N = n/V$ is the electron density, the electric field is given by

$$E = -\frac{\sigma}{\epsilon_0} = -\frac{Nex}{\epsilon_0}. \tag{2.2}$$

The equation of motion of the electron is obtained by combining Equations (2.1) and (2.2)

$$\ddot{x} + \frac{Ne^2}{\epsilon_0 m}x = 0. \tag{2.3}$$

Equation (2.3) represents a simple harmonic motion with angular plasma frequency

$$\omega_p = 2\pi f_p = \left(\frac{Ne^2}{\epsilon_0 m}\right)^{1/2} \tag{2.4}$$

where f_p is the plasma frequency (Chen, 1984; Davies, 1990). Following the same procedure and considering a single-charged positive ion (charge $+e$ and mass M for a single particle), the single-charged ion angular plasma frequency is

$$\omega_{p_i} = 2\pi f_{p_i} = \left(\frac{N_i e^2}{\epsilon_0 M}\right)^{1/2} \tag{2.5}$$

where f_{p_i} is the single-charged ion plasma frequency. Comparing Equations (2.4) and (2.5) and taking into account that $N \approx N_i$ (electrically neutral plasma), it follows that

$$\frac{f_p}{f_{p_i}} = \left(\frac{M}{m}\right)^{1/2} \tag{2.6}$$

Since positive ions are much heavier than electrons ($M \gg m \Longrightarrow f_p \gg f_{p_i}$) they appear immobile compared to electrons. It can thus be assumed that the plasma oscillates at the frequency f_p given by Equation (2.4) (Davies, 1990). The same equation allows to establish the relationship between the maximum density N_m of a specific layer of the ionosphere and the critical frequency f_c of that same layer, i.e. the maximum frequency that can be reflected from that layer at vertical incidence. This is achieved by substituting all parameters with their numerical values in Equation (2.4):

$$f_c \simeq 8.98 \times 10^{-6} \sqrt{N_m} \tag{2.7}$$

where f_c is in MHz and N_m in m^{-3} (White, 1970; Chen, 1984; Davies, 1990; McNamara, 1991; Kelley, 2009).

2.3 Ionospheric total electron content

The ionospheric total electron content (TEC) is a good descriptive quantity of the Earth's ionosphere. For Global Navigation Satellite System (GNSS) observations, TEC is defined as the total number of electrons contained in a tube of a cross-sectional area of 1 m^2 extending from a satellite to a receiver on the ground (Hofmann-Wellenhof *et al.*, 1992; Misra & Enge, 2006). It is expressed in TEC unit (1 TECU = 10^{16} electrons/m^2) and computed by integrating the electron density along the signal path according to the formula:

$$TEC = \int_S^R N_e(l)dl \tag{2.8}$$

$N_e(l)$ is the electron density, R and S in the integration limits stand for receiver and satellite positions respectively, and dl is an element of distance in such a way that

$$l = \int dl \tag{2.9}$$

represents the geometric distance measured along the straight line between a satellite and receiver (Hofmann-Wellenhof *et al.*, 1992; Misra & Enge, 2006). The integration of electron density over some distance is usually known as the total electron content and varies depending on the instrumentation used to compute this quantity (McNamara, 1985; Davies, 1990). Different ways that are used to obtain TEC include but not limited to Faraday rotation (e.g., Titheridge, 1972; McNamara, 1985; Davies, 1990), ionosondes (e.g., McKinnell *et al.*, 2007), incoherent scatter radars (ISR) (e.g., Makela *et al.*, 2000), low Earth orbit (LEO) satellites (e.g., Yue *et al.*, 2011), and GPS satellites (e.g., Gao & Liu, 2002; Araujo-Pradere, 2005; Davies, 1990). All these techniques/instruments can provide TEC but within different altitude ranges. For example, Titheridge (1972) reported that Faraday rotation measurements by geostationary satellites can provide TEC up to an altitude of 2000 km. On the other hand, TEC derived from ionosonde measurements was obtained up to the altitude of 1000 km (McKinnell *et al.*, 2007), while TEC from ISR was limited to an upper altitude of 1500 km (Makela *et al.*, 2000). Furthermore, derived TEC from differential Doppler measurements on radio transmissions from the Transit 4A satellite was limited to the satellite altitude of 880 km (Bhonsle *et al.*, 1965), whereas GPS TEC is an integrated quantity from the ground up to an altitude of about 20,200 km (Makela *et al.*, 2000).

TEC is a good indicator of ionospheric variability and can be derived from satellite measurements as aforementioned. L band signals of GNSS are delayed when passing through the ionosphere and this introduces positioning error which may go up to 100 m. As the ionospheric delay experienced by a signal is proportional to TEC, mitigation of satellite positioning errors can be achieved by studying the ionospheric TEC variability (Jakowski *et al.*, 2011). In the following section, temporal and spatial variability of the ionosphere, as well as its dependence on solar activity are described based on TEC.

2.3.1 Temporal and spatial variations of TEC

The main driver of the ionospheric variability is the Sun and the rate at which the photoionization occurs depends on the solar zenith angle. TEC exhibits both temporal and spatial variations since the energy received from the Sun is unequally distributed in the Earth's atmosphere. Figure 2.2 (a)-(d) illustrates the main ionospheric TEC variations which are diurnal, seasonal, spatial (latitude/longitude) and solar activity dependence, respectively.

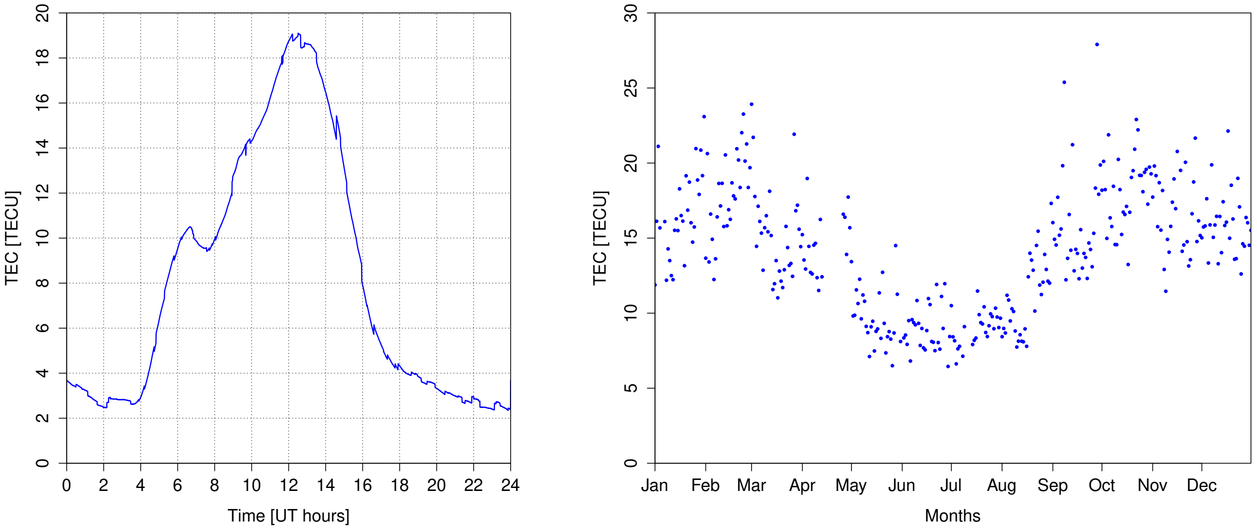

(a) Diurnal variation of TEC on 17 March 2018.

(b) Annual variation of TEC during 2017, at 10:00 UT.

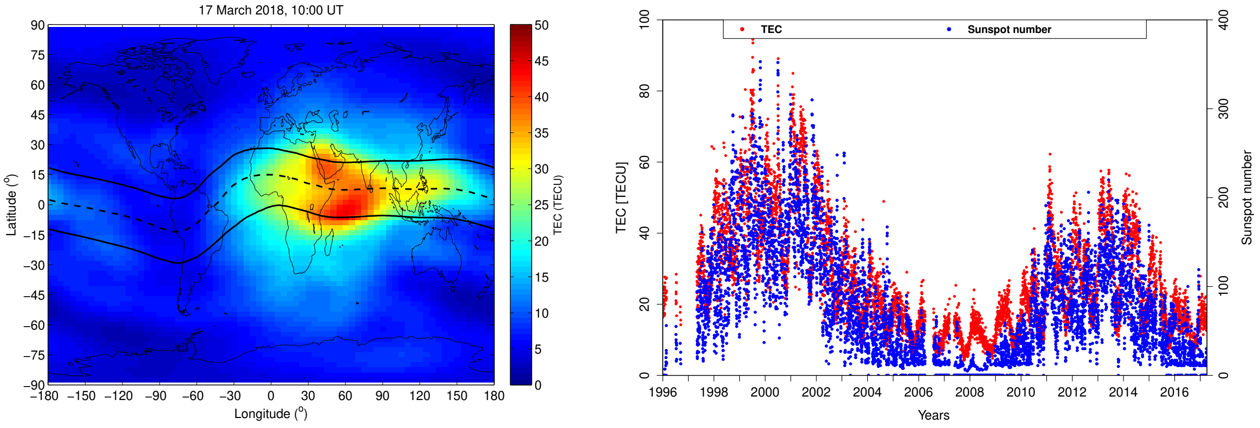

(c) Global TEC map for 17 March 2018, at 10:00 UT.

(d) TEC variation with solar activity.

Figure 2.2: (a) Diurnal variation of TEC over Hartebeesthoek (HRAO; 25.89 ° S, 27.68° E, 36.32° S, geomagnetic), South Africa, on 17 March 2018. Local time (LT) = UT + 2 hours. (b) Annual variation of TEC (only TEC values at 10:00 UT are presented) over HRAO during 2017. (c) Global TEC map for 17 March 2018 at 10:00 UT. Data used to generate the map were obtained from ftp://cddis.gsfc.nasa.gov/pub/gps/products/ionex. (d) TEC (at 10:00 UT) variation (red dots) with solar activity (represented by SSN, blue dots) over HRAO during the period 1996 - 2017.

2.3.1.1 Diurnal variation of TEC

As demonstrated in Figure 2.2 (a) which illustrates the diurnal variation of TEC over a mid-latitude station, Hartebeesthoek (HRAO; 25.89 ° S, 27.68° E, 36.32° S, geomagnetic), South Africa, on 17 March 2018, maximum TEC values are observed early afternoon (around 12:00 UT) while minimum values are observed at night. At local midday, the solar zenith angle is zero, meaning that the Sun is overhead. The solar radiation and thus, the photoionization rate, are maximum leading to higher TEC values around midday. Conversely, during nighttime, photoionization ceases and recombination and attachment dominate. The loss of electrons during nighttime is the reason for low TEC values observed after sunset until just before sunrise. A similar diurnal TEC trend has extensively been reported for different latitude locations (e.g., Davies, 1990; Bagiya *et al.*, 2009; Chauhan *et al.*, 2011; Oron *et al.*, 2013).

The morning overshoot in electron temperature T_e is another phenomenon that may influence TEC variation specifically in the early morning hours. It is a rapid increase of T_e in the early morning that occurs in the sunlit atmosphere (Stolle *et al.*, 2011). The morning overshoot has a direct effect on TEC variation in sense that when the temperature T_e increases, the recombination rate increases and consequently, TEC decreases. This could be the reason of the TEC decrease observed in the morning on 17 March 2018, between 06:00 and 08:00 (Figure 2.2 (a)).

There are physical phenomena such as pre-reversal enhancement (PRE) of the zonal electric field that cause irregular variations in electron density/TEC. The daytime eastward electric field in the E and F layers near the magnetic equator often shows a significant and sharp increase just some time before it reverses to nighttime westward direction. The suggested main cause of the PRE is the F region winds (F region dynamo) (e.g., Fejer *et al.*, 1979; Farley *et al.*, 1986), but some authors have also suggested the E region tidal winds (e.g., Walton & Bowhill, 1979). A consequential result of PRE is that, sometimes after sunset, just before the reversal of zonal electric field to westward, there is an uplifting of the F-layer which leads to an increase in TEC/electron density in low latitudes (e.g., Anderson & Klobuchar, 1983; England *et al.*, 2006; Ram *et al.*, 2006; Fagundes *et al.*, 2009).

2.3.1.2 Seasonal variation

Figure 2.2 (b) which illustrates TEC variation during 2017 (only at 10:00 UT) over HRAO, shows that maximum TEC values are observed during February - March and October - November, just around/during the equinoxial months (March and September). Davies (1990); Bagiya *et al.* (2009) reported the same observation in their study of the seasonal variation of TEC in low- and mid-latitude regions. The reason for this is that the Sun is at the zenith over the equatorial line during equinoxes and it thus shines more directly on the Earth during this period than during the rest of the year. Therefore, high TEC values around equinoxial months are a consequence of more pronounced photoionization during this period of the year. Minimum TEC values are observed during the winter season (June - August) and around the solstice months (June and December). Relatively higher values observed during summer compared to winter can be explained based on the noon solar zenith angle which is always greater in winter than the corresponding solar zenith angle in summer. This indicates that the Sun is more overhead in summer than in winter. Since the ionospheric variability is also influenced by other factors such as changes of the neutral atmosphere, the seasonal variation as described above may always not be the case.

Another feature of the seasonal variation of electron density/TEC, particularly in mid-latitude is the winter or seasonal anomaly, when daytime electron density at the F2 layer peak height ($NmF2$) is greater in winter than in summer (Davies, 1990; McNamara, 1991; Lee *et al.*, 2011). This is, however, not always the case, due to the seasonal variations exhibited by neutral atmospheric composition (McNamara, 1991).

2.3.1.3 TEC variation with latitude

The sunlight is more direct over the equatorial and low latitude regions than elsewhere. A direct consequential effect is that the photoionization rate is more pronounced over equatorial and low latitude regions than other latitude sectors, leading to higher TEC values over the equator and nearby locations. Since the intensity of solar radiation depends on the solar zenith angle, which increases as one moves towards polar regions, the sunlight hits the Earth's atmosphere at an oblique angle in the middle and high latitude regions. Thus, the rate at which photoionization occurs decreases with increasing latitude resulting in relatively lower TEC at middle and high latitudes (McNamara, 1991).

The fountain effect is a well-known phenomenon that significantly influences TEC variability in the low latitude ionosphere. The Lorentz force resulting from the E-region dayside electric field and the Earth's magnetic field lifts plasma upward to higher altitudes. As charged particles move upward, they loose part of their energy due to gravity and thus diffuse along the Earth's magnetic field lines towards mid-latitudes. A consequential net result is that, above the equatorial region, a trough of electron density is created while at about $\pm(15-20)^\circ$ from the magnetic equator crests of enhanced electron density are created. The entire region resulting from the fountain effect is called the equatorial ionization anomaly (EIA) (Appleton, 1946; McNamara, 1991; Lin *et al.*, 2007). Figure 2.2 (c) of the global TEC map at 10:00 UT shows high TEC values in the EIA within a latitudinal coverage of about $\pm 20^\circ$. As one moves farther from the EIA, TEC decreases gradually with increasing latitude.

2.3.1.4 TEC variation with solar activity

Figure 2.2 (d) illustrates the variation of TEC (shown in red dots) over HRAO for the duration of about two solar cycles (1996 - 2017). The sunspot number (SSN, shown in blue dots) as a good indicator of the activity on the Sun is also presented along with TEC values. As demonstrated in Figure 2.2 (d), TEC and SSN have similar trends with maxima and minima reached during high (1999 - 2001 and 2012 - 2014) and low (2005 - 2009) solar activity periods, respectively. Over the considered period, a correlation coefficient of about 74.51 % was found between the two quantities. A large number of sunspots at the Sun's photosphere indicates that there are many active regions which could possibly release energy towards the Earth. Solar flares are more frequent during the solar maximum and this could possibly be the reason for a higher photoionization rate and thus high TEC values during the solar maximum period (Davies, 1990). As solar flares are usually (although not always) accompanied with coronal mass ejections (CMEs), most of geomagnetic storms occurred during the solar maximum period. The dependence of geomagnetic storms on solar activity will be provided in the next chapter. Other studies that investigated the impact of solar activity on TEC found similar results (Huang & Cheng, 1995; Liu & Chen, 2009). For example, a correlation coefficient of about 0.92 between 12-month running averages of TEC and SSN was found in a study of TEC dependence on solar activity around the equatorial anomaly crest in eastern Asia (Huang & Cheng, 1995). Bagiya *et al.* (2009) reported a strong correlation between the 10.7 cm solar flux index and daytime peak TEC over near EIA crest, during solar minimum period of 2005 - 2007. A similar observation was noticed while studying the relationships between TEC over a low latitude station (Mbarara, Uganda) and F10.7 index on one hand, and SSN on the other hand, during the ascending phase of solar cycle (2010 - 2011) (Oron *et al.*, 2013).

2.4 Single particle motion in a magnetic field

When a positively charged particle q moves in a uniform magnetic field $\vec{B}$ with an initial velocity $\vec{v}$ perpendicular to the magnetic field (Figure 2.3 (a)), the magnetic force $\vec{F}_B$ of a constant magnitude qvB is perpendicular to $\vec{v}$ and $\vec{B}$. In this case, the particle is in a uniform circular motion in a plane perpendicular to $\vec{B}$ (Serway & Jewett, 2004, 2010). The radius of the particle trajectory is found by equalizing the magnetic force with centripetal force mv^2/r:

$$r = \frac{mv}{qB}. \tag{2.10}$$

m is the mass of the particle. The angular speed of the particle is

$$\begin{aligned} \omega &= \frac{v}{r} \\ &= \frac{qB}{m}, \end{aligned} \tag{2.11}$$

while the period of the motion is given by

$$T = \frac{2\pi}{\omega} = \frac{2\pi m}{qB}. \tag{2.12}$$

In the case where the initial velocity makes some arbitrary angle with respect to $\vec{B}$, the particle trajectory is a helix. Figure 2.3 (b) illustrates the case where the component v_x is in the direction of $\vec{B}$. The component of the force in the x direction (and hence, the accelaration a_x) is zero which implies that v_x remains constant. The magnetic force $\vec{F}_B = q(\vec{v} \times \vec{B})$ causes v_y and v_z to change with time, resulting in a helix motion whose axis is parallel to $\vec{B}$ (Serway & Jewett, 2004, 2010).

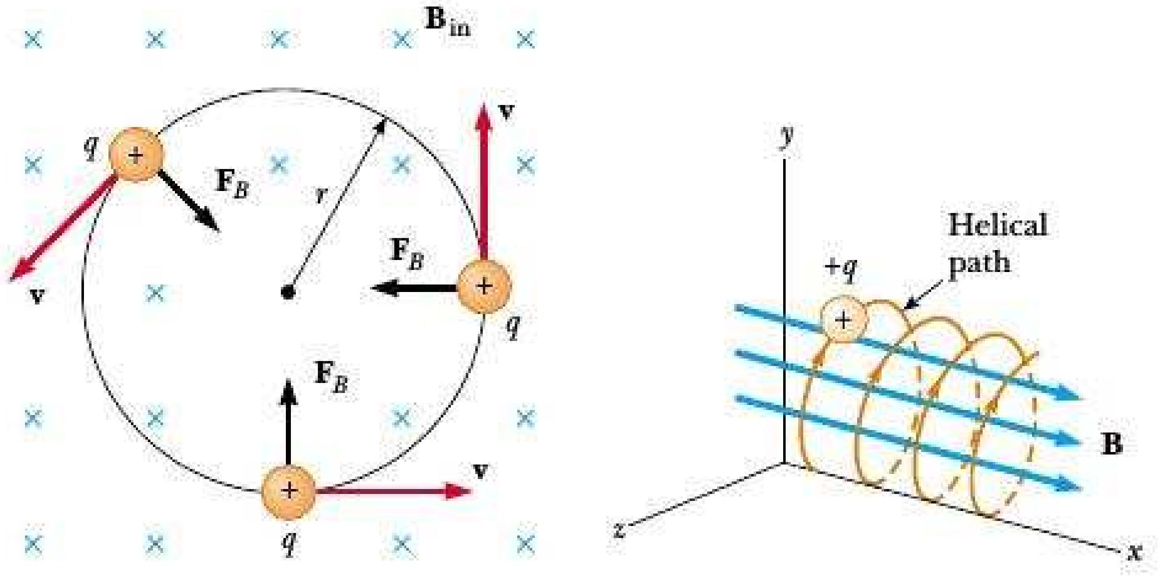

(a)

(b)

Figure 2.3: Motion of a charged particle in a uniform magnetic field: (a) initial velocity is perpendicular to the magnetic field, and (b) initial velocity makes some arbitrary angle with respect to the magnetic field (Serway & Jewett, 2004, 2010).

2.5 Solar wind and Earth's magnetosphere coupling

The solar wind consists of a stream of charged particles (mostly protons, helium nuclei, and electrons) emanating from the corona of the Sun, that travels supersonically in the interplanetary medium and carrying with it a magnetic field. The solar wind magnetic field is also called the interplanetary magnetic field (IMF) and corresponds to the Sun's magnetic field pulled out by the solar wind into the heliosphere (Moldwin, 2008). The region surrounding the Earth where the behaviour of electrically charged particles near the Earth is controlled by the Earth's magnetic field is called the magnetosphere. The boundary of the magnetosphere with outer space is defined by a balance between the magnetic pressure of the magnetosphere and solar wind pressure and is called the magnetopause (Page, 1973; Moldwin, 2008). The exact location of the magnetopause depends on the pressure exerted by the solar wind on the magnetosphere. The nominal location of the magnetopause is at ≈ 10 Earth radii on the dayside of the Earth and at a greater distance on the nightside (Rishbeth & Garriott, 1969). The magnetosphere contracts earthward or expands when the solar wind pressure increases or decreases. A schematic diagram of the Earth's magnetosphere is shown in Figure 2.4 (a) with the solar wind flow shown on the left and the north is up. Different parts of the Earth's magnetosphere are also labeled. Near the Earth, the dipole-like magnetic field region constitutes the inner magnetosphere while non dipole regions like the tail-like configuration observed on the nightside at around geosynchronous orbit (6.6 Earth radius) constitutes the outer magnetosphere (Moldwin, 2008). The region of cold and dense plasma just around the Earth and which co-rotates with the Earth is called the plasmasphere with its upper boundary called the plasmapause (Moldwin, 2008; Darrouzet *et al.*, 2009). The major constituents of the plasmasphere include Hydrogen and Helium and some amount of Oxygen. The Van Allen radiation belts often overlap with the plasmasphere.

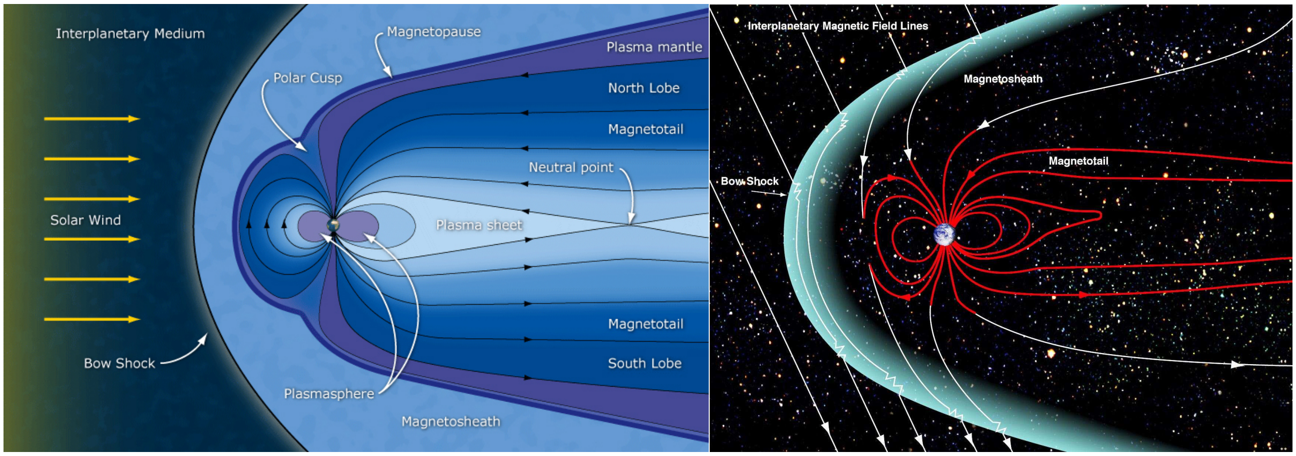

(a) Schematic diagram of the Earth's magnetosphere.

(b) Magnetic reconnection.

Figure 2.4: (a) A schematic diagram of the Earth's magnetosphere with solar wind shown on the left (`https://www.nasa.gov/mission_pages/ibex/news/spaceweather.html`), and (b) Magnetic reconnection between the solar wind and the Earth's magnetic fields (`https://www.nasa.gov/mission_pages/sunearth/multimedia/magnetosphere.html`).

When directed towards the Earth, the solar wind encounters the Earth's magnetosphere which acts as an obstacle. Due to the supersonic nature of the solar wind, a shock wave called the bow shock is formed upstream (at ≈ 3 Earth radii farther from the magnetopause, but the exact location is highly variable with solar wind Mach number) while on the nightside the magnetic field lines are stretched out and form a tail. The cylindrically-shaped region with tail-like configuration is called the magnetotail, while the region within the shock front is called the magnetosheath (Davies, 1990; Moldwin, 2008). In the case where the IMF and the Earth's magnetic field have the same orientation, the solar wind moves around the magnetosphere and its accompanying plasma does not enter the Earth's magnetosphere. Magnetic reconnection takes place when the solar wind magnetic field opposes (southward IMF) the Earth's magnetic field and there is cancellation of the magnetic field, and hence, the creation of a neutral region at the front or nose of the Earth's magnetosphere (Figure 2.4 (b)). Thus, the solar wind plasma combines with the plasma within Earth's magnetosphere (Page, 1973; Moldwin, 2008). The reconnection of the solar wind (white lines) and the Earth's magnetic fields (red lines) is illustrated in Figure 2.4 (b).

2.6 Geomagnetic and ionospheric storms

A geomagnetic storm occurs through solar wind - magnetosphere coupling via magnetic reconnection. The interaction between solar wind and its magnetic field with the Earth's magnetic field alters the Earth's magnetospheric topology. When the IMF B_z component is southward oriented (indicated by negative B_z values) for a prolonged time, as the Earth and solar wind magnetic fields are oppositely directed, the magnetosphere opens up and matter squirts in. Some of the solar wind particles trapped by the Earth's magnetic spiral around the magnetic field lines between the northern and southern poles. Under the influence of the Earth's magnetic field, trapped particles also drift around the Earth (Davies, 1990). The total motion of trapped particles generates an electric current in the form of a ring around the Earth known as ring current. The net effect at the Earth is to reduce the horizontal component of the Earth's magnetic field due to an induced magnetic field that opposes the total Earth's magnetic field. This temporary disturbance of the Earth's magnetic field caused by solar wind plasma and associated magnetic field is called a geomagnetic storm (Gonzalez *et al.*, 1994; Baumjohann *et al.*, 1997).

Four phases of a geomagnetic storm are the sudden storm commencement (SSC), an initial phase, a main phase, and a recovery phase (Gonzalez *et al.*, 1994; Campbell, 1996; Tsurutani, 2001). However, not all geomagnetic storms have necessarily all the four phases. The SSC corresponds to a sudden change in the Earth's magnetic field associated with a shock wave due to the arrival of the solar wind stream of electrically charged particles or coronal mass ejection (CME) at the Earth's magnetosphere (Gonzalez *et al.*, 1994). An increase in the solar wind ram pressure ($\sim \rho V_{sw}^2$) due to an increase in speed V_{sw} and density (ρ) at and behind the shock as the interplanetary shock wave hits the magnetosphere defines the initial phase of the storm (Tsurutani & Gonzalez, 1997). The beginning of the main phase is just when the magnetic reconnection takes place. The main phase corresponds to the period during which the solar wind charged particles are injected into the magnetosphere with effect of enhancing the ring current (Baumjohann *et al.*, 1997). The period when the loss of the ring current particles from the magnetosphere via different physical mechanisms (plasma convection, charge exchange with particles of the neutral atmosphere, Coulomb collisions and wave-particles resonant interactions) takes place corresponds to the storm recovery phase (Tsurutani, 2001).

There are two categories of geomagnetic storms to be distinguished: CME and co-rotating interaction region (CIR) driven storms (Borovsky & Denton, 2006; Denton *et al.*, 2006). A CME refers to a large volume of plasma released from the Sun's corona. When directed towards the Earth and it reaches the magnetosphere, its accompanying magnetic field interacts with the Earth's magnetic field through magnetic reconnection process. CME-driven storms are associated with solar events such as solar flares and eruptive prominences. They mostly occur during the solar maximum and are the major sources of large magnetic storms which cause more adverse societal impacts compared to CIR-driven storms (Gosling, 1993).

CIR-driven storms are numerous during the declining phase of the solar cycle and occur recurrently every 27 days (solar rotation). They are produced in response to interaction between high-speed solar wind streams emanating from the coronal holes and slow-speed solar winds in the interplanetary medium (Borovsky & Denton, 2006; Denton *et al.*, 2006). In general, CIRs are responsible for minor and moderate geomagnetic storms when they impinge on the Earth's magnetosphere (Srivastava & Venkatakrishnan, 2004; Tsurutani *et al.*, 2006a). The differences between CME- and CIR-driven storms are discussed in Borovsky & Denton (2006); Denton *et al.* (2006) and references therein.

The disturbance storm-time (Dst) index is used to characterize a geomagnetic storm. It allows identification of the storm occurrence, duration, and intensity. Normally, Dst varies around 0 nT indicating geomagnetically quiet conditions (Gonzalez *et al.*, 1994). The SCC is indicated by a positive sudden increase of Dst for CME-driven storms. Dst remains positive and relatively constant during the initial phase, while for CIR-driven storms, the onset of the initial phase occurs gradually. During the main phases of CME-related storms, Dst decreases monotonically with time until it reaches its minimum value while for CIR-related storms, their main phases are generally irregular in profiles and relatively weak in intensity (weak-to-moderate, and sometimes negligible). Generally, CIR-generated storms exhibit long recovery phases compared to CME-generated storms as monitored in Dst which increases slowly from its minimum value towards normal values around zero (Tsurutani *et al.*, 2006b). Illustrative examples of CME and CIR-driven storms based on Dst and K_p indices, solar wind proton density and speed V_{sw}, and IMF B_z component, are shown in Figure 2.5. Different storm phases based on Dst are labeled and distinguished for both category of the storms.

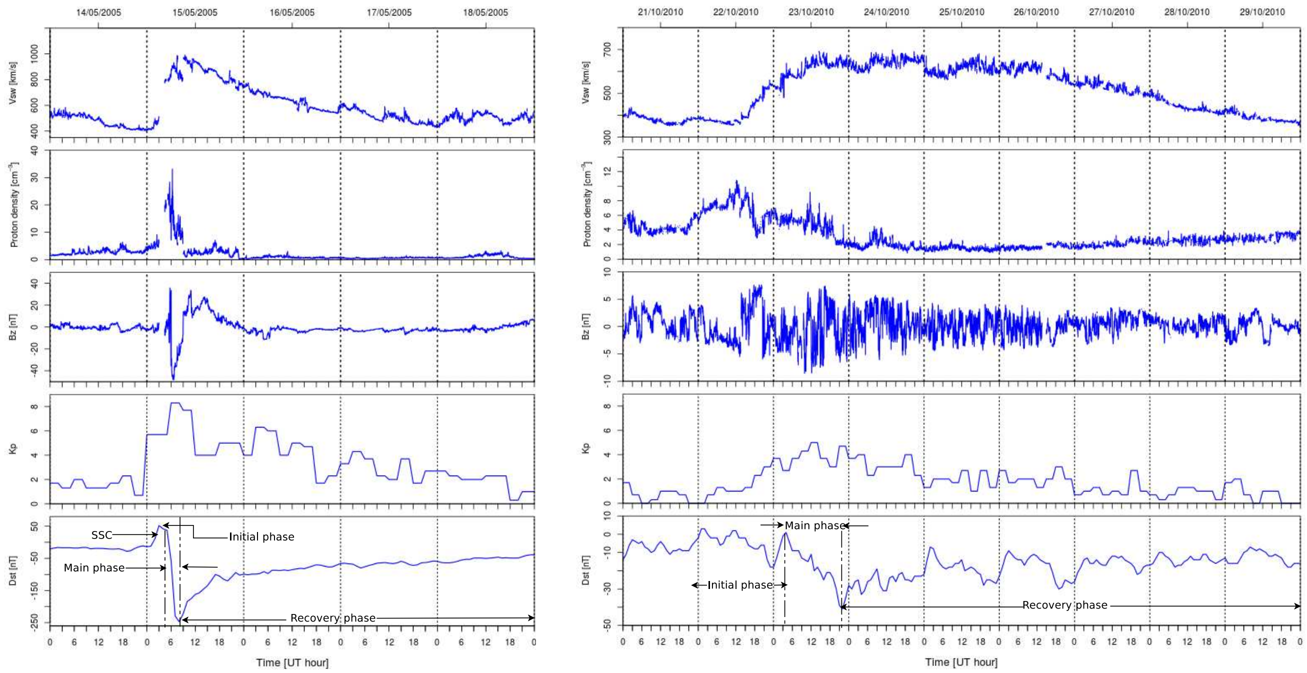

(a) CME-driven storm of 14 - 18 May 2005.

(b) CIR-driven storm of 21 - 29 October 2010.

Figure 2.5: (a) CME-driven storm of 14 - 18 May 2005, and (b) CIR-driven storm of 21 - 29 October 2010. Solar wind speed, V_{sw}, and proton density, as well as IMF B_z component are also presented along with Dst and K_p indices. Different storm phases based on Dst are labeled for each category of the storm.

The "quiet-time" magnetosphere is disturbed by solar events such as solar flares and CMEs. Such magnetospheric disturbances can, in turn, generate large changes in the ionospheric electron density distribution, TEC, and ionospheric current system. Ionospheric storms are merely the manifestations of the ionosphere in response to geomagnetic storms and substorms (Buonsanto, 1999). Ionospheric F2 region storms are known to be the most disruptive for radio communication (Davies, 1990).

2.6.1 Ionospheric responses due to geomagnetic storms

Geomagnetic storms may significantly alter the ionospheric electron density/TEC distribution. Relative to the background ionosphere, positive, negative, or non-significant storm effects correspond to an increase, decrease, or no clearly noticeable changes in electron density during the storm period (Prölss, 1980; Volland, 1995; Danilov & Lastovicka, 2001; Vijaya Lekshmi *et al.*, 2011; Ngwira *et al.*, 2012a; Habarulema *et al.*, 2013; Matamba *et al.*, 2015). The main causes of the response of the ionosphere to geomagnetic storms are discussed in the following section. Several authors identified storm-time ionospheric responses based on the monthly median TEC representation of the background ionosphere according to the formula

$$\Delta TEC = \frac{TEC_{obs} - TEC_m}{TEC_m} \times 100\% \tag{2.13}$$

where TEC_{obs} is the observed TEC during the storm and TEC_m is the monthly median TEC computed over the month when the storm occurred (e.g., Danilov & Lastovicka, 2001; Burešová & Laštovička, 2007; Matamba *et al.*, 2015, 2016; Matamba & Habarulema, 2018). A cutoff of ±45% for quiet-time TEC variability was applied and depending on whether ΔTEC falls above, below, or within this threshold, the storm phase was identified as positive, negative, or non-significant, respectively. Based on the above procedure, illustrative examples of positive, negative and non-significant storm effects are shown in Figure 2.6 for Hartebeesthoek (HRAO; 25.89 ° S, 27.68° E, 36.32° S, geomagnetic), South Africa. Dst and K_p are presented for each storm period to indicate the storm occurrence and intensity. During the period 06 - 10 September 2017, a positive storm effect was observed on 08 September 2017 as indicated by ΔTEC (red dotted lines) that exceeds 45 % (Figure 2.6 (a)). An increase in TEC is also noticeable on the same day. In contrast, a negative ionospheric response during the storm of 19 - 23 December 2015 was seen on 21 and 22 December 2015 as shown in Figure 2.6 (b) with ΔTEC slightly below -45 %. A decrease in TEC relatively to monthly median TEC was seen on 21 - 22 December 2015. A typical example of a non-significant storm effect for the 15 - 18 July 2000 storm is presented in Figure 2.6 (c). In this case, ΔTEC lies within ±45% and no significant changes in TEC magnitude are observed.

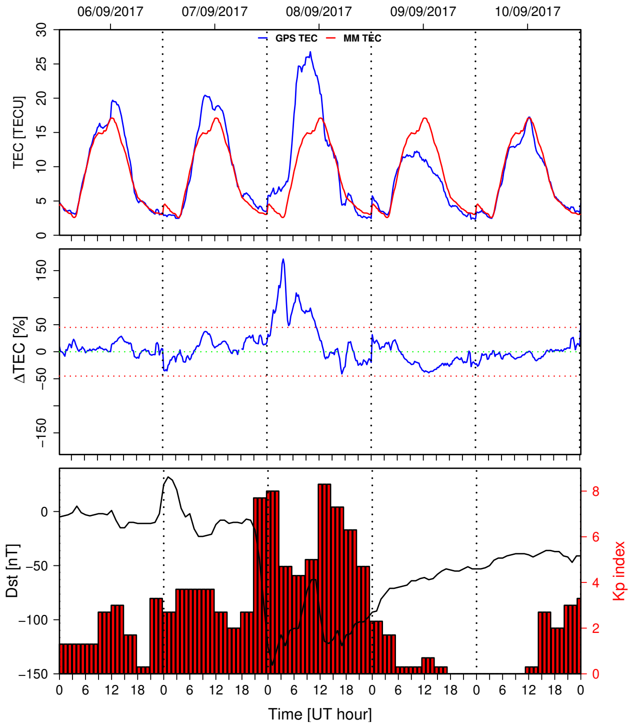

(a) Positive storm effect on 08 September 2017.

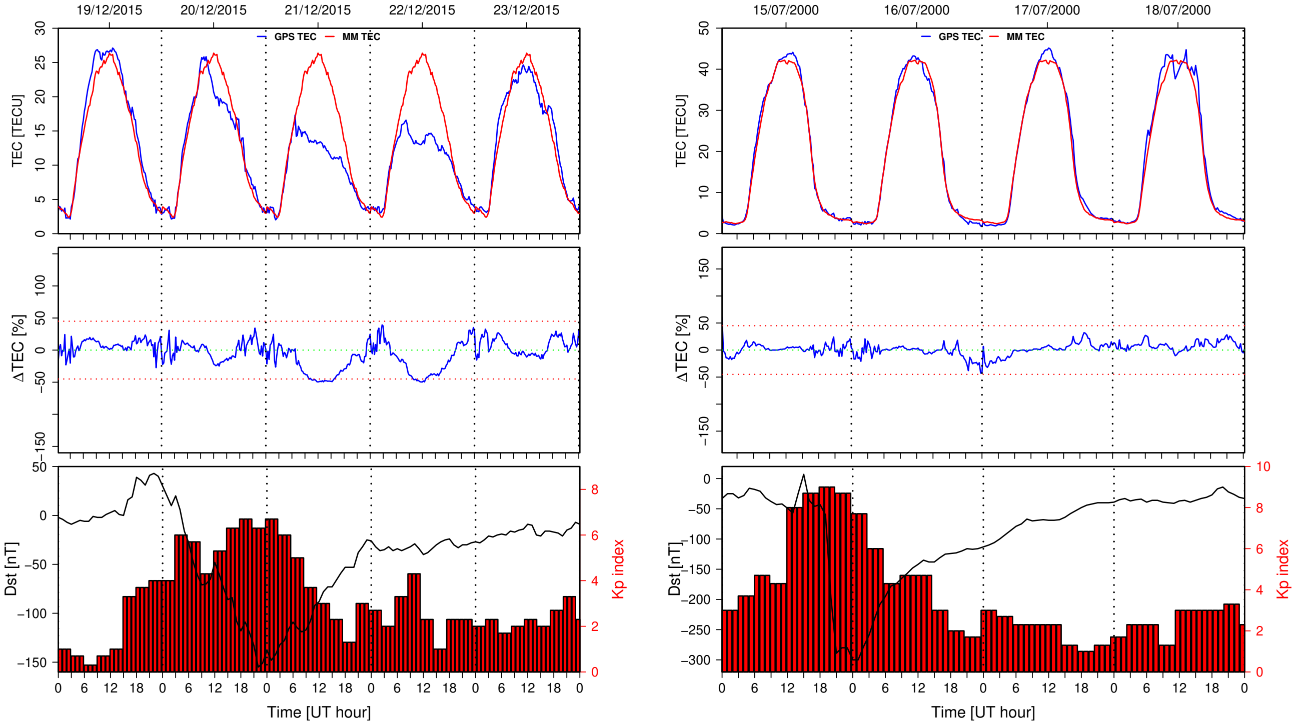

(b) Negative storm effect on 21 - 22 December 2015.

(c) Non-significant storm effect.

Figure 2.6: (a) Positive, (b) negative, and (c) non-significant storm effects as observed over Hartebeesthoek (HRAO; 25.89 ° S, 27.68° E, 36.32° S, geomagnetic), South Africa. The red line in the top panels represents the monthly median TEC (MM TEC) while the threshold of ±45% is shown by the red dotted lines in the middle panel of each storm period. Dst and K_p are also presented (bottom panel of each Figure) to indicate the storm time and intensity.

2.6.2 Driving mechanisms of ionospheric responses during storm conditions

Some of the mechanisms responsible for ionospheric responses due to geomagnetic storms are known and have long been documented (e.g., Forbes, 1989; Lu *et al.*, 2001; Lin *et al.*, 2009). Equatorward meridional neutral winds and associated travelling ionospheric disturbances (TIDs) (e.g., Forbes, 1989; Lu *et al.*, 2008), and prompt penetration electric fields (PPEFs) have been listed as the main causes of positive ionospheric responses (e.g., Forbes, 1989; Tsurutani *et al.*, 2004, 2006a; Fejer *et al.*, 2007; Tsurutani *et al.*, 2008; Negreti *et al.*, 2017). Conversely, changes in neutral gas composition have been listed to be responsible for negative ionospheric response (Forbes, 1989). Some of possible ways in which these mechanisms play a role in the responses of the ionosphere during storm conditions, will be discussed in the following sections.

2.6.2.1 Horizontal neutral winds

In the upper atmosphere and under quiet conditions, the temperature is highest near the subsolar point and lowest on the nightside. The resulting pressure difference drive neutral species (atoms and molecules) in the atmosphere from dayside to nightside. The net motion of neutral atoms and molecules from high to low pressure regions constitutes neutral winds in the atmosphere. Transport of charged particles by neutral winds is accomplished through collisions between neutral species and ions (Davies, 1990). Through collisions between neutrals and ions, the wind motion is transferred to the ions, and then to electrons by Coulomb attraction between ions of different polarities. Collisions are sufficiently numerous in the lower ionosphere (D, E, and lower F1 layers) and therefore, the plasma motion depends on neutral wind motions. In the upper ionosphere (F2 layer) where the collision frequency is relatively low, neutral winds have minimal effect on movement of ions across the Earth magnetic field (Davies, 1990). Meridional (south - north direction or vice versa) neutral winds have much effect on ionization transport since ionization can move freely along the magnetic field lines whereas zonal winds (east - west direction or vice versa) have little effect (Titheridge, 1995a). From this point of view, only the meridional winds and their effects on transport of charged particles, will be described.

Pressure gradients resulting from temperature changes at a specific height were highlighted as the main driver of neutral winds in the atmosphere. The absorption of the extreme ultraviolet (EUV) solar radiation is thought to be the major heat source at heights above 150 km (F region), while at high latitudes, the main heat sources are particle precipitation and large-scale convection of the magnetic field lines. Precipitating particles produce a continual ionisation which heats D and E regions at high latitudes during geomagnetically quiet conditions, while during geomagnetic storms the heat increases and extends to low latitudes (Titheridge, 1995b). Since winds blow from high pressure (high temperature) regions to low pressure (low temperature) regions, due to the high intensity of EUV radiation received in the low latitude region, the Earth's atmosphere is warmer in this region than elsewhere, resulting in the overall poleward motion of winds. On the other hand, particle precipitation and Joule heating at high latitudes cause a global motion of winds from both polar regions to low latitudes and into the opposite hemisphere (Fuller-Rowell *et al.*, 1994; Titheridge, 1995b). Another global wind motion is the seasonally-dependent transequatorial winds which blow from the summer hemisphere to winter hemisphere at low latitudes (Titheridge, 1995b).

While equatorward winds have a component directed upward along the Earth's magnetic field line, poleward winds have a component directed downward. As a consequence, equatorward winds lift ionisation to higher altitudes while poleward winds move down ionisation to lower altitudes. The lifted ionisation adds to the existing ionisation at higher altitudes and this increase in ionisation produces a large decrease in the overall loss rate. On the other hand, the ionisation that moves to low altitudes decays more rapidly due to the recombination process (Prölss, 1980; Fuller-Rowell *et al.*, 1994; Titheridge, 1995a). For a horizontal wind in the direction of the magnetic meridian with velocity W, only the component $WcosI$ parallel to the the Earth's magnetic field B, affects the ionisation (Titheridge, 1995a). Thus, the vertical drift of the ionisation has the component $WcosIsinI$ or equivalently, the effect of the horizontal wind on ionisation is the same as the effect that a vertical wind V would have, such that

$$\begin{aligned} V &= WcosIsinI \\ &= \frac{1}{2}Wsin2I \end{aligned} \tag{2.14}$$

where I represents the magnetic dip angle (or inclination angle) (Titheridge, 1995a; Lu *et al.*, 2008). Equation (2.14) shows that the effect of meridional winds in lifting or lowering plasma depends on latitude since the magnetic dip angle changes. Such an effect is zero at the magnetic equator ($I = 0°$) and at the south and north magnetic poles ($I = 90°$), and maximum at $I = 45°$.

During geomagnetic storms, the increased energy input at high latitudes due mainly to particle precipitation and Joule heating causes the atmosphere to heat and then expand. The resulting equatorward winds move ionisation up the magnetic field lines to regions of lower recombination, and therefore, enhanced electron density/TEC is observed (Fedrizz *et al.*, 2008; Kintner *et al.*, 2008; Ngwira *et al.*, 2012a). For some storms, studies have shown that the primary cause of the positive storm response is the meridional wind (Lu *et al.*, 2001; Yuan *et al.*, 2003; Lu *et al.*, 2008). The coexistence of positive and negative storm responses in opposite hemispheres has been interpreted as the result of transport of ionisation across the dip equator by the storm-generated transequatorial winds which depletes electron density from the upwind hemisphere and enhances it in the downwind hemisphere (Fesen *et al.*, 1989; Lu *et al.*, 2001).

2.6.2.2 Travelling ionospheric disturbances

Atmospheric gravity waves (AGWs) generated due to a perturbed high latitude atmosphere, manifest themselves through the atmosphere as wavelike structures called travelling atmospheric disturbances (TADs) and in the ionosphere as travelling ionospheric disturbances (TIDs) (Hines, 1959; Borries *et al.*, 2009; Ngwira *et al.*, 2012b; Borries *et al.*, 2016). TIDs can be monitored in TEC during geomagnetic storms. A study based on numerical simulations has shown that neutral winds and the passage of TADs are the main causes of the storm positive phase (Namgaladze *et al.*, 2000). TADs carry along equatorward neutral winds that lift charged particles to higher altitudes. As a consequence, positive ionospheric storms are observed at middle or low latitudes during the passage of TIDs (Yuan *et al.*, 2003). There exists cases where the positive ionospheric effects due to geomagnetic storms were thought to be caused by TIDs (Ngwira *et al.*, 2012b; Habarulema *et al.*, 2013). Studies have also reported the presence of TIDs during geomagnetic storms and their possible sources and effects on the ionosphere (Katamzi & Habarulema, 2013; Habarulema *et al.*, 2015, 2016, 2018). A shift in TEC enhancement from station to another within the same longitude sector during the storm period of 7 - 12 November 2004 has been partly attributed to the passage of TIDs (Habarulema *et al.*, 2013). TEC enhancements observed during the mid-latitude magnetic storm of 15 May 2005 were believed to be caused by neutral winds as well as the passage of TIDs (Ngwira *et al.*, 2012b).

2.6.2.3 Storm induced electric field

Prompt penetration electric fields (PPEFs) and long-lasting ionospheric disturbance dynamo electric fields (DDEFs) are two main causes of changes in plasma drifts and currents in the ionosphere under geomagnetically disturbed conditions (Blanc & Richmond, 1980; Scherliess & Fejer, 1997; Negreti *et al.*, 2017). Neutral winds together with diurnal and semi-diurnal tidal components in the atmosphere produce the so-called Sq (solar quiet) wind dynamo current that flows in the E region (about 100 - 120 km). The resulting electric field from this current is directed eastward from dawn to dusk and westward during nighttime at low latitudes and plays a significant role in transport of the plasma in the equatorial region, upward during daytime and downward during nighttime (Anderson *et al.*, 2006). The equatorial daytime electric field variations in the ionosphere depend on local time, location, season, and solar activity. Apart from this, the solar wind interplanetary electric field (IEF) variations have a direct influence on equatorial electric field perturbations as reported by Kelley *et al.* (1979); Scherliess & Fejer (1999) and Manoj *et al.* (2008). PPEF is an abrupt appearance of the IEF in the Earth's ionosphere and magnetosphere, immediately after being convected to the magnetosphere by the solar wind (Manoj *et al.*, 2008; Tsurutani *et al.*, 2008). PPEF has a direct influence on the equatorial $E \times B$ drift as it reinforces the fountain effect. As consequence, the enhanced fountain effect transports plasma from low to higher latitudes (Tsurutani *et al.*, 2004). A couple of studies on ionospheric responses due to geomagnetic storms have suggested PPEFs as one of the main causes of positive storm effect (e.g., Forbes, 1989; Tsurutani *et al.*, 2004, 2006a; Fejer *et al.*, 2007; Lu *et al.*, 2008; Tsurutani *et al.*, 2008; Singh & Sripathi, 2017; Negreti *et al.*, 2017). As an example, during the severe storm of 30 - 31 October 2003, it was found that the dayside equatorial and near-equatorial ionosphere was lifted to higher altitudes and latitudes where the recombination rate is lower due to PPEFs. The scenario was that, due to enhanced eastward electric field that reinforced the fountain effect (superfountain effect), crests of the EIA region expanded towards the mid-latitudes resulting in TEC enhancement (Tsurutani *et al.*, 2004). A similar observation was reported for the St. Patrick's Day storm of 17 - 18 March 2015 (Astafyeva *et al.*, 2015).

2.6.2.4 Changes in neutral gas composition

Negative and sometimes positive storms effects are caused by neutral composition changes (Prölss, 1980; Buonsanto *et al.*, 1989; Forbes, 1989; Fuller-Rowell *et al.*, 1994; Zhang *et al.*, 2004; Habarulema *et al.*, 2013; Katamzi & Habarulema, 2013; Astafyeva *et al.*, 2015). In response to the solar wind energy input at high latitudes, Joule heating over auroral latitudes increases. Induced equatorward winds due to the increase in pressure gradient reinforce the normal equatorward wind on the nightside while it weakens or even reverses the poleward wind on the dayside. The overall wind circulation therefore transports molecular air from high to lower latitudes leading to enriched molecular Nitrogen (N_2) and atomic Oxygen (O) densities at the middle and low latitude regions, respectively (Mendillo, 2006). Analysis of the ionospheric responses during the storm of 06 - 11 November 2004 have shown that the increase and significant depletion in O/N_2 were responsible for the positive and negative storm phases (Habarulema *et al.*, 2013). It was further found that a decrease in TEC observed during mid-latitude storms correlated well with a decrease in the O/N_2 ratio (Habarulema *et al.*, 2013; Katamzi & Habarulema, 2013). A significant depletion in O/N_2 was also noticed by Zhang *et al.* (2004) in their study of the storms of 01 - 04 October 2002.

2.7 Summary

This chapter briefly described the Earth's atmosphere, ionosphere and magnetosphere, with emphasis on TEC and its behaviour during geomagnetic storms. Mechanisms responsible for ionospheric responses during storm conditions were briefly discussed as well. In the next chapter, data sources and mathematical approaches exploited during TEC modelling are described.

Chapter 3

Data sources and modelling techniques

TEC, considered as observational data for the implementation and validation of the models, were derived from measurements provided by Global Navigation Satellite Systems (GNSS), and more precisely, the Global Positioning System (GPS) receiver stations. In this chapter, a brief introduction to the GNSS network with emphasis on GPS satellites is presented. Then, the main steps involved in TEC derivation, and the inputs for the storm-time models, are discussed. A summary of two climatological models, namely the International Reference Ionosphere (IRI) and the Horizontal Wind Model (HWM), used in the current work, is provided. Furthermore, the fundamentals of the Multi-Instrument Data Analysis System (MIDAS), which is an inversion algorithm for ionospheric tomography, are provided. This chapter ends with a brief description of different mathematical/modelling approaches explored for storm-time TEC modelling, namely empirical orthogonal functions (EOF) analysis, non-linear regression analysis (NLRA), the Metropolis-Hastings algorithm (MHA), and artificial neural networks (ANNs).

3.1 Global Navigation Satellite Systems (GNSS)

The term Global Navigation Satellite Systems (GNSS) refers to a variety of constellations of satellites launched by different governments with navigation as the primary objective. GNSS mainly comprises the Global Positioning Systems (GPS), controlled by the U.S. Department of Defense (DoD), Global'naya Navigatsionnaya Sputnikovaya Sistema (GLONASS) under control of the Russian Federation, BeiDou Navigation Satellite System (BDS), which is a Chinese satellite navigation system, Galileo with the European Union in charge, Quasi-Zenith Satellite System (QZSS) which is a Japanese satellite constellation, and the Indian Regional Navigation Satellite System (IRNSS) (Kaplan & Hegarty, 2006; Misra & Enge, 2006; Gleason & Gebre-Egziabher, 2009; Van Diggelen, 2009). The most widely used GNSS for Navigation is the Global Positioning Systems (GPS) which determines with high accuracy, the position, velocity, and in some cases, the attitude (or object orientation) of an object (or user) in space or on the Earth, by processing signals transmitted from satellites in known orbits (Misra & Enge, 2006). The following description will be limited to GPS satellites, given that TEC data used in this study were derived from GPS measurements.

3.1.1 GPS satellites

The GPS structure consists mainly of three parts, namely space, control, and user segments. The space segment consists of a baseline of 24 satellites, each at a nearly circular orbit with a radius of about 20,200 km, and with a period of about 12 hours. The GPS constellation has six orbital planes inclined at 55° with respect to the Earth's equatorial plane (Farrell & Barth, 1999). There are various ways to identify a satellite in the entire constellation. For example, a unique pseudorandom noise (PRN) code acts as a satellite identifier. A PRN-code is assigned to each satellite in the constellation and when the satellite transmits a signal, the decoded signal at the receiver location allows the user to identify the satellite (Hofmann-Wellenhof *et al.*, 1992). Another means of identification is by orbital number specification. A two-character code composed of a letter that identifies the orbital plane (from A to F as six orbits are available) and a number that specifies the satellite number in plane (from 1 to 4 as there are four satellites per orbit for the baseline constellation). For example, an identifier A4 indicates satellite number 4 in the orbital plane A (Misra & Enge, 2006). The constellation is designed in such a way that at least four satellites are visible at a given time and anywhere in the world. However, it may sometimes happen that the user observes six to eight satellites. Each individual satellite transmits synchronized signals and only signals from satellites in view are received by a user at slightly different times since satellites are different distances away. The receiver can thus calculate the position of the user with high accuracy (Farrell & Barth, 1999; Misra & Enge, 2006). The baseline GPS constellation is illustrated in Figure 3.1.

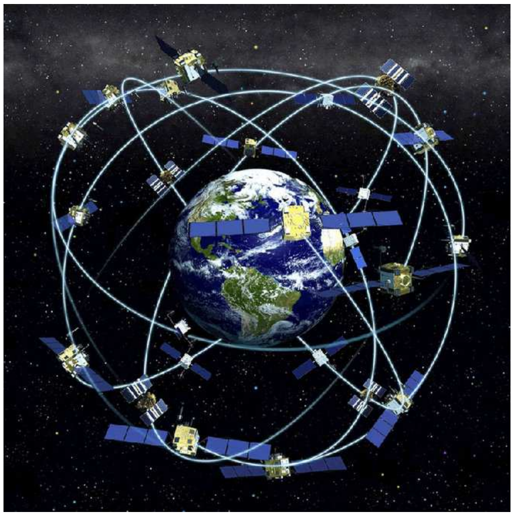

Figure 3.1: Baseline GPS constellation consisting of 24 satellites in orbital planes inclined at about 55° with respect to the Earth's equatorial plane. Credit: National Oceanic and Atmospheric Administration (NOAA) (`https://celebrating200years.noaa.gov/transformations/gps/Figure_1.html`).

The GPS control segment consists basically of a system of tracking stations, a Master Control Station (MCS), monitor stations, and ground antennas, with a primary objective of monitoring the status and health of the space segment. The MCS is responsible for satellite operation and provides commands and control functions. Monitor stations provide useful data for satellite orbit tracking and clock bias estimations while, ground antennas are used to communicate with the satellites. The GPS user segment consists of GPS receiver equipment, such as antennas and receiver-processors. The signals transmitted by GPS satellites are received via antennas and decoded by receiver-processors which specify the user position and velocity, as well as the precise timing information (French, 1996; Farrell & Barth, 1999; Misra & Enge, 2006).

3.1.1.1 Dual-frequency GPS signals

One of the frequency bands of the radio spectrum is the Ultra High Frequency (UHF) band which covers a frequency range of 0.3 - 3 GHz. The L-band, with a frequency range of 1 - 2 GHz is a subset of the UHF band and signals transmitted by GPS satellites are within this band. GPS satellite signals are continuously transmitted using two radio frequencies in the L-band commonly known as Link 1 (L1) and Link 2 (L2) and centered at $f_{L_1} = 1575.42$ MHz (for L1) and $f_{L_2} = 1227.60$ MHZ (for L2). f_{L_1} and f_{L_2} are derived from a fundamental frequency $f_0 = 10.23$ MHz such that $f_{L_1} = 154f_0$ and $f_{L_2} = 120f_0$ (Hofmann-Wellenhof *et al.*, 1992; Misra & Enge, 2006; Borre *et al.*, 2007). The three components of GPS signals are the carrier, codes, and navigation data/messages. The carrier consists of a sinusoidal radio wave/signal with frequency f_{L_1} or f_{L_2}. Codes are specific characteristic for each satellite and comprise the coarse/acquisition (C/A) and precision (P(Y)) codes. The C/A-code is reserved for civilians and is purposely modulated on L1 only, whereas the P-code is modulated on both L1 and L2 and is for US military and authorized users (Hofmann-Wellenhof *et al.*, 1992). Navigation data are binary-coded messages that comprises data related to satellite health status, ephemeris data used for satellite position and velocity computation, and other information, known as almanac, which concerns the status of the whole satellite constellation (Misra & Enge, 2006; Borre *et al.*, 2007).

3.1.1.2 Ionospheric effect on GPS signals

Radio signals from GPS satellites at an altitude of about 20,200 km are received by antennas at GPS receivers. Due to the non-uniform composition of the ionosphere, the refractive index of the medium varies along the signal path. Thus, multiple refractions experienced by GPS signals make the signal path to become longer than the geometrical straight-line path from the satellite to receiver. As a consequential observation, the time it takes a GPS signal to travel from the satellite to receiver is longer than the time it would have taken the same signal through vacuum (Misra & Enge, 2006). The time delay experienced by a GPS signal with frequency f is directly proportional to TEC encountered along the signal path, and inversely proportional to the square of the signal frequency (Hofmann-Wellenhof *et al.*, 1992). Thus, the ionospheric TEC encountered by GPS signals is the main source of positioning error particularly for single-frequency users (Araujo-Pradere, 2005). Mathematically, the travel time of a radio signal from satellite to receiver is found by integrating the refractive index profile $n(l)$ along the signal path (Misra & Enge, 2006):

$$\tau = \frac{1}{c}\int_S^R n(l)dl \tag{3.1}$$

where $c = 299,792,458$ m.s^{-1} is the speed of light in a vacuum and $n(l)$ is the variable refractive index along the signal path. It is obvious that the time it would have taken the signal to travel the same distance in a vacuum ($n(l) = 1$) is

$$\tau_0 = \frac{1}{c}\int_S^R 1 \cdot dl. \tag{3.2}$$

The difference $\Delta\tau = \tau - \tau_0$ represents the time delay in the signal propagation due to refraction and is equal to

$$\Delta\tau = \frac{1}{c}\int_S^R [n(l) - 1]dl \tag{3.3}$$

while the corresponding excess in path length is (Araujo-Pradere, 2005; Misra & Enge, 2006)

$$\begin{aligned} \Delta\rho &= c\Delta\tau \qquad (3.4) \\ &= \int_S^R [n(l) - 1]dl \end{aligned}$$

The ionosphere as a dispersive medium, the refractive index and the wave propagation speed depend on the signal frequency. The relation of dispersion of the ionosphere as a function of the plasma angular frequency $\omega_p = 2\pi f_p$, and electromagnetic signal angular frequency $\omega = 2\pi f$ is given by (Crawford, 1968):

$$\omega^2 = c^2k^2 + \omega_p^2. \tag{3.5}$$

The quantities $k = 2\pi/\lambda$, f, and f_p, are the wave number, the signal and plasma frequencies respectively, and λ is the wavelength of the electromagnetic signals. The plasma frequency f_p is the ionospheric characteristic/critical frequency for radio wave propagation through the ionosphere in a sense that signals with $\omega > \omega_p$ cross the ionosphere while signals with $\omega < \omega_p$ are reflected by the ionospheric medium (Davies, 1990; McNamara, 1991). From the Equation (3.5), the phase and group velocities are given by (Wells *et al.*, 1987)

$$\begin{aligned} v_{ph} &= \frac{\omega}{k} \\ &= \frac{c}{\sqrt{1 - \left(\frac{\omega_p}{\omega}\right)^2}} \end{aligned} \tag{3.6}$$

and

$$\begin{aligned} v_{gr} &= \frac{d\omega}{dk} \\ &= c\sqrt{1 - \left(\frac{\omega_p}{\omega}\right)^2} \end{aligned} \tag{3.7}$$

The refractive index of a medium ($n = c/v$) being defined as the ratio of the speed of propagation of the signal in a vacuum to the speed of propagation of the signal in that medium, v, (Hofmann-Wellenhof *et al.*, 1992), the phase and group refractive indices of the ionosphere can be expressed as

$$\begin{aligned} n_{ph} &= \frac{c}{v_{ph}} \\ &= \sqrt{1 - \left(\frac{\omega_p}{\omega}\right)^2} \end{aligned} \tag{3.8}$$

and

$$\begin{aligned} n_{gr} &= \frac{c}{v_{gr}} \\ &= \frac{1}{\sqrt{1 - \left(\frac{\omega_p}{\omega}\right)^2}} \end{aligned} \tag{3.9}$$

Substituting ω_p/ω by f_p/f into Equations (3.8) and (3.9), and using the approximation $(1+x)^\alpha \simeq 1 + \alpha x$, for $|x| \ll 1$, which is the case for the ratio f_p/f, the phase and group refractive indices are expressed as follows (Wells *et al.*, 1987):

$$n_{ph} \approx 1 - \frac{1}{2}\left(\frac{f_p}{f}\right)^2 \tag{3.10}$$

$$n_{gr} \approx 1 + \frac{1}{2}\left(\frac{f_p}{f}\right)^2 \tag{3.11}$$

Replacing the plasma frequency by its expression provided by Equation (2.4) (after substituting all parameters by their numerical values which leads to $f_p = 8.98\sqrt{N_e}$ with f_p in Hertz and N_e in m^{-3}) in Equations (3.10) and (3.11) we get

$$n_{ph} = 1 - \frac{40.3}{f^2} N_e \tag{3.12}$$

$$n_{gr} = 1 + \frac{40.3}{f^2} N_e \tag{3.13}$$

Comparing Equations (3.12) and (3.13), it can be noticed that $n_{gr} > n_{ph}$ which indicates that $v_{gr} < v_{ph}$. Thus, GPS code measurements are delayed while carrier phase measurements are advanced (Hofmann-Wellenhof *et al.*, 1992).

Substituting Equations (3.12) and (3.13) into Equations 3.3 and 3.4 and considering Equation 2.8, it follows that the excess phase delay (in seconds) experienced by a signal as it propagates through the ionosphere is (Hofmann-Wellenhof *et al.*, 1992; Misra & Enge, 2006)

$$\begin{aligned} \Delta\tau_{ph} &= \frac{1}{c}\int_S^R [n_p(l) - 1]dl \\ &= -\frac{1}{c}\int_S^R \frac{40.3 N_e(l)}{f^2} dl \\ &= -\frac{40.3}{cf^2} \cdot TEC \end{aligned} \tag{3.14}$$

while the corresponding excess phase delay (in meters) is

$$\begin{aligned} I_\Phi &= c\Delta\tau_{ph} \\ &= -\frac{40.3}{f^2} \cdot TEC. \end{aligned} \tag{3.15}$$

In a similar way, the group delay (in seconds) is given by

$$\Delta\tau_{gr} = \frac{40.3}{cf^2} \cdot TEC \tag{3.16}$$

and when expressed in meters, it becomes

$$\begin{aligned} I_\rho &= c\Delta\tau_{gr} \\ &= \frac{40.3}{f^2}\cdot TEC \end{aligned} \tag{3.17}$$

Except opposite signs, both ionospheric delay terms for measurements of carrier phase (Equation (3.15)) and pseudorange (Equation (3.17)) are equal in magnitude. The negative sign in Equation (3.15) indicates that the phase is advanced, while the appellation "group delay" is justified by the positive sign in Equation (3.17). On 17 March 2018, the peak TEC value was about 19.5 TECU and the corresponding excess phase delays on L1 and L2 are -3.17 m and -5.21 m, respectively, while the group delays are 3.17 m and 5.21 m for L1 and L2.

3.1.2 Deriving TEC from GPS measurements

In GPS theory, the observable refers to things being measured, while the measurement itself is known as the observation. The two types of observables are the pseudorange and the carrier phase. The pseudorange measurement consists of estimating the apparent satellite-receiver distance/range by taking into account the geometric distance between satellite and a receiver, path delays, as well as the effects of the satellite and receiver clock errors. The carrier phase measurement consists of estimating the apparent distance between a satellite and receiver in terms of cycles of the carrier frequency. However, it is not possible for the receiver to measure directly the total number of carrier cycles between a given satellite and a receiver. What can rather be measured is a change in the number of the carrier cycles (Farrell & Barth, 1999). TEC can be derived from GPS pseudorange or carrier phase measurements and literature on deriving TEC from GPS measurements is available (e.g., Gao & Liu, 2002; Araujo-Pradere, 2005; Carrano & Groves, 2009).

3.1.2.1 Deriving TEC from pseudorange measurements

The pseudorange observation equations are (Carrano & Groves, 2009):

$$P_1 = \rho + c(\triangle t_r - \triangle t_s) + I_1 + T + b^P_{1r} + b^P_{1s} + m^P_1 + \varepsilon^P_1 \tag{3.18}$$

and

$$P_2 = \rho + c(\triangle t_r - \triangle t_s) + I_2 + T + b^P_{2r} + b^P_{2s} + m^P_2 + \varepsilon^P_2 \tag{3.19}$$

where the subscripts 1 and 2 refer to L1 ($f_{L_1} = 1575.42 \times 10^6$ Hz) and L2 ($f_{L_2} = 1227.60 \times 10^6$ Hz) respectively. P is the pseudorange (m), ρ is the geometric range (m), $\triangle t_r$ and $\triangle t_s$ are the receiver and satellite clock errors (s), I and T are the ionospheric and tropospheric delays (m), b_r and b_s are instrumental biases for receiver and satellite, m^P is the multipath effect (m), and ε^P represents the thermal noise (m). From Equations (3.18) and (3.19) it follows that

$$\begin{aligned} P_2 - P_1 &= I_2 - I_1 + (b^P_{2r} - b^P_{1r}) + (b^P_{2s} - b^P_{1s}) \\ &= I_2 - I_1 + b^P_r + b^P_s \end{aligned} \tag{3.20}$$

where the multipath and thermal noise terms are neglected, and the geometric range, clock error and tropospheric terms cancel through subtraction. Using Equation (3.17) for the GPS dual signals into (3.20) and solving for TEC, we get

$$\begin{aligned} TEC &= \frac{1}{40.3}\left[\frac{f^2_{L_1} f^2_{L_2}}{f^2_{L_1} - f^2_{L_2}}\right][(P_2 - P_1) - (b^P_r + b^P_s)] \\ &= 9.52 \times 10^{16}[(P_2 - P_1) - (b^P_r + b^P_s)] \end{aligned} \tag{3.21}$$

in electron/m^2. When expressed in TECU, the expression of TEC derived from the pseudorange measurements is

$$TEC = 9.52[(P_2 - P_1) - (b^P_r + b^P_s)]. \tag{3.22}$$

The pseudorange TEC (without bias terms) is defined as (Carrano & Groves, 2009; Araujo-Pradere, 2005)

$$TEC_P = 9.52(P_2 - P_1). \tag{3.23}$$

Although TEC_P is unambiguous, it is noisy and thus inaccurate/imprecise quantity (Carrano & Groves, 2009).

3.1.2.2 Deriving TEC from carrier phase measurements

The carrier-phase observation equations are (Carrano & Groves, 2009)

$$\Phi_1 = \rho + c(\triangle t_r - \triangle t_s) + I_1 + T + b^\Phi_{1r} + b^\Phi_{1s} + \lambda_1 N_1 + m^\Phi_1 + \varepsilon^\Phi_1 \tag{3.24}$$

and

$$\Phi_2 = \rho + c(\triangle t_r - \triangle t_s) + I_2 + T + b^\Phi_{2r} + b^\Phi_{2s} + \lambda_2 N_2 + m^\Phi_2 + \varepsilon^\Phi_2. \tag{3.25}$$

With subscripts 1 and 2 referring to L1 and L2 GPS signals, Φ is the carrier phase (m), λ is the GPS signal wavelength (m), and N is the phase cycle ambiguity. In a similar manner as previously discussed, subtracting Equation (3.25) from Equation (3.24) yields

$$\begin{aligned}\Phi_1 - \Phi_2 &= I_1 - I_2 + (b_{1r}^{\Phi} - b_{2r}^{\Phi}) + (b_{1s}^{\Phi} - b_{2s}^{\Phi}) + (\lambda_1 N_1 - \lambda_2 N_2) \\ &= I_1 - I_2 + b_r^{\Phi} + b_s^{\Phi} + (\lambda_1 N_1 - \lambda_2 N_2)\end{aligned} \tag{3.26}$$

Using the expression of the ionospheric phase advance (Equation (3.15)) for both GPS signal frequencies gives

$$\Phi_1 - \Phi_2 = I_1 - I_2 + 40.3\left(\frac{1}{f_{L_2}^2} - \frac{1}{f_{L_1}^2}\right) TEC + b_r^{\Phi} + b_s^{\Phi} + (\lambda_1 N_1 - \lambda_2 N_2) \tag{3.27}$$

Solving this equation for TEC yields

$$TEC = \frac{1}{40.3}\left[\frac{f_{L_1}^2 f_{L_2}^2}{f_{L_1}^2 - f_{L_2}^2}\right][(\Phi_1 - \Phi_2) - (b_r^P + b_s^P) - (\lambda_1 N_1 - \lambda_2 N_2)] \tag{3.28}$$

$$= 9.52 \times 10^{16}[(\Phi_1 - \Phi_2) - (b_r^P + b_s^P) - (\lambda_1 N_1 - \lambda_2 N_2)]$$

in electron/m^2. Expressing Equation (3.28) in TECU, it becomes

$$TEC = 9.52[(\Phi_1 - \Phi_2) - (b_r^P + b_s^P) - (\lambda_1 N_1 - \lambda_2 N_2)] \tag{3.29}$$

The phase TEC is defined by

$$TEC_{\Phi} = 9.52(\Phi_1 - \Phi_2) \tag{3.30}$$

which is ambiguous but precise (Araujo-Pradere, 2005; Carrano & Groves, 2009).

3.1.2.3 Mapping from slant to vertical TEC

TEC measured along the signal path from satellite to receiver is called Slant Total Electron Content (STEC). Vertical TEC (VTEC) refers to TEC encountered along the vertical/zenith direction (overhead direction). Through the ionosphere, the path length in the zenith direction is the shortest and thus, VTEC is lower compared to STEC. Conversion from STEC to VTEC is performed with the assumption that the ionosphere is a single thin shell at the mean ionospheric height h_I (usually assumed to be in the range 300 km - 400 km) (Hofmann-Wellenhof *et al.*, 1992; Gao & Liu, 2002; Misra & Enge, 2006). The intersection of the line of sight between GPS receiver and the observed satellite with the thin shell ionosphere is called the ionospheric pierce point while its perpendicular projection onto the Earth's surface is called the subionospheric point. Figure 3.2 is a typical geometric representation of the thin-shell ionosphere.

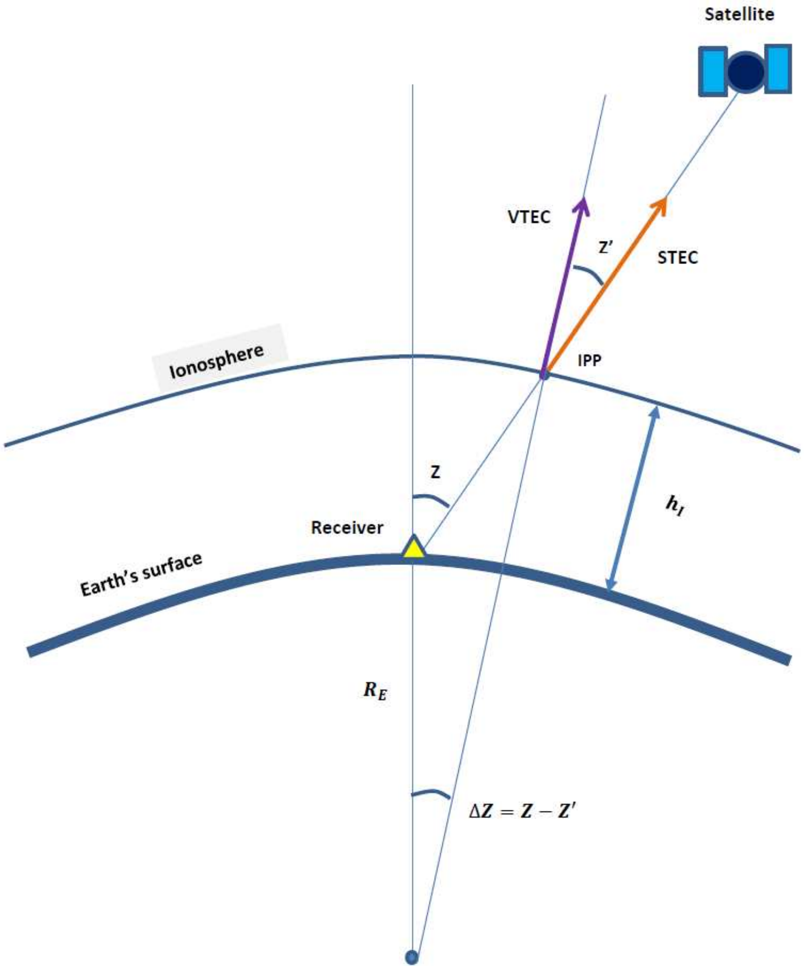

Figure 3.2: A schematic illustration of STEC to VTEC mapping (Adapted from Figure 5.8 in (Misra & Enge, 2006)).

Figure 3.2 indicates that mapping from STEC to VTEC and vice versa can be accomplished by using the formula

$$STEC = \frac{1}{cosZ'}VTEC \tag{3.31}$$

where the quantity $(cosZ')^{-1}$ is called the obliquity factor and Z' is the zenith angle of the satellite at the IPP. The relationship between the satellite zenith angle Z at the receiver position and Z' is obtained by applying the sine rule in trigonometry:

$$\frac{sinZ}{R_E + h_I} = \frac{sinZ'}{R_E} \tag{3.32}$$

where $R_E = 6371$ km is the average Earth radius.

3.1.2.4 GPS-TEC software used to derive TEC

Storm-time TEC considered as observations (GPS TEC), was derived from RINEX (Receiver INdependent EXchange) records using a software developed at Boston College (Seemala & Valladares, 2011), which allowed us to get both slant and vertical TEC. For a specific time of the day, TEC values for different satellites were averaged to get TEC at that time. The cutoff satellite elevation angle was limited to 20° in order to reduce multipath effects. It is well known that during TEC derivation from GPS records, some errors are introduced. Possible sources of error are due to instrumental biases, mapping function, and assumptions made during different steps involved in TEC derivation (Ho *et al.*, 1997). The GPS-TEC software used in this study reads the GPS raw data from RINEX files and calculates phase and code TEC values along with corresponding elevation and azimuth angles of the satellite(s) for the epochs, and then estimates biases as briefly described in the following steps (Uwamahoro *et al.*, 2018a).

A single shell mapping function (Mannucci *et al.*, 1993; Langley, 2002) is used to calculate the vertical TEC, assuming an ionospheric pierce point height of 350 km (Rama Rao *et al.*, 2006). Cycle slips in the phase TEC are corrected arithmetically by computing the difference between successive TEC values and comparing them with the mean difference of the last 20 values. This helps to reduce any noise at the start of data epoch or for low elevation angle. If the difference of the phase TEC at current epoch ($TECP_i$) to the previous value ($TECP_{i-1}$) is greater than 4 times the mean difference or 2 TEC units (considered for 30-second RINEX data), then the presence of a cycle slip (CS) is identified. The CS is then defined as $CS = TECP_i - TECP_{i-1} +$ *previous mean difference*. And from the values there on, this cycle slip is corrected as $TECP_i = TECP_i - CS$ (Uwamahoro *et al.*, 2018a).

After the cycle slip correction, the phase TEC is leveled to the code TEC to get absolute TEC without integer ambiguity. The differential satellite bias corrections published by the University of Bern (`ftp://ftp.unibe.ch/aiub/CODE/`) are used to remove satellite biases. The differential receiver bias is assumed to be constant for the current data set (daily RINEX file data) and is solved using the least squares method. A range of bias values for different satellites is added to the STEC, which is then used to calculate VTEC. Using the simple least squares method, the best bias value is selected. In this method, differences or error minimization were checked using a range of possible bias values (e.g., from -300 to +300 TECU in steps of 0.1 TECU), each of which is added to STEC and then VTEC is calculated. The resultant VTEC for the entire dataset for this range of biases are checked for minimized difference against average diurnal TEC. The bias value that generated the minimum difference is then taken as the receiver bias for that day. The procedure is repeated for all days and final biases are added to STEC followed by the recalculation of final VTEC

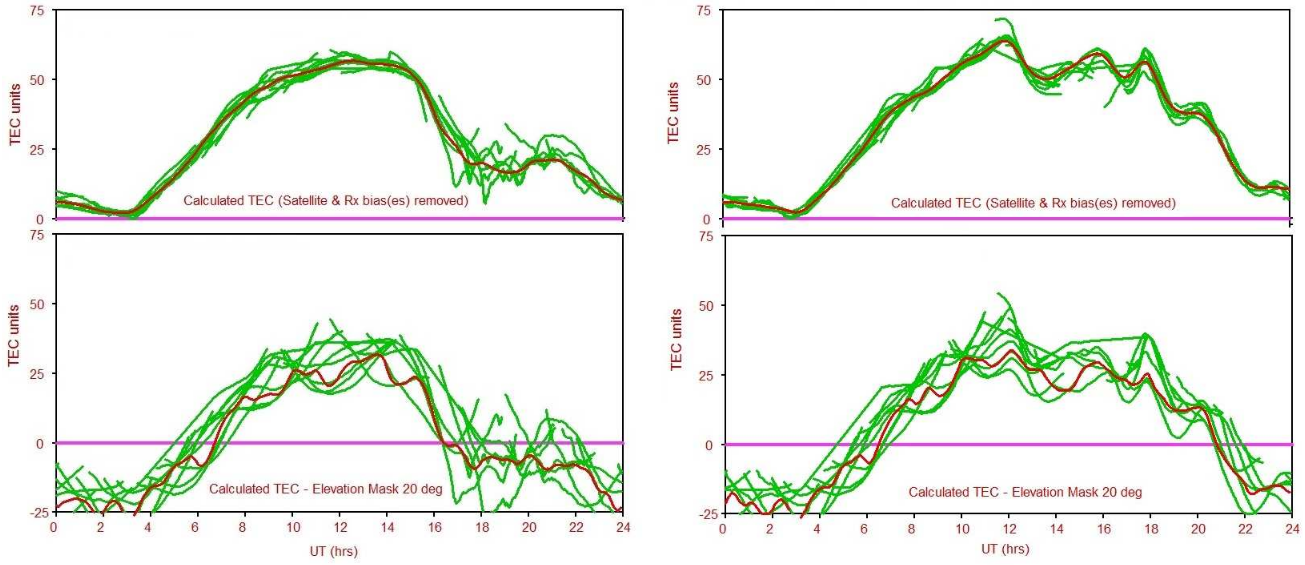

(a)

(b)

Figure 3.3: Calibrated (top panels) and uncalibrated (bottom panels) TEC over Nazret (NAZR, 8.57° N, 39.29° E, 0.25 ° S geomagnetic), by taking into account cycle slips, satellite and receiver biases for quiet (16 March 2015, Figure 3.3 (a)) and disturbed (17 March 2015, Figure 3.3 (b)) days. Red and green lines show the average VTEC over all satellites and VTEC from individual satellite, respectively.

by the GPS-TEC software. Figure 3.3 shows a typical example of the difference between calibrated (top panels) and uncalibrated (bottom panels) TEC over Nazret (NAZR, 8.57° N, 39.29° E, 0.25 ° S geomagnetic), Ethiopia, by taking into account cycle slips, satellite and receiver biases for quiet (16 March 2015, Figure 3.3 (a)) and disturbed (17 March 2015, Figure 3.3 (b)) days, using an elevation threshold of 20°. The green and red curves represent VTEC for individual PRNs and the average TEC, respectively (Uwamahoro *et al.*, 2018a). Owing to the assumptions in bias calculations, single shell mapping function used in conversion of Slant TEC to Vertical TEC (Mannucci *et al.*, 1998), and computation of average TEC for all visible satellites at a specific time of the day, the accuracy of the GPS-TEC software used in this work in terms of standard deviation, is of the order of a few TEC units (1 - 3 TECU) during geomagnetically quiet conditions; and this error may increase in disturbed conditions to about 3 to 6 TECU as demonstrated in Figure 3.4 with light-blue shaded areas. Figure 3.4 shows diurnal TEC over both mid-latitude (SUTH, 32.38° S, 20.81° E) and equatorial latitude (ADIS, 9.04° S, 38.77° E) locations, for a disturbed day (09 March 2012) and the most quiet day of the month (25 March 2012). The average TEC is plotted in blue while the shaded band within the red curves represents the range of standard deviation values. For ADIS and SUTH, it is clear that the error range is mostly between 1 - 3 TECU during quiet conditions (Figure 3.4, left panels), but may also increase during storm conditions up to 6 TECU as shown in Figure 3.4, particularly for SUTH (bottom right panel).

It is also important to note that the GPS-TEC software used in this study has been com-

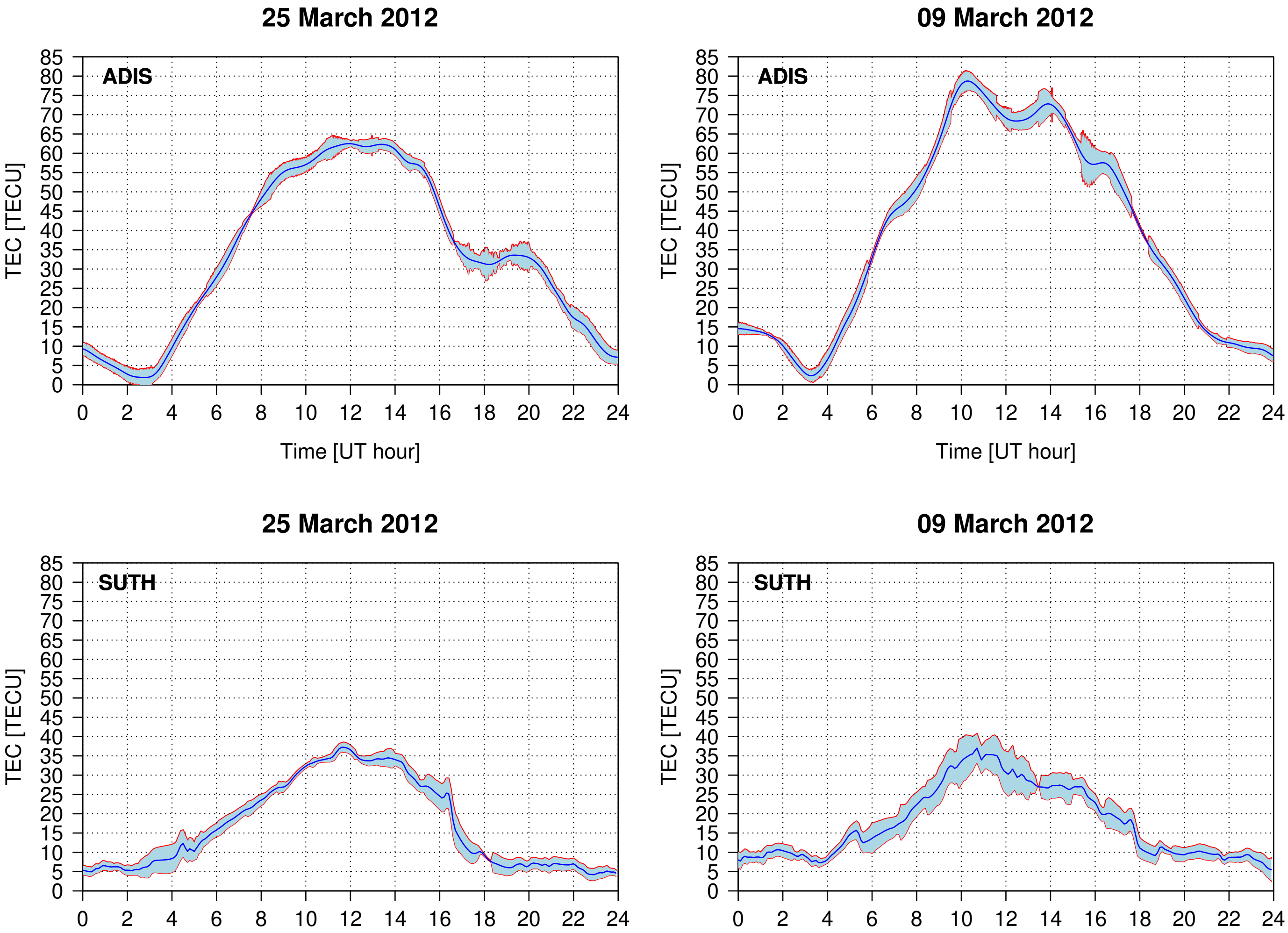

Figure 3.4: Diurnal VTEC (blue line) observed over mid-latitude (SUTH, 32.38° S, 20.81° E) and equatorial latitude (ADIS, 9.04° S, 38.77° E) during quiet (25 March 2012, left panels) and disturbed (09 March 2012, right panels) days. The light-blue shaded areas represent the standard deviations of VTEC values for all visible satellites at a specific time of the day.

pared with other techniques such as the one presented in Ciraolo *et al.* (2007) alongside the European Geostationary Navigation Overlay System (EGNOS) algorithm, which was used as a reference (Abe *et al.*, 2017). Generally, both softwares are consistent with the EGNOS algorithm, but the GPS-TEC software was found to be closer to EGNOS in low-latitudes. On the other hand, the technique described in Ciraolo *et al.* (2007) was more accurate for the mid latitudes, in estimating TEC derived from the EGNOS algorithm. It is also worth noting that the GPS-TEC software used in the current work has extensively been used to derive TEC as reported in different studies (Adewale *et al.*, 2011; Seemala & Valladares, 2011; Olwendo *et al.*, 2012; Akala *et al.*, 2013; Matamba *et al.*, 2015). In this work, to reduce multipath effects and at the same time keeping useful amount of data, VTEC values corresponding to elevation angles greater than a threshold of 20° were considered for both development and validation of the models.

3.2 Modelling inputs

As described in Chapter 2, some of the factors that influence TEC variability are known and where data are available, they should be taken into account for empirical TEC modelling. In this study, diurnal and seasonal variations of TEC were represented by time of day, t, and day number of the year, d, respectively. Geomagnetic and solar activities were also considered in storm-time TEC modelling by introducing their representative indices. Another input that was considered, is the meridional neutral wind velocity to represent the effect of neutral wind in transporting ionized particles along the Earth's magnetic field lines. The most popular geomagnetic indices include the auroral electrojet index AE, the disturbance storm-time Dst index (or $symH$), and the 3-hour K index, its equivalent on a planetary scale, namely planetary K_p, and their derivatives: 3-hour local index, a, 3-hour planetary index, a_p, as well as the daily A_p index. The solar indices used were the solar flux index at a wavelength of 10.7 cm, $F10.7$, its derivative, $F10.7p$, and sunspot number (SSN).

3.2.1 Solar indices

Solar indices are indicators of the Sun's activity level for a specific period of time (Richards *et al.*, 1994a; Perrone & De Franceschi, 1998; Tapping, 2013). Figure 3.5 illustrates the variation of SSN, $F10.7$ and $F10.7p$ for the period from 1996 to 2018 along with the number of geomagnetic storms which occurred within the same time interval. A geomagnetic storm was identified based on the storm criterion of $Dst \leqslant -50$ nT and/or $K_p \geqslant 4$. Figure 3.5 shows that a large number of geomagnetic storms occurred during solar maximum periods, while few storms were observed in the solar minimum, the period during which the solar activity level is low. In Figure 3.5, high and low solar activity periods are clearly identified by large and small values of the three solar indices, respectively.

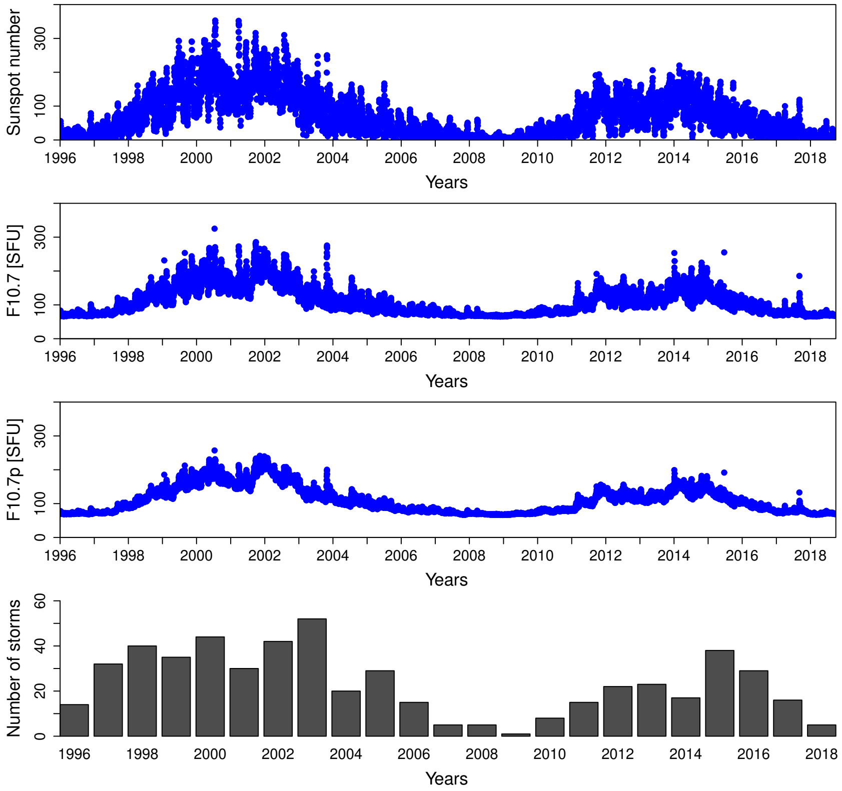

Figure 3.5: Variation of SSN, $F10.7$ and $F10.7p$ during the period from 1996 to 31 August 2018. The number of geomagnetic storms observed within the same period is also illustrated.

3.2.1.1 Sunspots and sunspot number

Sunspots are dark spots at the photosphere of the Sun (Figure 3.6). They appear darker than the surrounding area, because their surface temperature of about 3000 K is less than the temperature of the photosphere which is about 6000 K (Davies, 1990). The darkness of sunspots can be understood by imagining the Sun as a black body which emits thermal radiation at an effective temperature T_{eff}. Its luminosity, $L_\odot = 4\pi R_\odot^2 \sigma_{SB} T_{eff}^4$ ($R_\odot = 6.96 \times 10^5$ km and $\sigma_{SB} = 5.67 \times 10^{-8}$ Wm^{-2}K^{-4} are the solar radius and Stefan-Boltzmann constant, respectively) is proportional to the fourth power of the temperature and this shows that cooler regions (sunspots) radiate less compared to hotter regions (surrounding photosphere).

Sunspots are characterized by a strong magnetic field and often appear in pairs with opposite magnetic field polarities. Due to convective motions, the photosphere is heated by hotter particles from layers below. The strong magnetic field of sunspots holds matter so tightly in such a way that convective motions are inhibited. A consequential net result is that hotter constituents are prevented from reaching sunspot locations and they are thus cooler than surrounding regions (Meyer-Vernet, 2007). Sunspots appear and disappear with time and have a lifetime of a few days, and only a small number can last longer (about four to five solar rotations, each counting 27 days). The presence of sunspots on the solar surface indicates

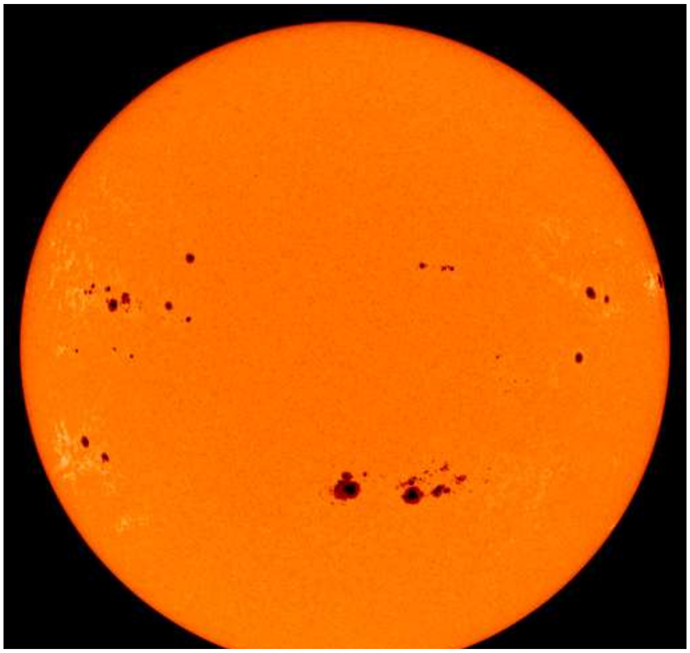

Figure 3.6: Image of sunspots taken by Solar and Heliospheric Observatory (SOHO) satellite on 27 September 2001. Sunspots are dark spots at the Sun's photosphere. Credit: National Aeronautics and Space Administration (NASA), (`https://science.nasa.gov/science-news/science-at-nasa/2008/30sep_blankyear`).

that the Sun is active and therefore, there is a possibility of releasing energy to space. Thus, the number of sunspots located at the solar surface facing the Earth is a good indicator of the global activity level that the Sun is having on the ionosphere (Davies, 1990; McNamara, 1991). Sunspots may occur by themselves or appear in sunspot groups, each group having several distinguishable spots. The number of sunspots is given by

$$R = k(10g + s) \tag{3.33}$$

where g and s are the numbers of sunspot groups and the observed individual spots, respectively. Both equipment and observer are taken into consideration within the correction factor k which is approximately equal to unity (Davies, 1990). The analysis of sunspot number variation with time has shown a nearly cyclic trend of a period of about 11 years. Troughs and crests of the solar cycle correspond to solar minimum and solar maximum periods, respectively, while ascending and declining phases represent moderate phases of solar activity. Long-term data for SSN are available at SILSO (Sunspot Index and Long-term Solar Observations) website (`http://sidc.oma.be/silso/datafiles`).

3.2.1.2 Solar radio flux indices

The $F10.7$ solar radio flux index is a measure of daily total radio emission from all sources present at the solar disk at a wavelength of 10.7 cm (or frequency of 2.8 GHz) (Davies, 1990; Tapping, 2013; Schonfeld *et al.*, 2015). The F10.7 index is measured in solar flux unit (1 SFU = 10^{-22} W.m^2.Hz) every day at the Penticton Radio Observatory in British Columbia, Canada. Like the SSN, the F10.7 index is a solar activity level indicator (Davies, 1990; McNamara, 1991; Tapping, 2013) and varies from near 65 during the solar minimum to a maximum of about 200 during the high solar activity period (Davies, 1990). Daily and monthly average values of $F10.7$ adjusted at 1 AU (1 AU = 1.5 $\times 10^{11}$ m is the astronomical unit) are available at different sources: 1) Solar-Geophysical Data (SGD) website (`https://www.ngdc.noaa.gov/stp/solar/sgd.html`), 2) omniweb data (`http://omniweb.gsfc.nasa.gov/form/dx1.html`). Details regarding the measurement of $F10.7$ are provided in Tapping (2013) and references therein.

A recent analysis of $F10.7$ variation with the solar EUV irradiance and critical frequency of F2 (foF_2) during the deep solar minimum (2007 - 2009), showed inconsistency in variation of these parameters with respect to each other, and this contradicted what was previously reported. The main findings revealed that $F10.7$ does not represent well the solar EUV irradiance, and its correlation with foF_2 drops during deep solar minimum (Chen *et al.*, 2011). Previous studies demonstrated that the modified solar flux index $F10.7p = (F10.7{+}F_{10.7A})/2$ (where $F_{10.7A}$ is 81-day running mean of $F10.7$) is a better indicator of the solar activity level than $F10.7$ (e.g., Richards *et al.*, 1994b; Liu *et al.*, 2006; Liu & Chen, 2009). On the basis of a long-term ionospheric data analysis, Liu *et al.* (2006) showed that $F10.7p$ is a better representation of the solar EUV flux than $F10.7$. It was also noticed that $F10.7p$ correlates well with the peak electron density of the F2 layer ($NmF2 = 1.24 \times 10^4 (foF2)^2$), compared to the correlation between $F10.7$ and $NmF2$. The concluding observation was that $F10.7p$ is a better representation of solar activity than $F10.7$.

3.2.2 Geomagnetic indices

Geomagnetic indices provide information about the state of the Earth's magnetic field. In this section, the description will be limited to the most frequently used geomagnetic indices, namely the K index and its derivatives, auroral electrojet (AE) index, and disturbance storm-time index.

3.2.2.1 K and Kp indices

The K index is an indicator of irregular variations associated with the Earth's magnetic field disturbances, as observed at a specific observatory. As a local index, the K-index is derived from data recorded at a single location and can only have values between 0 and 9, the former and the latter indicating geomagnetically very quiet and extremely disturbed conditions, respectively. For every 3-hour interval (00:00 - 03:00, 03:00 - 06:00, ..., 21:00 - 24:00) a value of K index is assigned, leading to eight values per day for each observatory

(Bartels *et al.*, 1939; Rostoker, 1972; Davies, 1990). The difference (measured in gamma ($1\ \gamma = 10^{-5}$ gauss (G) $= 10^{-9}$ Tesla (T) $= 1$ nT)), between the absolute maximum and absolute minimum values of a magnetic element, within the 3-hour interval, is called the amplitude range (R) and is used to define the K index. For each element D, H, and Z (D is the magnetic declination, H, and Z are the horizontal and vertical components of the Earth's magnetic field, respectively), or X, Y, and Z (where X and Y are the northward and eastward components of H, respectively), R is computed. Its largest value implies the most disturbed element and is thus considered as the basis for K index. The conversion table which is used to convert R to K index, differs from one observatory to another and the values in the table depend on geomagnetic latitude of the observatory. Since the K index range is between 0 and 9, R is such that the lower range limit for $K = 9$ equals 100 times the upper range limit for $K = 0$ (Bartels *et al.*, 1939; Rostoker, 1972; Davies, 1990). As an illustrative example, K index and R values for Hermanus (34.42° S, 19.22° E, geographic; 42.34° S, 82.14° E, geomagnetic) are provided in Table 3.1.

Table 3.1: Conversion table between K index and R for Hermanus (34.42° S, 19.22° E, geographic; 42.34° S, 82.14° E, geomagnetic).

K	0		1		2		3		4		5		6		7		8		9
R (nT)		3		6		12		24		42		72		120		198		300	

First introduced by Bartels *et al.* (1939), the planetary K index, commonly denoted as K_p, describes the worldwide level of geomagnetic activity for every 3-hour interval. Some of the major difficulties that are encountered when using K index for statistical studies, are the very pronounced diurnal variation (for example, the 3-hour intervals near local geomagnetic midnight are generally more disturbed than the rest of the day), and its seasonal dependence. To circumvent these difficulties, conversion tables subdivided by seasons and universal time (UT) intervals were developed by introducing a continuous variable K_s index (as opposed to the integer K index) ranging between 0.0 and 9.0, and expressed in thirds of an integer. Typical K_s ranges are 0 - 1/6, 1/6 - 3/6, 3/6 - 5/6, 5/6 - 7/6,... and the corresponding K_s codes (ranging from 0o to 9o) are 0o, 0+, 1-, 1o,..., respectively. The K_p is thus computed every 3-hour interval by averaging K_s from thirteen mid-latitude observatories presented in Table 3.2 (Bartels *et al.*, 1939; Rostoker, 1972). For further information related the computation of K_p, readers are referred to Bartels *et al.* (1939) and Rostoker (1972).

For the storm classification based on K_p index, the National Oceanic and Atmospheric Administration (NOAA) Space Weather Scale for geomagnetic storms available at `https://www.swpc.noaa.gov/NOAAscales` can be used. In this classification, K_p values of 5, 6, 7, 8, and 9, correspond to minor, moderate, strong, severe, and extreme geomagnetic storms, respectively. Locations of 13 observatories involved in the computation of K_p index are shown on the map in Figure 3.7.

Table 3.2: Geographic (GLat & Glon) and geomagnetic (GMLat & GMLon) coordinates of 13 observatories that are used to compute K_p index.

	Code	Name	Country	GLat	Glon	GMLat	GMLon
1	LER	Lerwick	Scotland	60.13	358.82	62.00	89.20
2	MEA	Meanook	Canada	54.62	246.67	61.70	305.70
3	SIT	Sitka	Alaska	57.05	224.67	60.40	279.80
4	ESK	Eskdalemuir	Scotland	55.32	356.80	57.90	83.90
5	UPS	Uppsala	Sweden	59.90	17.35	58.50	106.40
6	OTT	Ottawa	Canada	45.40	284.45	55.80	355.00
7	BFE	Brorfelde	Denmark	55.62	11.66	55.40	98.60
8	HAD	Hartland	England	50.97	355.52	54.00	80.20
9	WNG	Wingst	Germany	53.75	9.07	54.10	95.10
10	NGK	Niemegk	Germany	52.07	12.68	51.90	97.70
11	FRD	Fredericksburg	USA	38.20	282.63	48.60	353.10
12	CNB	Canberra	Australia	-34.70	149.00	-42.90	226.80
13	EYR	Eyrewell	New Zealand	-42.58	172.35	-47.20	253.80

3.2.2.2 a, a_p, A_p indices

The K index is naturally quasi-logarithmic and for some arithmetic manipulations, an index based on a linear scale is required. The equivalent of the local K and planetary K_p indices on a linear scale are the 3-hour a and a_p indices. Conversion from quasi-logarithmic indices to linear indices is performed using Table 3.3. It must be pointed out that the 3-hour a_p index is based on mid-latitude observations, as is the case for the K_p index. The daily magnetic activity is described by A_p index which is just the sum of eight values of a_p indices for a specific day.

Table 3.3: Table for conversion from K to a index.

K	0	1	2	3	4	5	6	7	8	9
a	0	3	7	15	27	48	80	140	240	400

The 3-hour K index for Hermanus was converted to 3-hour a index used during storm-time TEC modelling for Hermanus according to Table 3.3. The a_p and A_p indices used in this work were obtained from `https://omniweb.gsfc.nasa.gov/form/dx1.html`.

3.2.2.3 AE index

The planetary K_p describes the general state of geomagnetic activity on a planetary scale and contains at least contributions from both auroral electrojet and the ring current. Particular studies of geomagnetic activity at auroral latitudes require the auroral electrojet (AE) index, which was first introduced by Davis & Sugiura (1966). The AE index represents the geomagnetic activity perturbation caused by ionospheric currents (eastward and westward

Table 3.4: Geographic and geomagnetic coordinates of 12 observatories used to construct *AE* index. Source: `http://wdc.kugi.kyoto-u.ac.jp/aedir/ae2/AEObs.html`.

	Observatory	IAGA Code	GLat (° N)	GLon (° E)	GMLat (° N)	GMLon (° E)
1	Abisko	ABK	68.36	18.82	66.04	115.08
2	Dixon Island	DIK	73.55	80.57	63.02	161.57
3	Cape Chelyuskin	CCS	77.72	104.28	66.26	176.46
4	Tixie Bay	TIK	71.58	129.00	60.44	191.41
5	Cape Wellen	CWE	66.17	190.17	61.79	237.10
6	Barrow	BRW	71.30	203.25	68.54	241.15
7	College	CMO	64.87	212.17	64.63	256.52
8	Yellowknife	YKC	62.40	245.60	69.00	292.80
9	Fort Churchill	FCC	58.80	265.90	68.70	322.77
10	Poste-de-la-Baleine	PBQ	55.27	282.22	66.58	347.36
11	Narsarsuaq	NAQ	61.20	314.16	71.21	36.79
12	Leirvogur	LRV	64.18	338.30	70.22	71.04

auroral electrojets) flowing at auroral latitudes. The *AE* index is based on measurements from auroral and slightly sub-auroral zone stations, chosen so as to provide uniformly-spaced coverage around the auroral zone (Rostoker, 1972; Davies, 1990). Table 3.4 lists the 12 observatories which are used to calculate the *AE* index, while Figure 3.7 shows their locations (blue dots) on a map.

For the construction of *AE* index, only the *H*-component of the perturbation field at each observatory is used with a quiet time baseline as a reference level. When *H*-components from various observatory magnetograms are superimposed, the amplitudes of the upper (*AU*) and lower (*AL*) envelopes represent the maximum magnetic perturbations generated by eastward and westward electrojets, respectively. The *AE* index is defined as $AE = AU - AL$, and represents the difference, expressed in gammas, between the upper and lower amplitudes at a given time (Rostoker, 1972; Davies, 1990), while the *AO* index defined as the average value of *AU* and *AL* ($AO = (AU + AL)/2$), provides a measure of the equivalent zonal current (Davis & Sugiura, 1966; Davies, 1990). *AE* is available at different sources such as `http://wdc.kugi.kyoto-u.ac.jp/aedir/index.html`, `https://omniweb.gsfc.nasa.gov/form/dx1.html` (hourly and daily values), and `https://omniweb.gsfc.nasa.gov/form/omni_min.html` (1 and 5-minute resolution). The *AE* used in the current work was obtained from the last two sources. The locations of 13, 12, and 4 observatories involved in the computation of K_p, *AE*, and *Dst* indices, respectively, are shown on the world map presented in Figure 3.7.

3.2.2.4 Disturbance storm-time index

The magnetic field of the Earth controls the motions of charged particles in the Earth's environment. The three types of motion executed by charged particles trapped by the Earth's

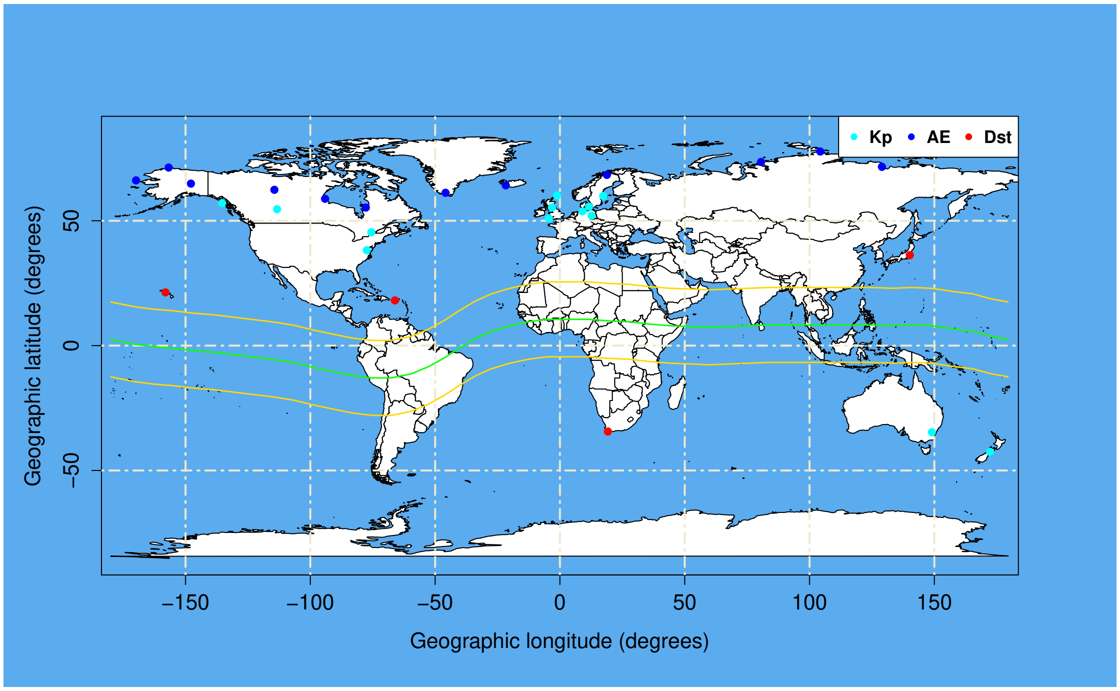

Figure 3.7: Locations of geomagnetic observatories used to compute K_p (light-blue dots), AE (blue dots), and Dst (red dots) indices. The green line represents the geomagnetic equator, while the dark yellow lines located at ±15° from the geomagnetic equator indicate the locations of the EIA crests.

magnetic field are drift motion across the Earth's magnetic field lines, spiral/gyro motion around the magnetic field lines, and bouncing motion back and forth along the magnetic field lines between two turning/mirror points (Chen, 1984; Baumjohann *et al.*, 1997). Figure 3.8 illustrates the three types of motions of charged particles under control of the Earth's magnetic field.

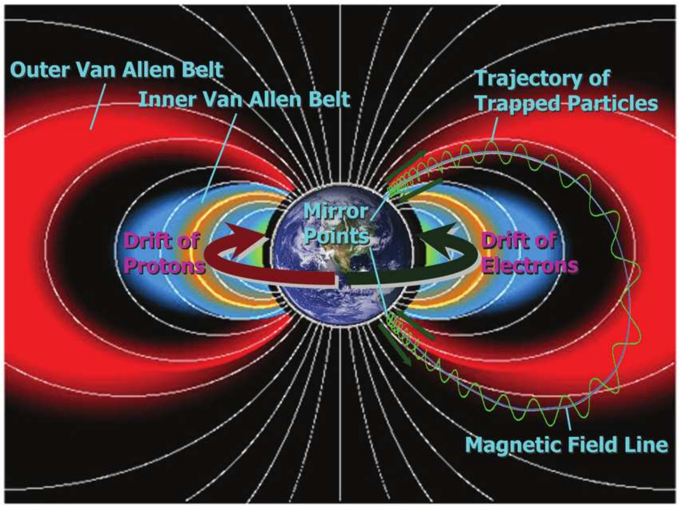

Figure 3.8: Motions of charged particles in the Earth's magnetosphere (Karavaev, 2010).

The drift motion is so that positively charged particles move westward around the Earth

Table 3.5: Geographic and geomagnetic coordinates for four observatories used to compute the *Dst* index. Source: `http://wdc.kugi.kyoto-u.ac.jp/dstdir/dst2/onDstindex.html`.

Observatory	Country	GLat	Glon	GMLat	GLon
Hermanus	South Africa	-34.40	19.22	-42.33	82.15
Kakioka	Japan	36.23	140.18	29.04	211.49
Honolulu	USA (until April 1960)	21.30	201.90	21.64	269.43
	(after April 1960)	21.32	201.98	21.66	269.50
San Juan	USA (until January 1965)	18.31	293.88	28.97	9.90
	(after January 1965)	18.11	293.88	28.78	9.87

whereas electrons drift eastward. The current generated by this double transport of charged particles is called the ring current ("ring" because it encircles the Earth) and flows in the equatorial plane in the westward direction (Baumjohann *et al.*, 1997; Moldwin, 2008). The disturbance storm-time (*Dst*) index is an indicator of change in the ring current intensity in sense that when the ring current intensity increases, *Dst* decreases. In fact, injection of particles by the solar wind into the Earth's magnetosphere during the main phase of the storm leads to enhancement of the ring current. Since the ring current itself induces a magnetic field directed oppositely to the Earth magnetic field, the increase in ring current intensity leads to enhancement of the induced magnetic field and thus, to a decrease in the Earth's magnetic field intensity. The *Dst* index (normally expressed in nanotesla (nT)) is a measure of the depression/decrease in the horizontal component, H, of the Earth's magnetic field in equatorial/low latitude region due to an increase in the magnetospheric ring current (Gonzalez *et al.*, 1994). Thus, four low-latitude magnetic observatories (listed in Table 3.5) are used to compute the *Dst* index.

The *Dst* index is often used to define a geomagnetic storm and serves as an indicator of the storm occurrence time, duration, and its intensity. In the current work, geomagnetic storms were identified based on the storm criterion of $Dst \leqslant -50$ nT and/or $K_p \geqslant 4$. The storm classification based on *Dst* and according to Loewe & Prölss (1997) is presented in Table 3.6. Long-term data (from 1957 to date) of *Dst* index can be found at `http://wdc.kugi.kyoto-u.ac.jp/`.

Table 3.6: Classification of geomagnetic storms according to Loewe & Prölss (1997).

Range of minimum *Dst*	Storm classification
-30 nT $\geqslant$ min(Dst) > -50 nT	Weak
-50 nT $\geqslant$ min(Dst) > -100 nT	Moderate
-100 nT $\geqslant$ min(Dst) > -200 nT	Strong
-200 nT $\geqslant$ min(Dst) > -350 nT	Severe
$\leqslant$ -350 nT	Great

Figure 3.9 displays the variation of hourly AE, AU, AL, a_p, K_p, and Dst indices during

the period 06 - 11 September 2017. Significant changes in all indices are observed during the storm main phase which was on 07 - 08 September 2017 according to the Dst index. According to the NOAA Space Weather Scale of geomagnetic storms, the 07 - 08 September 2017 storm with K_p index of about 8 was a severe storm, while according to the Loewe & Prölss (1997) classification, the storm is strong based on the minimum Dst index of -142 nT which is within -100 nT and -200 nT.

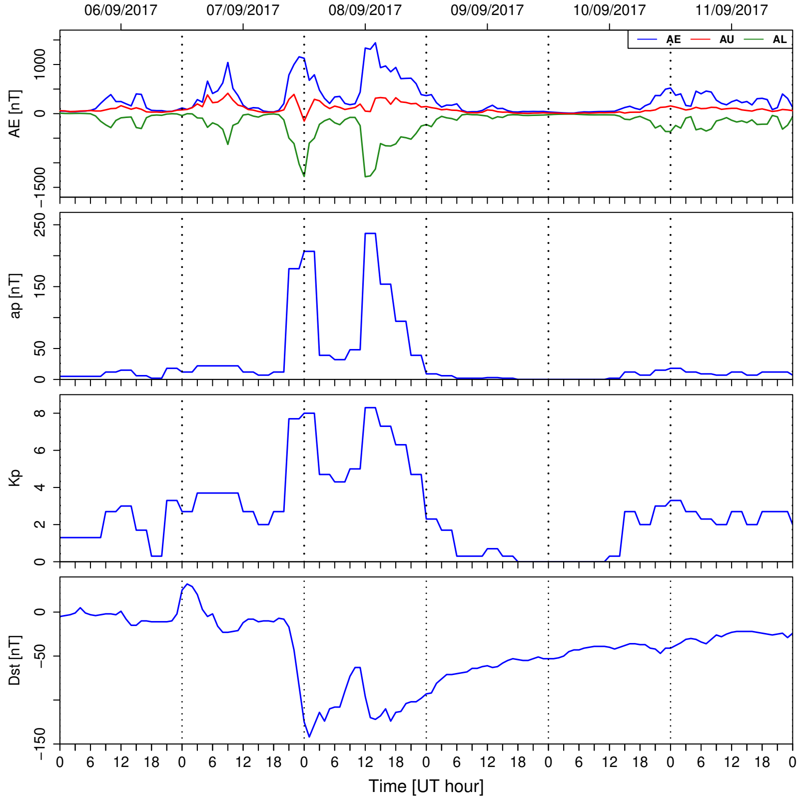

Figure 3.9: Variation of AE, AU, AL, a_p, K_p, and Dst indices during the period 06 - 11 September 2017.

3.2.2.5 Energy coupling function of Akasofu

When electromagnetic waves travel through space, their energy can be transferred to objects encountered in their path (Serway & Jewett, 2004). The rate of energy flow in electromagnetic waves is described by the poynting vector defined by

$$\vec{S} = \frac{\vec{E} \times \vec{B}}{\mu_0} \tag{3.34}$$

where $\vec{E}$ and $\vec{B}$ are electric and magnetic fields, and $\mu_0 = 4\pi \times 10^{-7}$ N/A is the permeability of free space (Griffiths, 1999). With regard to the solar wind and magnetosphere coupling, $\vec{E}$ and $\vec{B}$ represent the solar wind electric and magnetic fields. The magnitude of the poynting vector is the energy flux density or equivalently, the energy per unit time (power), per unit area, transported by electromagnetic fields ($\vec{E}$ and $\vec{B}$). Since the energy per unit time crossing the infinitesimal surface $d\vec{a}$ (energy flux) is $\vec{S} \cdot d\vec{a}$, the total energy per unit time flowing through a closed surface A can be expressed as

$$\begin{aligned} \oint_A \vec{S} \cdot d\vec{a} &= \frac{EB}{\mu_0}(4\pi l_0^2) \\ &= \frac{(vB)B}{\mu_0}(4\pi l_0^2) \\ &= \frac{4\pi}{\mu_0} vB^2 l_0^2 \end{aligned} \tag{3.35}$$

where $l_0 = 7R_E$, R_E is the radius of the Earth, and $A = 4\pi l_0^2 = 4\pi(7R_E)^2 \approx \pi(14R_E)^2$ total area. Equation (3.35) gives the total energy per unit time passing through a surface of a circle of which the radius is $14R_E$, which is roughly the magnetopause radius at the terminator (Koskinen & Tanskanen, 2002). From the idea above, the interplanetary energy flux in terms of the poynting vector

$$\begin{aligned} \varepsilon &= \frac{4\pi}{\mu_0} vB^2 l_0^2 sin^4\left(\frac{\theta}{2}\right) \\ &= 10^7 vB^2 l_0^2 sin^4\left(\frac{\theta}{2}\right) \qquad [Watts]. \end{aligned} \tag{3.36}$$

This equation represents the solar wind energy input (power) into the magnetosphere during geomagnetic storms (Perreault & Akasofu, 1978; Akasofu, 1981, 2007). $E = vB$ is the interplanetary electric field (IEF) intensity, v is the solar wind velocity, B represents the interplanetary magnetic field (IMF) strength, and θ is the IMF clock angle defined by

$$\theta = tan^{-1}\left(\frac{\mid B_y \mid}{\mid B_z \mid}\right), \qquad B_z > 0. \tag{3.37}$$

or

$$\theta = 180^\circ - tan^{-1}\left(\frac{\mid B_y \mid}{\mid B_z \mid}\right), \qquad B_z < 0. \tag{3.38}$$

In the future, the plan is to investigate if the energy transferred by the solar wind into the magnetosphere during geomagnetic storms, may contribute to storm-time ionospheric modelling.

3.3 Climatological models

This section is limited to a discussion of the climatological models that were used in this study, namely the International Reference Ionosphere (IRI) and the Horizontal Wind Model (HWM).

3.3.1 International Reference Ionosphere (IRI)

The IRI is an empirical (data-based) standard model that estimates ionospheric plasma parameters within an altitude range of 60 - 2000 km for a given location and at a specific time (Bilitza, 2003). When date, time (UT or LT), and location (geographic or geomagnetic coordinates) are specified, the IRI model gives monthly averages of electron and ion densities, temperatures, and velocities, ion composition (percentage of O^+, H^+, He^+, N^+, NO^+, O_2^+, and cluster ions). Additional parameters that are provided by the IRI model include vertical ionospheric TEC (specification of the upper height limit is required for the integration of electron density profile), low-latitude ion vertical drift, the occurrence probabilities of F1 layer and spread F (percentage of days per month during which the F1 layer and spread F are expected), as well as auroral boundaries (Bilitza, 2003; Bilitza & Reinisch, 2008; Bilitza *et al.*, 2014; Bilitza, 2014; Bilitza *et al.*, 2017).

The IRI project was established and is sponsored by the Committee on Space Research (COSPAR) and the International Union of Radio Science (URSI), which are also responsible for its improvement and update as new data and models become available (Bilitza *et al.*, 2011, 2014; Bilitza, 2014; Bilitza *et al.*, 2017). As an empirical model, IRI is based on observations of the ionospheric plasma recorded by space-based and worldwide ground based instruments. IRI data resources include ionosondes (electron density profile from E to F peak), incoherent scatter radars (entire profile of electron density, E - valley), topside sounders (topside electron density profile), rockets (D-region plasma parameters), Global Navigation Satellite Systems (for TEC), and low Earth orbit (LEO) satellites (electron density profile) (Bilitza & Reinisch, 2008; Bilitza *et al.*, 2011; Bilitza, 2017).

Inputs required for the IRI model include solar (12-month running mean of SSN (R12), $F_{10.7}$, $F_{10.7A}$, and 12 month running mean of $F_{10.7}$) and geomagnetic (A_p and 3-hour a_p) indices, the Global ionospheric index (IG) (ionosonde IG index 12-month running mean), and COSPAR International Reference Atmosphere (CIRA) neutral densities and temperatures. Optional inputs consists of measured values of the peak plasma frequencies foF2, foF1, foE, and foD, or alternatively the peak densities NmF2, NmF1, NmE, NmD, and/or peak heights hmF2 (or the correlated propagation factor M(3000)F2), hmF1, hmFE, and hmD (Bilitza *et al.*, 2014).

As an empirical model, the IRI has the advantage that it does not rely on theoretical understanding of physical processes that govern ionospheric dynamics. However, since the IRI model strongly depends on underlying database, it has the disadvantage of being inaccurate for locations (oceans and most of the southern hemisphere) and time periods that are not well represented (Rawer *et al.*, 1978; Bilitza *et al.*, 2011; Bilitza, 2014).

One of the models used in the IRI to provide the topside electron density profiles, is the NeQuick topside model developed by Radicella & Leitinger (2001) and Coïsson *et al.* (2006), which is based on ionosonde and topside sounder data (Bilitza, 2009). A performance evaluation of the NeQuick topside model (IRI-2007-NeQ) compared to the IRI-2007-corrected model (a correction of the IRI-2001 model, and which is another topside model developed by Bilitza (2004), showed the superiority of the former over the latter in terms of providing better results. However, the IRI-2007-corrected model was found to provide a more realistic representation for the EIA region, specifically in terms of altitudinal - latitudinal structure (Bilitza, 2009). Since it was found to be more accurate than other topside models, we have used in the current work the NeQuick model as topside option.

It is worth noting that both NeQuick2 and IRI models have recently been validated in the low latitude East African region by comparing their predictions with GPS TEC measurements (Mengistu *et al.*, 2018). The study examined the performances of NeQuick2, IRI-2016 (latest version which is currently available), IRI-2012, and IRI-2007 models, in describing the monthly and seasonal mean TEC. Particularities for each model in terms of solar activity and seasonal dependences were highlighted.

Related to IRI geomagnetic storm modelling, the model developed by Timothy J. Fuller - Rowell and described in Fuller-Rowell *et al.* (1998) and Fuller-Rowell *et al.* (2000), is incorporated in the IRI model (Bilitza, 2003). The IRI storm-time model was found to be more efficient in capturing negative phases for summer mid-latitude ionospheric storms, while its inefficiency was highlighted particularly in following the winter mid-latitude positive ionospheric phases (Fuller-Rowell *et al.*, 2000). Since this study deals with geomagnetic storms, the IRI model currently available at `https://ccmc.gsfc.nasa.gov/modelweb/models/iri2016_vitmo.php`, with STORM option on, was used.

3.3.2 Horizontal Wind Model (HWM)

The HWM is an empirical model that provides a statistical representation of the horizontal wind patterns in the Earth's atmosphere (Drob *et al.*, 2008). The HWM07 has a quiet-time component (Drob *et al.*, 2008) and a geomagnetic storm-time component, known as the disturbance wind model (DWM07) which describes on average, the storm-induced perturbations of the neutral winds in the upper thermosphere (Emmert *et al.*, 2008). The latest version of the HWM is HWM14 developed based on a database of about 73×10^6 measurements recorded over a period of 60 years by 44 different instruments all over the world (Drob *et al.*, 2015). For the update from the HWM07 to the HWM14 version, the geomagnetic storm time component (DWM07) was left unchanged (Drob *et al.*, 2015). However, as it can be seen at `https://github.com/timduly4/pyglow/blob/master/pyglow/models/dl_models/hwm14/hwm14.f90#L76`, the DWM07 is incorporated in the HWM14 used to compute the meridional wind velocity. When position (latitude, longitude, altitude) and time (day of the year and time of the day) are specified, HWM14 provides the meridional and zonal components of the horizontal neutral winds for an altitude range 0 - 500 km, i.e., from ground to exosphere (Drob *et al.*, 2008, 2015). Details about the HWM are provided in a number of sources (Hedin *et al.*, 1988, 1991, 1996; Drob *et al.*, 2008; Emmert *et al.*, 2008; Drob *et al.*, 2015).

Since this research mostly concerns the African sector, it is worth noting that the HWM has been validated for the African low- and mid-latitude regions. The HWM predictions were found to be in good agreement with the Fabry Perot interferometer (FBI) observations in low- and mid-latitude locations (Fisher *et al.*, 2015; Tesema *et al.*, 2017). The meridional neutral wind velocity used in this study was obtained from the HWM14, accessed via pyglow package available at `https://github.com/timduly4/pyglow/`. Results related to the use of the meridional wind velocity as a new input for TEC modelling during storm conditions are presented in Chapter 6.

3.4 Modelling and reconstructing techniques

Several empirical models have been employed to model TEC for geomagnetic storm conditions. The models considered in this study are based on empirical orthogonal functions (EOF) analysis, Non-linear regression analysis (NLRA), the Metropolis - Hastings Algorithm (MHA), and artificial neural networks (ANNs). For storm-time TEC reconstruction, the Multi-Instrument Data Analysis System (MIDAS) algorithm was applied for Equatorial, low- and mid-latitude regions. Brief summaries of the modelling and reconstruction techniques explored in this work are presented in the following subsections.

3.4.1 Empirical orthogonal functions (EOF) analysis

Empirical orthogonal functions (EOF) analysis, also known as principal component analysis (PCA) or natural orthogonal component (NOC) algorithm (Ercha *et al.*, 2012), is a statistical method used to examine inter-relations among a set of variables of a dataset in order to identify hidden structures in the data. Through an orthogonal transformation, a dataset of intercorrelated variables is transformed to a new dataset of uncorrelated variables that still contains most of the information in the original dataset. As a powerful tool of data analysis, some particular advantages of EOF analysis include:

- reducing the dimensionality of a dataset, i.e. from a large number of interrelated variables to a small number of uncorrelated variables (lower dimension) without much loss of information (Venegas, 2001; Smith *et al.*, 2002; Shlens, 2003).
- revealing hidden patterns in a dataset and classifying them according to the percentage of the total variance in the original dataset they account for (Smith *et al.*, 2002; Shlens, 2003)
- reducing redundancy and filtering some of the noise in the data (Mankin, 2014)
- preparing data for further analyses (Mankin, 2014).

In ionospheric research, EOF analysis has widely been applied to the modelling of ionospheric parameters such as TEC (Mao *et al.*, 2005, 2008; Ercha *et al.*, 2012; Chen *et al.*, 2015; Uwamahoro & Habarulema, 2015; Dabbakuti *et al.*, 2016; Le *et al.*, 2016; Dabbakuti & Ratnam, 2017), critical frequency of the F2 layer (foF_2) (Zhang *et al.*, 2009; Ercha *et al.*, 2011; Yu *et al.*, 2015) ionospheric peak height of F1 (hmF_1) (Yu *et al.*, 2015) and F2 layers (hmF_2) (Zhang *et al.*, 2010; Lin *et al.*, 2014; Yu *et al.*, 2015), and the ionospheric propagation factor, $M(3000)F2$ (Liu *et al.*, 2008; Zhang *et al.*, 2010; Yu *et al.*, 2015). Except for the study by Uwamahoro & Habarulema (2015), which for the first time in TEC modelling, used the EOF analysis for storm conditions, other studies focused on ionospheric modelling for geomagnetically quiet conditions. Apart from being used as analytical model for ionospheric parameters, EOF analysis was capable to reveal hidden structures in TEC data. For example, through EOF decomposition, features such as diurnal and long-term TEC variability, the hemispherically asymmetric pattern manifesting the summer-to-winter annual variation, and the EIA phenomenon were well described through EOF mode analysis (Ercha *et al.*, 2012). In comparison with other modelling techniques such as IRI, EOF analysis based models were found to be more accurate in modelling ionospheric parameters specifically during geomagnetically quiet conditions (e.g., Mao *et al.*, 2005; Ercha *et al.*, 2012; Dabbakuti *et al.*, 2016). The first application of EOF analysis to the modelling of mid-latitude geomagnetic storms led to encouraging results in reproducing TEC variability particularly for non-significant ionospheric storm effects (Uwamahoro & Habarulema, 2015).

According to the theory of EOF analysis, a continuous space-time field $X(t, s)$ can be decomposed in terms of EOF basis functions $E_k(s)$ (functions of space) and associated EOF coefficients $C_k(t)$ (functions of time) according to the equation (Hannachi *et al.*, 2007)

$$X(t,s) = \sum_{k=1}^{m} C_k(t) \times E_k(s). \tag{3.39}$$

m denotes the number of modes contained in the field, t and s are time and spatial position respectively. E_k are the eigenvectors of the covariance matrix Σ constructed from the original data X. Σ is defined by

$$\Sigma = X^T X \tag{3.40}$$

where the superscript T denotes the transpose of the matrix X (Weare & Nasstrom, 1982; Björnsson & Venegas, 1997; Xu & Kamide, 2004; De Michelis *et al.*, 2010). Other definitions of the covariance matrix provided in the literature are $\Sigma = \frac{1}{n} X^T X$ (e.g., Hannachi *et al.*, 2007; Mao *et al.*, 2008), and $\Sigma = \frac{1}{n-1} X^T X$, where n is the number of samples within the dataset (e.g., Shlens, 2003; Hannachi, 2004; Goodfellow *et al.*, 2016). They differ from Equation (3.40) by a constant and this does not matter, since the computation of basis functions with any of the definitions above, will only differ by a constant (Björnsson & Venegas, 1997). The m eigenvectors/EOF basis functions $(E_1, E_2, E_3, ..., E_m)$ are obtained by first determining the corresponding eigenvalues $(\lambda_1, \lambda_2, \lambda_3, ..., \lambda_m)$, solving the characteristic equation

$$|\Sigma - \lambda I| = 0, \tag{3.41}$$

and then using the equation

$$\Sigma E_i = \lambda_i E_i \tag{3.42}$$

with $i = 1, 2, 3, ..., m$. In Equation (3.41), I is the identity matrix of dimension $m \times m$ and λ, a parameter of which the values obtained by solving Equation (3.41) are the eigenvalues λ_i. Before determining the eigenvectors from Equation (3.42), the eigenvalues should be arranged such that $\lambda_1 > \lambda_2 > ... > \lambda_m$. Such a decomposition provides a new frame of reference defined by $E = (E_1, E_2, ..., E_m)$ where the variables in this new frame are uncorrelated. EOF basis functions/eigenvectors are orthogonal to each other and hence, the appellation empirical orthogonal functions. This simply means that EOF basis functions are uncorrelated over space (Björnsson & Venegas, 1997). The orthogonality condition of basis functions is

$$E^T E = E E^T = I \tag{3.43}$$

Graphically, the eigenvectors indicate the directions in which the data are most spread out, with E_1 (which corresponds to the highest eigenvalue λ_1) pointing in the direction of the greatest variation, E_2 (associated with λ_2) in the direction with the next highest variation, and so on (Björnsson & Venegas, 1997). Once the matrix E of EOF basis functions is found, the matrix C of EOF expansion coefficients can be deduced from the matrix equation

$$X = CE \tag{3.44}$$

and the orthogonality condition expressed by Equation (3.43) as (Zhang *et al.*, 2009)

$$\begin{aligned} C &= XE^{-1} \\ &= XE^{T}. \end{aligned} \tag{3.45}$$

An alternative for the calculation of EOF basis functions and associated coefficients without using the covariance matrix, is by means of the singular value decomposition (SVD) method, as described in Goodfellow *et al.* (2016). Any m by n data matrix X can be written in terms of two orthonormal matrices, V (m by m) and W (n by n), as follows:

$$X = V\Lambda W^{T} \tag{3.46}$$

where Λ (m by n) is a diagonal matrix of singular values of the data matrix X. The singular values of X are related to eigenvalues previously described by $\gamma_i = \sqrt{\lambda_i}$ and should also be arranged from the greatest to the lowest value ($\gamma_1 > \gamma_2 > ... > \gamma_m$) while applying the SVD method. Λ has diagonal elements equal to and is padded out by zeros to make it a $m \times n$ matrix. The left singular vectors or equivalently, the column vector of the matrix V are the EOF basis functions previously described, while EOF expansion coefficients are given by

$$A = \Lambda W^{T}. \tag{3.47}$$

One of the advantages of EOF analysis is the quick convergence of the series represented by Equation (3.39). Thus, rather than considering all m EOF components $A_i \times E_i$ (with i = 1, 2, ..., m) to reconstruct the original data, a few components may be enough to account for a large percentage of variance in the original data. Since the sum of diagonal elements of the covariance matrix (trace of Σ) is the total variance of the original dataset, the fraction of variance explained by the first k components is given by (Boyd *et al.*, 1992; Venegas, 2001; Zhang *et al.*, 2009)

$$\rho_{1\to k} = \frac{\sum_{i=1}^{k} \lambda_i}{\sum_{j=1}^{n} \lambda_j} \times 100\% \tag{3.48}$$

while the percentage of variance explained by the k-th component is

$$\rho_k = \frac{\lambda_k}{\sum_{j=1}^{n} \lambda_j} \times 100\%. \tag{3.49}$$

Since the first EOF basis function, E_1, corresponds to the highest eigenvalue λ_1, the highest percentage of variance in the original dataset is explained by $A_1 \times E_1$. There are different ways of selecting the number of EOF components to be retained and some are listed below:

- The number of EOF components to be retained can be determined by ignoring components of which the variance explained is less than the average variance, when the covariance matrix is used during EOF decomposition, or less than 1 when a correlation matrix is used (Holland, 2016).
- In the context of EOF analysis, a graph of eigenvalues (or variances) versus the corresponding PC rank is called a scree plot. The position of the "elbow" of a scree plot corresponds roughly to the number of EOF components that should be retained. Figure 3.10 is an example of a scree plot and one may decide to retain between 2 and 4 components. It is important to emphasise that the localisation of the exact position of an elbow on a scree plot may not always be straightforward and thus, the scree test is not considered as always a good method (Bremner, 2009).

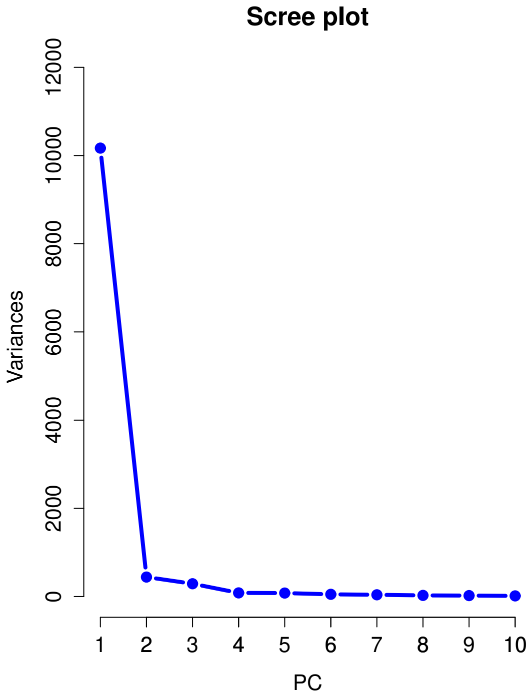

Figure 3.10: An illustrative example of a scree plot.

- Ignore high order/last EOF components that explain roughly equal percentages of variance (Holland, 2016).
- Knowing in advance the percentage of variance that may be suitable for the case being examined, one may decide to keep EOF components that explain the desired variance in the original dataset (Holland, 2016).

3.4.2 Linear and non-linear regression analysis

Regression analysis is a mathematical method that allows the establishment/examination of relationships between one or more variables, commonly referred to as dependent variables (or response variables, explained variables, predicted variables, or regressands), and several independent variables (also called explanatory variables, control variables, or regressors) (Chatterjee & Hadi, 2013). Apart from allowing to establish a relationship between dependent and independent variables, a regression analysis model allows also to predict the dependent variable based on independent variables, and determine which independent variable contributes more than others to the response of dependent variable (Yan, 2009). Mathematically, a regression analysis model that relates dependent and independent variables Y and X respectively, is expressed approximately as follows

$$Y \approx f(X, \beta) \tag{3.50}$$

where β represents a set of unknown parameters and are determined using statistical methods for optimization (Chatterjee & Hadi, 2013). The difference between the true/observed value Y of the dependent variable and the estimated value $\tilde{Y}$ is called the residual ($\varepsilon = Y - \tilde{Y}$). A regression is termed linear or non-linear if the dependent variable is a linear or non-linear combination of the parameters. Three types of regression are distinguished: simple linear regression (SLR), multiple linear regression (MLR), and non-linear regression (NLR) (Yan, 2009). In SLR, the dependent and independent variables are related by equation

$$y = \beta_0 + \beta_1 x + \varepsilon \tag{3.51}$$

where β_1 is the slope of the regression line, β_0 is the y intercept, and ε is the random error. SLR can thus be used to model a linear relationship between two variables y and x. In contrast, MLR relates one dependent variable to several independent variables according to expression

$$y = \beta_0 + \beta_1 x_1 + \beta_2 x_2 + \beta_3 x_3 + ... + \beta_p x_p + \varepsilon. \tag{3.52}$$

ε represents the random error and β_0, β_1, β_2, β_3, ..., β_p are regression coefficients. In the case where the relationship between a dependent variable and an independent variable is not linear in regression parameters, we have a non-linear regression (NLR) model (Pawitan, 2001). A typical example of such a model is

$$y = \frac{\alpha}{1 + e^{\beta x}} + \varepsilon \tag{3.53}$$

where α and β are the regression parameters and ε is the random error. The regression parameters of a model are unknown and should be estimated from the data. Finding the regression parameters of a model from a given dataset is referred to as model fitting or parameter estimation (Chatterjee & Hadi, 2013). In this study, the least squares method, which is the most commonly used method to determine the unknown coefficients of a model, and the Bayesian approach based on the MHA, were used.

3.4.3 Metropolis - Hastings Algorithm (MHA)

In this work, the Metropolis - Hastings algorithm (MHA) was applied for the first time in TEC modelling during storm conditions. MHA was used to determine the coefficients of a NLRA-based model and the task was accomplished by maximizing the likelihood function which represents the probability of getting the data given the model. The MHA advantage is that not only it allows the determination of the model unknown coefficients, but also provides the error bars and confidence intervals for all parameter estimates (Lewis & Bridle, 2002). MHA belongs to the class of algorithms that generate Markov chains i.e. a set of random variables having the property that the next state in the sequence depends only on the previous one and not on the states that preceded it (Christensen *et al.*, 2001, 2003; Doran & Müller, 2004; Liddle, 2009; Akeret *et al.*, 2013). Hence, MHA is known as one of the Markov Chain Monte Carlo (MCMC) techniques. MHA generates samples from a probability distribution in such a way that the more samples are generated, the more closely their distribution approximates the desired/targeted distribution (Lewis & Bridle, 2002; Christensen *et al.*, 2003). First developed by Metropolis and then later generalized by Hastings (Metropolis *et al.*, 1953; Hastings, 1970), the MHA has been a standard tool in statistical mechanics for solving numerical problems (Hastings, 1970). Nowadays, the MHA is widely used in cosmology as a standard technique for estimating cosmological parameters (Christensen *et al.*, 2001; Knox *et al.*, 2001; Lewis & Bridle, 2002; Christensen *et al.*, 2003; Rubino-Martin *et al.*, 2003; Doran & Müller, 2004; Jewell *et al.*, 2004; Dunkley *et al.*, 2005; Liddle, 2009; Akeret *et al.*, 2013).

The likelihood function is formulated based on the observed data defined by the data matrix $D = (D_i)$, with $i = 1, 2, ..., M$, and a set of unknown parameters $\Theta = (\theta_1, \theta_2, ..., \theta_N)$ that defines the NLRA. D_i are data points, M and N are total numbers of data points and the model's parameters respectively. The likelihood $L(D|\Theta) = P(data/model)$ represents the probability of obtaining the data given the model (Pawitan, 2001). Representing the true model by $f(\Theta)$, the noise is just the difference between the data and the model estimates. Similarly as established in Bretthorst (1988), under a Gaussian likelihood assumption, the likelihood function was defined as

$$\begin{aligned} L &\propto \prod_{i=1}^{M} exp\left\{-\frac{1}{2}\left(\frac{D_i - f_i(\Theta)}{\sigma_i}\right)^2\right\} \\ &= exp\left\{-\frac{1}{2}\sum_{i=1}^{M}\left(\frac{D_i - f_i(\Theta)}{\sigma_i}\right)^2\right\} \\ &= exp\left(-\frac{1}{2}\chi^2\right) \end{aligned} \tag{3.54}$$

where

$$\chi^2 = \sum_{i=1}^{M}\left(\frac{D_i - f_i(\Theta)}{\sigma_i}\right)^2 \tag{3.55}$$

and σ_i are the error per each data point. In a matrix form, Equation 3.54 can be generalized as follows

$$L \propto exp\left\{-\frac{1}{2}(D - F)^T\Sigma^{-1}(D - F)\right\} \tag{3.56}$$

where Σ is the covariance matrix of the observed dataset and F is the matrix of the model's estimates. The task is to find a set of parameters $\theta_1, \theta_2, ..., \theta_N$ that maximizes the likelihood, or equivalently, that minimizes χ^2. MHA is a computational way of maximizing the likelihood and can be summarized as follows (Doran & Müller, 2004; Liddle, 2009):

1. Choose randomly a starting point $\Theta_0 = (\theta_{01}, \theta_{02}, ..., \theta_{0N})$ within the parameter space. Save Θ_0 as a starting point of the chain.

2. Compute $L_0 = L(D|\Theta_0)$, i.e. the value of the likelihood that corresponds to the starting set of parameters.

3. Generate a new set of parameters $\Theta_i = (\theta_{i1}, \theta_{i2}, ..., \theta_{iN})$ from a proposed distribution. In the current work, this was accomplished by sampling the step size from a Gaussian distribution with 0 mean and standard deviation equal to the step size. By considering $\Theta_0 = \Theta_{i-1}$ (and $L_0 = L_{i-1}$), the new point Θ_i is obtained by moving a small step size $\Delta\Theta_{i-1}$ from the previous point Θ_{i-1}: $\Theta_i = \Theta_{i-1} + \Delta\Theta_{i-1}$.

4. Compute the likelihood $L_i = L(D|\Theta_i)$ i.e. the value of the likelihood that corresponds to the new set of parameters Θ_i.

5. If $L_i \geqslant L_{i-1}$, take the step. Save Θ_i as a new point in the chain and go to (3).

6. If $L_i < L_{i-1}$, there is a possibility of taking the following step, but with a certain probability. Generate a random number u from [0, 1]. If $u \leqslant L_i/L_{i-1}$, take the step as

in (5). If $u > L_i/L_{i-1}$, reject Θ_i and then save Θ_{i-1} as new point in the chain and go to (3).

7. Repeat (3) - (6) until the chain converges to the optimum solution.

The output is a chain i.e. matrices of N columns (number of the unknown coefficients) and rows equal to the number of steps taken. In the case of perfectly behaving Gaussian distributions, for each column of the chain, a corresponding distribution is made and its mean value is considered as the best estimate of the parameter associated to that column while the standard deviation represents the error bar. Optimization in Bayesian sense, as the one performed in the present work, consists of maximizing the Posterior distribution. Monte Carlo techniques (one implementation being the Metropolis-Hastings Algorithm) have the merit to provide sampling of both the posterior and likelihood distributions and their maxima. Figure 3.11 is an illustration of how the best estimate of a randomly chosen model coefficient/parameter, error bar and confidence interval can be extracted from a posterior distribution. The mean ($\mu \simeq -0.376 \times 10^{-03}$) as shown by the vertical red line, is the best estimate of the coefficient. It corresponds to the maximum value of the posterior distribution. The standard deviation is $\sigma \simeq 0.24 \times 10^{-04}$ while $\mu \pm \sigma$ defines the lower and upper limits of 1σ confidence interval.

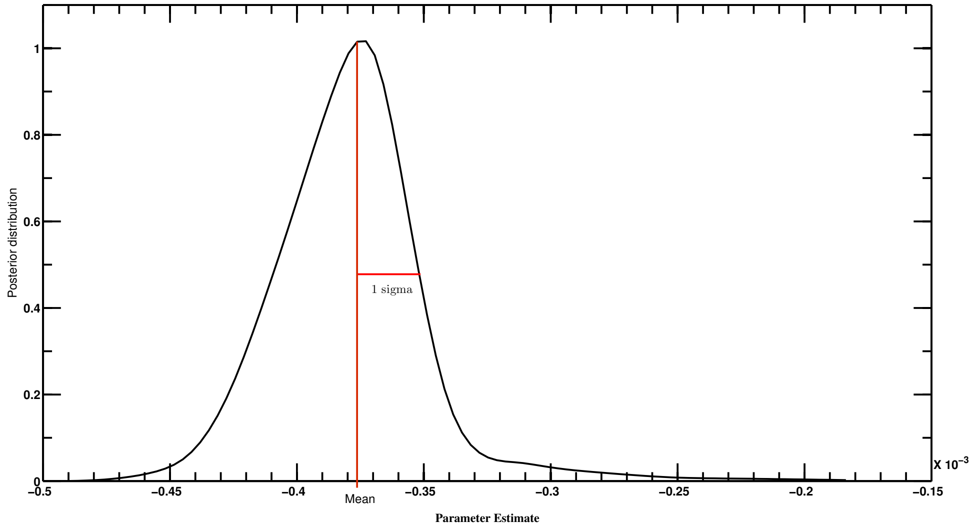

Figure 3.11: Typical illustration of the posterior distribution of a random model coefficient.

3.4.4 Artificial Neural Networks (ANNs)

3.4.4.1 Basics of an artificial neural network

An artificial neural network (ANN), also referred to as neural network (NN), is a computer programme/information processing system that learns and generalizes relationships between input(s) and the corresponding known (observed/measured) output(s) provided to it, and then estimates a desired output (Haykin, 1994; McKinnell & Poole, 2004; Oyeyemi *et al.*, 2006). An ANN is mainly composed of a set of neurons, also called nodes, units or cells, and connection links between them (Fausett, 1994; Gurney, 1997; Gershenson, 2003; Kriesel, 2005). Neurons can be seen as information processing units or simply, computational units where models that process information are inspired (Fausett, 1994; Gershenson, 2003). Connection links connect two neurons, and allow the information flow between them. For each connection link, there is an associated strength or weight. The weight can be understood as the strength or amplitude of a connection between two nodes. Thus, its role is to strengthen or multiply the inputs of a given neuron in such a way that, the higher the weight is, the stronger the input multiplied with it will be (Fausett, 1994; Gershenson, 2003). As an example, if three neurons X_1, X_2, and X_3 transmit signals x_1, x_2, and x_3 to a neuron Y, and we denote by w_1, w_2, and w_3, the weights associated with connection links from X_1 to Y, X_2 to Y, and X_3 to Y, respectively, then the input signal to neuron Y is $y_{in} = x_1 w_1 + x_2 w_2 + x_3 w_3$. Such a quantity is termed as the weighted sum (Kriesel, 2005). More generally, consider n signals $x_1, x_2, ..., x_i, ..., x_n$ from neurons X_1, X_2, ..., X_i, ..., X_n to a neuron Y_j, and store them in the input vector of the network $x = (x_1, x_2, ..., x_i, ..., x_n)$. There are n weights associated with connection links from X_1, X_2, ..., X_i, and X_n to Y, denoted w_{1j}, w_{2j}, ..., w_{ij}, ..., w_{nj}, where for example, w_{ij} symbolizes the weight on connection link from neuron X_i to neuron Y_j. If the weights are stored in a matrix $W = (w_{ij})$, the vector of weights (the j^{th} column of the matrix W) is $w_{.j} = (w_{1j}, w_{2j}, ..., w_{ij}, ..., w_{nj})^T$, where T denotes the transpose (Fausett, 1994; Kriesel, 2005). Thus, the net input y_{in_j} to the neuron Y_j will be

$$\begin{aligned} y_{in_j} &= x \cdot w_{.j} \\ &= \sum_{i=1}^{n} x_i w_{.j}. \end{aligned} \tag{3.57}$$

Considering an additional input $x_0 = 1$ with weight $w_{0j} = b_j$ called the bias, the input vector becomes $x = (1, x_1, x_2, ..., x_i, ..., x_n)$ and therefore, the net input y_{in_j} to the neuron Y_j is

$$\begin{aligned} y_{in_j} &= x \cdot w_{.j} \\ &= \sum_{i=0}^{n} x_i w_{ij} \\ &= x_0 w_{0j} + \sum_{i=1}^{n} x_i w_{ij} \\ &= b_j + \sum_{i=1}^{n} x_i w_{ij} \end{aligned} \tag{3.58}$$

Thus, in an ANN, a bias acts in a similar way as a weight does, but on a connection link of which the activation is equal to 1. The introduction of non-linearity into the output of a neuron is performed by an activation function also called a squashing function. This process is important, given that most of the real world data are non-linear and the aim is to learn these non-linear patterns within datasets. Typical examples of activation functions are provided in Fausett (1994); Kriesel (2005); Goodfellow *et al.* (2016).

3.4.4.2 Artificial neural network architectures

When neurons are visualized as arranged in layers, ANNs can be classified as single-layer or multilayer (Fausett, 1994; Haykin, 1994). The number of layers within an ANN can be obtained by simply counting the layers of connection links contained in that same network. Alternatively, the same task can be achieved by counting the number of the layers of neurons contained in the network , excluding the layer of the input neurons, since these do not perform any computation (Fausett, 1994). As shown in Figure (3.12) (a), a single-layer NN has one layer of connection links, or equivalently one layer of neurons (the output layer, in this case). In such a network, the links directly join the input to the output neurons. Figure (3.12) (b) shows a multilayer NN with two layers of connection links. A multilayer NN is generally composed of an input layer, one (case of Figure 3.12) or several hidden (or middle) layer(s) of which the computational units are called hidden neurons, and an output layer (Haykin, 1994; Fausett, 1994; Gurney, 1997).

The input layer which consists of a set of inputs, feeds information contained in the inputs to the network (Oyeyemi *et al.*, 2006). The number of neurons in the input layer equals the number of inputs fed to the network. The hidden layer is an intermediate layer between the input and the output layers. The activity of each hidden neuron depends on the activities of the input neurons and weights associated with the connection links between input and hidden neurons. The output layer consists of a set of outputs and the number of output neurons equals the number of outputs provided by the network.The behaviour of the output neurons depends on both the activity of hidden units and the weights associated with the

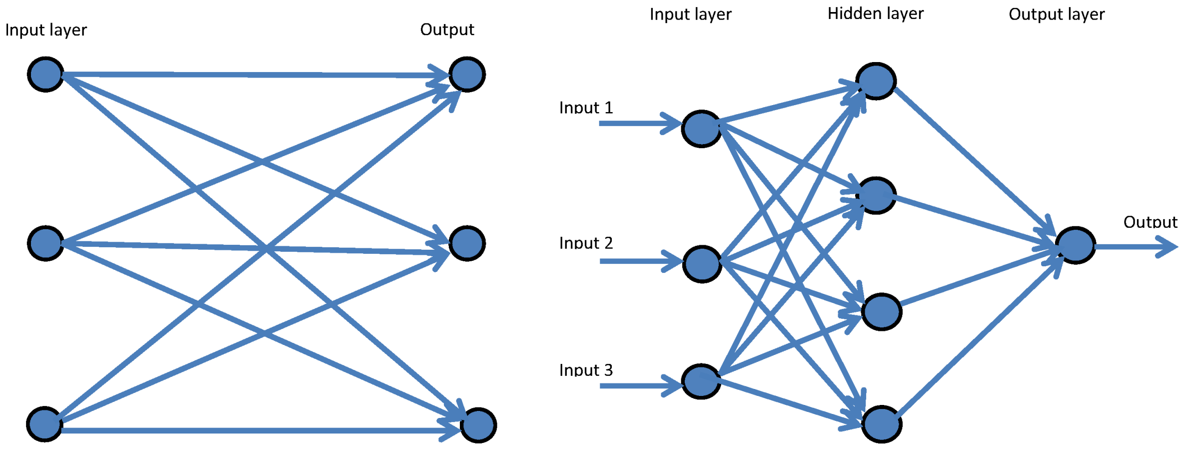

(a) Single-layer neural network.

(b) Multilayer neural network.

Figure 3.12: A schematic illustration of single-layer and multilayer feed-forward neural networks.

connection links between hidden and output units (Goodfellow *et al.*, 2016).

An ANN that allows the information flow in one direction, from input to the output neurons, is termed a feed-forward neural network (FFNN) (Fausett, 1994; Haykin, 1994). In a such network, there are no feedback or loops, meaning that the output information from a specific layer does not affect that same layer. Figure (3.12) illustrates a typical example of a single-layer FFNN (Figure (3.12) (a)) and a multilayer FFNN (Figure (3.12) (b)). When loops are introduced in an ANN, then information can flow in both directions (forward and backward). In this case, the network is a termed feedback neural network (FBNN). FBNNs are very powerful networks and sometimes extremely complicated.

3.4.4.3 Training an artificial neural network

An ANN should be trained in order to perform a given task. Training an ANN consists of a fine adjustment of weight and threshold in order to achieve a required functionality (Gurney, 1997). This process begins by randomly choosing initial weights. Appropriate algorithms are used during the training process. There are two ways of training an ANN, namely supervised and unsupervised training. In the former, the desired output is presented to the network with the inputs. In unsupervised training no desired output is presented to the network and the network itself has to learn the inputs without outside help (Fausett, 1994).

In this work, only supervised training was done and the FFNN with back propagation algorithm was used. This training algorithm is called as such because, during the training process, the ANN output is compared with the desired value and the error computed by the network is sent back to the input layer for a better adjustment of the weights and bias for each neuron. This iteration process is repeated over and over until the error converges to the optimum value (Fausett, 1994; Haykin, 1994; Sur *et al.*, 2015). The Leverberg-Marquardt backpropagation algorithm was used during training because of its time saving advantage (Hagan *et al.*, 1996; Habarulema & McKinnell, 2012)

3.4.5 Multi-Instrument Data Analysis System (MIDAS) algorithm

MIDAS is a general package that provides a time varying 3D image of the ionosphere. A number of studies related to ionospheric tomography imaging based on MIDAS inversion algorithm are available (Mitchell & Spencer, 2003; Yin *et al.*, 2004; Materassi & Mitchell, 2005; Meggs *et al.*, 2005; Dear & Mitchell, 2006; Muella *et al.*, 2011; Chartier *et al.*, 2014; Rose *et al.*, 2014; Giday *et al.*, 2016; Jayawardena *et al.*, 2016; Giday & Katamzi-Joseph, 2018). Using data from a network of GPS receivers over the USA mid-latitudes, it has been proven that MIDAS can produce images of electron concentration and TEC during extreme geomagnetic conditions ($K_p = 9$) that are in good agreement with observations (Yin *et al.*, 2004). The maximum electron density of the F2 layer (NmF_2) and peak height (hmF_2) obtained from MIDAS reconstruction using data from GPS receivers within South Africa have shown good agreement with the ionosonde measurements (Giday *et al.*, 2016). The authors further showed that MIDAS provides more accurate estimates of NmF_2 than IRI model while the reverse was noticed for hmF_2. With respect to the NmF_2 values extracted from MIDAS reconstruction during geomagnetic storms, it was found that MIDAS performs well for some storms while for others, relatively high deviations were observed (Giday *et al.*, 2016). For the European and North American regions, a good agreement between the reconstructed TEC by MIDAS and IRI with observations was observed despite some discrepancies for some periods of solar activity between 1998 - 2009 (Chartier *et al.*, 2012). MIDAS has also been applied to generate electron density and TEC maps for the equatorial ionosphere over the South America using data from GPS receivers distributed throughout the region of interest (Materassi & Mitchell, 2005).

Due to the dispersive nature of the ionosphere, dual-frequency radio signals transmitted from a GPS satellite experience differential phase changes, which are directly proportional to TEC between a satellite and receiver (Davies, 1990; Yin *et al.*, 2004; Jayawardena *et al.*, 2016). MIDAS starts from differential phase observations and then generates a matrix of slant TEC (STEC). From the definition

$$STEC = \int_S^R N_e(r, \theta, \phi) dl, \tag{3.59}$$

MIDAS, as an inversion method, uses $STEC$ as input data and computes the electron density N_e (Yin *et al.*, 2004). In Equation (3.59), S and R represent the satellite and receiver positions, r, θ, and ϕ are the radial distance from the center of the Earth to satellite, latitude and longitude, respectively, while l is the distance along the signal path from satellite to receiver. A detailed description of MIDAS is provided in Mitchell & Spencer (2003); Meggs *et al.* (2005); Jayawardena *et al.* (2016) and the summary presented here is based on these articles. To do imaging, the region of the ionosphere that is required to be imaged is subdivided into three-dimensional elements called voxels, bounded in latitude, longitude and altitude. Lengths of ray path elements of radio signals from satellites as observed within each voxel can be measured and stored in matrix A. Assuming that the electron density is constant within each voxel, the task is to solve a system of linear equations:

$$Ax = b \tag{3.60}$$

where x is the column matrix of electron densities within voxels, and b is the column matrix of the observed $STEC$. Since Equation 3.60 cannot be solved directly due to the complicated nature of the matrix A (e.g., A is a rectangular matrix and can therefore not be inverted), a new matrix X of orthonormal basis functions is introduced in such a way that the unknowns are just the coefficients of orthonormal basis functions. Representing the unknowns with the matrix W, Equation (3.60) can be written

$$AXW = b \tag{3.61}$$

The basis functions X can be generated using spherical harmonic expansion to represent the horizontal variation of the electron concentration, while empirical orthonormal functions (EOFs) which are for radial representation of the electron concentration, can be obtained from Chapman function or IRI model (Mitchell & Cannon, 2002; Mitchell & Spencer, 2003). For example, the basis functions used in Mitchell & Cannon (2002), consisted of 60 Legendre polynomials which represented the latitudinal variation of the electron concentration, while two EOFs generated using SVD decomposition from a limited range of Chapman profiles with peak heights ranging from 250 km to 350 km, were used to describe the variation of the radial electron concentration (Mitchell & Cannon, 2002; Mitchell & Spencer, 2003). Figure 3.13 illustrates the two EOFs derived from the Chapman function during the inversion problem. Solving Equation 3.61 for W we get

$$W = (AX)^{-1}b \tag{3.62}$$

According to singular value decomposition (SVD) theory, the matrix $(AX)^{-1}$ can be written in terms of orthonormal matrices V and U and a diagonal matrix ($D = diag(1/w)$) of singular values w:

$$(AX)^{-1} = VDU^T \tag{3.63}$$

Then W is obtained by substituting this expression into Equation (3.62):

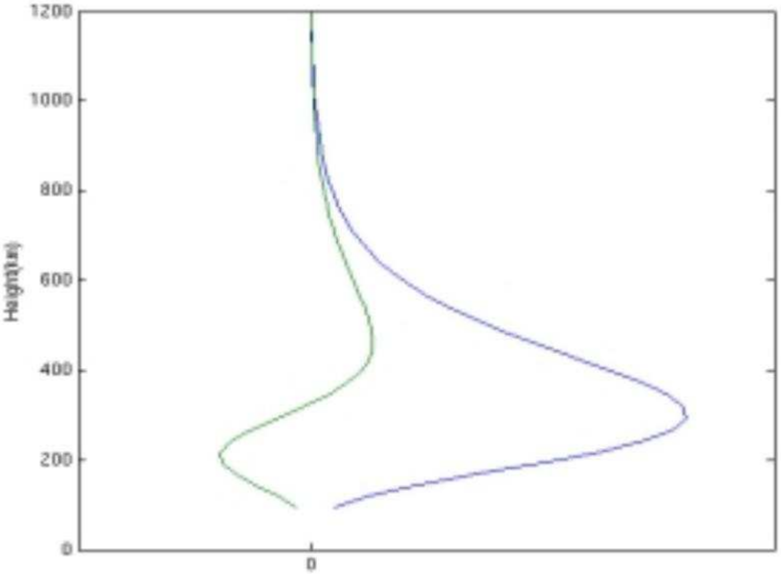

Figure 3.13: EOFs generated using SVD decomposition from a limited range of Chapman profiles with peak heights ranging from 250 km to 350 km (Mitchell & Cannon, 2002).

$$W = (VDU^T).b \tag{3.64}$$

Once W is found, the electron densities within voxels can finally be calculated by comparing Equations (3.60) and (3.61):

$$x = XW, \tag{3.65}$$

MIDAS computes Vertical TEC by vertical integration of the electron density obtained following the above procedure. Detailed theory about MIDAS can be found in a number of literature sources (Mitchell & Spencer, 2003; Meggs *et al.*, 2005; Bust *et al.*, 2007; Spencer & Mitchell, 2007; Jayawardena *et al.*, 2016; Yin *et al.*, 2017) and references therein. For more information about the recent MIDAS algorithm used in this study, readers are referred to Spencer & Mitchell (2007), and Yin *et al.* (2017).

3.5 Summary

This chapter briefly described the data sources, modelling inputs, as well as different techniques/algorithms considered during storm-time TEC modelling. In the following chapter, results based on ANNs and NLRA complimented with the MHA, are presented. The performance evaluation of MIDAS compared to ANNs, to reconstruct TEC during storm conditions, for the African low- and mid-latitude regions, is also discussed.

Chapter 4

Storm-time TEC modelling and reconstruction for various African latitudes

Solar radiation is the main driver of TEC variability. In this chapter, a simultaneous evaluation of the contributions of three solar activity indices $F10.7$, $F10.7p$, and SSN, to TEC modelling during storm conditions, for a mid-latitude station, Hermanus, (HNUS, 34.40° S, 19.22° E geographic; 42.33° S, 82.15° E geomagnetic), South Africa, is presented. The results are compared with the results of the NLRA model complemented by the Metropolis-Hastings Algorithm (MHA), specifically used to determine the unknown coefficients of the NLRA model. The results on TEC reconstruction for various African latitude regions based on Multi-Instrument Data Analysis System (MIDAS) inversion algorithm and ANNs, are also presented and compared. This comparative study of MIDAS and ANN results for the African low- and mid-latitude regions was published in Uwamahoro *et al.* (2018a).

4.1 Simultaneous evaluation of solar indices in storm-time TEC modelling

Three storm-time ANN models with same modelling inputs but different from the solar index considered ($F10.7p$, $F10.7$, or SSN) were developed and statistically evaluated. The results were compared with the NLRA model complemented by MHA, the latter having been specifically used for the model parameter estimation.

4.1.1 Data and description of modelling techniques

4.1.1.1 Data

Measurements at Hermanus, South Africa, GPS receiver station (HNUS, 34.40° S, 19.22° E geographic; 42.33° S, 82.15° E geomagnetic), for 2000 - 2017, were used to derive TEC. Only storm-time data for the period 2000 - 2017 were selected based on criterion of $Dst \leqslant -50$ nT and/or $K_p \geqslant 4$, and used to implement the models. Storm periods considered for validation were chosen based on the storm intensity, and the period of the solar activity when the storm happened. Thus, four geomagnetic storm periods were considered for each level of solar activity (high, moderate, low). Great, severe, strong, and moderate storms (as classified by Loewe & Prölss (1997)) are all represented in the validation dataset. Table 4.1 lists the storm periods selected for validation and their classification by Loewe & Prölss (1997). The minimum Dst and maximum K_p indices reached during the storms are also given.

Table 4.1: Storm periods selected for validation and their classification according to Loewe & Prölss (1997).

Storm period	Period of solar activity	Minimum Dst (nT)	Storm classification	Maximum K_p
15 - 23 July 2000	High	-301	Severe	9
28 - 31 October 2003	High	-383	Great	9
17 - 24 January 2005	Low	-103	Strong	8
26 - 30 September 2011	Moderate	-118	Strong	6.3
06 - 12 November 2013	High	-80	Moderate	5
27 February - 02 March 2014	High	-97	Moderate	5.3
06 - 12 September 2015	Moderate	-98	Moderate	7.0
12 - 17 April 2016	Moderate	-59	Moderate	5.0
12 - 15 October 2016	Moderate	-104	Strong	6.3
27 - 30 March 2017	Low	-73	Moderate	6.3
07 - 10 November 2017	Low	-70	Moderate	6.3
17 - 19 March 2018	Low	-50	Moderate	6.0

The modelling inputs for both ANN and NLRA models comprise universal time (t) of the day which represents diurnal variation of TEC, day number (d) of the year to account for seasonal, annual and semiannual variations of TEC, solar activity representations ($F10.7p$, $F10.7$, SSN for the ANN model, and $F10.7p$ for the NLRA model), as well as the local 3-hour magnetic index (a) derived from the 3-hour K index recorded at Hermanus Magnetic Observatory, and the symmetric disturbance field in the horizontal component of the Earth's magnetic field H ($symH$), which both represent geomagnetic activity. The $symH$ as an equivalent of high resolution Dst index, is a measure of geomagnetic activity related to ring currents that flow in the equatorial plane (Saba *et al.*, 1997). Studies have shown that geomagnetic activity due to CME-driven storms is well represented by the Dst index, and hence $symH$, whereas the K_p index better describes geomagnetic activity due to CIRs-driven storms (e.g., Huttunen *et al.*, 2002; Denton *et al.*, 2006). This is thus the reason for using both $symH$ and a (derived from K index) indices in storm-time modelling to represent geomagnetic activity, since the storm criterion of $Dst \leqslant -50$ nT and/or $K_p \geqslant 4$ considers both types of geomagnetic storms. The lone solar activity proxy $F10.7p$ was used in the NLRA model because of the exorbitant computational cost for the MHA while determining the NLRA model coefficients.

4.1.1.2 Description of ANN architectures

The ANN architectures considered in this study were defined by nine inputs (tc, ts, dc_1, ds_1, dc_2, ds_2, a, $symH$, and one of each $F10.7_p$, $F10.7_p, SSN$ indices, n hidden nodes, and 1 output node (TEC). The quantities tc, ts, dc_1, ds_1, dc_2, ds_2 defined by

$$tc = cos\left(\frac{2\pi \times t}{24}\right), \qquad ts = sin\left(\frac{2\pi \times t}{24}\right) \tag{4.1}$$

$$dc_1 = cos\left(\frac{2\pi \times d}{365.25}\right), \qquad ds_1 = sin\left(\frac{2\pi \times d}{365.25}\right) \tag{4.2}$$

$$dc_2 = cos\left(\frac{4\pi \times d}{365.25}\right), \qquad ds_2 = sin\left(\frac{4\pi \times d}{365.25}\right), \tag{4.3}$$

are cosine and sine components of time of the day (tc, ts), cosine and sine components of day number d of the year with periods of one year (dc_1, ds_1) to account for annual variation of TEC, and period of half a year (dc_2, ds_2) for the semiannual variation of TEC. Such time and day number decomposition into sine and cosine arguments was recommended by earlier studies in order to get rid of unrealistic trends sometimes observed at midnight (Poole & McKinnell, 2000; McKinnell & Poole, 2004; Oyeyemi *et al.*, 2006; Habarulema *et al.*, 2007). Such unrealistic trends are not related to the physics around midnight, but rather to inappropriate treatment of continuity at midnight (Poole & McKinnell, 2000). For each of the solar activity indices $F10.7p$, $F10.7$, SSN, ANN models were developed and validated. These are referred to as MF107p, MF107, and MSSN, respectively. For each model, the relationship between TEC and modelling inputs can be approximated as

for MF107p:

$$TEC \approx F_1(tc, ts, dc_1, ds_1, dc_2, ds_2, F107p, a, symH), \tag{4.4}$$

for MF107:

$$TEC \approx F_2(tc, ts, dc_1, ds_1, dc_2, ds_2, F107, a, symH), \tag{4.5}$$

and for MSSN:

$$TEC \approx F_3(tc, ts, dc_1, ds_1, dc_2, ds_2, SSN, a, symH). \tag{4.6}$$

Each of the ANN models was trained 12 times by changing the number of hidden neurons from 9 to 20 (random selection) and its accuracy was evaluated by computing the root mean square error (RMSE) defined by

$$RMSE = \sqrt{\frac{1}{N}\sum_{i=1}^{N}(TEC_{mod} - TEC_{obs})^2} \tag{4.7}$$

between the observed TEC in validation dataset and the corresponding ANN output. The RMSE is a measure of the spread between the observed and modelled TEC, which means that the smaller the RMSE, the better the model. N is the number of observations, while TEC_{obs} and TEC_{mod} are the observed and modelled TEC, respectively. Figure 4.1 illustrates the variation of RMSE with the number of hidden neurons within the range 9 - 20.

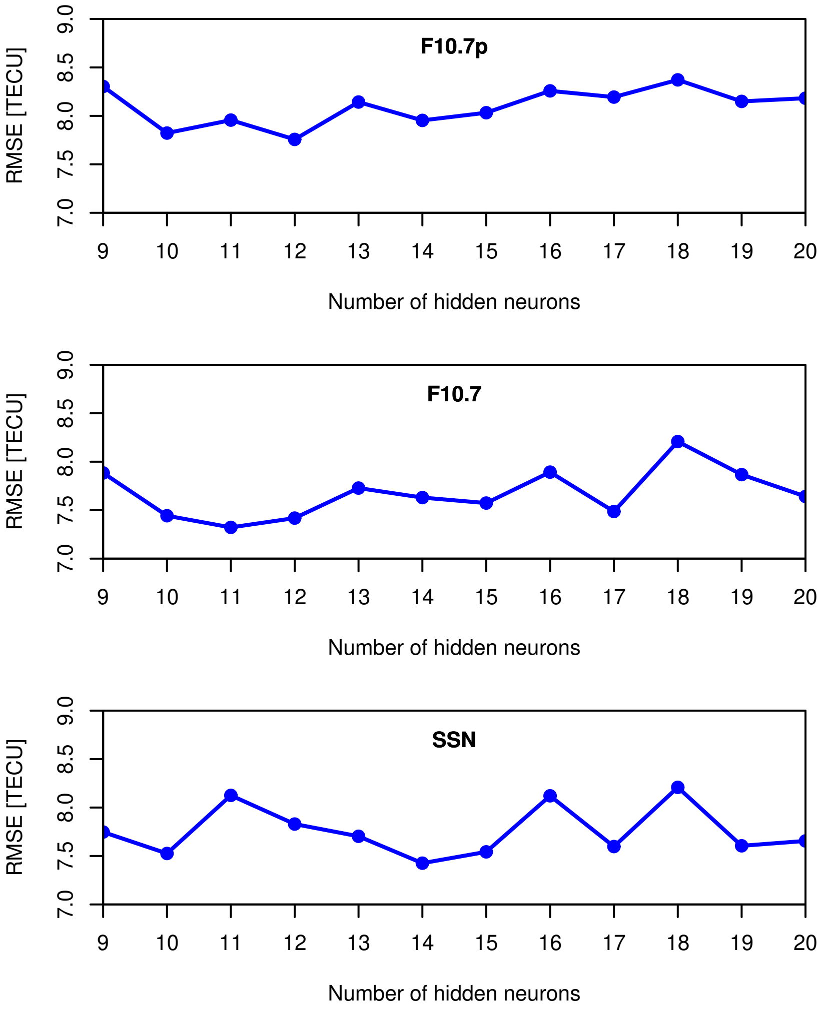
F10.7p

F10.7

SSN

Figure 4.1: Variation of RMSE with number of hidden neurons.

Figure 4.1 shows that the suitable numbers, (corresponding to the lowest RMSE values) of hidden nodes are 12 (MF107p), 11 (MF107), and 14 (MSSN). Therefore, the selected ANN architectures are 9 - 12 - 1, 9 - 11 - 1, 9 - 14 - 1 for MF107p, MF107, and MSSN, respectively. An ANN architecture/configuration of type 9 - 12 - 1 shows that there are nine input neurons, twelve hidden neurons, and one output neuron, in the input, hidden, and output layers, respectively.

4.1.1.3 Analytical representation of NLRA

The NLRA model of TEC was established as a product of different functions which individually represent different drivers of TEC variability during geomagnetic storms. For instance, diurnal variation of TEC was taken into account within an analytical expression f_1 of both sine and cosine components of time t of the day, defined as

$$f_1(t) = \alpha_0 + \alpha_1.cos\left(\frac{2\pi \times t}{24}\right) + \alpha_2.sin\left(\frac{2\pi \times t}{24}\right), \tag{4.8}$$

where α_0, α_1, and α_2 are constants. Annual, semiannual, and seasonal variations of TEC were all represented by an analytical function f_2, containing harmonic functions of day number of the year d, with periods of a year and half of the year:

$$f_2(d) = \beta_0 + \sum_{k=1}^{n=2}\left[\beta_k.cos\left(k\frac{2\pi \times d}{365.25}\right) + \beta_{k+2}.sin\left(k\frac{2\pi \times d}{365.25}\right)\right] \tag{4.9}$$

where β_0, β_1,..., β_4 are constants. Solar and geomagnetic activities were included in the model via a linear function f_3, defined in terms of solar and geomagnetic indices, as follows

$$f_3(F107.p, a, symH) = \gamma_0 + \gamma_1.(F107.p) + \gamma_2.a + \gamma_3.symH, \tag{4.10}$$

with γ_0, ..., γ_3 being constants. Thus, storm-time TEC was estimated with a non-linear expression defined as

$$TEC(t, d, F107.p, a, symH) = [f_1(t) \times f_2(d) \times f_3(F107.p, a, symH)]^{\kappa} \tag{4.11}$$

where κ is a constant that should be chosen such that the left side of equation (4.11) is positive, given that TEC is a positive quantity. The development of the product in equation (4.11) leads to 60 unknown constants and these were determined by using MHA as described in Chapter 3. The constant κ was determined statistically, using two measures of model accuracy: RMSE and correlation coefficient between observed and modelled TEC. The Pearson correlation coefficient is a measure of the capacity of a model to reproduce the observed trend and is defined as (e.g., Suhov & Kelbert, 2005):

$$\begin{aligned} R &= \frac{cov(TEC_{obs}, TEC_{rec})}{\sigma_{obs}\sigma_{rec}} \\ &= \frac{\sum_{i=1}^{N}(TEC_{obs_i} - \overline{TEC}_{obs})(TEC_{rec_i} - \overline{TEC}_{rec})}{\sqrt{\sum_{i=1}^{N}(TEC_{rec_i} - \overline{TEC}_{rec})^2}\sqrt{\sum_{i=1}^{N}(TEC_{obs_i} - \overline{TEC}_{obs})^2}}. \end{aligned} \tag{4.12}$$

where $cov(TEC_{obs}, TEC_{rec})$ represents the covariance between the observed (TEC_{obs}) and reconstructed TEC (TEC_{rec}), σ_{rec} and σ_{obs} are standard deviations of the reconstructed

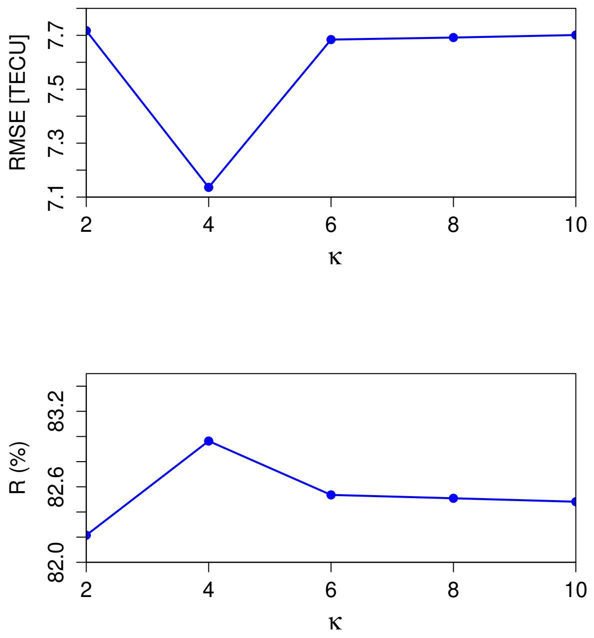

Figure 4.2: Variation of RMSE and R with κ.

and observed TEC, respectively. TEC_{obs_i} and TEC_{rec_i} represent the $i-th$ observation and the corresponding reconstructed TEC, while $\overline{TEC}_{obs}$ and $\overline{TEC}_{rec}$ are the mean values of the observed and reconstructed TEC, respectively. In Equation (4.11), we have arbitrarily considered the values of κ (even number to ensure the positivity of TEC) in the range 2 - 10 in steps of 2, followed by computation of the $RMSE$ and R between observations and modelled TEC for a given value of κ. The obtained values and the corresponding κ values are shown in Table 4.2. Figure 4.2 illustrates the variation of $RMSE$ (top panel) and R (bottom panel) with κ.

Table 4.2: RMSE and R values for different values of κ.

κ	2.00	4.00	6.00	8.00	10.00
RMSE	7.72	7.14	7.68	7.69	7.70
R (%)	82.22	82.96	82.54	82.51	82.48

Both Table 4.2 and Figure 4.2 show that for $\kappa = 4.00$, the RMSE is the lowest and R value is the highest. Thus, TEC obtained using Equation 4.11 corresponded to $\kappa = 4.00$. The case of $\kappa = 1$ has been considered while validating Equation 4.11. It was excluded from the selected values of κ because, for some geomagnetic storms considered for validation, negative TEC values were found and this is unrealistic.

4.1.2 Results and discussions

The results of modelling storm-time TEC with ANN and NLRA models are presented and compared in Figures 4.3 - 4.5. The geomagnetic activity during the selected storms, as observed at Hermanus GPS receiver location is described by the local 3-hour K index and its derivative 3-hour magnetic index. The equivalent description on a planetary scale is represented by the 3-hour K_p index, while the intensity and occurrence time of the storm is identified by means of Dst index. All these geomagnetic indices are presented along with modelled and GPS TEC (considered as observed TEC).

Figure 4.3 compares observed TEC (black curve) with MF107p (green curve), MF107 (red curve), MSSN (blue curve) and NLRA (light blue curve) predictions for storm periods that occurred during the solar maximum. Figures 4.3 (a), (b), (c) and (d) consist of the storm periods of 15 - 23 July 2000, 28 - 31 October 2003 (Halloween storm), 06 - 12 November 2013, and 27 February - 02 March 2014, respectively. Throughout the 17 - 23 July 2000 storm period, MF107p and MF107 provide close predictions which are in good agreement with actual data, specifically on 17 - 19 July 2000. For all the models, large discrepancies between modelled TEC and observations are noticed from 20 - 23 July 2000 where all the models underestimate the magnitude of daytime TEC. The negative storm effect on 16 July 2000 is better reflected by MSSN than by other modelling techniques. For the Halloween storm of 28 - 31 October 2003, all the models overestimate daytime TEC, while a reverse observation is seen for the moderate storm period of 27 February - 02 March 2014. For all the storms between 06 - 12 November 2013 (Figure 4.3 (c)) underestimation of TEC by all the models is observed on 06 - 10 November 2013 (exception with MSSN). The decrease in TEC observed on 11 November 2013 is more accurately estimated by MF107p than by MF107, MSSN, and NLRA models, while on 12 November 2013, MSSN predictions are in good agreement with observations.

The results of MF107p, MF107, MSSN, and NLRA models for storms which occurred during the moderate solar activity period are presented along with the observed TEC in Figure 4.4. Figure 4.4 (a) shows that all the models provide daytime predictions that exceed observations for almost the entire storm period of 06 - 12 September 2015, with large discrepancies specifically by the NLRA model. Figure 4.4 (b) shows that, although all the models fail to capture the observed TEC enhancement on 13 October 2016, the NLRA model estimates TEC better than other modelling techniques for the rest of the period. Figure 4.4 (c) shows that the NLRA model performs better than MF107p, MF107, and MSSN, where it estimates TEC magnitude accurately, with few exceptions, specifically during the afternoon where NLRA model results exceed observations. As shown in Figure 4.4 (d), all the models make almost the same predictions which are generally lower than observed TEC, specifically during daytime.

Figure 4.5 compares MF107p, MF107, MSSN, and NLRA results with observed TEC for four geomagnetic storm periods which occurred during the solar minimum period. Figure 4.5 (a) which consists of the storm period of 07 - 10 November 2017 shows that all the models fail to accurately estimate TEC on 07 November 2017. For 08 - 09 November 2017, the NLRA model provides more accurate estimates of the magnitude of TEC than MF107p, MF107, and MSSN, while an opposite case is seen on 10 November 2017. Figure 4.5 (b) (storm period of 27 - 30 March 2017) shows that daytime TEC is underestimated by all the models, except for 30 March 2017 where MSSN predictions agree well with actual data, specifically around midday. Figure 4.5 (c) which consists of the storm period of 17 - 19 March 2018 shows that, despite the shift in peak on 19 March 2018, the NLRA model provides more accurate predictions than other models, of which the predictions exceed observations, mostly in the afternoon. A comparison of the MF107p, MF107, MSSN, and NLRA results with GPS TEC for a sequence of geomagnetic storms which occurred between 17 - 24 January 2005 is presented in Figure 4.5 (d). The MF107, MSSN, and NLRA models largely overestimate daytime TEC on 17 - 20 January 2005, while MF107p makes predictions which are fairly close to observations. TEC enhancement observed on 21 January 2005 is seen by the MF107, MSSN, and NLRA models, while the 22 January 2005 TEC depletion is slightly followed by MF107.

Figure 4.6 presents the RMSE and R values for the twelve storm periods considered for validation. Evaluating the performance of MF107p, MF107, and MSSN (three models that differ from the solar activity index used) based on RMSE values (top panel of Figure 4.6), it was found that MF107p is more accurate (smaller values of RMSE) than MF107 and MSSN for 5 out of 12 storm periods. However, MF107 provides more accurate predictions than MF107p and MSSN for 4 out of 12 storm periods, while MSSN was found to predict TEC better than MF107p and MF107 for 3 out of 12 storm periods. These results show that a model with $F10.7p$ index as solar proxy is likely to be more accurate than models with $F10.7$ or SSN as solar activity representation. This agrees with empirical results presented by Liu *et al.* (2006) and Liu & Chen (2009) who demonstrated that, in a statistical sense, $F10.7p$ is a better representation of solar activity than $F10.7$ index.

Explanations for the fact that MF107p and MF107 perform better than MSSN may be linked with the interpretation of $F10.7$ and SSN indices. The SSN, which is the number of sunspots on the Sun's photosphere, indicates that there are active regions on the Sun surface that could possibly release energy towards the Earth. On the other hand, $F10.7$ represents the total amount of solar flux being received at a wavelength of 10.7 cm. Thus $F10.7$ has a direct influence on the Earth's ionosphere compared with SSN and this could be the reason

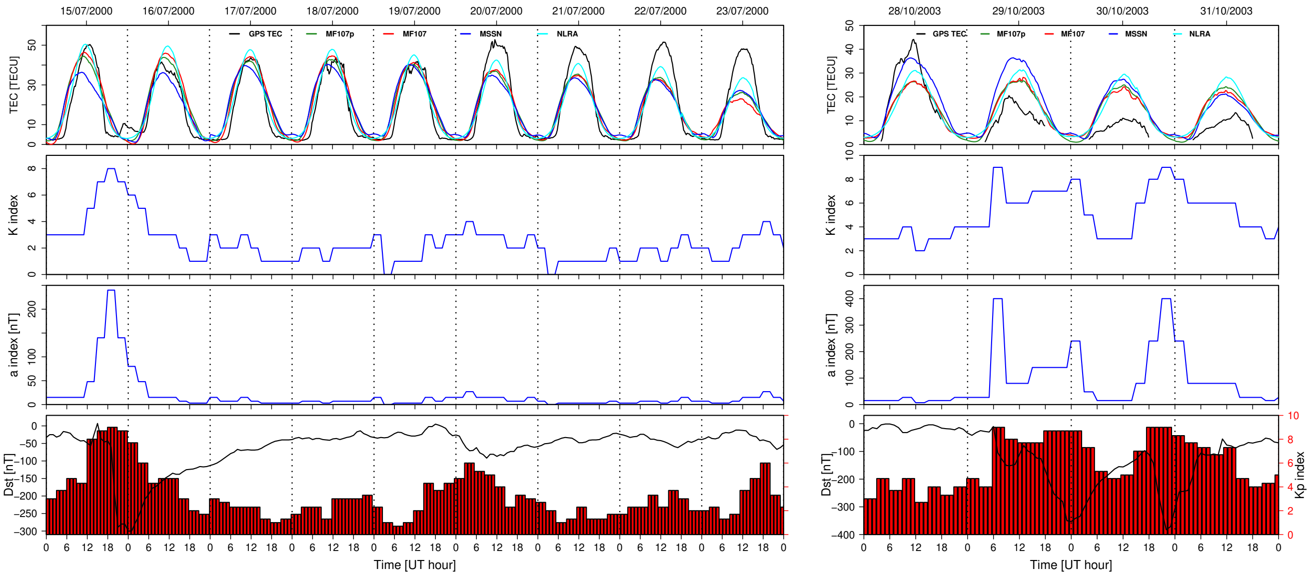

(a) Storm period of 15 - 23 July 2000.

(b) Storm period of 28 - 31 October 2003.

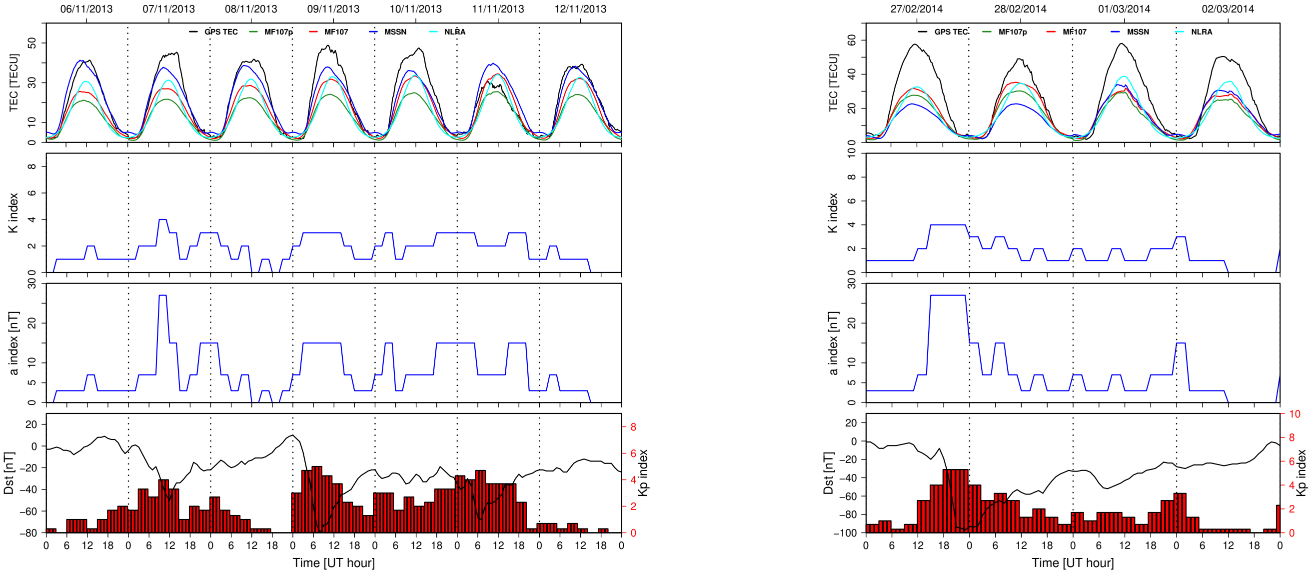

(c) Storm period of 06 - 12 November 2013.

(d) Storm period of 27 February - 02 March 2014.

Figure 4.3: Comparison of observed and modelled TEC for the solar maximum storm periods.

for the better performance of MF107p and MF107 than MSSN.

When comparing the performances of the ANN-based models, MF107p, MF107, and MSSN, with the NLRA model, Figure 4.6 (top panel) shows that the NLRA model is more accurate than other models for 6 out of the 12 storm periods that were considered for validation. This is indicated by the relatively smaller values of RMSE noticed for 15 - 23 July 2000, 27 February - 02 March 2014, 12 - 17 April 2016, 12 - 15 October 2016, 07 - 10 November 2017, and 17 - 19 March 2018. The higher accuracy of the NLRA model compared with other models is confirmed by the relatively high values of R mostly for NLRA (Figure 4.6, bottom panel). This indicates its ability to reproduce the general trend of the observed TEC. It is how-

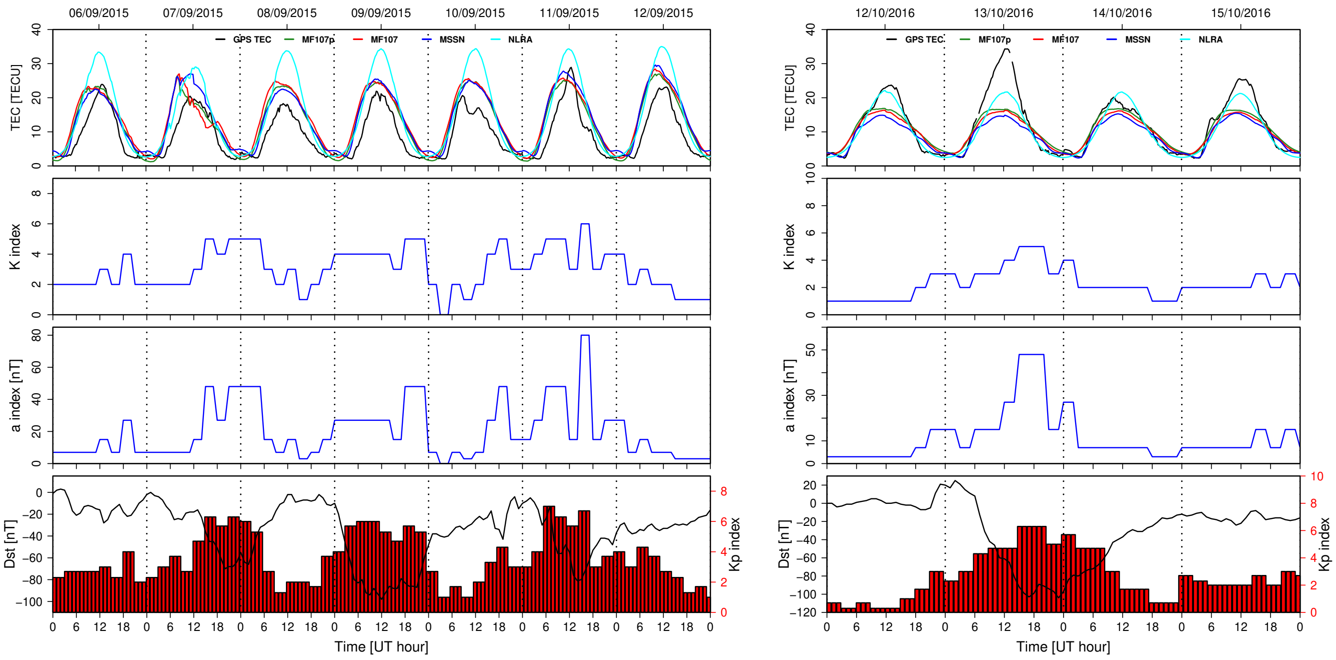

(a) Storm period of 06 - 12 September 2015.

(b) Storm period of 12 - 15 October 2016.

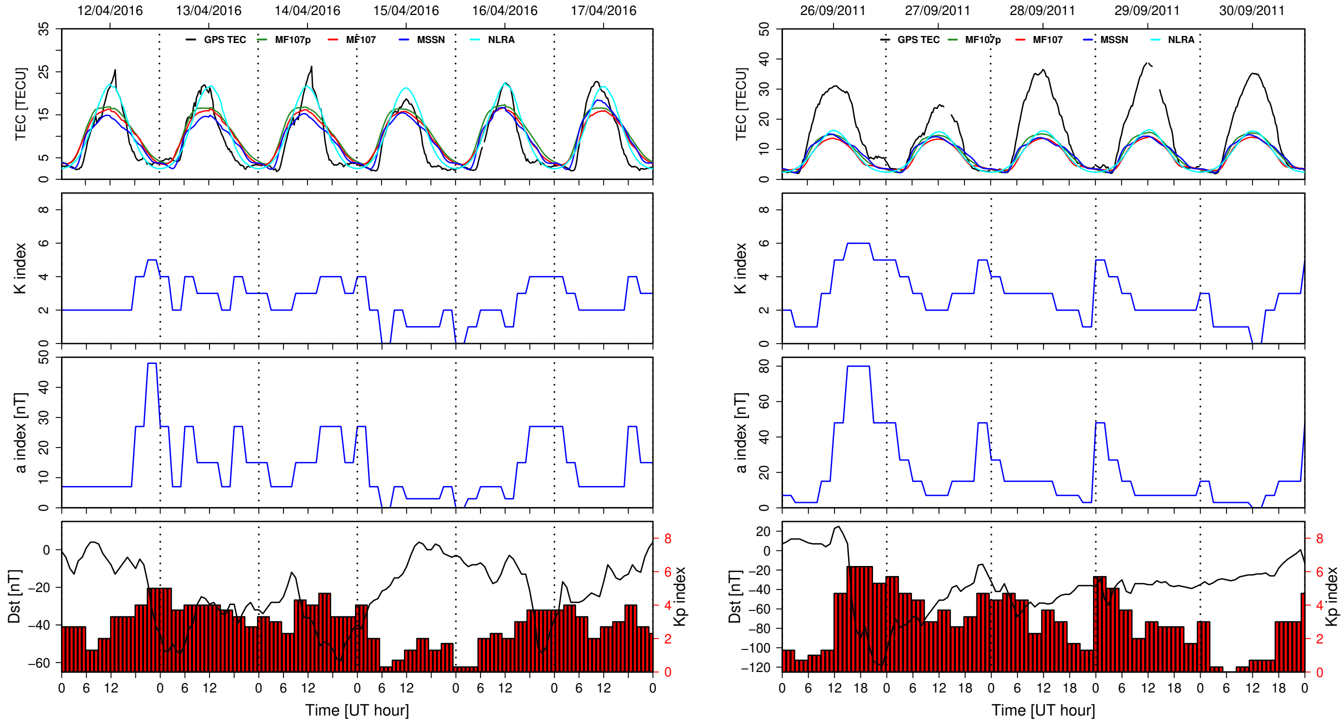

(c) Storm period of 12 - 17 April 2016.

(d) Storm period of 26 - 30 September 2011.

Figure 4.4: Comparison of the observed and modelled TEC for the storm periods which occurred during the moderate solar activity period.

ever important to point out that short terms features are not captured by the NLRA model (e.g., 28 - 31 October 2003) and for some cases, the model is insensitive to TEC dynamics observed during storms (e.g., 15 - 23 July 2000). The ability of a regression analysis (RA) based technique to estimate TEC during geomagnetically quiet conditions was highlighted by

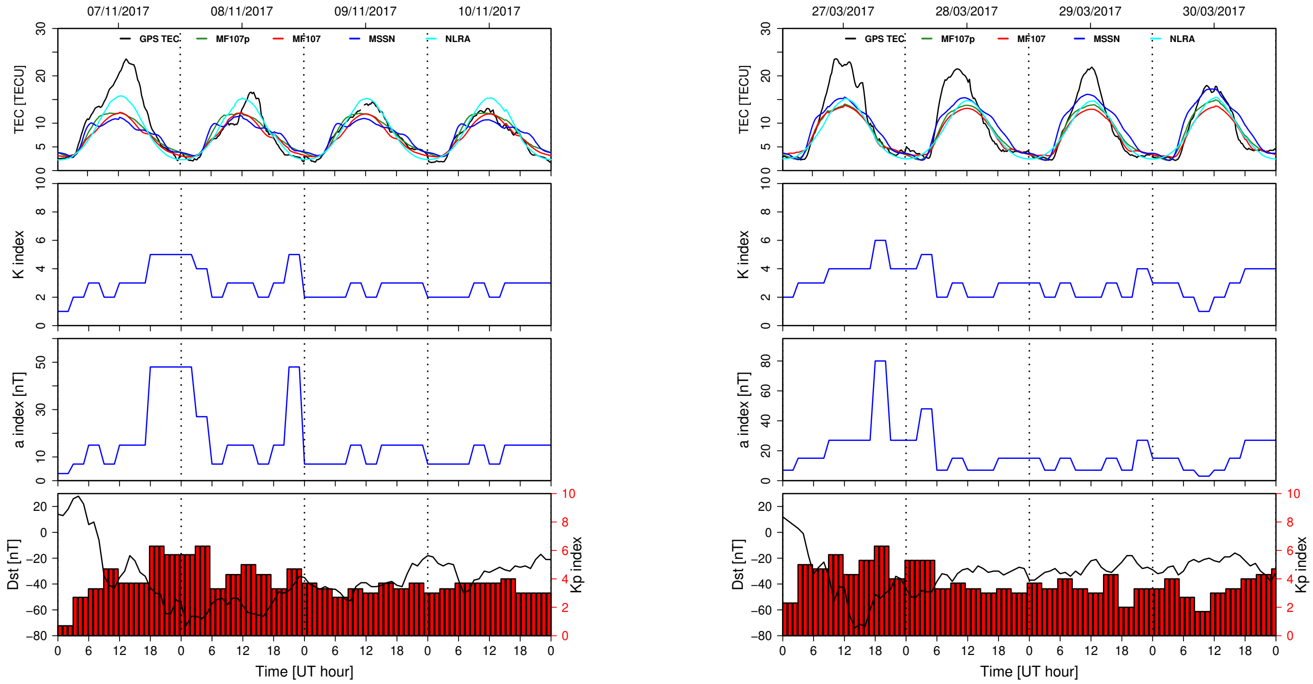

(a) Storm period of 07 - 10 November 2017.

(b) Storm period of 27 - 30 March 2017.

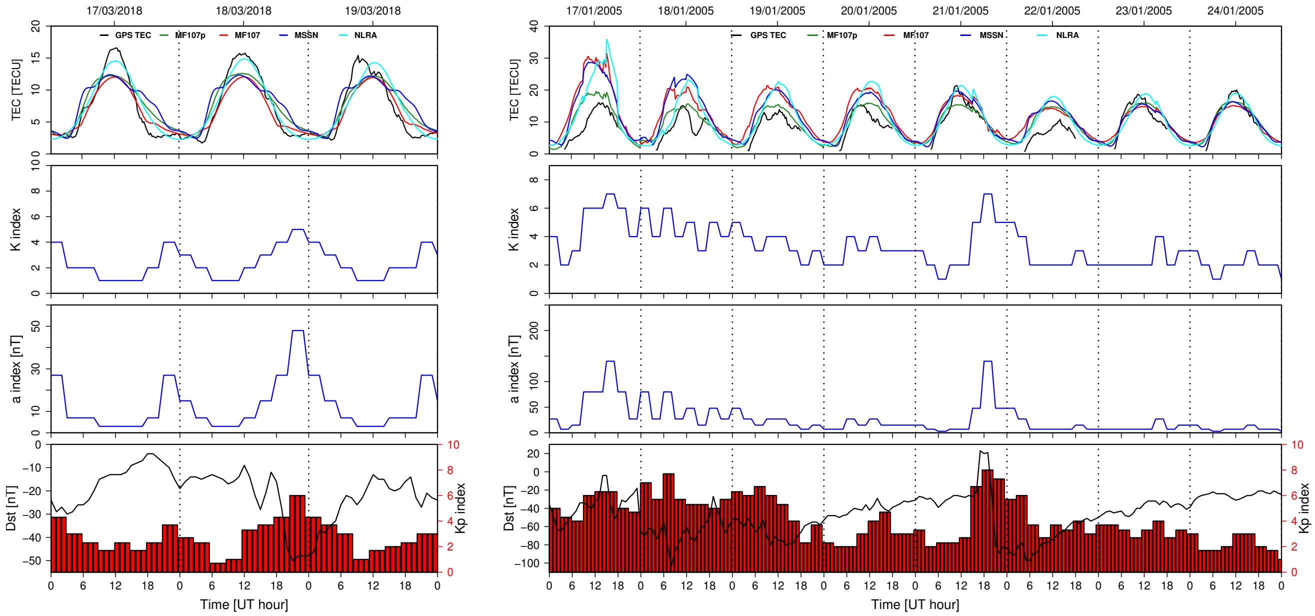

(c) Storm period of 17 - 19 March 2018.

(d) Storm period of 17 - 24 January 2005.

Figure 4.5: Comparison of the observed and modelled TEC for the storm periods which occurred during the solar minimum.

Feng *et al.* (2016) who developed an empirical TEC model for the northeast region of China (40° – 50° N, 120° – 130° E). The efficiency of an empirical TEC model based on RA was reported by Hajra *et al.* (2016) when modelling quiet-time TEC over the northern equatorial ionization anomaly (EIA) crest (Calcutta). Quiet-time TEC modelling over Taiwan (120° E, 24° N) based on functional fitting has been developed and validated (Kakinami *et al.*, 2009). The range of RMSE values ($\sim 4-14$ TECU) obtained for quiet-time modelling by Kakinami

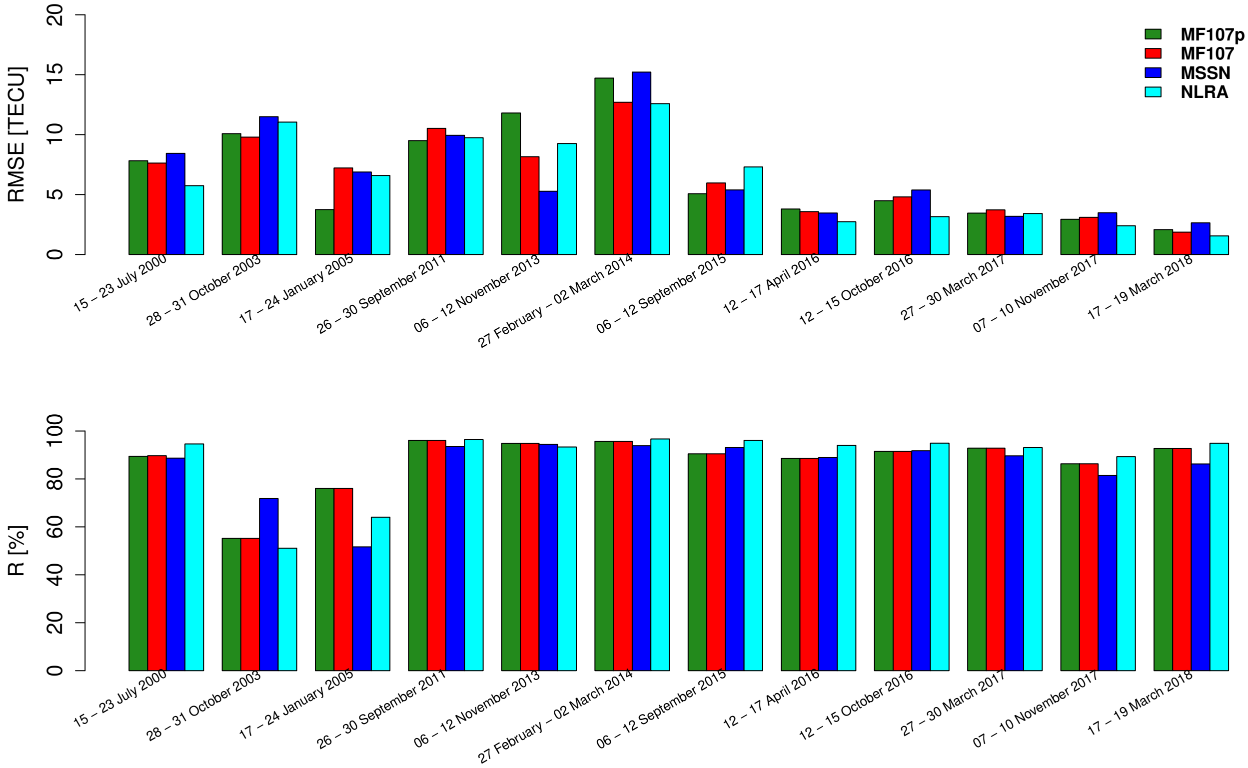

Figure 4.6: RMSE and R values between observed and modelled TEC for storm periods considered for validation.

et al. (2009) is comparable with the values obtained by the NLRA model ($\sim 1 - 13$ TECU) for storm conditions.

The average RMSE values ($RMSE^{av}$) computed over 12 storm periods considered for validation are 6.56, 6.59, 6.73, and 6.25 TECU for MF107p, MF107, MSSN, and NLRA models, respectively. The performance of each model with respect to another can be evaluated using the expression

$$\frac{RMSE^{av}_{Model_1} - RMSE^{av}_{Model_2}}{RMSE^{av}_{Model_2}} \times 100\%, \tag{4.13}$$

which indicates how much percentage, on average, model 2 is more accurate than model 1. The application of Equation (4.13) shows that MF107p performs $\sim$ 0.46 % and 2.59 % better than MF107 and MSSN models, respectively, while the NLRA model performs 7.68 %, 5.44 %, and 4.96 % better than MSSN, MF107, and MF107p models, respectively. Previously, the weakness of the ANN model to specifically predict the positive storm effect, or both positive and negative storm effects within a single storm period, has been reported by Habarulema *et al.* (2010, 2011); Uwamahoro *et al.* (2018b). The fact that such types of storms are more dominant in the storm-time dataset reserved for validation may be the reason that the ANN model failed to provide accurate storm-time predictions compared with NLRA model. However, intensive computation of NLRA model coefficients based on MHA requires high computing facilities, and this makes ANN model to be more employed for most of the work presented in this study for time saving and computational cost reduction. In the following section, the ANN model is evaluated and compared with MIDAS performance along various latitudes of the African regions.

4.2 Performance evaluation of MIDAS and ANNs to reconstruct storm-time TEC

In Chapter 3, we provided examples of studies that applied ANNs and MIDAS to TEC reconstruction in low and mid-latitude regions. Although MIDAS and ANNs have separately been tested under both geomagnetically quiet and disturbed conditions, no study has compared their performances relative to each other over various latitudes (low and mid-latitude regions). In this perspective, we aimed at performing a statistical evaluation, for the first time, of the capability of MIDAS compared with ANNs to reconstruct storm-time TEC over the African low and mid-latitude regions. Additionally, MIDAS and ANN results are compared with IRI-2016 TEC predictions. A study like the one presented in the current work which compares different modelling/reconstructing techniques of the ionospheric TEC during geomagnetic storms, is important for future improvements in ionospheric modelling. Evaluation of how much percentage and under which circumstances a model is more accurate with respect to another, is a contribution towards the efforts to implement a more efficient optimization algorithm for storm-time TEC modelling/reconstruction. This study is particularly useful for the IRI community considering the fact that, since its establishment, the IRI model has continuously been improved and is still being updated as new data and more accurate models become available. The work presented in this section was published in Uwamahoro *et al.* (2018a).

4.2.1 Data and methods

4.2.1.1 Data selection

Using a storm criterion of $Dst \leqslant -50$ nT and/or $K_p \geqslant 4$, databases of historical storm-time TEC data were built and used for TEC modelling based on ANNs. In this study, individual ANN models were developed for each location considered. Storm-time TEC data used to implement ANN models were derived from GPS measurements over receiver stations representing mid-latitude: Tete (TETE, 16.15° S, 33.58° E; 26.94° S geomagnetic), Mozambique; low latitude: Moiu (MOIU, 0.29° N, 35.29° E; 9.17° S geomagnetic), Kenya; Nazret (NAZR, 8.57° N, 39.29° E, 0.25 ° S geomagnetic), Ethiopia; and Sheb (SHEB, 15.85° N, 39.05° E;

7.36° N geomagnetic), Eritrea. Due to the lack of data specifically for ANN model development, the African mid-latitude in the northern hemisphere wasn't part of this study. Four geomagnetic storm periods were selected to evaluate the ability of MIDAS, ANNs and IRI to reconstruct/predict storm-time TEC. The selected validation periods were chosen in different stages of solar cycle: 06 - 13 March 2012 and 18 - 24 February 2014, 16 - 22 March 2015, and 24 - 30 October 2016, for high, moderate, and low solar activity periods, respectively. The classification of the selected storms based on their intensity is presented in Table 4.3.

Table 4.3: Classification of the selected storm periods by K_p (NOAA Space Weather Scales) and Dst (Loewe & Prölss, 1997).

Storm period	Solar activity	Maximum K_p	Classification (NOAA)	Minimum Dst (nT)	Classification (Loewe & Prölss, 1997)
06 - 13 March 2012	High	8	Severe	-145	Strong
18 - 24 February 2014	High	6	Moderate	-116	Strong
16 - 22 March 2015	Moderate	8	Severe	-223	Severe
24 - 30 October 2016	Low	6	Moderate	-64	Moderate

For independent validation-data, the four validation storms periods were excluded in databases used to develop ANN models. In the case of missing data for some of the storm periods selected, the closest stations such as Addis Ababa (ADIS, 9.04° N, 38.77° E; 0.18° N geomagnetic), Ethiopia; Zomba (ZOMB, 15.38° S, 35.33° E; 26.07° S geomagnetic), Malawi; and Debarek (DEBK, 13.15° N, 37.89° E; 4.32° N geomagnetic), Ethiopia; were used for NAZR, TETE and SHEB, respectively. Note that it has been demonstrated that a model developed at one station can be validated over any other location within a latitudinal and longitudinal coverage of 8.7° and 10.6°, respectively (Uwamahoro & Habarulema, 2015). Table 4.4 presents geographic coordinates and magnetic latitudes (MLA) ($tan(MLA) = 0.5 \times tanI$) of GPS ground receiver stations considered to develop and validate ANN models, while their locations are shown on the map in Figure 4.7. For each station, the magnetic inclination I that was used to compute MLA was obtained from the International Geomagnetic Reference Field (IGRF) model.

Table 4.4: Geographic (GLat & GLon) coordinates and magnetic latitudes (MLA) of the ground receiver stations used for the development (shown with *) and validation of the ANN models.

Station name	Station ID	Country	GLat (°)	GLon (°)	MLA (°)
Debarek	DEBK	Ethiopia	13.15	37.89	6.21
Sheb*	SHEB	Eritrea	15.85	39.05	9.71
Nazret*	NAZR	Ethiopia	8.57	39.29	0.78
Addis Ababa	ADIS	Ethiopia	9.04	38.77	1.28
Moiu*	MOIU	Kenya	0.29	35.29	-10.52
Tete*	TETE	Mozambique	-16.15	33.58	-33.01
Zomba	ZOMB	Malawi	-15.38	35.33	-31.45

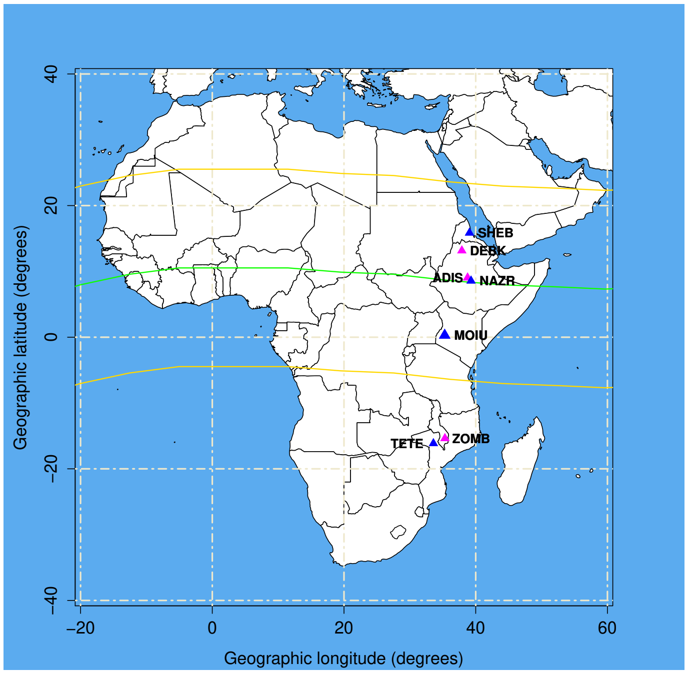

Figure 4.7: Location of ground-based GPS receiver stations used to develop and validate ANN models (blue triangles). Shown in magenta are stations used for validation in the case of missing data at primary locations.

For each station considered for validation, IRI TEC data were obtained by running the online IRI-2016 model currently available at `https://ccmc.gsfc.nasa.gov/modelweb/models/iri2016_vitmo.php`, with NeQuick as topside option and with the STORM option on. It is worth noting that the validity of the storm-time model incorporated in the IRI has been evaluated for mid-latitude storms and it was found that the model captures negative ionospheric effects fairly well during summer season, but that it was inaccurate in predicting positive storm effects for winter mid-latitude storms (Fuller-Rowell *et al.*, 2000). It is also important to mention that IRI model provides TEC values up to the altitude of 2000 km (Chartier *et al.*, 2012; Habarulema & Ssessanga, 2017).

4.2.1.2 MIDAS

In the current study, the African region within −30° to 36° latitude and 30° to 44° longitude was considered during inversion, with voxel elements defined by a grid of 2° latitude × 2° longitude, and an altitude range of 100 to 1200 km in steps of 40 km. Slant TEC used as input to MIDAS is an integrated quantity along the satellite - receiver signal path and thus, ray path elements intercepting within a given voxel contain some plasmasphere contribution. It is therefore likely that an unknown amount of plasmaspheric TEC is included at ionospheric heights during reconstruction (Chartier *et al.*, 2012; Kinrade, 2013). Since the matrix of ray path elements is rectangular and therefore can not be directly inverted, a set of orthonormal basis functions and an appropriate mapping matrix are required to perform the inversion

(Mitchell & Spencer, 2003). The introduction of basis functions permits the representation of temporal and spatial distributions of the ionospheric electron density separately (Mitchell & Cannon, 2002). The set of empirical orthogonal functions (EOF) can be generated from ionospheric models such as IRI and Chapman function (Mitchell & Spencer, 2003; Yin *et al.*, 2017) and the latter was used in the current work. MIDAS uses observation data from a user-defined time window centered at the time of the inversion. However, depending on the choice of the length of the time window, which translates into the amount of observation data ingested in each time step of the inversion process, the final output may vary. Short temporal variations may not be captured when a wide time-window is used, but also the amount of observation data that goes into the inversion matters. Therefore, a compromise needs to be made between the amount of observation data that goes into a single run for a single solution and width of the time-window. In a region of sparse GPS receivers such as the one considered in this study, shorter time windows mean less observation data for the inversion. Thus, observations from a sliding time window of 5.5 h was used in the inversion to obtain electron densities at every 30-minute interval. Also a non-linear optimization method was used to produce the results presented in this study since it has an advantage of avoiding negative values of electron density. Vertical TEC from MIDAS was computed by vertical integration of the electron density obtained following the above procedure.

4.2.1.3 ANN configuration

Feed-forward neural networks (FFNNs) with the Levernberg-Marquardt backpropagation algorithm were used during training in the current work. Such type of configuration is preferred especially the training algorithm that is well known for its time saving while implementing the input-output mapping process (Jang *et al.*, 1997), and has previously been applied to quiet and storm time TEC modelling over the South African mid-latitude region (Habarulema & McKinnell, 2012; Uwamahoro & Habarulema, 2015). The selection of modelling inputs was done based on factors that influence TEC variability such as diurnal, seasonal, annual and semiannual variations, solar and geomagnetic activities (Habarulema *et al.*, 2007; Ercha *et al.*, 2012). Diurnal variation is represented by time of the day t, while day number of the year d represents annual and seasonal variation of TEC. The time of the day and day number of the year were decomposed into cosine and sine components of time (tc, ts) and day (dc, ds) as previously defined by equations (4.1) and (4.2). The solar activity was represented by the modified solar flux index $F_{10.7p}$. For geomagnetic activity, the planetary 3-hour ap index, auroral electrojet index AE (5-minute time resolution), and the symmetric disturbance field in the horizontal component of the Earth's magnetic field H (5-minute time resolution), $symH$, were all used during storm-time TEC modelling. The $symH$ is a measure of geomagnetic activity due to ring currents as observed in low latitude (Saba *et al.*, 1997). AE stands for geomagnetic activity that results from ionospheric currents flowing in the auroral ionosphere

(Saba *et al.*, 1997; Ballatore & Maclennan, 1999), and in the current work we think that, given the amount of storm-time data used, there is a possibility that some of these currents may also affect the mid-latitude. In addition to this, AE also plays a significant role in computation of the total magnetospheric energy consumption rate during magnetic storms and substorms (Akasofu, 1981). The 3-hour a_p index is derived from K_p index and the latter represents the intensity of magnetic activity on a planetary scale as seen at sub-auroral latitudes (Rostoker, 1972; Saba *et al.*, 1997). Previous studies (e.g., Huttunen *et al.*, 2002; Denton *et al.*, 2006) have shown that K_p index is a good representation of magnetic activity for CIR-driven storms, while Dst index and hence, $symH$, represents well geomagnetic activity for CME-driven storms. Thus, considering that original datasets are composed of a large number of storms, taking also into account that CIR and CME-driven storms are both included in the datasets, the three geomagnetic indices were all used to globally represent, at a latitudinal scale, different geomagnetic activity contributors to TEC changes due to storms. There also exists a couple of works that included all three geomagnetic indices in modelling over different latitude sectors (Ercha *et al.*, 2012; Dabbakuti *et al.*, 2016; Dabbakuti & Ratnam, 2017; Tshisaphungo *et al.*, 2018). The number of input neurons was therefore eight as defined by eight different inputs: tc, ts, dc, ds, $F107p$, ap, AE, $symH$ whereas there was one output neuron corresponding to the modelled parameter, TEC. For a specific station, the ANN architecture used during training was determined by selecting the number of hidden neurons that corresponds to the minimum RMSE. For each location, the network was trained by varying the number of hidden neurons from 6 - 20 (range selected randomly), followed by computation of the RMSE between the observed and the reconstructed/predicted TEC when ANN models are tested on validation datasets. Figure 4.8 illustrates the variation of RMSE with number of hidden neurons for different locations.

It is clear from Figure 4.8 that 15, 14, 11, 15 hidden neurons were used for MOIU, NAZR/ADIS, SHEB/DEBK and TETE/ZOMB respectively, because they correspond to the lowest RMSE over the validation period. Therefore, the corresponding architectures (which gave minimum RMSE values) considered for TEC reconstruction by ANN are 8-15-1, 8-14-1, 8-11-1, and 8-15-1. The amount of data used for the development of ANN models and the fact that TEC varies with latitude differently, are likely the main reasons of different ANN architectures. Table 4.5 shows the selected architectures, data coverage periods, and number of data points within datasets used to develop ANN models.

4.3 Results and discussion

For each storm period used for validation the intensity and the occurrence time of the storm are shown by Dst and Kp indices. Figure 4.9 shows validation results from MIDAS, ANN and IRI-2016 models along with GPS TEC observations for storms that occurred during high solar

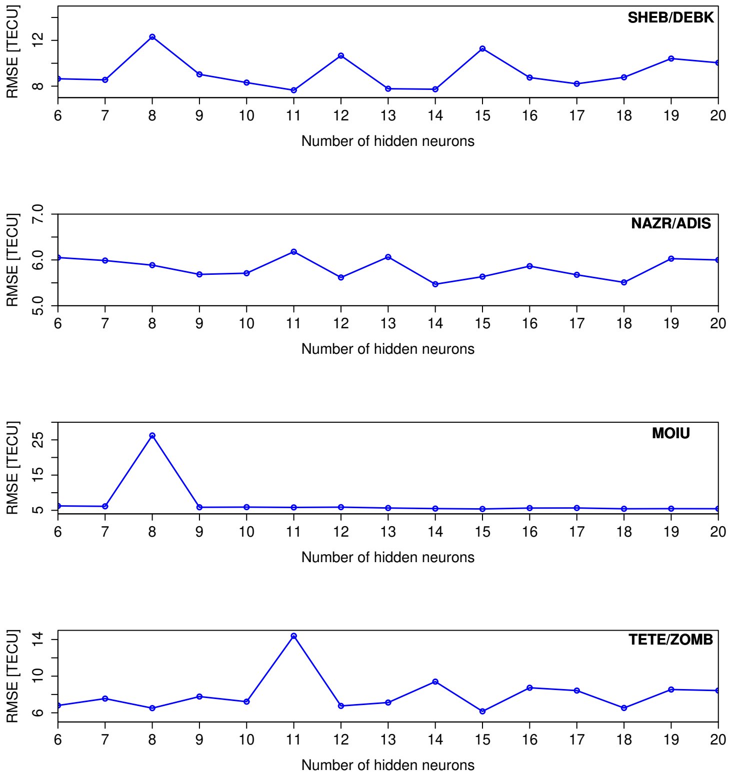

Figure 4.8: Variation of RMSE between GPS TEC observations and ANN predictions with number of hidden nodes for validation storm periods.

Table 4.5: ANN architectures, data coverage periods, and number of data points within datasets used to develop ANN models.

Station	Architecture	Period	Number of data points
SHEB	8-11-1	2004 - 2016	178946
NAZR	8-14-1	2007 - 2016	206162
MOIU	8-15-1	2008 - 2016	224491
TETE	8-15-1	2011 - 2016	178258

activity, between 06-13 March 2012. The last panel of Figure 4.9 shows Dst and Kp indices which indicate that the 06 - 13 March 2012 storm period consisted of a succession of storms with different intensities. For the entire storm period and for all stations, MIDAS reconstructs the storm-time TEC well and short term features are accurately captured. Similarly, ANN model reconstructed TEC well for almost the entire storm period except some overestimations observed during daytime on 08 March 2012 for DEBK, ADIS and MOIU. In contrast to what was observed for MIDAS and ANNs, IRI model shows large daytime underestimations of GPS TEC for the entire storm period specifically for DEBK and ADIS. For DEBK and ADIS, RMSE values between IRI predictions and observations are about 9.83 and 15.69 TECU, respectively. IRI model provides more accurate predictions for MOIU and TETE with respective RMSE values of 8.77 and 8.17 TECU. However, some discrepancies dominated

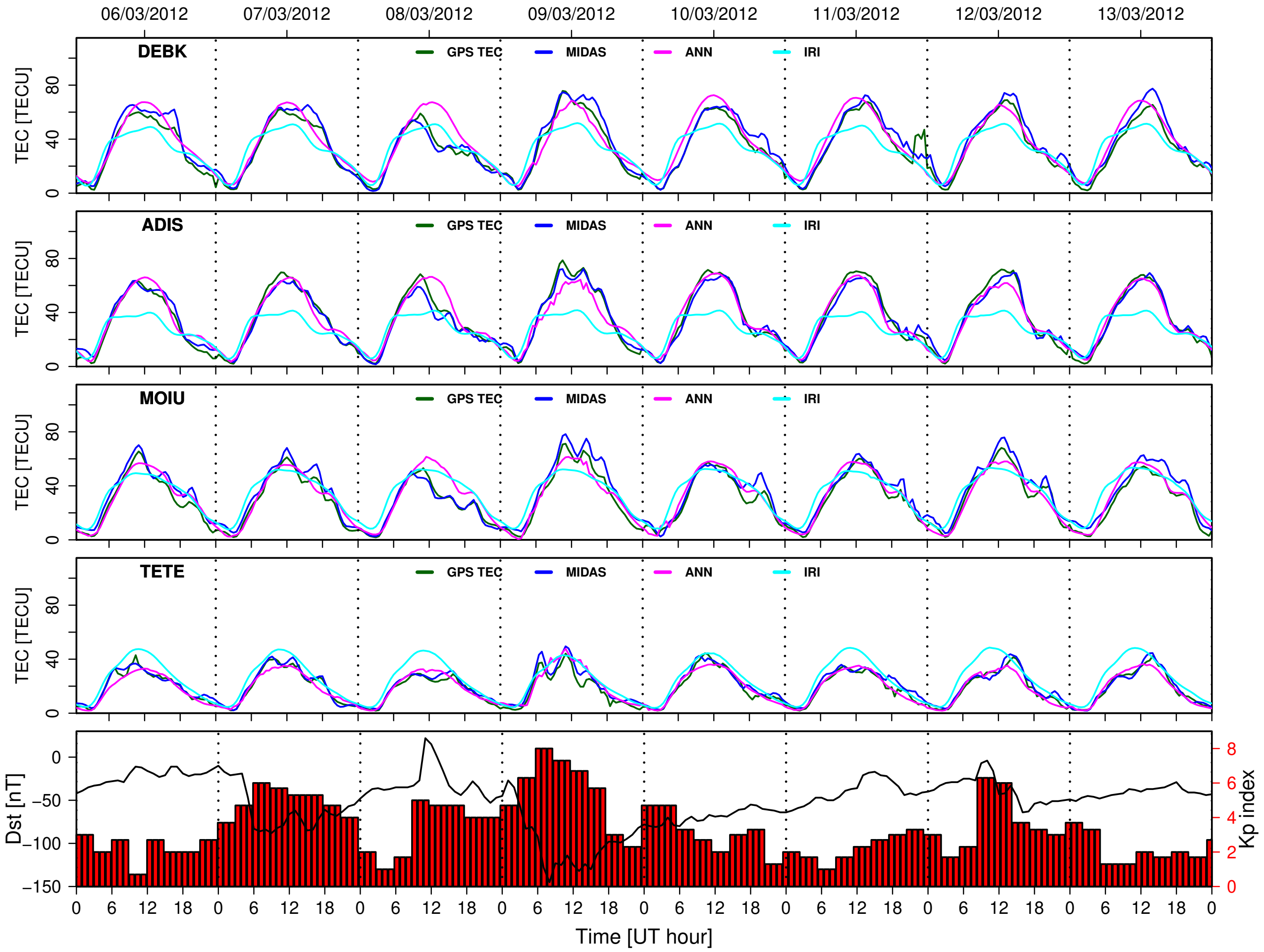

Figure 4.9: Comparison of the observed and reconstructed TEC for the storm period of 06 - 13 March 2012.

by underestimations and overestimations for MOIU and TETE, respectively, are observed specifically during daytime.

Figure 4.10 is similar to Figure 4.9 but for the storm period of 18 - 24 February 2014 and stations DEBK, NAZR, MOIU and TETE. The 18 - 24 February 2014 storm period consisted of a sequence of storms as indicated by $Dst \leqslant -50$ nT or $Kp \geqslant 4$. It can be seen from Figure 4.10 that MIDAS TEC agrees well with observations for NAZR and TETE. However, remarkable discrepancies mainly dominated by daytime overestimations are seen for DEBK and MOIU. What can also be noticed is the MIDAS good capability to capture short term variations of the observed TEC and follow the TEC depletion over MOIU on 20 February 2014. ANN model estimates the observed TEC accurately in spite of some clear deviations on 19 February 2014 for DEBK, NAZR and MOIU and on 23 February 2014 for DEBK. Except on 20 February 2014 where a good performance of IRI model in estimating the storm-time TEC magnitude is noticed for TETE and MOIU, IRI underestimates daytime TEC magnitude for the entire storm period.

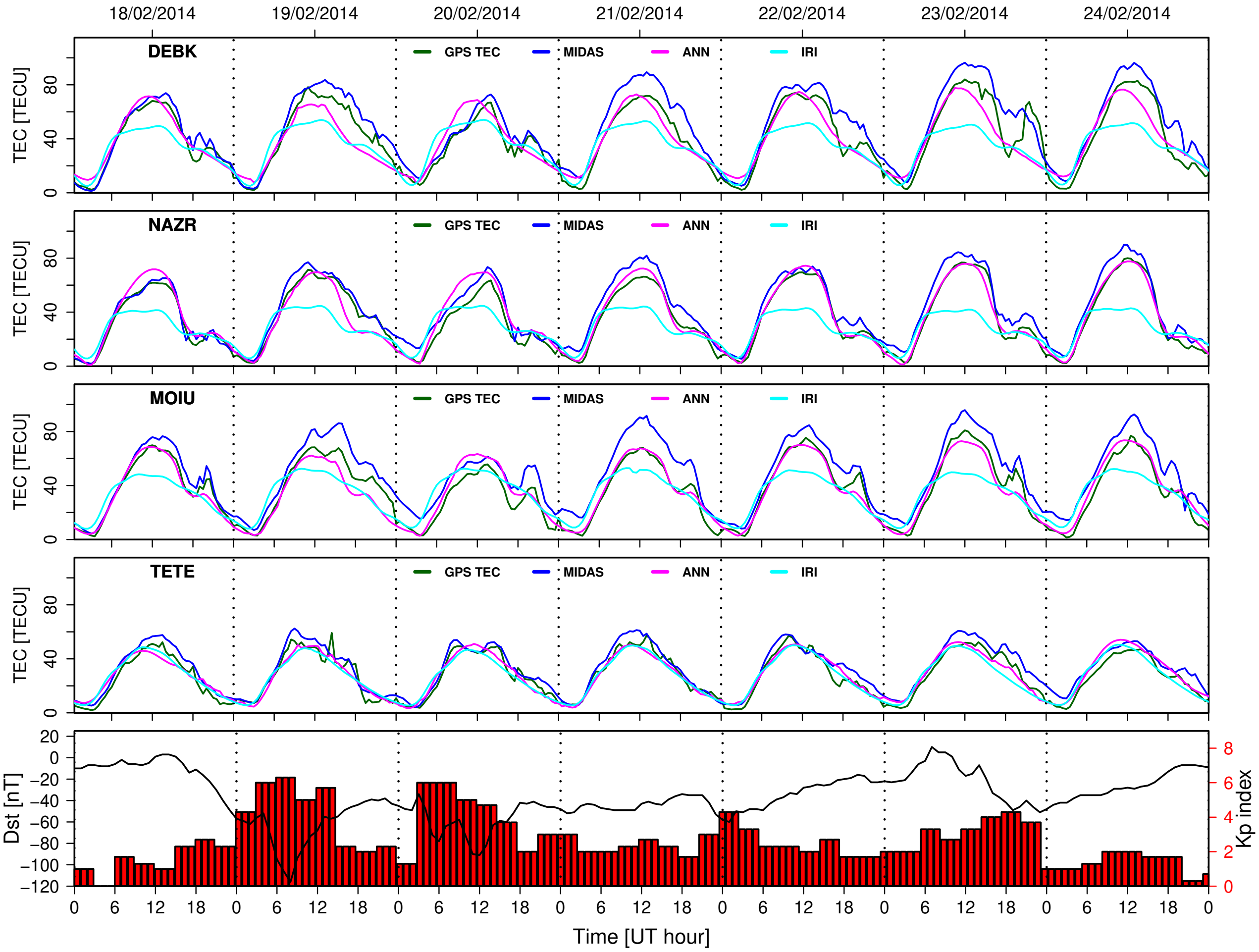

Figure 4.10: Comparison of the observed and reconstructed TEC for the storm period of 18 - 24 February 2014.

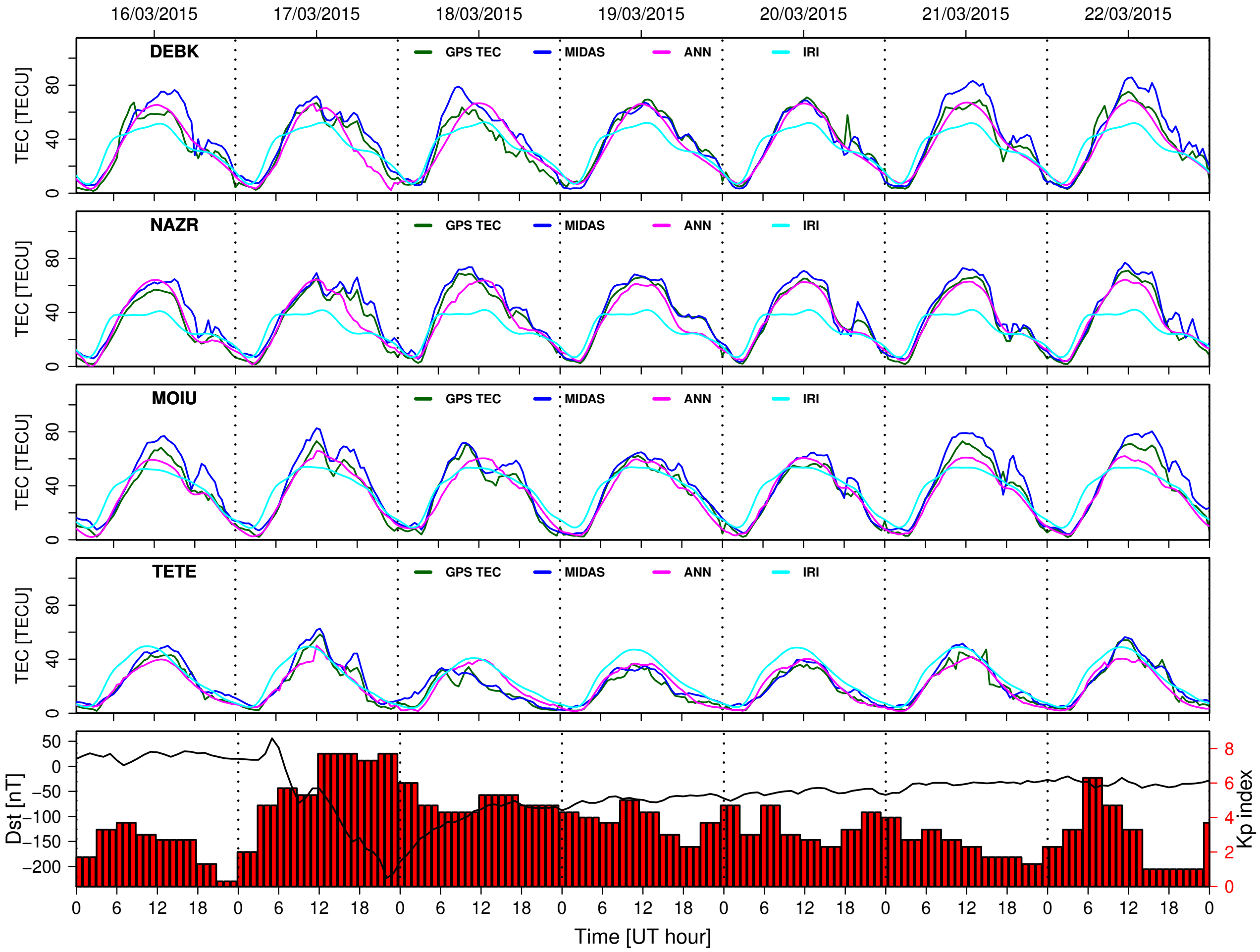

Figure 4.11: Comparison of the observed and reconstructed TEC for the storm period of 16 - 22 March 2015.

Figure 4.11 presents MIDAS, ANN and IRI results along with observations over DEBK, NAZR, MOIU, and TETE stations during the storm period of 16 - 22 March 2015. As indicated by the minimum *Dst* (-223 nT) and maximum *Kp* (of about 8) indices, the 16 - 22 March 2015 storm period consisted of one severe storm. The storm had a very long recovery phase that lasted for about 5 days as shown by *Dst* index below -50 nT. Both MIDAS and ANNs reconstruct TEC accurately over all stations although for some days, daytime overestimations and underestimations are observed for DEBK and MOIU. TEC enhancement observed over TETE on 17 March 2015 is better followed by MIDAS than by ANNs. The IRI model underestimates TEC mainly during daytime for the entire storm period for DEBK and NAZR and some days for MOIU while relatively small overestimations are observed over TETE.

Figure 4.12 illustrates GPS TEC observations over DEBK, ADIS, MOIU, and ZOMB stations along with MIDAS, ANN and IRI results, for a sequence of moderate geomagnetic storms which occurred between 24 - 30 October 2016. Except on 30 October 2016 where daytime overestimation is observed, MIDAS makes accurate estimations of TEC for DEBK, MOIU, and ZOMB for the rest of the storm period. The TEC depletion observed on 26 October 2016 over DEBK, MOIU, and ZOMB is also captured well by MIDAS. However, MIDAS underestimates daytime TEC over ADIS for almost the entire storm period. On the other hand, ANN model estimates the magnitude of TEC accurately for DEBK and MOIU but fails to capture the depletion observed on 26 October 2016. For ADIS and ZOMB, daytime TEC is underestimated for almost the entire storm period. Except for 26 October 2016 where the TEC depletion observed over the four stations is not seen by the IRI model, for the rest of the storm duration IRI predictions are in good agreement with observations specifically for DEBK and MOIU. However, for ADIS, daytime TEC magnitude is underestimated for some days while for ZOMB an overestimation is observed throughout the storm period. The common characteristics of the three methods used for storm-time TEC reconstructions are their high accuracy for early morning and sometimes around midnight hours, and where over/under-estimations exist, these are generally observed during daytime.

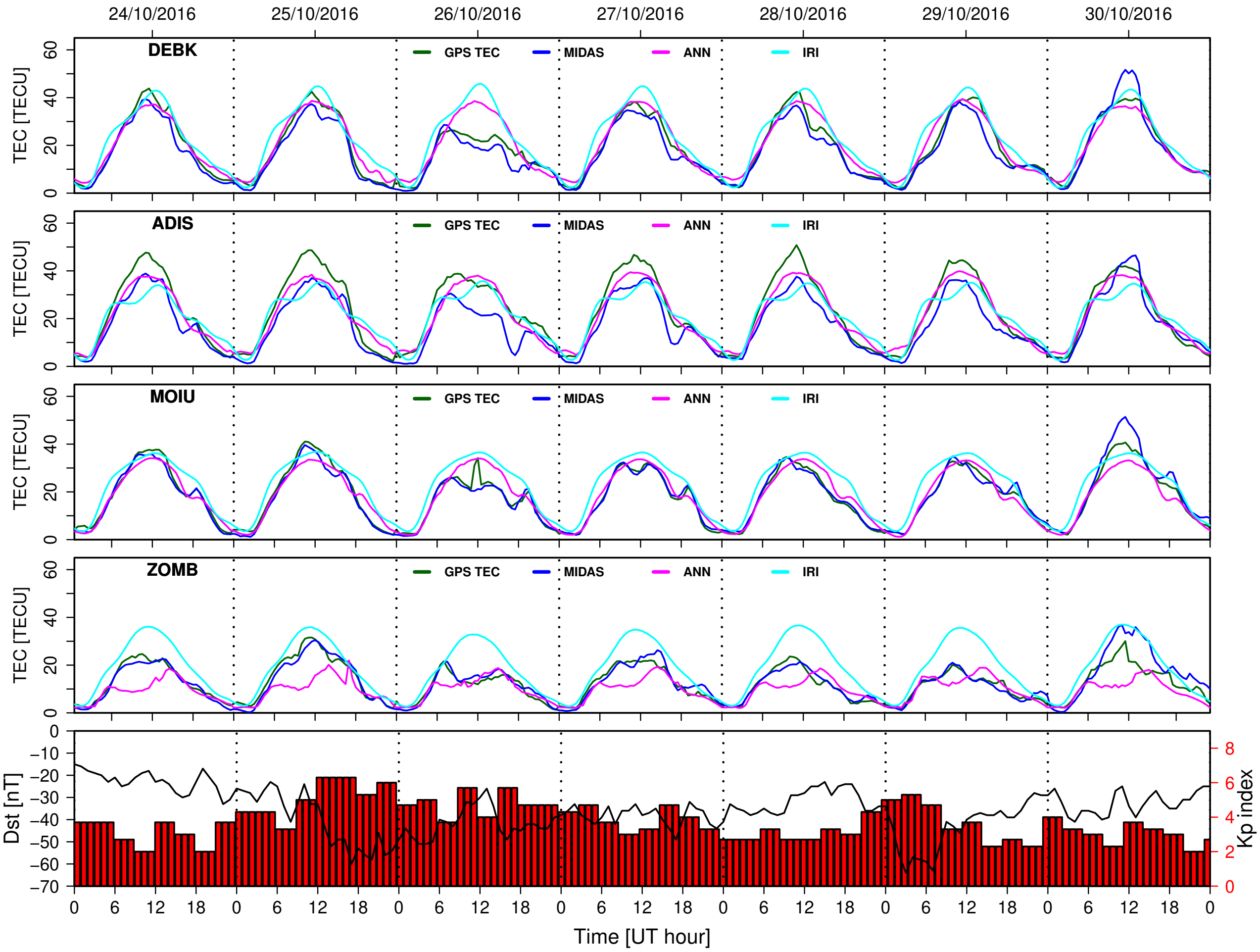

Figure 4.12: Comparison of the observed and reconstructed TEC for the storm period of 24 - 30 October 2016.

To be able to determine which model/technique between MIDAS, ANNs or IRI best reconstructs the storm-time TEC over different African latitude regions, a statistical analysis was done based on the mean absolute error (MAE) and Pearson's correlation coefficient (defined by equation (4.12)) between the observed and reconstructed TEC. Starting from the definition of the absolute error (AE) (Habarulema *et al.*, 2007; Leandro & Santos, 2007):

$$AE = |TEC_{rec} - TEC_{obs}|, \tag{4.14}$$

MAE is given by (Mitchell & Spencer, 2003; Willmott & Matsuura, 2005)

$$MAE = \frac{1}{N}\sum_{i=1}^{N}|TEC_{rec} - TEC_{obs}| \tag{4.15}$$

where N is the number of observations, TEC_{rec} and TEC_{obs} are the reconstructed and observed TEC respectively. MAE represents the average of the vertical distances between the observed and predicted quantities and has been proven to be a good parameter to use over the RMSE in assessing the performance of a model (Willmott & Matsuura, 2005). Figure 4.13 shows the calculated MAE values (left panels) and correlation coefficients (right panels) for all validation storm periods. For the storm periods of 06 - 13 March 2012 and 24 - 30 October 2016, smaller values of MAE generally found for MIDAS reveal that, on average, MIDAS reconstructs storm-time TEC better than ANN and IRI models. In contrast, for 18 - 24 February 2014 and 16 - 22 March 2015 storm periods, ANN model shows higher accuracy, on average. Except for TETE where MAE values for IRI model are comparable with the values obtained for ANNs specifically for the storm period of 18 - 24 February 2014, MAE values for IRI model are higher for all other cases. This indicates that IRI model is not as good as MIDAS and ANN techniques in making accurate storm-time TEC reconstructions. A similar observation was highlighted in previous works that compared MIDAS reconstructions with IRI predictions (Chartier *et al.*, 2012; Giday *et al.*, 2016), and ANN estimations with IRI predictions (Habarulema *et al.*, 2007, 2009a; Watthanasangmechai *et al.*, 2012; Okoh *et al.*, 2016). The underestimation of TEC by IRI model compared to MIDAS and ANN can be attributed to differences in the altitude ranges at which TEC is estimated (Kenpankho *et al.*, 2011; Chartier *et al.*, 2012; Habarulema & Ssessanga, 2017). IRI model does generate TEC for the altitude range 60 - 2000 km and the contribution of the plasmasphere is therefore not fully taken into account in IRI model. In contrast, it is worth noting that the input for MIDAS include GPS ray paths that contain information of the plasmasphere (Chartier *et al.*, 2012). Similarly for ANNs, GPS TEC used to develop ANN models was derived based on the line integral of the electron density along the signal path from GPS satellites (at the altitude of about 20200 km) to ground receivers. These may be some of the reasons that make MIDAS and ANNs more accurate in estimating the magnitude of TEC compared to IRI model. Particularly for ANN models, the amount of data used for training and the choice

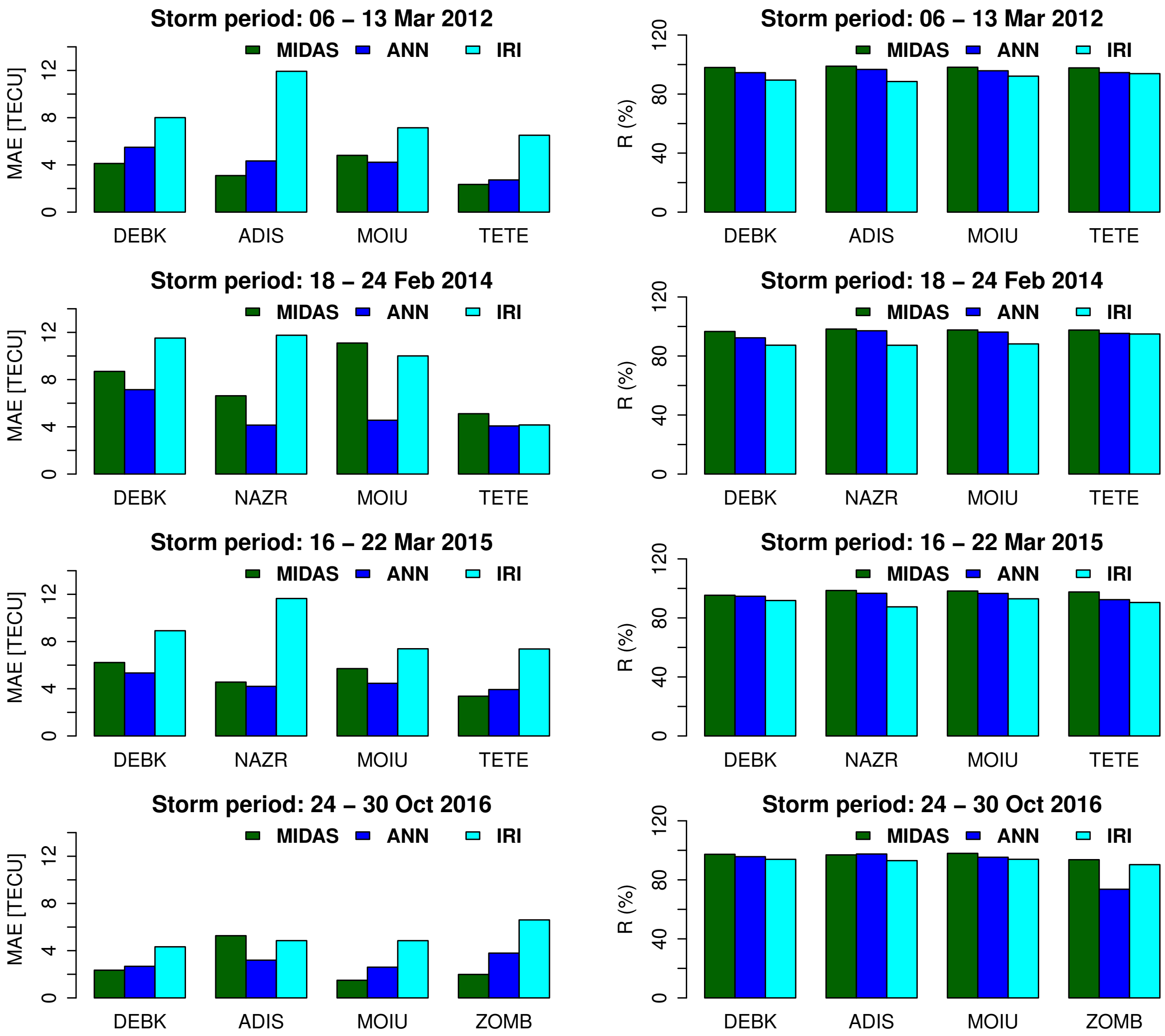

Figure 4.13: MAE and correlation between the observed and reconstructed TEC by MIDAS, ANN and IRI.

of the number of hidden nodes also influenced the modelling results. The fact that MIDAS captures short term features and follows TEC enhancements and depletions observed during geomagnetic storms better than ANN and IRI models can be explained in terms of data used when applying or developing the techniques. MIDAS uses direct measurements around the specific time of inversion/reconstruction while ANNs and IRI are empirical models based on historical data.

Table 4.6: Average MAE values (in TECU) computed over four storm periods for a specific station (columns 2 to 5) and for all stations considered for validation (last column).

Technique	DEBK	NAZR/ADIS	MOIU	TETE/ZOMB	Average over all stations
MIDAS	5.35	4.89	5.78	3.20	4.81
ANN	5.16	3.96	3.96	3.63	4.18
IRI	8.19	10.05	7.35	6.16	7.94

It can also be seen from Figure 4.13 that relatively high values of MAE were generally found for the low latitude stations (DEBK, NAZR, ADIS, MOIU) compared to the mid-latitude stations (TETE, ZOMB). The average MAE values computed over the four validation storm periods per location (Table 4.6) confirm that higher error values were found for low latitudes. The reconstructing techniques used in this work estimate TEC better for the mid-latitude than the low latitude. This agrees well with what was previously reported about the performance of IRI (Kumar *et al.*, 2015) and MIDAS (Chartier *et al.*, 2014) in low and mid-latitude. Generally, the difficulty in reconstructing/modelling the low latitude ionosphere has been frequently reported (Materassi & Mitchell, 2005; Adewale *et al.*, 2011; Kenpankho *et al.*, 2011; Panda *et al.*, 2015). Overall high values of MAE observed for the low latitude compared to mid-latitude are likely due to higher TEC gradients caused by the equatorial ionisation anomaly as a result of the fountain effect. The influence of high TEC variability due to fountain effect on TEC modelling/reconstruction was reported as the major cause that makes modelling difficult for the low latitude ionosphere. This observation was reported by Chartier *et al.* (2014) when performing the tomography of the African ionosphere during geomagnetically quiet conditions, and Panda *et al.* (2015) during TEC reconstruction with IRI model over low latitude in the Indian sector. It can therefore be considered that TEC reconstruction is more difficult for the low latitude than mid-latitude and this agrees well with what was previously reported (Chartier *et al.*, 2014; Kumar *et al.*, 2015).

Similar to equation (4.13), to evaluate how accurate a model performs with respect to another, the percentage improvement (PI) was computed according to the following Equation (Muslim *et al.*, 2015):

$$PI = \frac{MAE_1^{av} - MAE_2^{av}}{MAE_2^{av}} \times 100\% \tag{4.16}$$

where MAE_1^{av} and MAE_2^{av} are the average values of MAE for model 1 and model 2, respectively. In the context of this work, model 1 and model 2 represent any of MIDAS, ANNs or IRI. Equation (4.16) indicates how much percentage model 2 performs better than model 1. Over the storm periods considered for validation, we found that, on average, ANN model performs 3.69 %, 23.48 %, 45.96% better than MIDAS for DEBK, NAZR/ADIS, MOIU, respectively. The average PI of 24.37 % obtained for the three locations shows higher accuracy of ANN in the low latitude compared to MIDAS. The fact that individual storm-time ANN models were developed for different locations and not a regional model that covers the entire region of interest might be another contributing factor for the good performance of ANNs over MIDAS and IRI in the low latitude ionosphere. However, we also note that a regional ANN model over the African region would be prone to significant errors due to few/lack of observations in some latitude regions. On the other hand, MIDAS performs better for the mid-latitude station TETE/ZOMB by 13.44 % compared to ANN model. Figure 4.14

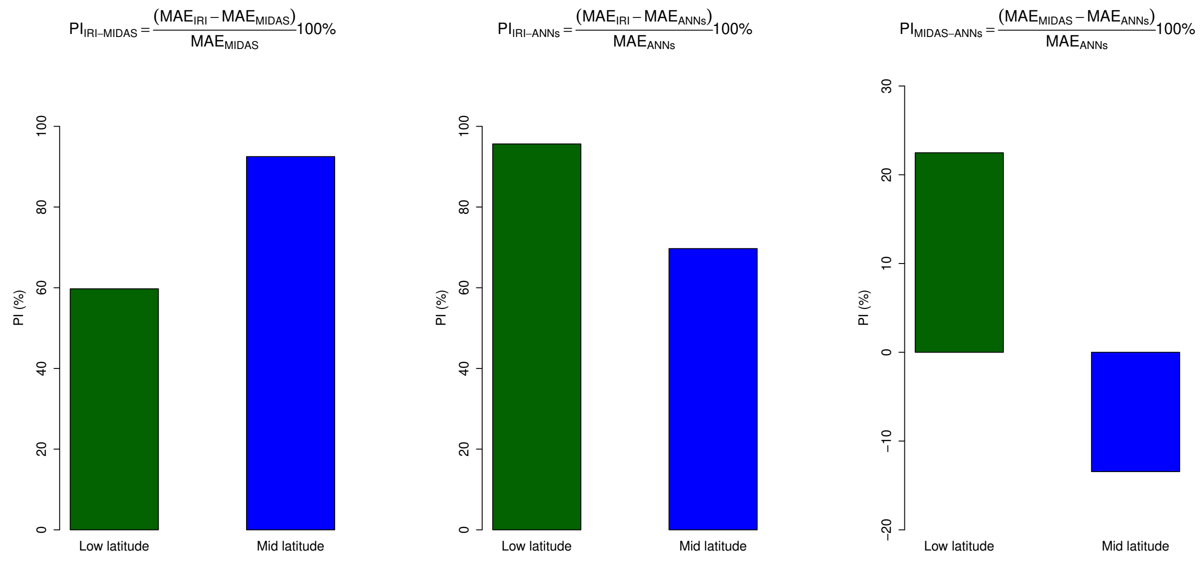

Figure 4.14: PI values for African low and mid-latitude regions: IRI and MIDAS (left panel), IRI and ANNs (middle panel), MIDAS and ANNs (right panel). Also shown above each panel, are formulas used to compute PI values.

illustrates PI values computed for African low and mid-latitude regions. Since we have three locations (DEBK, NAZR/ADIS, MOIU) that represented the low latitude in this study, average MAE over these locations was first calculated for each technique/model to represent the low latitude with a single value. Then the formulas presented in Figure 4.14 were applied to compute PI values for both low and mid-latitude locations. Positive PI values shown on the left (IRI and MIDAS) and the middle (IRI and ANNs) panels of Figure 4.14 indicate that MIDAS and ANNs perform better than IRI for both low and mid-latitude African regions. However, the right panel shows good performance of ANNs in low latitude compared to MIDAS while a reverse situation is noticed in the mid-latitude.
The high accuracy of ANN model in TEC modelling has previously been reported for both low (Acharya *et al.*, 2011; Watthanasangmechai *et al.*, 2012) and mid-latitude regions (Huang & Yuan, 2014). Over all stations considered for validation, we wish to note that the average MAE values of 4.81, 4.18 and 7.94 TECU were found for MIDAS, ANN and IRI, respectively. This confirms that, overall, MIDAS and ANN provides comparable results, and are both better than IRI model for storm-time TEC reconstruction.

All three techniques considered in this work gave high correlation coefficients (between 73 - 99 %). In the context of this study, high correlation coefficients confirm good performance of MIDAS, ANN and IRI techniques in reproducing diurnal trend of the observed TEC. Over all stations, the highest correlation coefficients found for MIDAS indicate that there is a strong positive linear relationship between observations and MIDAS estimations compared to other techniques. It can therefore be concluded that MIDAS reconstructs short term features and follows the storm-time TEC dynamics more accurately than IRI and ANN models. The high performance of MIDAS during disturbed conditions was noticed and reported by (Yin *et al.*, 2004) when reconstructing the electron density over the USA. As it can be seen from Figure 4.13, there is no clear dependence of performances of MIDAS, ANNs and IRI on the storm intensity. As an example, smaller MAE values were generally obtained for the severe storms of 16 - 22 March 2015 (Minimum Dst of -223 nT) compared to strong storms of 18 - 24 February 2014 (Minimum Dst of -116 nT).

4.4 Summary and conclusions

In this chapter, we investigated the contribution of each of the solar activity indices $F10.7p$, $F10.7$ and SSN to storm-time TEC modelling over a mid-latitude station, Hermanus, (HNUS, 34.40° S, 19.22° E geographic; 42.33° S, 82.15° E geomagnetic), South Africa. The task was performed based on ANN models (MF107p, MF107, and MSSN) which differ from each other by the solar index used. It was shown that a model with $F10.7p$ as solar proxy, is likely to lead to more accurate results compared to models that considered $F10.7$ and SSN as solar activity representations. Thus, from here onwards, $F10.7p$ will be used as the solar proxy during storm-time TEC modelling. This agrees with statistical results presented in Liu *et al.* (2006); Liu & Chen (2009) where it was shown that $F10.7p$ represents the solar activity better than $F10.7$. A comparative study of MF107p, MF107, MSSN, with a NLRA developed at the same location shows that the latter is 7.68 %, 5.44 %, and 4.96 % better than MSSN, MF107, and MF107p models, respectively.

We have statistically evaluated the capability of MIDAS compared with ANNs to reconstruct storm-time TEC for the African low and mid-latitude regions. It was found that MIDAS and ANNs provide comparable results in reconstructing the storm-time TEC over different African latitudes with MAE values of 4.81 and 4.18 TECU, respectively. On the other hand, statistics show that, on average, ANN model performs 24.37 % better than MIDAS in estimating storm-time TEC over low latitudes while MIDAS accuracy is 13.44 % higher than ANN in mid-latitude. However, it has been shown that MIDAS captures short term variations of the observed TEC and follows enhancements and depletions observed during geomagnetic storms more accurately than ANNs. Both MIDAS and ANN model provide more accurate storm-time TEC reconstructions than IRI model in African low and mid-latitude regions. Similar to previous studies (Chartier *et al.*, 2014; Kumar *et al.*, 2015; Panda *et al.*, 2015), storm-time TEC reconstruction/modelling is more difficult for the low latitude than mid-latitude ionosphere. The fountain effect and the resulting higher TEC gradients over low latitude ionosphere are likely to be the causes of the difficulty in reconstructing/modelling

TEC over this region. The performance of MIDAS, ANNs and IRI do not seem to depend on the storm intensity. For example, it was shown that MIDAS, ANNs and IRI can even reconstruct storm-time TEC more accurately for severe storms (e.g., 16 - 22 March 2015) than it does for strong storms (e.g., 18 - 24 February 2014).

Chapter 5

Highlights about the performances of different storm-time TEC models

In this chapter, statistical evaluation of storm-time TEC modelling techniques over various latitudes of the African sector and surrounding areas is presented. For each selected receiver station, three different storm-time models based on empirical orthogonal functions (EOF) analysis, non-linear regression analysis (NLRA), and Artificial neural networks (ANNs), were implemented. Such a comparative study that involves these three modelling techniques, along different latitudes, and during storm conditions, is performed for the first time, and this forms the main objective of this chapter. Storm-time GPS TEC data used for both development and validation of the models were selected based on the storm criterion of $Dst \leqslant -50$ nT and/or $K_p \geqslant 4$ to take into account both CME and CIR-driven storms, respectively. To make an independent test of the models, storm periods considered for validation were excluded from datasets used during the implementation of the models and results are compared with observations (GPS TEC), monthly median TEC values, and International Reference Ionosphere (IRI-2016) predictions. Results presented in this chapter and their discussions are mostly derived from a published paper (Uwamahoro *et al.*, 2019).

5.1 Data selection and modelling inputs

In order to assess the performances of the models over different latitudes, data from 6 GPS receiver stations were selected for the implementation of the models. Among the six stations considered, two belong to the southern hemisphere mid-latitude (HRAO: 36.32° S geomagnetic, ZAMB: 26.27° S geomagnetic), one in the northern hemisphere mid-latitude (TEHN: 30.62° N geomagnetic), and three in low latitude, at the nominal trough (NAZR: 0.25° S geomagnetic), southern crest (SEY1: 13.55° S geomagnetic) and northern crest (YIBL: 16.10° N geomagnetic) of the equatorial ionization anomaly (EIA). In cases of unavailable data for some storms selected for validation at the primary locations (used to implement the models), co-located/close stations with available data were considered for validation. Thus, MONG (25.98° S geomagnetic) and MAUA (30.83° S geomagnetic) were used for ZAMB, whereas SEYG (13.55° S geomagnetic), ADIS (0.18° N geomagnetic), KUWT (23.50° N geomagnetic) replaced SEY1, NAZR, and YIBL, respectively. For clarity, it is of great importance to point out that validating a model developed for specific location using data from co-located/close stations has been studied. It was shown that results agree with observations quite reasonably when such validation is performed within a latitudinal and longitudinal separations of 8.7° and 10.6°, respectively, from the primary station (Uwamahoro & Habarulema, 2015). Details about stations selected for development and validation of the models and data coverage periods are provided in Table 5.1. Locations of the considered stations in this study are shown on the map in Figure 5.1.

Table 5.1: Geographic and geomagnetic latitudes and longitudes of the GPS receiver stations used during development (shown with *) and validation of the models. Also presented, are data coverage periods considered while implementing the models.

Station ID	Name	Country	GLat (°)	GLon (°)	GMLat (°)	GMLon (°)	Data
HRAO*	Hartebeesthoek	South Africa	-25.89	27.69	-36.32	94.69	1996 - 2016
ZAMB*	Zambia	Zambia	-15.43	28.31	-26.27	98.40	2002 - 2016
MONG	Mongu	Zambia	-15.25	23.15	-25.98	93.03	-
MAUA	Maun	Botswana	-19.90	23.53	-30.83	92.33	-
SEY1*	Seychelles	Seychelles	-4.67	55.48	-13.55	126.73	1998 - 2016
SEYG	Seychelles	Seychelles	-4.68	55.53	-13.55	126.73	-
NAZR*	Nazret	Ethiopia	8.57	39.29	-0.25	111.01	2007 - 2016
ADIS	Addis Ababa	Ethiopia	9.04	38.77	0.18	110.47	-
YIBL*	Yibal	Oman	22.19	56.11	16.10	128.13	2010 - 2016
KUWT	Kuwait	Kuwait	29.33	47.97	23.50	119.69	-
TEHN*	Tehran	Iran	35.70	51.33	30.62	123.26	2004 - 2016

For validation, six storm periods (four were reserved for interpolation and two for extrapolation) were selected based on their intensities (storm classification by Loewe & Prölss (1997)), and the period of solar activity. It is worth noting that none of the storms selected for validation were included in the primary datasets considered to develop the models. This is of a particular importance for independent data-model validation. Details about selected storm for validation are provided in Table 5.2.

Table 5.2: Storm periods selected for validation and their classification according to Loewe & Prölss (1997).

Storm period	Period of solar activity	Minimum Dst (nT)	Storm classification	Maximum K_p	Stations used for validation
07 - 14 October 2012	High	-109	Strong	6.7	HRAO, ZAMB, SEY1, ADIS, YIBL, TEHN
03 - 09 January 2015	Moderate	-105	Strong	6.3	HRAO, ZAMB, SEYG, ADIS, YIBL, TEHN
22 - 29 June 2015	Moderate	-204	Severe	8.3	HRAO, MONG, SEYG, NAZR, YIBL, TEHN
24 - 30 October 2016	Low	-64	Moderate	6.3	HRAO, ZAMB, SEYG, ADIS, KUWT, TEHN
28 February - 04 March 2017	Low	-61	Moderate	5.7	HRAO, MAUA, SEYG, ADIS, KUWT, TEHN
27 - 30 May 2017	Low	-125	Strong	7.0	HRAO, MAUA, SEYG, ADIS, KUWT, TEHN

The inputs used during the development of the models comprise the time of the day (diurnal variation), day number of the year (seasonal variation), the $F10.7p$ solar flux index (solar activity), and geomagnetic activity representations (3 hourly planetary a_p, auroral electrojet

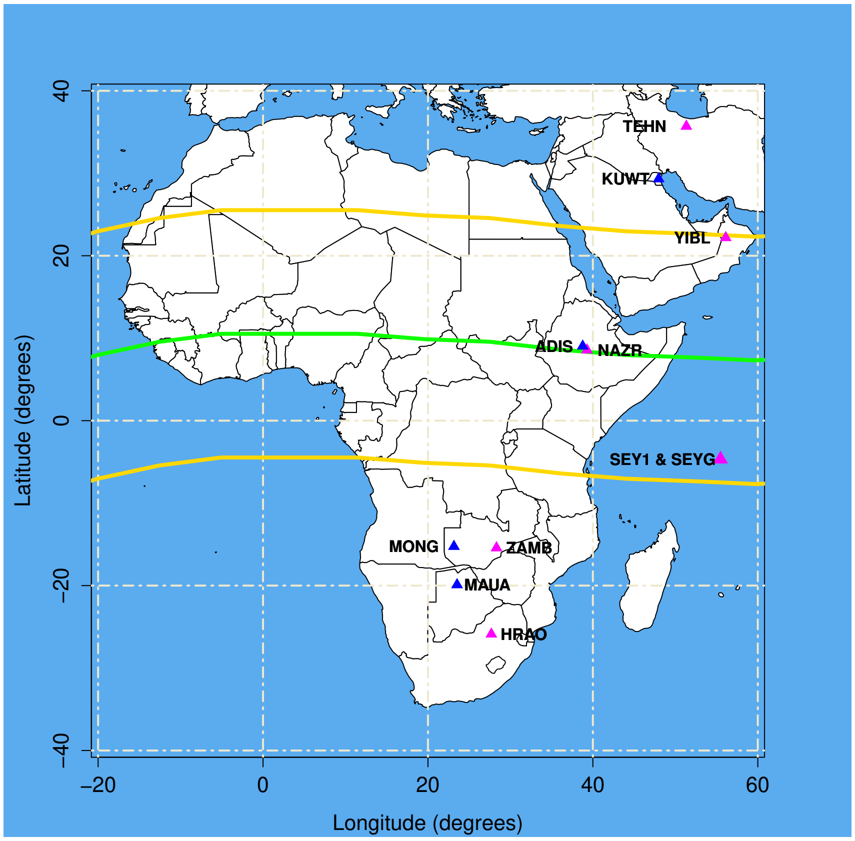

Figure 5.1: Locations of GPS receiver stations used to implement and validate the models (shown in magenta). Shown in blue, are stations considered for validation in the cases of unavailable data at the primary locations.

AE, and symmetric disturbance in the horizontal component of the Earth's magnetic field $symH$).

5.2 Analytical formulation of storm-time TEC modelling techniques

5.2.1 Empirical orthogonal functions (EOF) analysis

EOF analysis was applied to TEC modelling by first decomposing the original dataset into basis functions and expansion coefficients. An EOF-based model was developed for each location shown with * in Table 5.1. We considered 15-minute resolution TEC data which lead to 96 TEC values per day and hence, the original TEC data matrix was defined by 96 columns, and the number of rows equal to the number of storm days with complete observations (1327, 592, 528, 332, 263, and 321 for HRAO, ZAMB, SEY1, NAZR, YIBL, and TEHN, respectively) considered for a given station during the development of the EOF models. Thereafter the original TEC dataset was decomposed into basis functions $E_k(UT)$ representing diurnal variation of TEC and expansions coefficients which represent long-term variations (solar cycle, annual, semiannual, and seasonal) of TEC according to

$$TEC(UT, d) = \sum_{k=1}^{n=96} C_k(d) \times E_k(UT) \tag{5.1}$$

where UT is the universal time. The quick convergence of the EOF series defined by equation (5.1) allows to reconstruct storm-time TEC data using only 10 out of 96 EOF components ($C_j \times E_j$, with $j = 1, 2, ..., 10$) without loosing much information in the original data. The fractions of the total variances (computed using equation (3.48)) accounted for by the first ten EOF components retained while developing EOF models are presented in Table 5.3, and clearly, all are greater than 97.0 % for all stations considered.

Table 5.3: Percentage of variances accounted for by first 10 EOF components.

EOF component	Variances (%)					
	HRAO	ZAMB	SEY1	NAZR	YIBL	TEHN
$C_1 \times E_1$	90.130	81.950	83.700	86.920	71.370	75.860
$C_2 \times E_2$	3.914	6.731	5.166	4.935	7.622	8.760
$C_3 \times E_3$	2.568	4.288	3.386	2.246	6.287	5.583
$C_4 \times E_4$	0.728	1.640	1.787	2.001	3.454	2.481
$C_5 \times E_5$	0.697	1.052	1.215	0.888	3.193	2.290
$C_6 \times E_6$	0.445	0.753	0.856	0.643	2.142	1.475
$C_7 \times E_7$	0.349	0.627	0.521	0.432	1.188	0.853
$C_8 \times E_8$	0.227	0.495	0.507	0.383	0.783	0.652
$C_9 \times E_9$	0.187	0.395	0.406	0.283	0.643	0.429
$C_{10} \times E_{10}$	0.126	0.264	0.291	0.247	0.399	0.328
Total variance	99.369	98.193	97.834	98.983	97.083	98.715

As an illustration, Figure 5.2 shows diurnal and long-term variations of EOF basis functions and coefficients, respectively, for HRAO station. It can be seen from Figure 5.2 (a) that E_1 represents well the diurnal mean TEC computed over the entire dataset. Correlation coefficient between the diurnal average TEC and E_1 was found to be 99.34 %. Similarly, E_2 have some features of diurnal mean TEC with a correlation of 70.94 %, while high order EOF basis functions represent short-term variations due to day-to-day variations in the observed TEC. Figure 5.2 (b) shows that C_1 and $F_{10.7p}$ have similar trends with a correlation coefficient of 78.90 %. This confirms that C_1 has clear patterns of solar activity. High order EOF coefficients have also some features of solar activity remarked from their high and low values noticed for solar maximum and minimum periods, respectively.

After TEC dataset decomposition into basis functions and associated coefficients, factors that influence TEC variability were taken into account by expressing the expansion coefficients in terms of modelling inputs as follows:

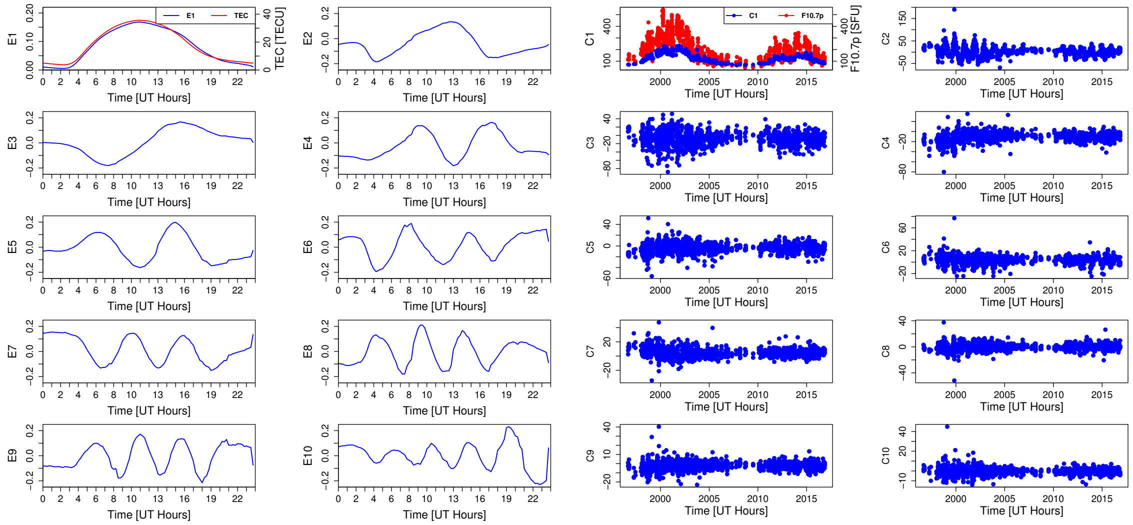

(a) Diurnal variation of EOF basis functions. (b) Long-term variation of EOF coefficients.

Figure 5.2: (a) Diurnal variation of the first ten EOF basis functions and (b) Long-term variation of the first ten EOF coefficients, for HRAO station.

$$
\begin{aligned}
C_k(d) \;=\;& \zeta_{k0} + \zeta_{k1}.F_{10.7p}(d) + \zeta_{k2}.A_p(d) + \zeta_{k3}.AE(d) + \zeta_{k4}.Dst(d) \\
&+[\zeta_{k5} + \zeta_{k6}.F_{10.7p}(d) + \zeta_{k7}.A_p(d) + \zeta_{k8}.AE(d) + \zeta_{k9}.Dst(d)]cos\left(\frac{2\pi \times d}{365.25}\right) \\
&+[\zeta_{k10} + \zeta_{k11}.F_{10.7p}(d) + \zeta_{k12}.A_p(d) + \zeta_{k13}.AE(d) + \zeta_{k14}.Dst(d)]sin\left(\frac{2\pi \times d}{365.25}\right) \\
&+[\zeta_{k15} + \zeta_{k16}.F_{10.7p}(d) + \zeta_{k17}.A_p(d) + \zeta_{k18}.AE(d) + \zeta_{k19}.Dst(d)]cos\left(\frac{4\pi \times d}{365.25}\right) \\
&+[\zeta_{k20} + \zeta_{k21}.F_{10.7p}(d) + \zeta_{k22}.A_p(d) + \zeta_{k23}.AE(d) + \zeta_{k24}.Dst(d)]sin\left(\frac{4\pi \times d}{365.25}\right)
\end{aligned}
\tag{5.2}
$$

where $k = 1, 2, 3, ..., m$, and m (equal to 10 for all stations) is the number of retained EOF components. The factor 0.25 located at the denominator of cosine and sine arguments accounts for the extra day in each leap year. $A_p(d)$ represents the daily planetary magnetic index and is obtained by averaging 8 values of the 3-hour a_p index for a given day d. $AE(d)$ and $Dst(d)$ are daily auroral electrojet and disturbance storm-time indices, respectively. For each $C_k(d)$, the unknown coefficients $\zeta_{k0}, ..., \zeta_{k24}$ were determined using the method of least squares. Once the the unknown coefficients in Equation 5.2 are found, the same equation is used to estimate the EOF expansion coefficients when $F_{10.7p}(d)$, $AE(d)$, $A_p(d)$ and $Dst(d)$ are provided for a specific day d. The modelled TEC at a specific day was obtained using the modelled EOF coefficients ($\tilde{C}$) together with EOF basis functions according to the equation

$$
TEC(UT, d) = \sum_{k=1}^{m=10} \tilde{C}_k(d) \times E_k(UT) \tag{5.3}
$$

5.2.2 Non-linear regression analysis (NLRA)

Relationship between TEC and modelling inputs was established using a non-linear mathematical expression that comprises harmonic functions with periods of one year and half a year to represent the annual and semiannual variation of TEC, respectively. The amplitude of each of the harmonic functions varies with components of time, solar and geomagnetic indices while seasonal variation of TEC is represented by day number of the year. The modelled TEC were then obtained using the expression

$$\begin{aligned} TEC^{\alpha} &= c_0 + c_1.tc + c_2.ts + c_3.F_{10.7p} + c_4.a_p + c_5.AE + c_6.symH \\ &+[c_7 + c_8.tc + c_9.ts + c_{10}.F_{10.7p} + c_{11}.a_p + c_{12}.AE + c_{13}.symH].cos\left(\frac{2\pi \times d}{365.25}\right) \\ &+[c_{14} + c_{15}.tc + c_{16}.ts + c_{17}.F_{10.7p} + c_{18}.a_p + c_{19}.AE + c_{20}.symH].sin\left(\frac{2\pi \times d}{365.25}\right) \\ &+[c_{21} + c_{22}.tc + c_{23}.ts + c_{24}.F_{10.7p} + c_{25}.a_p + c_{26}.AE + c_{27}.symH].cos\left(\frac{4\pi \times d}{365.25}\right) \\ &+[c_{28} + c_{29}.tc + c_{30}.ts + c_{31}.F_{10.7p} + c_{32}.a_p + c_{33}.AE + c_{34}.symH].sin\left(\frac{4\pi \times d}{365.25}\right) \end{aligned} \tag{5.4}$$

where tc and ts defined as follows

$$tc = cos\left(\frac{2\pi \times h}{24}\right), \qquad ts = sin\left(\frac{2\pi \times h}{24}\right), \tag{5.5}$$

are cosine (tc) and sine (ts) components of time t of the day. The parameter α can randomly be chosen in such a way that the right side of Equation 5.4 is positive since TEC is always a positive quantity. In this work, three different values of α (0.125, 0.25, and 0.5) were tested and 0.5 was found to lead to minimum error. Thus, α was assigned a value of 0.5 for all stations considered during implementation of NLRA models. For each station, the unknown coefficients $c_0, c_1, ..., c_{34}$ were determined using the method of least squares.

5.2.3 Artificial neural networks (ANNs)

The ANN architectures considered in this work were defined by 10 inputs ($F10.7_p$, a_p, AE, $symH$, tc, ts, dc_1, ds_1, dc_2, ds_2), n hidden nodes, and 1 output node (TEC). The quantities tc and ts are the same as presented in equation 5.5 while dc_1, ds_1, dc_2, ds_2 defined as follows

$$dc_1 = cos\left(\frac{2\pi \times d}{365.25}\right), \qquad ds_1 = sin\left(\frac{2\pi \times d}{365.25}\right), \tag{5.6}$$

$$dc_2 = cos\left(\frac{4\pi \times d}{365.25}\right), \qquad ds_2 = sin\left(\frac{4\pi \times d}{365.25}\right), \tag{5.7}$$

are cosine and sine components of day number d of the year, with periods of one year (dc_1, ds_1) and half a year (dc_2, ds_2). They represented the annual and semiannual variations of TEC in the ANN models. For a specific station, a suitable number (corresponding to lowest error) n of hidden nodes was statistically determined based on the mean absolute error (MAE) computed according to the formula (Mitchell & Spencer, 2003)

$$MAE = \frac{1}{N}\sum_{i=1}^{N}|TEC_{mod} - TEC_{obs}| \tag{5.8}$$

where TEC_{obs} and TEC_{mod} are observed and modelled TEC, respectively, and N is the number of observations. For each station considered to implement ANN models, a sequence of sixteen ANN trainings was performed by varying the number of hidden nodes from 10 to 25 (range selected arbitrarily). Thereafter, MAEs were computed for all sixteen sets of results obtained for each station using storm-time TEC data reserved for validation (all six storm periods considered for validation combined together) and the corresponding output obtained for each training process. For a given station, the selected number of hidden neurons corresponded to the lowest MAE value obtained within the range 10 - 25. Difference in numbers of data points within training datasets and in TEC gradients at various latitudes may be the reason of different optimum numbers of hidden neurons obtained for different locations. Figure 5.3 illustrates the variation of MAE values versus the number of hidden nodes for the six stations used to implement ANN models, while Table 5.4 presents the selected architectures (number of input-hidden-output neurons) as well as the number of data points considered during training.

Table 5.4: ANN architectures and amount of data points used to develop ANN models. The numbers 10 and 1 correspond to the number of input and output layer neurons, respectively. Shown in between, are the numbers of hidden layer neurons.

Station	ANN architecture	Number of data points
HRAO	10 - 24 - 1	829459
ZAMB	10 - 14 - 1	369315
SEY1	10 - 19 - 1	325213
NAZR	10 - 11 - 1	206162
YIBL	10 - 16 - 1	158440
TEHN	10 - 11 - 1	196706

5.3 Results and discussion

The modelled TEC by EOF, ANN, NLRA, and IRI models, and monthly medians (MM) TEC values representing the background ionosphere are presented along with observations for different storm periods and locations selected for validation. Also shown at the bottom

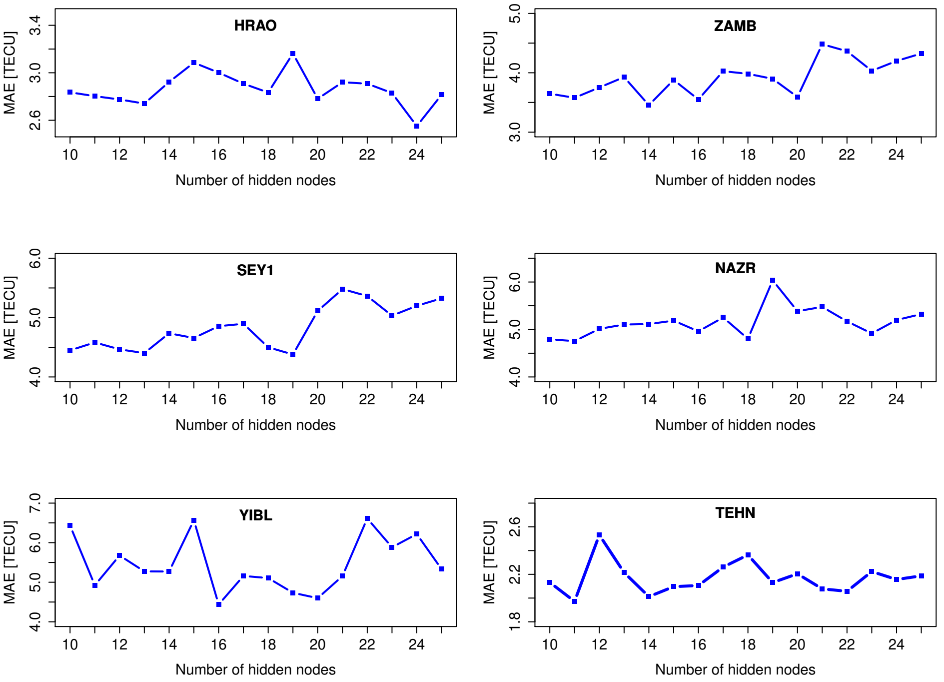

Figure 5.3: Variation of MAE values with number of hidden nodes for different locations.

of each graph, are K_p and Dst indices from which a geomagnetic storm is identified by $Dst \leqslant -50$ nT or $K_p \geqslant 4$. MM TEC values were computed using TEC data for quiet days of the month when the storm occurred. It is evident to point out that comparison of NLRA, EOF, and ANN predictions with IRI estimations is critical since IRI was developed using a very large earlier dataset of density measurements and provides monthly averages of the ionospheric parameters while other models are based on real observations.

5.3.1 Interpolation results

Results for the storm period of 07 - 14 October 2012 are presented in Figure 5.4 for six stations considered for validation. EOF, NLRA, ANN and IRI model results are plotted as dark yellow, red, blue, and light blue curves, respectively. TEC observations and respective monthly medians are represented as black and green curves respectively. EOF, NLRA, ANN models provide comparable predictions which for some locations, are in good agreement with the actual data despite a few discrepancies (e.g., TEHN, YIBL, SEY1, ZAMB, and HRAO), while for ADIS, underestimations are more dominant. Also remarked, are deviations from the observations during TEC enhancements (e.g., 09 October 2012 for ADIS, and 14 October 2012 for YIBL and SEY1), and depletions (e.g., 10 October 2012 for ZAMB, and 10 - 11 October 2012 for HRAO). Except for SEY1 and HRAO where IRI predictions are most of the time close to observations, overestimations of the observed TEC are noticed for TEHN, YIBL, and ZAMB, while underestimations are observed for ADIS. As expected for TEC enhancements over YIBL and SEY1 on 14 October 2012, the background TEC is below observations whereas a reverse situation is noticed for ZAMB and HRAO where MM TEC values exceed observations specifically on 10 October 2012 for ZAMB, and 10 - 11 October 2012 for HRAO. In some cases when GPS TEC is not visible, it may be due to good agreement with one of the models (e.g., in the afternoon of 10 October 2012 for YIBL) or lack of observations for a given period (e.g., on 11 October 2012 for YIBL, SEY1, and ZAMB).

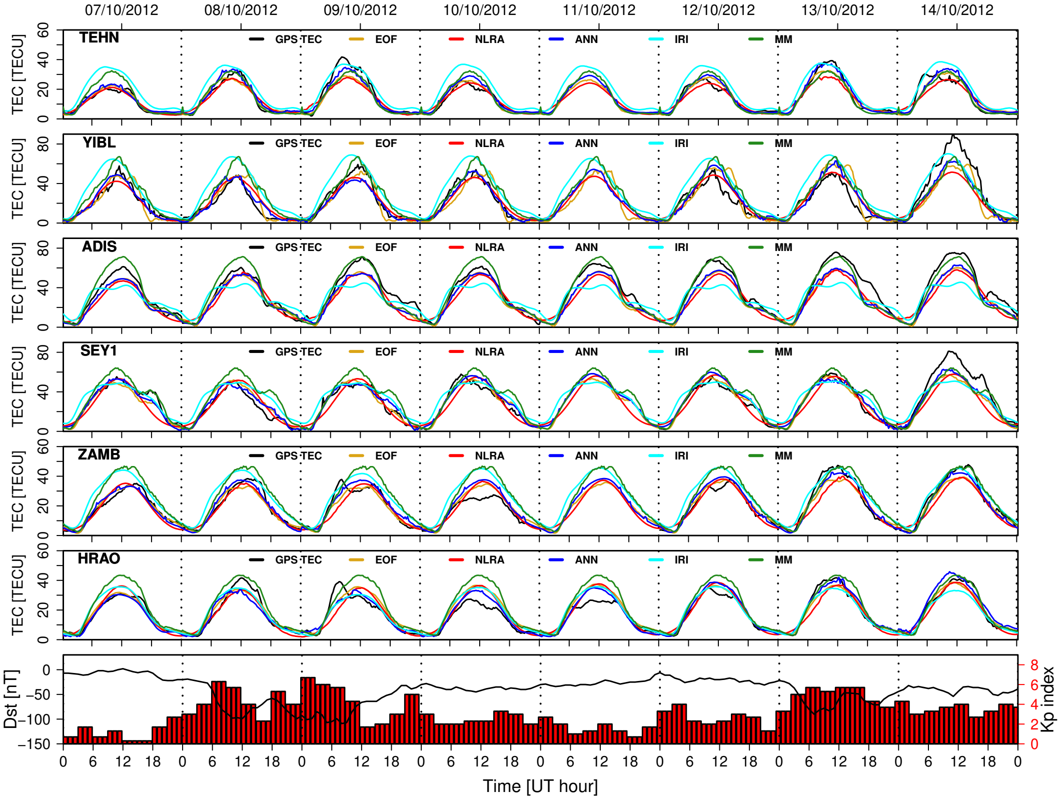

Figure 5.4: Comparison of EOF, NLRA, ANN, and IRI results with the observed TEC for the storm period of 07 - 14 October 2012.

Illustrated in Figure 5.5, are EOF, NLRA, ANN, and IRI results, as well as MM estimates for the storm period of 03 - 09 January 2015. For TEHN and ADIS, EOF and ANN models make more accurate TEC predictions than NLRA and IRI models (e.g., For TEHN, MAE_{EOF} = 1.54 TECU, MAE_{ANN} = 1.78 TECU, MAE_{NLRA} = 2.78 TECU, MAE_{IRI} = 3.19 TECU). NLRA model underestimates daytime TEC over TEHN between 05 - 09 October 2015, and ADIS between 06 - 09 January 2015, while for IRI model, over- and underestimations are respectively observed for TEHN and ADIS almost throughout the storm period. For the cases when both negative (depletion relative to MM TEC) and positive (enhancement relative to MM TEC) ionospheric responses are observed within the same storm period (e.g., 05 January 2015 and 08 January 2015 for YIBL, and 05 January 2015 and 07 January 2015 for ZAMB and HRAO), none of the models follow accurately TEC variations. However, modelling results are close to MM estimates throughout the storm period for SEYG, ZAMB, and HRAO.

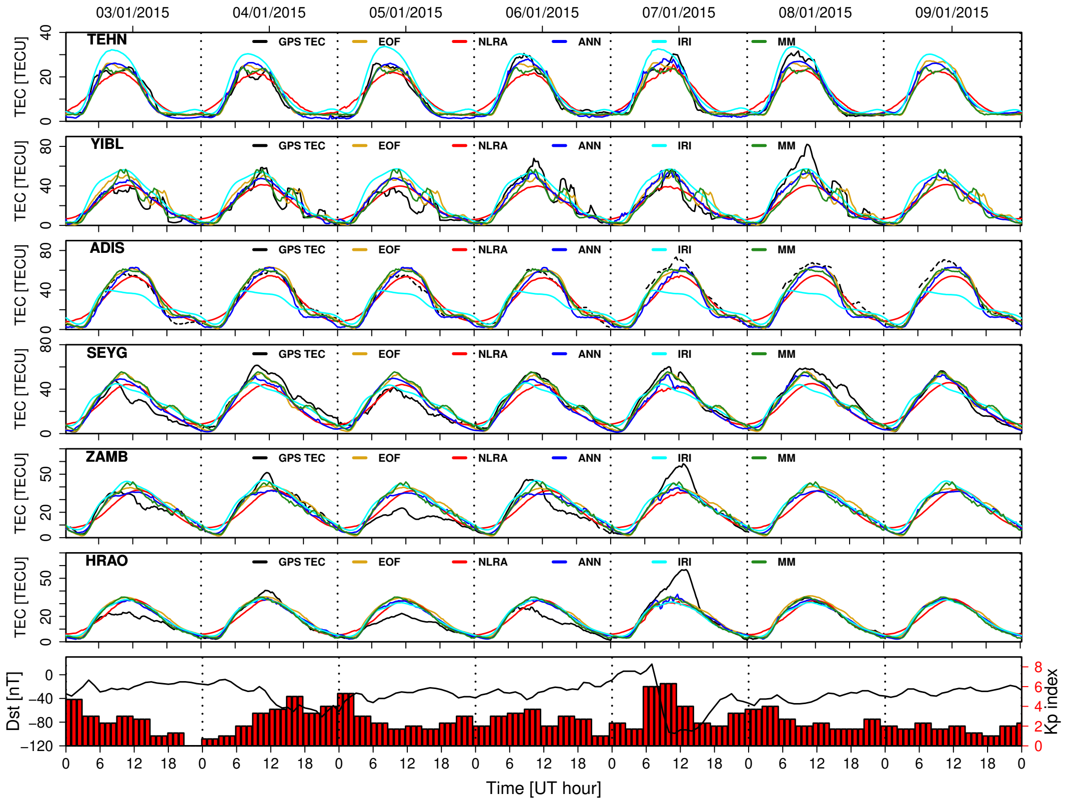

Figure 5.5: Comparison of EOF, NLRA, ANN, and IRI results with the observed TEC for the storm period of 03 - 09 January 2015.

Results displayed in Figure 5.6 are for the severe storm of 22 - 29 June 2015, for TEHN, YIBL, NAZR, SEYG, MONG, and HRAO stations. Except for IRI model which largely overestimates GPS TEC specifically for TEHN, YIBL, and SEYG, other models provide comparable results which also are in good agreement with observations except on 22 June 2015 for NAZR, SEYG, MONG, and HRAO. Furthermore, the models are capable of capturing negative ionospheric response over TEHN and TEC enhancements over MONG and HRAO observed on 23 June 2015. Large discrepancies between modelling results and MM estimates are noticed during TEC enhancement over MONG and HRAO whilst good agreement between modelled TEC and MM TEC with observations are observed during the storm recovery phase particularly for NAZR, MONG, and HRAO.

Figure 5.7 is similar to Figure 5.6 but for the 24 - 30 October 2016 moderate storms. In spite of some daytime deviations from the observations, EOF and ANN models are more accurate over ZAMB (MAE_{EOF} = 2.37 TECU, MAE_{ANN} = 2.04 TECU, MAE_{NLRA} = 2.69 TECU, MAE_{IRI} = 3.92 TECU), while for HRAO, EOF, ANN, and IRI models perform better than NLRA model which largely over predicts daytime observations. In contrast, for ADIS station, NLRA (MAE_{NLRA} = 4.05 TECU) estimates TEC more accurately than EOF (MAE_{EOF} = 4.57 TECU) and IRI (MAE_{IRI} = 5.05 TECU) models. For all the models, large discrepancies between observations and predictions are remarkable for KUWT whereas MM estimates agree

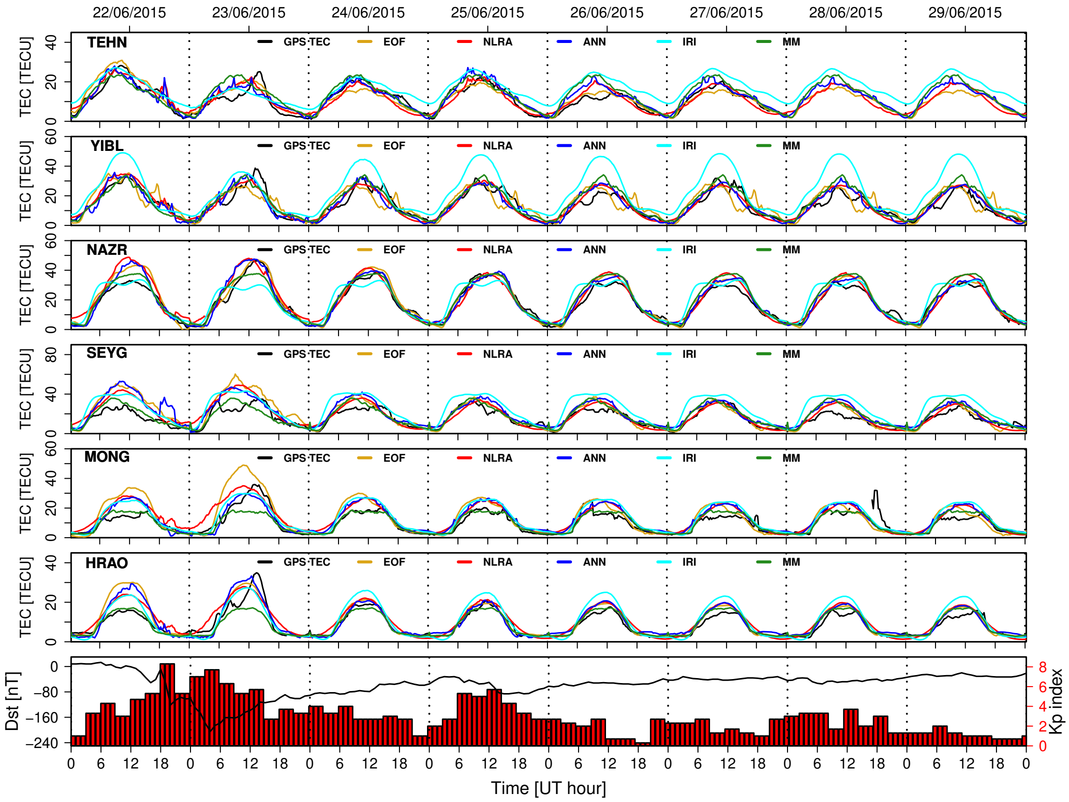

Figure 5.6: Comparison of EOF, NLRA, ANN and IRI results with the observed TEC for the storm period of 22 - 29 June 2015.

well with observations. Also noticed is the failure of EOF, NLRA, ANN, and IRI models to capture short-term features (e.g., TEHN) as well as the decrease in TEC observed on 26 October 2016 (e.g., ZAMB and HRAO) identified from large daytime deviations below the MM values. Particularly for NLRA model, large daytime overestimations of GPS TEC are seen over HRAO.

5.3.2 Extrapolation results

Extrapolation results are presented in Figure 5.8 along with GPS TEC and MM TEC for the storm periods of 28 February - 04 March 2017 (Figure 5.8 (a)) and 27 - 30 May 2017 (Figure 5.8 (b)). It can be seen from Figure 5.8 (a) that EOF estimates are smaller than observations throughout the storm period, specifically for TEHN station. For other models, despite some overestimates seen during the day, there is no much difference between observations, MM estimates, and modelled TEC. The models however, provide TEC values that exceed actual data for KUWT, specifically around midday and in the afternoon. A reverse case is observed for ADIS where all the models underpredict daytime TEC throughout the storm period. For SEYG and MAUA, there is not much difference between EOF, ANN, and IRI estimates and these are comparable with TEC values observed during the negative storm response on 03

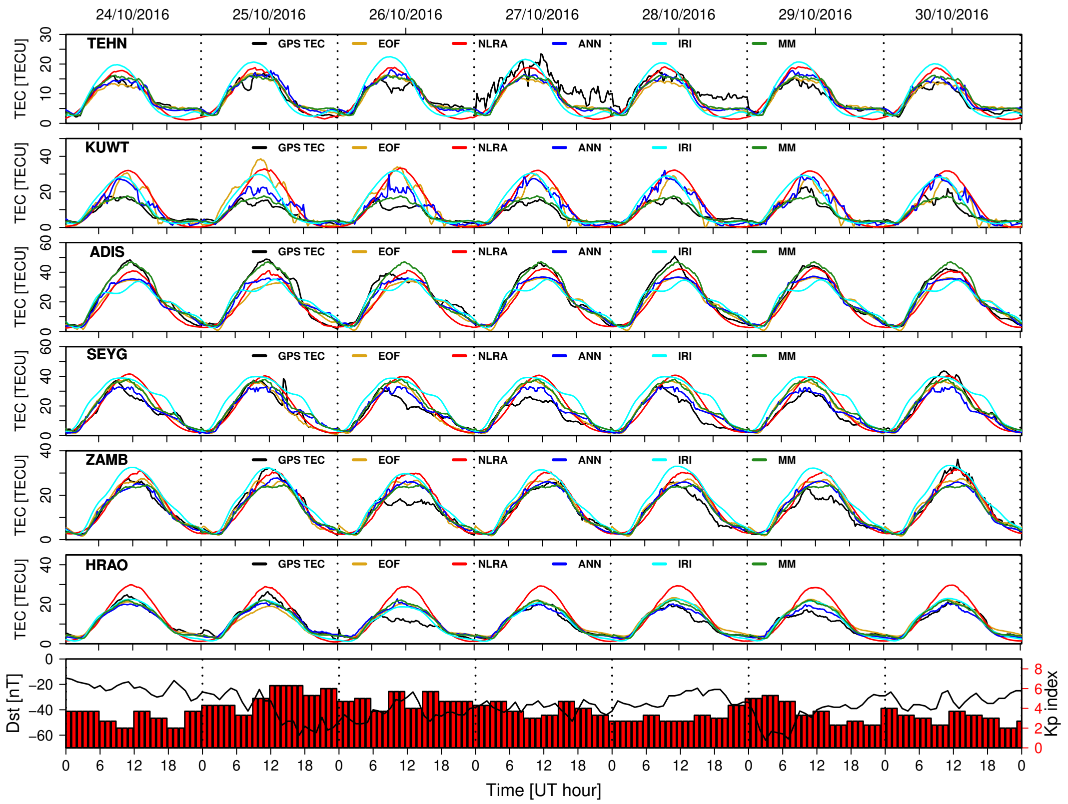

Figure 5.7: Comparison of EOF, NLRA, ANN and IRI results with the observed TEC for the storm period of 24 - 30 October 2016.

March 2017. NLRA model estimates well the amplitude of the observed TEC for SEYG with exception on 03 March 2017. However, for MAUA station, NLRA daytime values exceed observations on 02 - 04 March 2017. Although NLRA captures well the slight increase seen on 01 March 2017 over HRAO, it fails to follow TEC decrease on 03 March 2017. An opposite situation related to both increase and decrease on 01 March 2017 and 03 March 2018, respectively, is noticed for the rest of the models. Relatively large deviations between GPS TEC and MM medians are remarkable during positive TEC enhancements (e.g., 01 March 2017, HRAO; 02 March 2017, KUWT) and negative ionospheric responses on 03 March 2017 over HRAO.

Figure 5.8 (b) shows that TEC enhancements that occurred on 28 May 2017 over MAUA and HRAO are seen by EOF, NLRA, and ANN models. For the rest of the storm period NLRA daytime predictions exceed observations. MM TEC is largely below observations during the positive storm responses seen over MAUA and HRAO. On 27 May 2017, EOF, NLRA, and IRI daytime predictions exceed observations for TEHN whereas for the rest of the period, the observed TEC is accurately estimated by ANN model compared to other modelling techniques. The high accuracy for IRI and ANN models (MAE_{IRI} = 3.19 TECU, MAE_{ANN} = 3.55 TECU) with respect to others (MAE_{EOF} = 5.32 TECU, MAE_{NLRA} = 5.71 TECU) is noticed for KUWT station. For all the models, overestimations are dominantly seen in the afternoon for ADIS station, while in the morning and during nighttime, TEC is accurately estimated. Except for IRI model which slightly over predicts the observations over SEYG, other models make accurate predictions almost throughout the entire storm period.

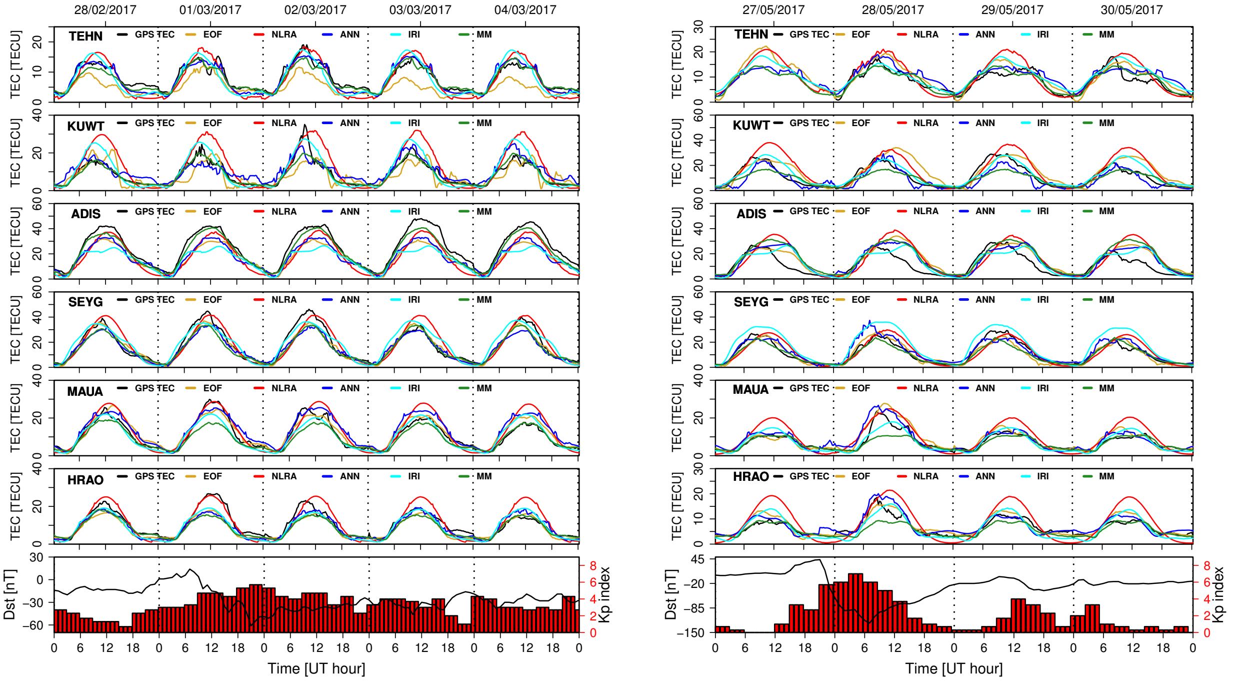

(a)

(b)

Figure 5.8: Comparison of EOF, NLRA, ANN and IRI results with the observed TEC for the storm periods of (a) 28 February - 04 March 2017 and (b) 27 - 30 May 2017.

The presented results show that, generally, all the models make accurate predictions for nighttime and early morning and can follow positive and negative ionospheric responses for some storms and fail to do so for others. Also short-term variations observed in GPS TEC are not sufficiently captured by the models. The failure of storm-time models to accurately predict the storm impact has been reported by Fuller-Rowell *et al.* (2000) when validating simulation results provided by the coupled thermosphere ionosphere model (CTIM) with ionosonde measurements of $foF2$. It is however worth noting that storm-time TEC modelling does not fully depend on the analytical expressions or optimization techniques used in this study, but also on the representations of physical mechanisms that drive the storms. Some of these include horizontal neutral winds which are among the transport mechanisms of ionized particles within the ionosphere and can thus cause both positive (Titheridge, 1995b; Lu *et al.*, 2008) and negative ionospheric responses (Lu *et al.*, 2001); the superfountain effect (enhanced fountain effect) which was stated to be responsible of positive ionospheric enhancements when dayside low and a part of mid-latitude ionosphere are uplifted due to interplanetary electric field (IEF) shock (Tsurutani *et al.*, 2004); travelling ionospheric disturbances (TIDs) responsible for positive ionospheric responses, and changes in neutral composition responsible of negative storm effects (Lu *et al.*, 2001). Lack of the inputs that represent well the main geomagnetic storm drivers may be attributed to the failure, in some cases, of all the models to reproduce TEC dynamics observed during the storms.

Particularly for IRI and NLRA models, under/overestimations are more frequently observed for some validation periods when compared to ANN and EOF models. The reason specified for the IRI model is the lack of plasmasphere contributions within the model as TEC computation is performed between 60 - 2000 km while GPS TEC is derived along the receiver-satellite line of sight which extends up to an altitude of 20 200 km (Kenpankho *et al.*, 2011; Chartier *et al.*, 2012; Habarulema & Ssessanga, 2017). The case of NLRA to over/underestimate observations can be attributed to analytical expression itself which may not be more sensitive to change in TEC. However, NLRA model is more efficient for storms with non-significant ionospheric responses. We wish to note that the inefficiency of a regression analysis (RA) based model to capture positive storm response was also reported by Mukhtarov *et al.* (2013b).

Both ANN and EOF models tend to perform better compared to NLRA and IRI models although they also fail to predict the storm impacts especially when both positive and negative ionospheric responses are observed within a single storm period. Reminding that the number of hidden nodes was statistically determined within the range 10 - 25 for individual location, training an ANN over a very wide range may lead to more accurate results. Thus, ANN results can thus be improved by extending the range 10 - 25 to a large interval, and this is one of the key advantage of using ANNs in modelling as different choices of hidden neurons may lead to different solutions. We emphasize that, in some cases, the increasing of the amount of neurons in the hidden layers may cause performance improvements. However, depending on the data set and the problem under investigation, a large amount of neurons can lead to a loss of generalization (overfitting), leading to a reduction of ANN performance. It is also important to note that ANN and NLRA models were implemented considering high temporal resolution (5 minutes) data while for the EOF model, daily indices were used. High resolution geomagnetic indices used for ANN may probably be the reason of its superiority relative to EOF in terms of accuracy. The ability of EOF model to reveal hidden features in TEC databases, and to reconstruct TEC with fewer components at the same time keeping as much as the information in the original datasets, are its advantages when compared to other models.

5.3.3 Statistical analysis

Accuracies of EOF, NLRA, ANN, and IRI models are evaluated on basis of statistical parameters such as mean absolute error (MAE), mean absolute percentage error (MAPE) and correlation coefficient (R) computed using observations (GPS TEC) and modelled TEC. To evaluate how close predictions are from observations MAE values computed according to Equation 5.6 were used. Since TEC varies differently at different latitudinal regions, the performance of a model at different locations can further be evaluated by introducing MAPEs to make the comparison scale-free. MAPEs were calculated using the formula (Mitchell & Spencer, 2003)

$$MAPE = \frac{1}{N}\sum_{i=1}^{N}\frac{|TEC_{mod} - TEC_{obs}|}{TEC_{obs}} \times 100\%. \tag{5.9}$$

The measure of how much accuracy the observed trend is reproduced by the model was evaluated by the Pearson correlation coefficient R provided by equation (4.11). All statistical parameters for individual storm periods are provided in Figure 5.9 (a), the left, middle, and right panels, representing MAE, MAPE, and R values, respectively.
It is clear from the left panel of Figure 5.9 (a) that smaller values of MAE were generally found for ANN and EOF models and this shows that both models are more accurate than NLRA and IRI models in estimating the magnitude of the observed TEC. More specifically, 20 out of 36 cases (with 17 out 24 cases for interpolation and 6 out of 12 for extrapolation) presented on the left panel of Figure 5.9 (a), indicate that MAE values for ANN model are smaller than the values obtained for EOF model and this reveals that ANN is better than EOF in general. Also noticed from the same panel, are high values of MAE generally found for IRI (interpolation results) and NLRA (extrapolation results) compared to other modelling techniques. It can thus be considered that NLRA performs better than IRI during interpolation while the latter is more accurate than the former during extrapolation. This is based on the fact that, 20 out of 36 cases (including 17 out of 24 for interpolation and 3 out of 12 for extrapolation) show higher values of MAE for NLRA compared to IRI model.

The middle panel of Figure 5.9 (a) also indicates that, for most of the cases, MAPE values for IRI and NLRA are generally higher than the values obtained for ANN and EOF models. This confirms the good performance of ANN and EOF models with respect to NLRA and IRI models. From the right panel of Figure 5.9 (a) it is clear that R values are high (between 82 - 99 %) for all modelling techniques considered in this study. It can hence be concluded that all the models are capable of reproducing the general diurnal trend of TEC for all storm periods considered for validation.

To qualitatively evaluate the performances of the models at each location, statistics were carried out over six storm periods combined together for individual station. Statistical results are presented in Figure 5.9 (b): MAE (top left), MAPE (top right), percentage accuracy, PA (bottom left), as well as R values (bottom right). Both top left and right panels of Figure 5.9 (b) show that, for most of the cases, highest MAE and MAPE values correspond to sta-

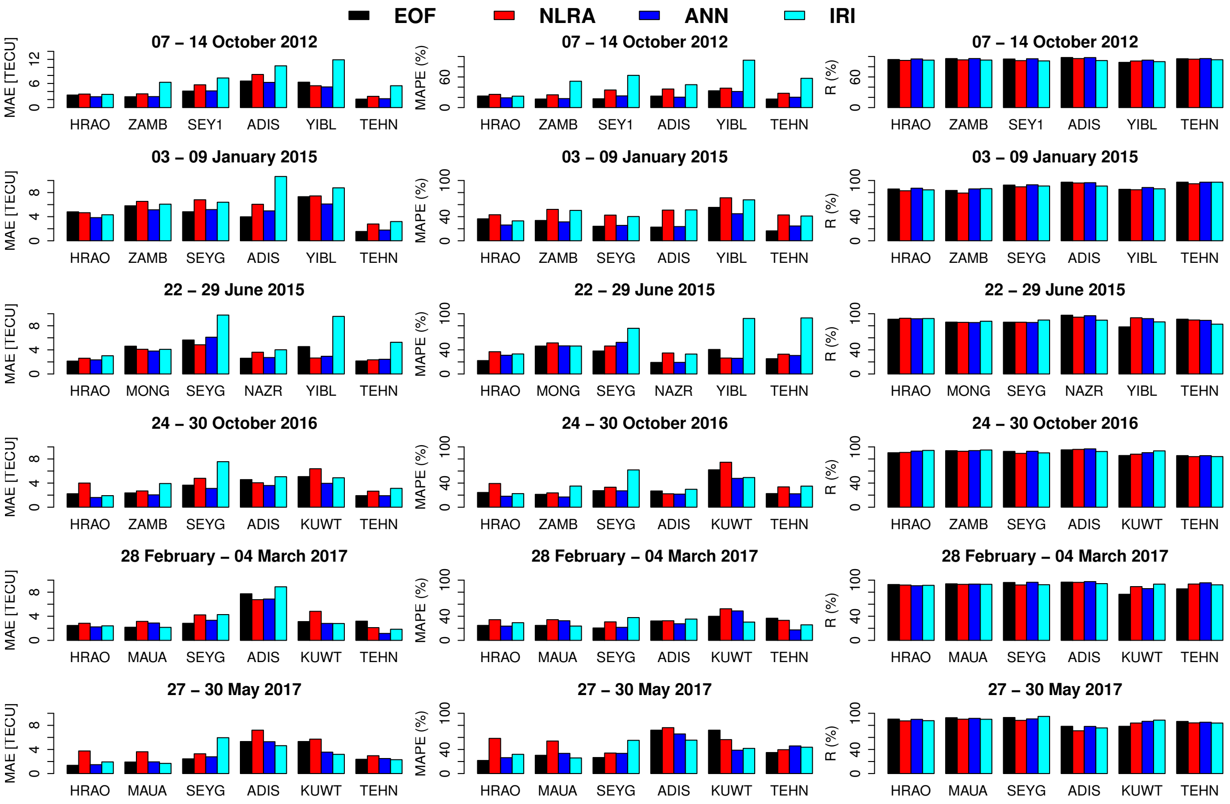

(a) MAE (left panel), MAPE (middle panel), and R (right panel) values for each storm period.

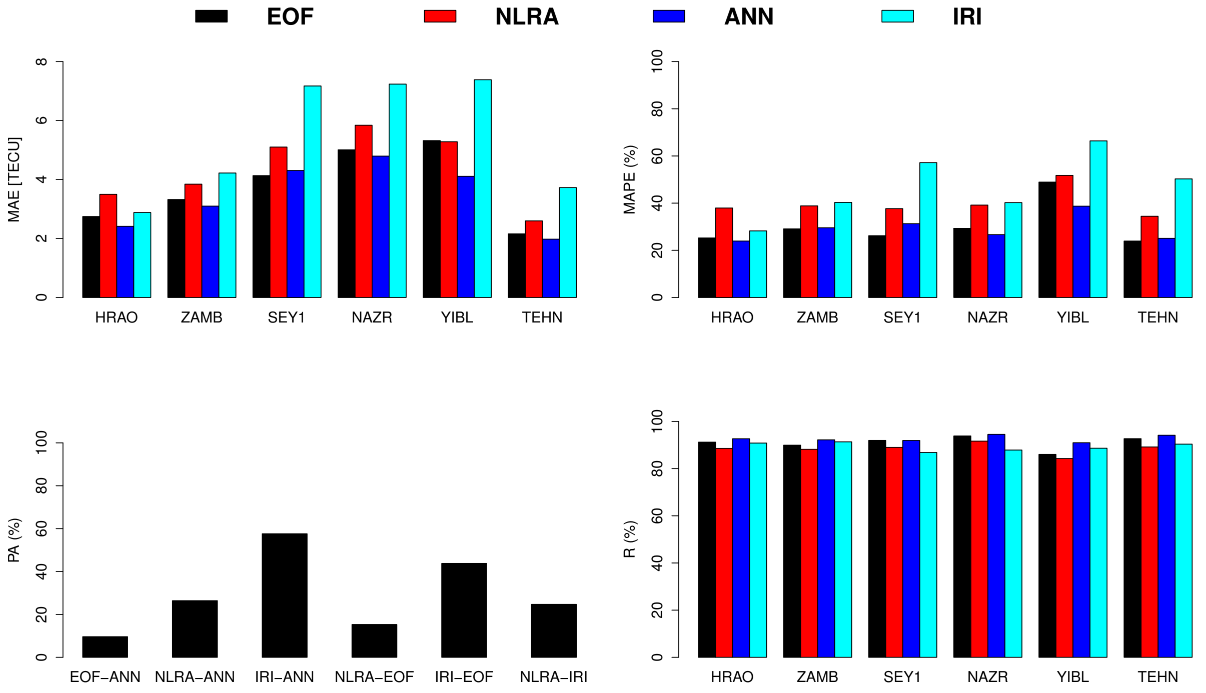

(b) MAE (top left panel), MAPE (top right panel), PA (bottom left panel) and R (bottom right panel) values for combined storm periods.

Figure 5.9: MAE, MAPE, PA, and R values.

tions located at the trough and crests/ near the crests of EIA. Thus, ionospheric responses to geomagnetic storms in low latitudes are difficult to model, perhaps due to a couple of complex mechanisms such as fountain effect, which may become even more complex during disturbed conditions: “superfountain effect” (Tsurutani *et al.*, 2004), and thermospheric neutral winds that compete with fountain effect during plasma transport in the low latitude ionosphere (Fesen *et al.*, 1989).

PA values computed according to the formula

$$PA_{Model_1/Model_2} = \frac{MAE_{Model_1} - MAE_{Model_2}}{MAE_{Model_2}} \times 100\%, \tag{5.10}$$

reveal that, over all six storm periods considered for validation, ANN model performs 9.62 %, 26.41 %, and 57.61 %, better than EOF, NLRA, and IRI models, respectively; while EOF is 15.31 %, and 43.78 % more accurate than NLRA and IRI, respectively. Moreover, the accuracy of NLRA was found to be 24.69 % higher than IRI model accuracy. This is also confirmed with relatively higher values of R obtained for ANN model compared to other models (bottom right panel of Figure 5.9 (b)). The superiority of ANN model relative to other techniques was noted in previous modelling studies that compared ANN with IRI (Habarulema *et al.*, 2007, 2010; Watthanasangmechai *et al.*, 2012; Okoh *et al.*, 2016), and ANN with EOF model in mid-latitude (Uwamahoro & Habarulema, 2015).

Statistical results presented above were computed by considering GPS TEC as reference. Bearing in mind that IRI model is based on monthly average values, and taking into consideration that positive and negative storms are part of our analysis, we have also performed a statistical analysis referring to the background ionosphere represented by monthly median values. Computations were done using Equations (5.8) - (5.10), where TEC_{obs} was substituted by MM TEC. The summary of the results (not all shown) are presented in Tables 5.5 and 5.6 along with results obtained when GPS TEC was considered as reference, for comparison purposes.

Table 5.5 presents MAE values obtained per location, when all storm periods selected for validation are combined together. The standard deviations (SD) are also presented in the last column of the table. In both cases (GPS and MM TEC as references), for all models, and for all stations, the results presented in Table 5.5 show that difference between MAE values with respect to GPS TEC and MM TEC does not exceed 1.5 TECU. Average MAE values found with respect to both considered references confirm that ANN model is more accurate than other modelling techniques considered in this study.

The range of error obtained in this study are generally smaller or comparable with errors reported in different studies. For example, the average MAE values found for storm-time TEC modelling/reconstruction over mid-latitude locations are 3.20, 3.63, and 6.16 TECU for MIDAS, ANNs, and IRI models, respectively (Uwamahoro *et al.*, 2018a) while in the current study, 2.74, 3.31, 2.46, and 3.61 TECU, were found for EOF, NLRA, ANN, and IRI mod-

Table 5.5: MAE values (in TECU) between modelled and GPS TEC (as reference) on one hand, modelled and MM TEC (as reference) on the other hand, for each location considered during development or validation of the models. For each location, all storm periods are combined within a single dataset. MAE_{av} and SD represent average value of MAE and standard deviation, respectively.

Method	Reference	TEHN	YIBL	NAZR	SEY1	ZAMB	HRAO	MAE_{av}	SD
EOF	GPS TEC	2.16	5.32	5.01	4.13	3.32	2.75	3.78	1.26
	MM TEC	1.89	5.17	3.89	3.84	3.46	1.91	3.36	1.26
NLRA	GPS TEC	2.60	5.28	5.84	5.10	3.84	3.50	4.36	1.24
	MM TEC	2.46	5.07	4.95	5.62	4.30	3.32	4.29	1.19
ANN	GPS TEC	1.98	4.11	4.79	4.31	3.10	2.41	3.45	1.13
	MM TEC	1.47	3.63	3.68	4.06	2.94	2.15	2.99	1.00
IRI	GPS TEC	3.73	7.39	7.24	7.17	4.22	2.88	5.44	2.05
	MM TEC	3.40	5.63	6.82	6.43	2.93	2.24	4.58	1.95

Table 5.6: PA values (in %) computed by separately considering GPS TEC and MM TEC as references.

Reference	EOF/ANN	NLRA/ANN	IRI/ANN	NLRA/EOF	IRI/EOF	IRI/NLRA
GPS TEC	9.62	26.41	57.61	15.31	43.78	24.69
MM TEC	12.40	43.33	52.96	27.51	36.08	6.72

els, respectively. Although in some cases different error metrics have been used to evaluate statistically a storm-time model performance, relatively high errors in TEC modelling were found. For instance, the root mean square errors reported in Uwamahoro & Habarulema (2015) and Mukhtarov *et al.* (2013a) are within the range $\sim 2.0 - 12.5$ for storm conditions.

Table 5.6 presents PA values (in %) between a pair of models as indicated by Equation 5.10. It can clearly be seen that PA of given model with respect to IRI model has been reduced when MM values are considered as reference compared to the case when GPS TEC is taken as reference. For example, the last column of Table 5.6 indicates that NLRA model is 24.69 % and 6.72 % more accurate than IRI model when GPS TEC and MM TEC are separately considered as references, respectively. The reason of PA reduction particularly computed between other models with respect to IRI when MM TEC is considered as a reference is that, IRI modeled values are based on monthly averages, and are therefore relatively close to MM TEC values. In contrast, for other cases where IRI model is excluded, PA values increase and this depends on how close the model predictions are close to MM values. Statistical results based on MM values also show the superiority of ANN with respect to other modelling techniques presented in this study.

5.4 Summary and conclusions

In this chapter, we compared the performances of EOF, NLRA, ANN, and IRI models to predict TEC during geomagnetic storm conditions over various latitudes based on a statistical analysis. Based on their accuracies, storm-time TEC models considered can generally be classified (from high to low accuracy) as follows: ANNs, EOF, NLRA, and IRI. With GPS TEC as a reference for statistical computations, PA values have showed that ANN model is about 10 %, 26 %, and 58 % more accurate than EOF, NLRA, and IRI models, respectively, while EOF was found to perform 15 %, and 44 % better than NLRA and IRI, respectively. On the other hand, the NLRA accuracy was found to be 25 % higher than the accuracy of IRI model. Statistical results referring to background ionosphere represented by MM TEC values have also shown the superiority of ANN with respect to other modelling techniques, followed by EOF, NLRA, and then IRI model. Generally, highest errors were observed at the locations of both crests of EIA and at the magnetic equator, and then at mid-latitude locations. The accuracies of the models increase with increasing latitude. It was however noticed that all the models are capable to capture some of ionospheric responses and fail to do so for others. In the next chapter the contribution of meridional neutral winds to TEC modelling will be evaluated. From now onward, ANN based model will be used as it was found to be more accurate than other models considered in this work.

Chapter 6

Contribution of meridional neutral winds to storm-time TEC modelling

This chapter presents storm-time total electron content (TEC) modelling results based on artificial neural networks (ANNs), for both low- and mid-latitude African regions. The developed storm-time TEC models were based on Global Positioning System (GPS) observations from GPS receiver stations selected in low, northern and southern mid-latitude regions of the African sector. GPS data selection was based on a storm criterion of $Dst \leqslant$ -50 nT and storm datasets used to develop the models were within the periods 2001 - 2015, 2000 - 2015, and 1998 - 2015, for African low, northern and southern hemisphere mid-latitude regions, respectively. For the first time in storm-time TEC modelling, the meridional wind velocity was introduced as an additional input to the well-known TEC modelling inputs (diurnal variation, seasonal variation, solar activity, and geomagnetic activity representations) to take into account the effect of neutral winds in moving ionisation within the ionosphere along the magnetic field lines. The results presented in this chapter have been published in Uwamahoro *et al.* (2018b).

6.1 Data selection and modelling inputs

Storm-time TEC data used to develop ANN models were derived from GPS measurements at three locations: RABT (33.99° N, 6.85° W; 23.88° N, geomagnetic), Morocco; MBAR (0.60 ° S, 30.73° E; 10.22 ° S, geomagnetic), Uganda; and SUTH (32.38° S, 20.81° E, 41.09° S, geomagnetic), South Africa. RABT and SUTH are in mid-latitude region while MBAR is in the low latitude region, in the nominal equatorial ionisation anomaly (EIA) region. For a given station, when there are missing data for a specific storm period selected for validation, the closest station with available data was used. In this instance, Tetouan (TETN; 35.56° N, 5.36° W, 26.18° N, geomagnetic), Morocco; Malindi (MAL2; 2.99° S, 40.19° E, 12.42° S, geomagnetic), Kenya; and Hartebeesthoek (HRAO; 25.89 ° S, 27.68° E, 36.32° S, geomagnetic), South Africa; were used to replace RABT, MBAR and SUTH respectively. Table 6.1 shows the geographic and geomagnetic coordinates of stations used in this study while Figure 6.1 displays their locations on the African map.

Table 6.1: Geographic and geomagnetic latitudes and longitudes of the GPS receiver stations used for development and validation of the models.

Station ID	Name	Country	GLat (°)	GLon (°)	GMLat (°)	GMLon (°)
RABT	Rabat	Morocco	33.99	-6.85	23.88	69.23
TETN	Tetouan	Morocco	35.56	-5.36	26.18	70.68
MBAR	Mbarara	Uganda	-0.60	30.73	-10.22	102.36
MAL2	Malindi	Kenya	-2.99	40.19	-12.42	111.86
SUTH	Sutherland	South Africa	-32.38	20.81	-41.09	84.76
HRAO	Hartebeesthoek	South Africa	-25.89	27.68	-36.32	94.69

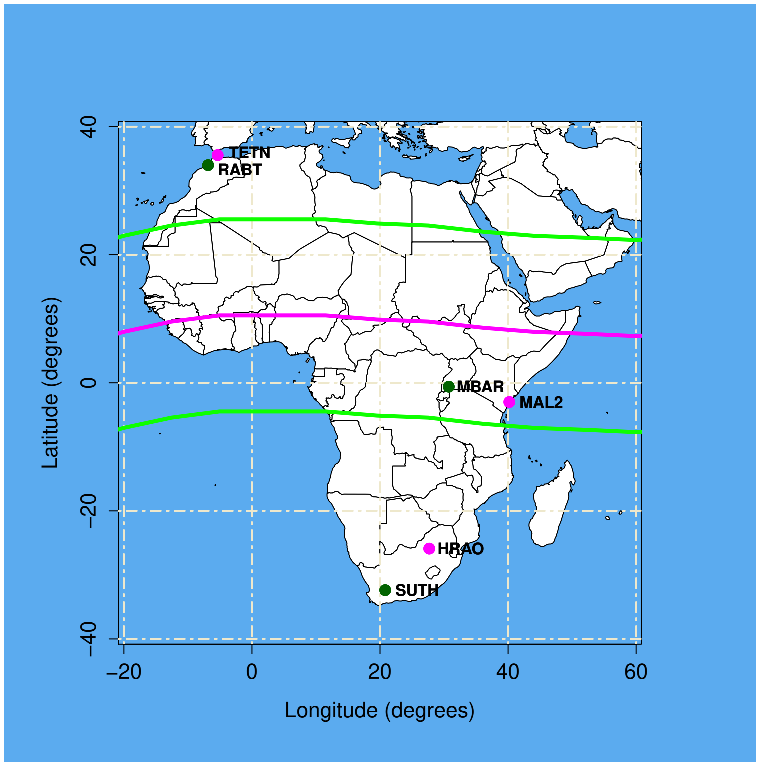

Figure 6.1: Locations of GPS receiver stations used during development and validation of the models.

For development and validation of the models, only storm-time TEC data (5-minute time resolution) selected based on the storm criterion of $Dst \leqslant$ -50 nT was considered. Original datasets used to implement the models consisted of historical storm-time data (all storm periods with available data) within the coverage periods 2000 - 2015, 2001 - 2015, and 1998 - 2015, for RABT, MBAR, and SUTH, respectively. Thus, for each station, positive, negative, and non-significant storms are all included in a single dataset used to implement the ANN model for that station. Also taken into account while selecting validation storm periods is the period of solar activity (low, moderate and high). Two storm periods per each solar activity period were chosen for validation within 2000 - 2015 (interpolation) while outside the data range used during modelling, two storm periods in 2016 were reserved for extrapolation. It is of great importance to point out that the selected validation storm periods were excluded from the original datasets used while implementing the models to make an independent validation. Table 6.2 shows the selected storm periods and stations used for validation, as well as the storm intensities as indicated by the minimum Dst index reached during the storm main phase.

Table 6.2: Selected geomagnetic storm periods and GPS receiver stations used for validation.

Storm period	Solar activity period	Minimum Dst (nT)	Stations used for validation
14 - 16 Dec 2006	Low	-162	RABT, MBAR, SUTH
21 - 23 Jul 2009	Low	-83	RABT, MBAR, HRAO
05 - 07 Aug 2011	Moderate	-107	RABT, MBAR, SUTH
16 - 21 Mar 2015	Moderate	-223	TETN, MBAR, SUTH
06 - 10 Mar 2012	High	-74, -131	RABT, MAL2, SUTH
18 - 24 Feb 2014	High	-116, -91, -60, -51	RABT, MBAR, SUTH
31 Dec 2015 - 02 Jan 2016	Low	-110	RABT, MAL2, HRAO
05 - 08 Mar 2016	Low	-98	RABT, MBAR, SUTH

The common modelling inputs considered are universal time (t) which represents diurnal variation of TEC, day number (d) of the year to account for seasonal, annual and semiannual variations of TEC, modified solar flux index ($F10.7p$) for solar activity representation, and geomagnetic activity indices: 3-hour planetary magnetic index (a_p), symmetric disturbance field in the horizontal component of the Earth's magnetic field H ($symH$) as well as the auroral electrojet (AE) index. The three geomagnetic indices were all used to globally represent, at a latitudinal scale, different geomagnetic activity contributors to TEC changes due to geomagnetic storms. For a specific location, two ANN models were developed, the difference being that one contains the meridional wind velocity (v) as an extra input, obtained from the HWM.

6.2 Description of the modelling technique

The modelling technique described here consists of two main steps: determination of the suitable altitude for the meridional wind computation using non-linear regression analysis (NLRA) technique, and development of storm-time TEC models based on ANNs.

6.2.1 Determination of suitable altitude for the computation of v

Since the meridional wind velocity varies with altitude, we first determined statistically the appropriate altitude for the meridional wind velocity (v) computation. In this context, the altitude range of 100 - 500 km was considered in steps of 50 km. Thus, for each considered location, v was computed at altitudes of 100, 150, 200, 250, 300, 350, 400, 450, and 500 km.

Then, the computed v at a specific altitude was used together with TEC modelling inputs t, d, $F10.7p$, a_p, AE, $symH$ in Equation (6.1) to estimate TEC.

$$\begin{aligned} ln(TEC) = {} & \zeta_0 + \zeta_1.cos\left(\frac{2\pi \times t}{24}\right) + \zeta_2.sin\left(\frac{2\pi \times t}{24}\right) \\ & + \zeta_3.F10.7p + \zeta_4.a_p + \zeta_5.AE + \zeta_6.symH + \zeta_7.v \\ & + [\zeta_8 + \zeta_9.F10.7p + \zeta_{10}.a_p + \zeta_{11}.AE + \zeta_{12}.symH + \zeta_{13}.v]cos\left(\frac{2\pi d}{365.25}\right) \\ & + [\zeta_{14} + \zeta_{15}.F10.7p + \zeta_{16}.a_p + \zeta_{17}.AE + \zeta_{18}.symH + \zeta_{19}.v]sin\left(\frac{2\pi d}{365.25}\right) \\ & + [\zeta_{20} + \zeta_{21}.F10.7p + \zeta_{22}.a_p + \zeta_{23}.AE + \zeta_{24}.symH + \zeta_{25}.v]cos\left(\frac{4\pi d}{365.25}\right) \\ & + [\zeta_{26} + \zeta_{27}.F10.7p + \zeta_{28}.a_p + \zeta_{29}.AE + \zeta_{30}.symH + \zeta_{31}.v]sin\left(\frac{4\pi d}{365.25}\right) \end{aligned} \tag{6.1}$$

The established standard expression comprises Fourier series with amplitudes changing with $F10.7p$, a_p, AE, $symH$. The semiannual and annual variations of TEC were also taken into account by introducing harmonic functions with periods of half year and year respectively. The natural logarithm was taken on the left hand side of Equation (6.1) to ensure that the modelled TEC is a positive quantity. The unknown constants ζ_0, ζ_1, ζ_2, ..., ζ_{31} in Equation (6.1) were found using the least squares method at each time the altitude for computation of v changed, followed by computation of root mean square error (RMSE) defined by

$$RMSE = \sqrt{\frac{1}{N}\sum_{i=1}^{N}(TEC_{mod} - TEC_{obs})^2} \tag{6.2}$$

where TEC_{mod} and TEC_{obs} are the modelled/reconstructed and observed TEC respectively, and N is the number of observations. The variation of RMSE with altitude is illustrated in Figure 6.2. It can be seen from Figure 6.2 that the smallest RMSE was obtained at the altitude of 350 km. Above 350 km, the RMSE is almost constant. Therefore, the altitude of 350 km was selected as the appropriate altitude at which v was computed to get the optimum solution. The constant values of RMSEs at high altitudes can be understood based on the theory presented in Titheridge (1995b). Theoretically, it is known that the atmospheric gas density, ρ, decreases exponentially with altitude (Davies, 1990; Titheridge, 1995b). Due to their relative motions, horizontal winds at different heights are subjected to frictional drag which is proportional to μ/ρ, where μ is the viscosity coefficient. A decrease in density causes an increase in frictional drag in such a way that for the altitudes above about 250 km, the horizontal wind velocity is independent of the altitude (Titheridge, 1995b).

The reliability of the HWM in the African sector has been verified by comparing its predictions with actual data from the Fabry - Perot Interferometer (FPI), for both low and

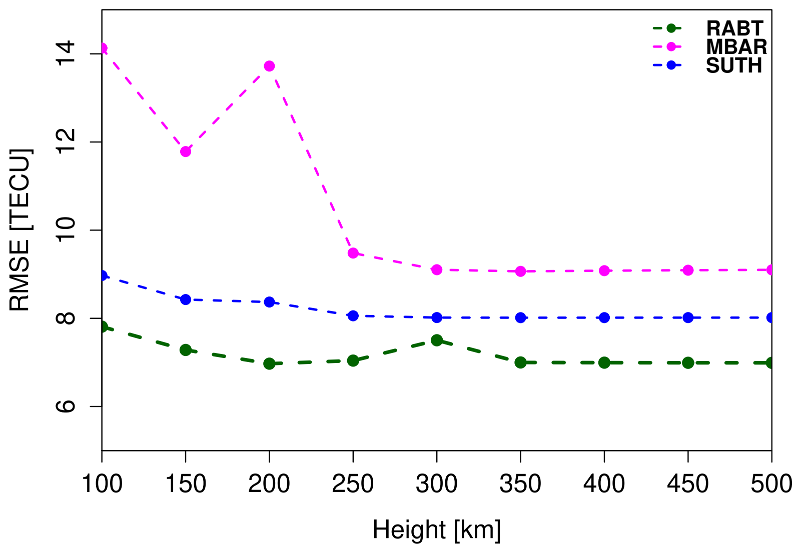

Figure 6.2: Variation of RMSE values between the observed and reconstructed TEC with altitude. RMSEs were computed for three GPS receiver stations: RABT (dark green), MBAR (magenta) and SUTH (blue).

mid-latitude regions (Fisher *et al.*, 2015; Kaab *et al.*, 2017; Tesema *et al.*, 2017). A study carried out over a period of half a year showed that the HWM estimates the meridional neutral winds well over Bahir Dar, Ethiopia (11.6°N, 37.4°E; 3.7° N, geomagnetic). It was further showed that the zonal wind is well reproduced by the HWM although an overestimation (of about 25 m/s) was remarked during winter months (Tesema *et al.*, 2017). On the other hand, the climatology of quiet time thermospheric winds based on FPI measurements has been done for the African mid-latitude, precisely at Oukaimeden, (32.20°N, 7.87°W; 21.21°N), Morrocco. A comparative study between FPI measurements and HWM predictions showed how well the HWM makes accurate estimates for both meridional and zonal winds over Oukaimeden during winter season (Fisher *et al.*, 2015). The authors however have noticed a tendency of the HWM to overestimate the meridional wind during equinox, and the magnitude of equatorward winds around local midnight. While validating the HWM14 over Oukaimeden, Kaab *et al.* (2017) found that most of the features in the FPI measurements were captured by the HWM14 with a exception in zonal winds specifically during summer, where an offset in peaks of about four hours was noticed. Figure 6.3 displays comparisons between monthly averages of FPI horizontal neutral wind measurements (blue) (meridional and zonal components), with airglow-weighted model results provided by the HWM07, and neutral winds estimates from HWM14.

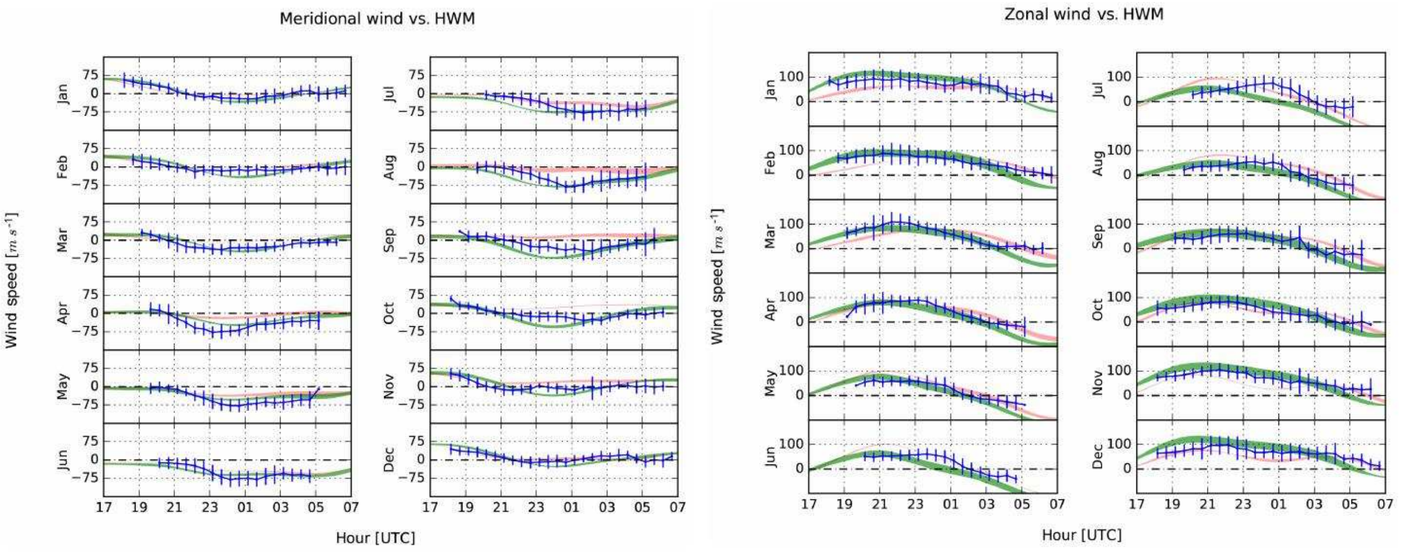

(a) Comparisons of meridional winds from FPI and HWM.

(b) Comparisons of zonal winds from FPI and HWM.

Figure 6.3: Comparisons of monthly averages (period of January 2014 to February 2016) of neutral wind measurements from FPI (blue curve), with (a) meridional components, and (b) zonal components, of airglow-weighted results from HMW07 (red curve) and HWM14 estimates (green curve). Source: (Kaab *et al.*, 2017).

6.2.2 Artificial neural network configuration

Two different ANN models per each considered location were developed, with 10 and 11 input neurons for model 1 and model 2, respectively. The 10 input neurons for model 1 correspond to sine and cosine components of time t of the day, and day number d of the year as defined in Chapter 4 by equations (4.4), (4.5), and (4.6), as well as solar and geomagnetic activity representations: $F10.7_p, a_p, AE, symH$. For model 2, an extra neuron that stood for the meridional wind velocity v was added making a total number of 11 input neurons. Relationships between TEC and modelling inputs can therefore be established as follows:
Model 1:

$$TEC \approx f_1(tc, ts, dc_1, ds_1, dc_2, ds_2, F10.7_p, a_p, AE, symH) \tag{6.3}$$

Model 2:

$$TEC \approx f_2(tc, ts, dc_1, ds_1, dc_2, ds_2, F10.7_p, a_p, AE, symH, v) \tag{6.4}$$

where f_1 and f_2 are functions of modelling inputs. The output layer is defined by 1 neuron which stands for TEC as the modelled parameter, while the number of hidden neurons were determined statistically. For each considered location, ANN was trained 15 times by varying the number of hidden neurons from 11 to 25 (range selected randomly) followed by a computation of RMSE between the observed TEC and ANN output.

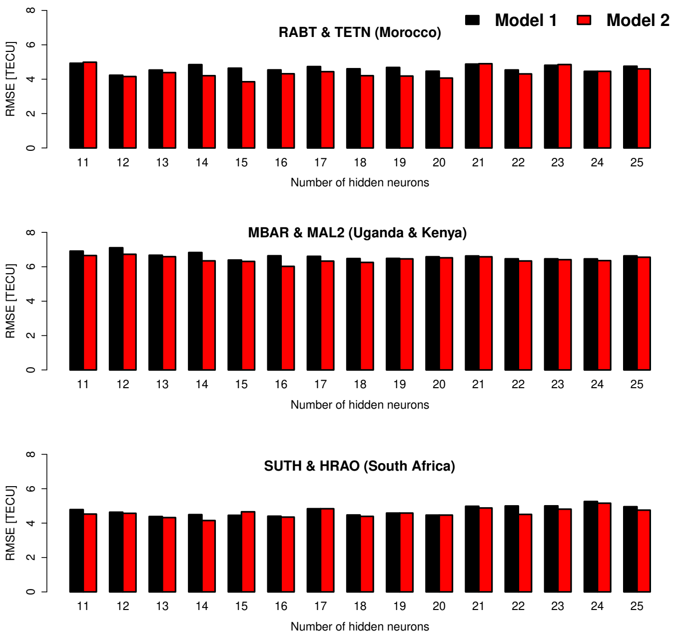

Figure 6.4: Variation of RMSE with number of hidden neurons.

Figure 6.4 shows the variation of RMSE with the number of hidden neurons when models are tested on validation datasets. For both models, the selection of numbers of hidden neurons considered in this study was based on the lowest RMSE values observed within the range 11 - 25. For the case of RABT/TETN (top panel of Figure 6.4), an architecture of 10-12-1 selected for model 1 means that there were 10, 12 and 1, input, hidden and output neurons, respectively. For model 2, 11 input neurons were used and the additional input neuron stood for the meridional wind velocity. Thus, 11 - 15 - 1 architecture was considered for model 2. In the same manner, 10 - 15 - 1 (model 1) and 11 - 16 - 1 (model 2) architectures were chosen for MBAR/MAL2 while for SUTH/HRAO, 10 - 13 - 1 (model 1), 11 - 14 - 1 (model 2) were selected.

6.3 Results

Validation results of models 1 and 2 are presented for both interpolation (2000 - 2015) and extrapolation (2016) storm periods and compared with actual GPS TEC (5 minute time resolution). We wish to note that validation datasets were not used when developing the models and 2016 falls outside the data range considered during the implementation of the models. For each storm period, validation was done for three locations at different latitudinal regions. Dst and K_p indices are also presented for each storm period to indicate the time and the strength of the storm. For all the results presented in this study, a geomagnetic storm can be identified for $Dst \leq -50$ nT or $K_p \geq 4$.

6.3.1 Interpolation (2006 - 2015) and extrapolation (2016) results

Figure 6.5 shows the observed and estimated TEC by models 1 and 2 for four geomagnetic storm periods of 14 - 16 December 2006 and 21 - 23 July 2009 (interpolation results), 31 December 2015 - 02 January 2016 and 05 - 08 March 2016 (extrapolation results), belonging to low solar activity period. For each storm period, the presented results are for three different latitudinal locations considered for validation based on data availability. The good performance of ANNs in following positive (e.g., 15 December 2006 (Figure 6.5 (a)) for RABT) and negative (e.g., 01 January 2016 (Figure 6.5 (c)) for HRAO, 07 March 2016 (Figure 6.5 (d)) for SUTH) storm effects can be noticed. However, there are some cases where ANNs fail to follow negative ionospheric responses (e.g., 15 December 2006 (Figure 6.5 (a)) for MBAR), and the case where the depletion is seen by the models but they could not predict accurately the magnitude of the depletion (e.g., 01 January 2016 (Figure 6.5 (c)) for MAL2). Considering the performances of models 1 and 2 separately, it can be seen from Figure 6.5 (a) that both models make different TEC predictions over RABT, MBAR and SUTH. TEC enhancement observed over RABT on 15 December 2006 is followed by both models while TEC depletion over MBAR is not captured. For SUTH, model 2 largely overestimates daytime TEC on 15 December 2006 compared to model 1 while a reverse situation is observed on 16 December 2006. As shown in Figure 6.5 (b), the 21 - 23 July 2009 storm effect is not really significant over RABT, MBAR and HRAO. Both models provide comparable TEC predictions over RABT and MBAR although some over/underestimations of the observed TEC are observed at midday and sometime in the afternoon. Despite some underestimations, model 2 estimates TEC better than model 1 over HRAO. Figures 6.5 (c) and (d) show that both models are capable of following TEC depletions observed during the two storm periods (e.g., on 01 January 2016 for MAL2 and HRAO, and on 07 March 2016 for SUTH) although some daytime overestimations are observed. Generally, the results for both models are encouraging specifically in estimating storm-time TEC magnitude.

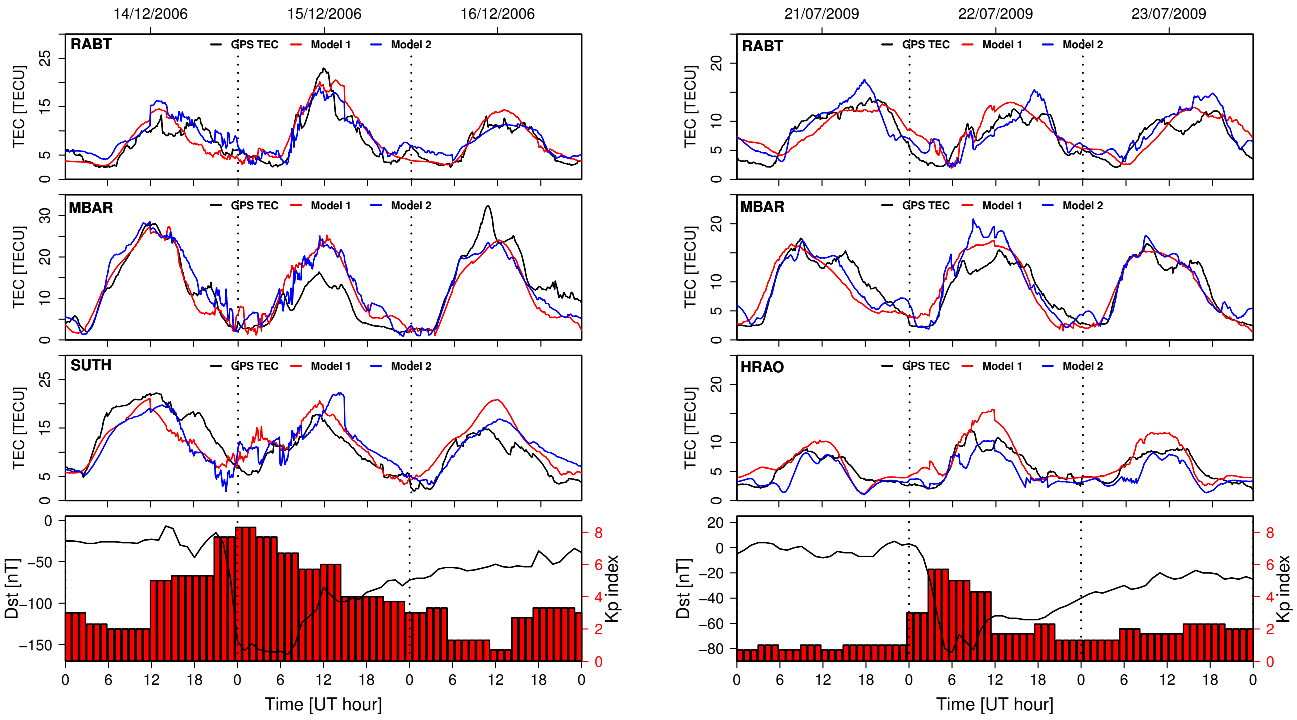

(a) Storm period of 14 - 16 December 2006.

(b) Storm period of 21 - 23 July 2009.

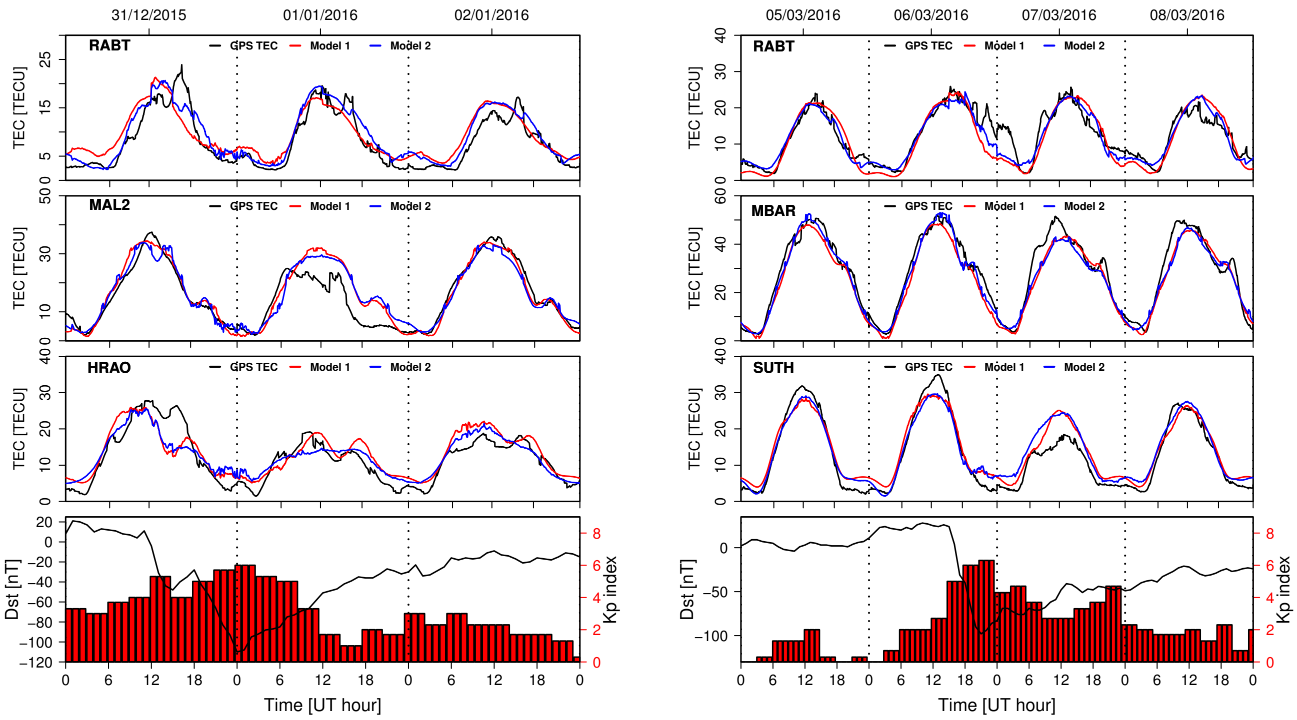

(c) Storm period of 31 December 2015 - 02 January 2016.

(d) Storm period of 05 - 08 March 2016.

Figure 6.5: Comparison of the observed and modelled TEC for storms that occurred during the low solar activity period.

Figure 6.6 is similar to Figure 6.5 but for geomagnetic storms which occurred during moderate

(05 - 07 August 2011 and 16 - 21 March 2015) and high (06 - 10 March 2012 and 18 - 24 February 2014) solar activity periods. The accuracy of ANNs in following TEC enhancement is noticed on 06 August 2011 (Figure 6.6 (a) for SUTH), 17 March 2015 (Figure 6.6 (b) for TETN and SUTH), 09 March 2012 (Figure 6.6 (c) for RABT), and on 20 February 2014 (Figure 6.6 (d) for RABT). On 18 March 2015, a remarkable shift in TEC peak is noticed for TETN while the negative storm effect observed over SUTH is identified by the models even though predictions exceed observations. Some TEC overestimations are observed in the afternoon throughout the 06 - 10 March 2012 storm period for MBAR, during daytime specifically on 06 and 08 March 2012 for SUTH (Figure 6.6 (c)), and on 19 February 2014 for SUTH (Figure 6.6 (d)). Comparing the performances of both models, Figures 6.6 (a) and (b) show that models 1 and 2 make close TEC predictions for all stations considered for validation. Both models make accurate TEC predictions for the 05 - 07 August 2011 storm period except on 05 August 2011 for RABT and 06 August 2011 for MBAR where overestimations are observed. Positive storm response observed on 17 March 2015 over TETN and SUTH is seen by both models while the magnitude of TEC depletion observed over SUTH on 18 March 2015 is not accurately estimated. Despite some daytime overestimations, both models make accurate TEC predictions for the two storm periods selected within the moderate solar activity period. Figures 6.6 (c) and (d) show that both models make TEC predictions that are close to each other except for some few cases. It can be seen from Figure 6.6 (c) that TEC magnitude is well estimated for RABT, while overestimations are observed in the afternoon and around midday for MBAR and SUTH, respectively. The performance of models 1 and 2 can also be appreciated in Figure 6.6 (d) where TEC is well estimated for all three stations, except an overestimation observed in the early afternoon, for SUTH, on 19 February 2014.

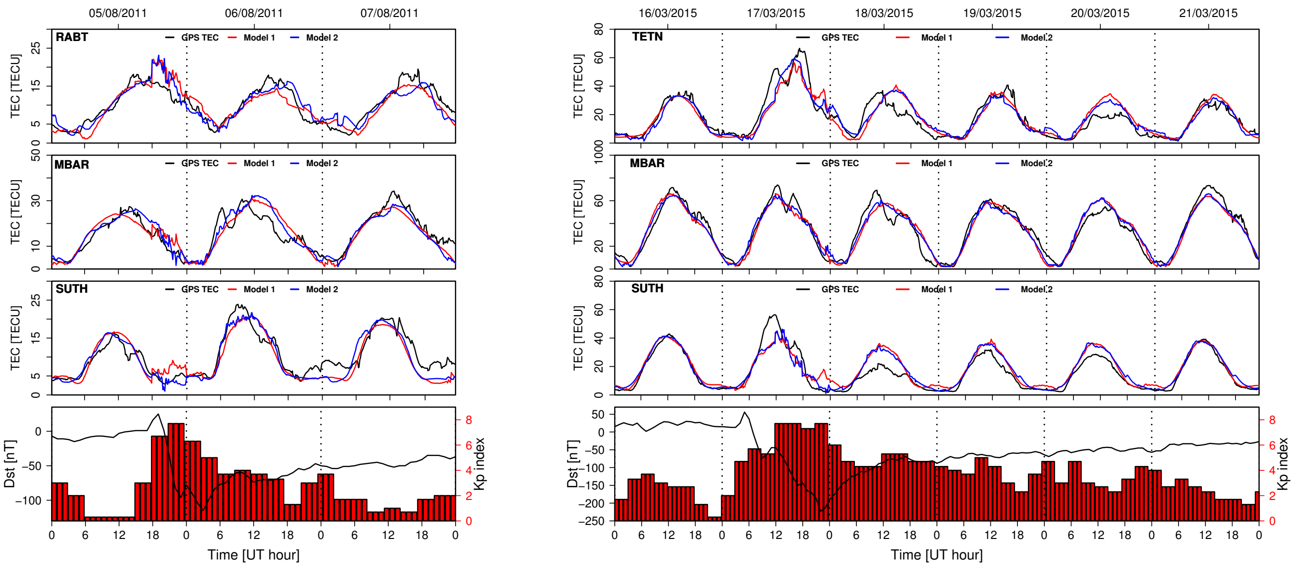

(a) Storm period of 05 - 07 August 2011.

(b) Storm period of 16 - 21 March 2015.

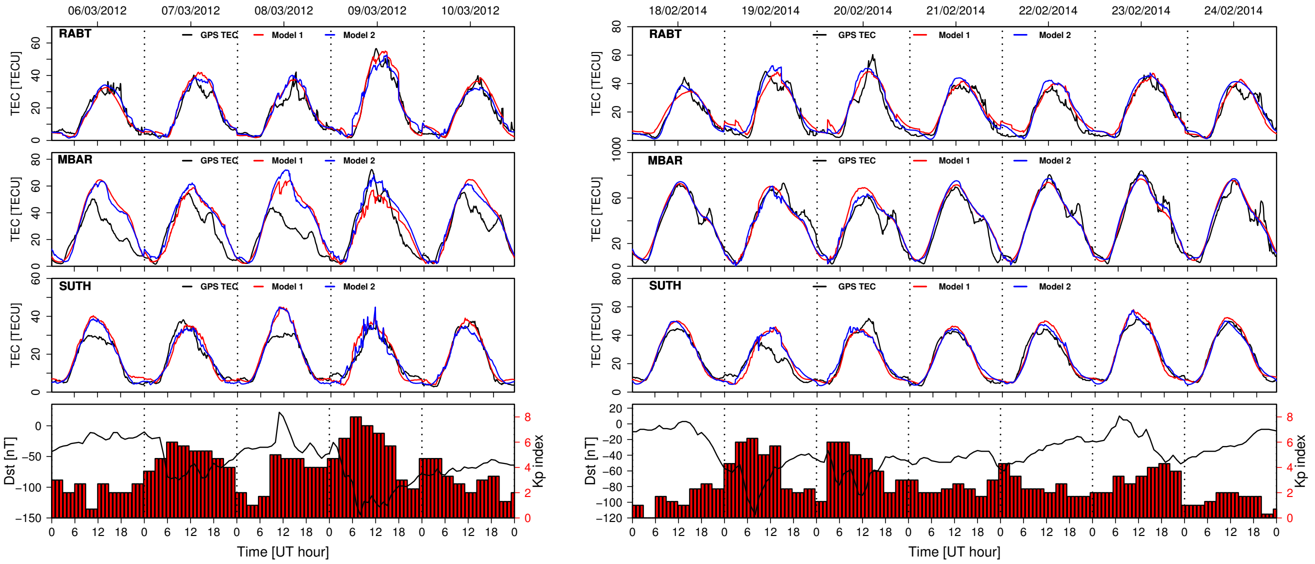

(c) Storm period of 06 - 10 March 2012.

(d) Storm period of 18 - 24 February 2014.

Figure 6.6: Comparison of the observed and modelled TEC for storms that occurred during moderate and high solar activity periods.

6.3.2 Statistical analysis

To quantitatively evaluate which of the models performs better in estimating TEC at different latitudinal regions, RMSEs, percentage improvement (PI) as well as correlation coefficients between the observed and modelled TEC were calculated. RMSE can be understood as an average distance measured along the vertical line between the observed and modelled points, with the property that the smaller the RMSE, the better the model (e.g., Zhang *et al.*, 2009). Thus, RMSE is a good indicator of the accuracy of a model and RMSE values presented in this work were computed using Equation (6.2). On the other hand, the percentage improvement defined by

$$PI = \frac{RMSE_1^{av} - RMSE_2^{av}}{RMSE_2^{av}} \times 100\% \tag{6.5}$$

was used to evaluate the contribution of v to TEC modelling. Equation (6.5) shows how much percentage, on average, model 2 performs better than model 1. PI was calculated based on average RMSEs for models 1 ($RMSE_1^{av}$) and 2 ($RMSE_2^{av}$) computed over 8 storm periods selected for validation. Correlation coefficient as a measure of how much information in the observed TEC is covered in the estimated TEC was also taken into account to assess the accuracy of the models. All statistical parameters are presented in Figure 6.7 for all 8 validation storm periods. For individual storm period, RMSE values obtained for three different locations are compared (Figure 6.7 (a)) to evaluate the accuracy of ANN models at various latitudes. The top and bottom panels of Figure 6.7 (a) correspond to model 1 and model 2, respectively. It can be seen from Figure 6.7 (a) that relatively high RMSE values were generally found for low latitude locations (MBAR/MAL2) indicating that both ANN models perform better in mid-latitude regions than in the low latitude. Figure 6.7 (b) shows a direct comparison of RMSE values obtained for models 1 and 2. For almost all the cases, it can be seen that RMSE values for model 1 are greater than the values obtained for model 2 indicating that the latter performs, on average, better than the former. PI values presented in Figure 6.7 (c) show that improvements in TEC modelling results were obtained for 8 out of 8 (100 %), 6 out of 8 (75 %) and 6 out 8 (75 %) validation storm periods, for RABT/TETN, MBAR/MAL2, and SUTH/HRAO, respectively, when v was included. On case-case basis, the highest improvements of about 32 %, 13 %, and 12 % were found for storm periods of 05 - 08 March 2016 (RABT), 16 - 21 March 2015 (MBAR), and 31 December 2015 - 02 January 2016 (HRAO), respectively. High correlation coefficients presented in Figure 6 (d) shows that both models capture well the observed TEC trend for both low and mid-latitude regions. It is well known that more storms occur during solar maximum compared to solar minimum period (Matamba *et al.*, 2015). Thus, in our developed empirical (data-based) models, datasets used to implement the ANN models are mostly dominated by high solar activity storms. Slightly lower values of correlation coefficients and the failure for ANNs to capture accurately the low solar activity storms can partly be attributed to the lack of sufficient amount of data representing the low solar minimum periods within the datasets considered for the models' implementation.

6.4 Discussion

The implemented ANN models are capable of predicting both positive and negative storm effects for some storms while for others, the storm impact is not well captured. A statistical

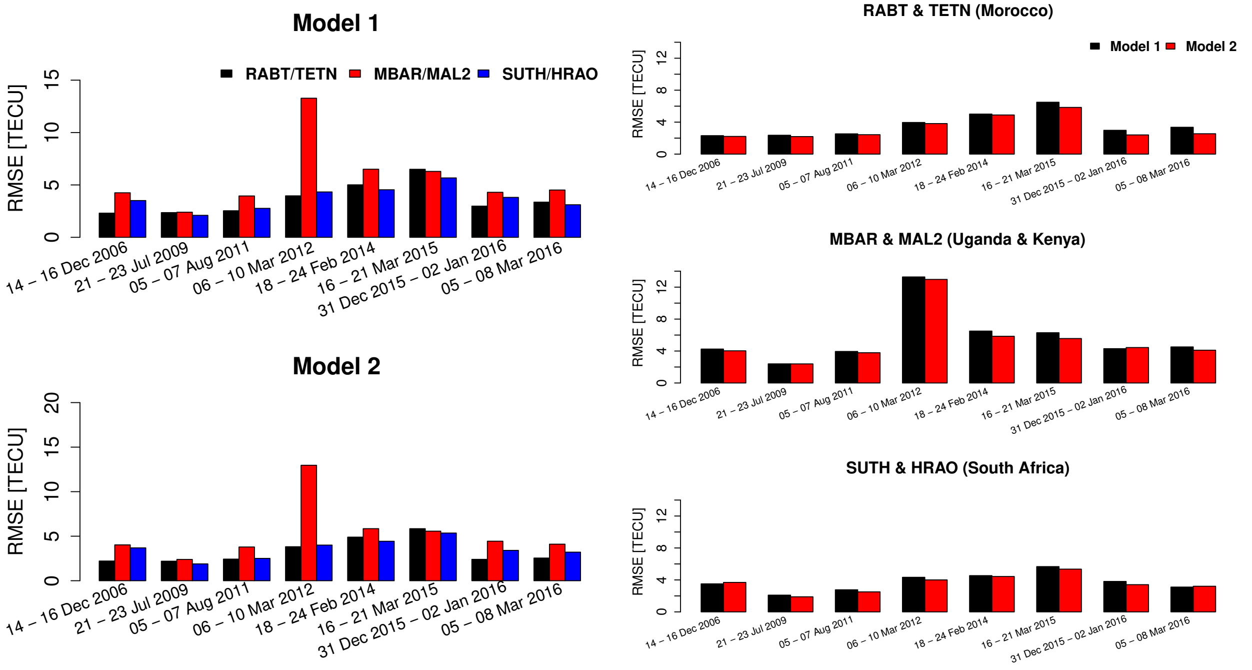

(a) Comparison of RMSE values between the observed and modelled TEC for different latitudinal regions.

(b) Comparison of RMSE values between the observed and modelled TEC for models 1 and 2.

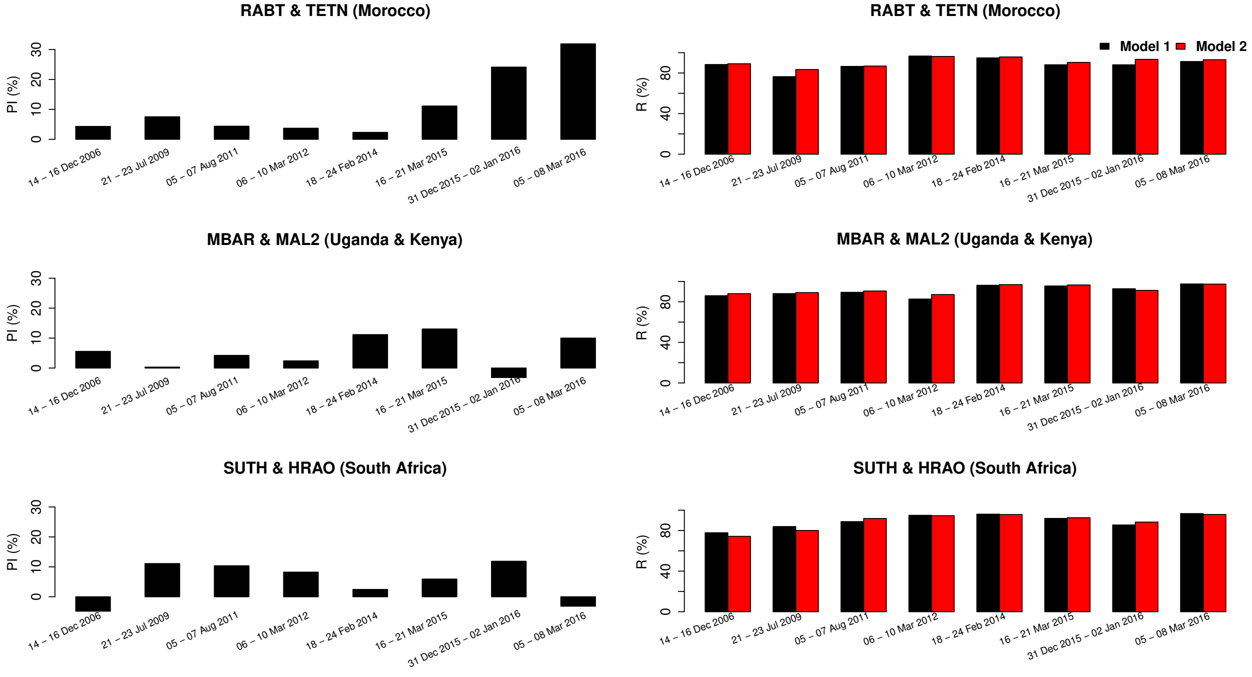

(c) Percentage improvements.

(d) Correlation between the observed and modelled TEC.

Figure 6.7: Statistical evaluation of models 1 and 2: (a) Comparison of RMSE values per location (b) Comparison of RMSE values per model (c) Percentage improvement (d) Correlation coefficients.

analysis revealed that storm-time TEC modelling is more difficult in low latitude compared to mid-latitude ionosphere. The presence of the equatorial ionisation anomaly (EIA) and complicated low latitude electrodynamics during storm conditions are probably the reasons that make it difficult to model TEC for the low latitude region. The difficulty in modelling TEC for the low latitude ionosphere due to mixture of complex mechanisms happening in this region was also highlighted in different TEC modelling literatures (Liu *et al.*, 2013; Kumar *et al.*, 2015; Sur *et al.*, 2015). Previous empirical TEC modelling studies mainly considered diurnal variation, seasonal variation, solar and geomagnetic activity representations as modelling inputs (Mao *et al.*, 2005; Habarulema *et al.*, 2007; Mao *et al.*, 2008; Habarulema *et al.*, 2009a,b, 2010, 2011; Ercha *et al.*, 2012; Habarulema & McKinnell, 2012; Watthanasangmechai *et al.*, 2012; Chen *et al.*, 2015; Uwamahoro & Habarulema, 2015; Dabbakuti *et al.*, 2016; Le *et al.*, 2016). The performances of models 1 and 2 in following TEC enhancements and depletions for some storms are very encouraging when compared to previous works where the failure of ANN, IRI, EOF and other empirical models in following storm-time TEC enhancement was noticed (Habarulema *et al.*, 2010, 2011; Olwendo *et al.*, 2012; Mukhtarov *et al.*, 2013a; Kumar *et al.*, 2015; Uwamahoro & Habarulema, 2015). For example, Mukhtarov *et al.* (2013a) noted some large underestimations of TEC enhancements observed within the storm periods of 05 - 13 April 2000 and 06 - 13 November 2004. For the first time, the current work evaluated the contribution of the meridional winds in improving TEC modelling results during geomagnetic storms. For the northern hemisphere mid-latitude, improvements were obtained for all 8 storm periods considered for validation. Over RABT/TETN, meridional wind directions from HWM were dominantly northward (poleward) during daytime and southward (equatorward) during nighttime for 8 validation storm periods. As observed over SUTH/HRAO, the wind direction was dominantly southward during daytime and northward during nighttime. For example, Figure 6.8 illustrates changes of v for the storm case of 16 - 21 March 2015, where $v > 0$ and $v < 0$ corresponds to northward and southward wind direction, respectively. Perturbations in the background wind are observed during the storm main phase over TETN, MBAR and SUTH. Inclusion of v provided an improvement of 11.12 %, 13.05 %, and 6.00 % for TETN, MBAR, and SUTH, respectively.

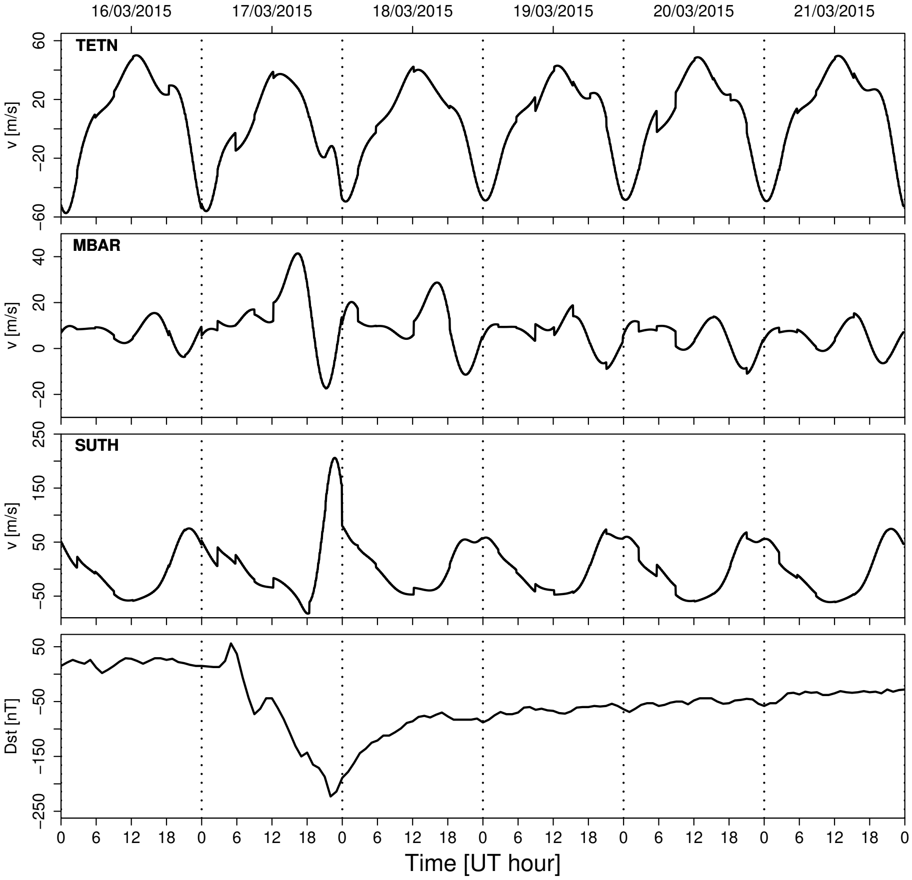

Figure 6.8: Meridional wind velocity from HWM over TETN, MBAR, and SUTH, during the storm period of 16 - 21 March 2015. *Dst* (nT) index is displayed in the last panel to show the intensity of the storm during this period.

From the literature, it is known that the main driver of equatorward winds is the pressure gradient resulting from Joule heating and particle precipitation over polar regions which increases during geomagnetic storms and then generate equatorward winds which penetrated further into the opposite hemisphere. The existence of such winds from polar regions to low latitudes has been reported in different literatures (Buonsanto *et al.*, 1989; Fuller-Rowell *et al.*, 1994; Titheridge, 1995b). Storm-generated winds were highlighted as the main cause of changes in the global wind circulation during geomagnetic storms (Buonsanto *et al.*, 1989; Emmert *et al.*, 2002) and have direct effect on transport of ionisation. This effect is strengthened during storm conditions when storm-generated winds reinforce the background winds. Equatorward winds move ionisation up the magnetic field lines to higher altitudes, into regions of lower recombination while poleward winds move ionisation down to lower altitudes, into regions of stronger recombination (Anderson & Klobuchar, 1983; Fuller-Rowell *et al.*, 1994; Titheridge, 1995a). In this point of view, simulation studies have concluded that meridional winds are the primary cause of the positive storm response when NmF_2 and hmF_2 are positively correlated (Fuller-Rowell *et al.*, 1994; Lu *et al.*, 2001, 2008; Bhattacharyya *et al.*, 2011; Balan *et al.*, 2013). As the energy increases at high latitudes during geomagnetic storms (increase in particle precipitation and Joule heating), the resulting equatorward winds move ionisation up the magnetic field lines to higher altitudes where a large decrease in overall loss rate is observed. This leads to an increase in hmF_2 and NmF_2, and hence, an enhancement of electron density/TEC (Lu *et al.*, 2001; Fedrizz *et al.*, 2008; Lu *et al.*, 2008; Kintner *et al.*, 2008). Such an effect is very significant in the mid-latitude due to its dependence on $sin2I$ where I is the magnetic dip, and zero at the magnetic equator ($I = 0°$) and poles ($I = 90°$) (Titheridge, 1995a,b). Thus, improvements obtained for some of the mid-latitude storms can probably be attributed to the effect of meridional winds of lowering or lifting (e.g., storm case of 16 - 21 March 2015 over SUTH) ionisation below or above the magnetic field lines.

For the low latitude ionosphere, improvements in TEC modelling were found for six storm periods and the wind direction over MBAR/MAL2 was northward for four storm periods and southward for two storm periods belonging to south hemisphere winter (21 - 23 July 2009, 05 - 07 August 2011). Inter-hemispheric flow of meridional winds driven by plasma pressure gradients between summer and winter hemispheres has been suggested as one of the causes of the ionisation transport in the low latitude region (Fesen *et al.*, 1989; Fuller-Rowell *et al.*, 1994; Titheridge, 1995b; Lu *et al.*, 2001). Another fact that contributes to the ionisation transport in the low latitude is the fountain effect. Meridional winds and the fountain effect compete in moving ionisation in such a way that, simultaneous equatorward winds oppose the fountain effect since they move plasma horizontally from the Appleton peaks to the equator while simultaneous poleward winds enhance electron density at the Appleton peaks and deplete it at the equator. Winds blowing in one direction across the equator deplete electron concentrations from one Appleton peak and enhance them in the other Appleton peak in the opposite hemisphere (Fesen *et al.*, 1989). This double transport of ionisation (fountain effect and horizontal meridional winds) are probably linked with the improvements obtained for low latitude.

Coexistence of positive and negative storm responses in opposite hemispheres was interpreted as a result of transport of ionisation across the dip equator by storm-generated transequatorial winds which deplete electron density from the upwind hemisphere and enhances it in the downwind hemisphere (Fesen *et al.*, 1989; Lu *et al.*, 2001). However, this can only be investigated with a further analysis about wind direction over two stations approximately at the same latitude but with different ionospheric responses. We wish to note that improvements in TEC modelling when neutral winds were taken into consideration were also reported in the work by Anderson & Klobuchar (1983); Sur *et al.* (2015, 2017), during quiet conditions. Being mindful that in this study the meridional wind velocity used during modelling was obtained from HWM, further studies based on real observations are required to accurately evaluate the contribution of neutral winds to storm-time TEC modelling. However, as mentioned before, it is of utmost importance to state that the HWM has been validated with Fabry-Perot Interferometer (FPI) measurements in African low and mid-latitudes over Bahir Dar, Ethiopia (11.6°N, 37.4°E; 3.7° N, geomagnetic) and Oukaimeden, Morrocco (32.20°N, 7.87°W; 21.21°N) respectively (Fisher *et al.*, 2015; Kaab *et al.*, 2017; Tesema *et al.*, 2017).

It should also be noted that not all storm-time ionospheric responses are driven by neutral winds. Changes in neutral composition were highlighted as the main cause of negative storm effect (Prölss, 1980), while the expansion of the equatorial ionisation anomaly (EIA), prompt penetrating electric fields (PPEF) (Tsurutani *et al.*, 2004) and large-scale traveling ionospheric disturbances (Borries *et al.*, 2009) were found to be the causes of positive storm effect in the mid-latitude. Thus, the failure of ANN models to accurately predict the storm impacts may partly be attributed to the lack of modelling inputs that represents mechanisms responsible for storm-time ionospheric responses. Different mechanisms at play even during the same storm period over different latitude regions may be the reason why models 1 and 2 fail to capture both the magnitude and dynamics for some storms. Therefore other potential inputs to TEC modelling could include electric field information from both prompt penetration and ionospheric disturbance dynamo, and thermospheric composition changes which could be represented by O/N_2 ratio. These storm-related mechanisms have some associated challenges in terms of quantitatively representing them in TEC modelling. For-example, for African low/equatorial latitudes, the current available way of getting an idea about electric field varitions is through the differential magnetometer approach where magnetometer measurements are used for locations at the magnetic equator and one displaced by roughly $6° - 9°$ away (Anderson *et al.*, 2004; Yizengaw *et al.*, 2012). This technique is only applicable during local daytime. Some magnetometer data for applying this method are simultaneously available over Addis Ababa, AAE (0.2°N,110.5°E, geomagnetic) and Adigrat, ETHI (6.0°N,111.1°E, geomagnetic) only during 2008 - 2013 which is a smaller portion of the period (2001 - 2015) used in our TEC modelling. Additionally, 2008 - 2013 had few geomagnetic storms as it mostly consisted of low solar activity period. With regard to thermospheric composition changes, it has been reported that the variability of O/N_2 ratio agrees with TEC changes during geomagnetic storms over the African region using the Global Ultraviolet Imager and GPS TEC data (e.g., Habarulema *et al.*, 2013). However, satellite data does not provide the required continuous data coverage to be included in single station/longitude modelling, in addition to its limitation in the time resolution covered by TEC models. The alternative for O/N_2 ratio inclusion would be the investigation of outputs from empirical approaches such as the NRLMSISE-00 model of the atmosphere (Picone *et al.*, 2002). Such empirical approaches require validation over the African region with actual data (which is non-existent according to our knowledge). Nevertheless, these sources will be investigated in future TEC modelling.

6.5 Summary and conclusions

This chapter evaluated the performance of ANN models in the African low and mid-latitude regions. It also investigated for the first time, the role of meridional neutral winds to storm-time TEC modelling. Statistically, it was shown that TEC modelling is more difficult for low latitude compared to mid-latitude region. Inclusion of the meridional wind velocity in TEC modelling during geomagnetic storms led to percentage improvements of about 10 % (northern hemisphere mid-latitude), 5 % (low latitude) and 5 % (southern hemisphere mid-latitude), for RABT/TETN, MBAR/MAL2 and SUTH/HRAO, respectively. These improvements in modelling results may be attributed, on one hand, to the storm-induced surges in meridional winds due to an increase in energy (Joule heating and particle precipitation) at high latitudes during the storm periods; on the other hand, to inter-hemispheric blows of the meridional winds across the magnetic equator, from summer to winter hemisphere. However, the lack of knowledge of the main drivers of some storms may have contributed to the failure of the models for some storm periods. These include the "superfountain" effect and prompt penetrating electric fields (PPEF) (Tsurutani *et al.*, 2004), large-scale traveling ionospheric disturbances (Borries *et al.*, 2009), as well as changes in neutral composition (Prölss, 1980).

Chapter 7

General conclusions and future work

In this study, several methods to model TEC at times of geomagnetic storms are tried, and attempts to identify the best method are made. The developed models were based on empirical orthogonal functions (EOF) analysis and non-linear regression analysis (NLRA), with the least squares method and Metropolis-Hastings Algorithm (MHA) as optimization techniques. Artificial neural networks (ANNs) and the International Reference Ionosphere (IRI) models were also applied to TEC modelling and their performances were evaluated and compared with the performances of the developed analytical models. Also employed for storm-TEC reconstruction along different African latitudinal regions, was the Multi-Instrument Data Analysis System (MIDAS) inversion algorithm. The observational TEC data that were used to develop and validate storm-time TEC models were derived from GPS measurements over African stations and surrounding areas, the storm criterion being $Dst \leqslant -50$ nT and/or $K_p \geqslant 4$. Thus, this study was based only on storm-time TEC data for both the development and validation of the models. General observations and findings are summarised in the next section.

7.1 Conclusions

Since solar radiation is the main driver of ionospheric variability, the contribution of each of the solar activity indices, $F10.7p$, $F10.7$ and SSN, to storm-time TEC modelling over the mid-latitude station, Hermanus, (HNUS, 34.40° S, 19.22° E geographic; 42.33° S, 82.15° E geomagnetic), South Africa, was simultaneously evaluated for the first time. The task was accomplished by training ANN models (hereafter named MF107p, MF107, and MSSN) which differed from each other by the type of solar index used as input. It was found that more accurate storm-time TEC modelling results can be achieved when $F10.7p$ is used as the solar proxy. This finding agrees with statistical results reported by Liu *et al.* (2006); Liu & Chen (2009) in which the superiority of $F10.7p$ over $F10.7$ as representing the solar activity was highlighted. The performance evaluation of MF107p, MF107, and MSSN, compared with a NLRA model developed at the same location, and whose coefficients were found using the MHA, shows that the latter is about 8.00 %, 5.00 %, and 5.00 % better than MSSN, MF107, and MF107p models, respectively. Thus, NLRA complemented with MHA can be used to model TEC during storm conditions and achieve fair results. With its advantage of providing the error bar for each estimated coefficient, MHA is a better technique for finding unknown coefficients of analytical expressions when compared with regression analysis (RA) since the ranges of the MHA estimates covers the RA estimates. However, the intensive computation of the MHA technique requires high-performance computing facilities. This posed a big challenge and was the reason for adopting the ANN model for most of this work.

A statistical evaluation of the capability of MIDAS compared with ANNs to reconstruct storm-time TEC over the African low and mid-latitude regions, showed that MIDAS and ANNs provide comparable results with respective MAE values of 4.81 and 4.18 TECU. It was further found that, on average, the ANN model is 24.37 % better than MIDAS at estimating storm-time TEC over low latitudes, while MIDAS is 13.44 % more accurate than ANN in mid-latitude. MIDAS, however, captures short-term variations of the observed TEC and follows enhancements and depletions observed during geomagnetic storms more accurately than ANNs. Compared with the IRI model, both MIDAS and the ANN model were found to provide more accurate storm-time TEC reconstructions than the IRI model for African low and mid-latitude regions (Uwamahoro *et al.*, 2018a). It was proven statistically that TEC reconstruction/modelling is more difficult for the low latitude than the mid-latitude ionosphere as previously reported in different literatures (Chartier *et al.*, 2014; Kumar *et al.*, 2015; Panda *et al.*, 2015). Complex low-latitude electrodynamic mechanisms such as the fountain effect and the resulting higher TEC gradients are among the reasons why it is difficult to reconstruct/model TEC for low latitude region. The intensity of the storm does not seem to have an impact on storm-time TEC modelling. MIDAS, ANNs, and IRI were found to reconstruct storm-time TEC more accurately for severe storms (e.g., 16 - 22 March 2015) than strong storms (e.g., 18 - 24 February 2014) (Uwamahoro *et al.*, 2018a).

On a basis of statistical analysis, a comparative study of the performances of EOF, NLRA, ANN, and IRI models to predict TEC during geomagnetic storm conditions over various latitudes was carried out. From high to low accuracy, the evaluated models are classified as follows: ANNs, EOF, NLRA, and IRI. Considering GPS TEC as a reference for statistical computations, results showed that ANN model is about 10 %, 26 %, and 58 % more accurate than EOF, NLRA, and IRI models, respectively, while EOF was found to perform 15 %, and 44 % better than NLRA and IRI, respectively. It was further found that the accuracy of NLRA model is 25 % higher than that of the IRI model (Uwamahoro *et al.*, 2019). The reason for the IRI model inaccuracy to estimate TEC during geomagnetic storms as the other models, can be partly attributed to the fact that IRI is based on monthly median values (climatological model) and the integration of electron density profiles is performed between the altitude range 60 - 2000 km (Bilitza *et al.*, 2014; Kenpankho *et al.*, 2011; Chartier *et al.*, 2012; Habarulema & Ssessanga, 2017). Thus, the plasmaspheric contribution is not taken into account fully in the IRI model, while other models were developed based of storm-time TEC data obtained along the line of sight extended from GPS receivers on the ground up to GPS altitude of about 20,200 km. The superiority of ANN model with respect to other modelling techniques, followed by EOF, NLRA, and then IRI model, was also noticed when performing a statistical analysis referring to background ionosphere represented by monthly median (MM) TEC values (Uwamahoro *et al.*, 2019). It can thus be concluded that the ANN model is more accurate storm-time TEC estimation when compared to other models examined in this study. The greatest errors were generally observed at the locations of both crests of the EIA and at the magnetic equator, and then at mid-latitude locations. It can thus be reconfirmed that storm-time TEC modelling is more difficult for low and equatorial latitudes than for the mid-latitude.

This study also investigated, for the first time, the role of the meridional neutral winds (from the HWM) in storm-time TEC modelling for the low latitude, northern and southern hemisphere mid-latitude regions of the African sector, based on ANN models. Statistics have shown that the inclusion of the meridional wind velocity in TEC modelling during geomagnetic storms lead to percentage improvements of about 5 % for the low latitude, 10 % and 5 % for the northern and southern hemisphere mid-latitude regions, respectively. The storm-induced surges in meridional winds due to an increase in energy (Joule heating and particle precipitation) at high latitudes during the storm periods, and the inter-hemispheric meridional winds across the magnetic equator from summer to winter hemisphere, may be the main reasons for the improvements obtained when meridional wind velocity was included in storm-time TEC modelling (Uwamahoro *et al.*, 2018b). Since the meridional wind velocity was obtained from the HWM, further studies that use actual data are required for accurate evaluation of the contribution of neutral winds to storm-time ionospheric modelling.

In light of the fact that each latitudinal region has its own challenges in terms of modelling, it is suggested that for a regional/global model development it would be better to develop individual regional models for different latitudinal regions within the region of interest and then combine them into a regional/global model.

7.2 Future work

Although some efforts have been made towards the improvement of TEC modelling for storm conditions, further work toward accurate storm-time ionospheric modelling is still a research priority. The challenge of storm-time modelling may be due to insufficient knowledge about the mechanisms that drive the storms, and lack of inputs that may accurately represent them. Different mechanisms at play even during the same storm period over different latitudinal regions may be another contributing factor to the failure of storm-time TEC models to capture both the magnitude and dynamics of some storms. The solution to this problem for the space weather community, may be approached by considering both mathematical approaches/optimization techniques that may lead to more accurate models, and by introducing new representations of storm driven-mechanisms.

With regard to the first suggestion, the exploration of advanced optimization algorithms and more sophisticated modelling platforms such as deep learning and the Kalman filtering data assimilation method, could be beneficial to storm-time TEC modeling.

Some of the driving mechanisms of ionospheric responses due to geomagnetic storms are well-known and documented. These include the prompt penetrating electric fields (PPEF) and the "superfountain" or enhanced fountain effect (e.g., Tsurutani *et al.*, 2004), neutral winds (e.g., Titheridge, 1995a,b), large-scale travelling ionospheric disturbances (e.g., Borries *et al.*, 2009), and changes in neutral composition (e.g., Prölss, 1980). Future plans include the representation of thermospheric composition changes by O/N_2 ratio from the NRLMSISE-00 empirical model of the atmosphere (Picone *et al.*, 2002). As more data becomes available, the low-latitude vertical drift velocities could also be included in storm-time ionospheric modelling in the sense that the fountain or superfountain effect may be represented in storm-time ionosphere modelling specifically for the low latitude region.

Apart from including in ionospheric modelling parameters representing some of the mechanisms responsible for ionospheric responses due to geomagnetic storms, another potential input could be the energy transferred by the solar wind into the magnetosphere during storms (ongoing work). The energy coupling function of Akasofu defined by equation (3.36), was used to compute the energy per unit time (power) that is transferred by the solar wind into the magnetosphere during storms. The computed energy for negative and positive storms of 19 - 23 December 2015 and 09 - 11 September 2017 for Hartebeesthoek (HRAO, 25.89° S, 27.68° E), South Africa, is shown in figure 7.1, along with TEC and geomagnetic indices.

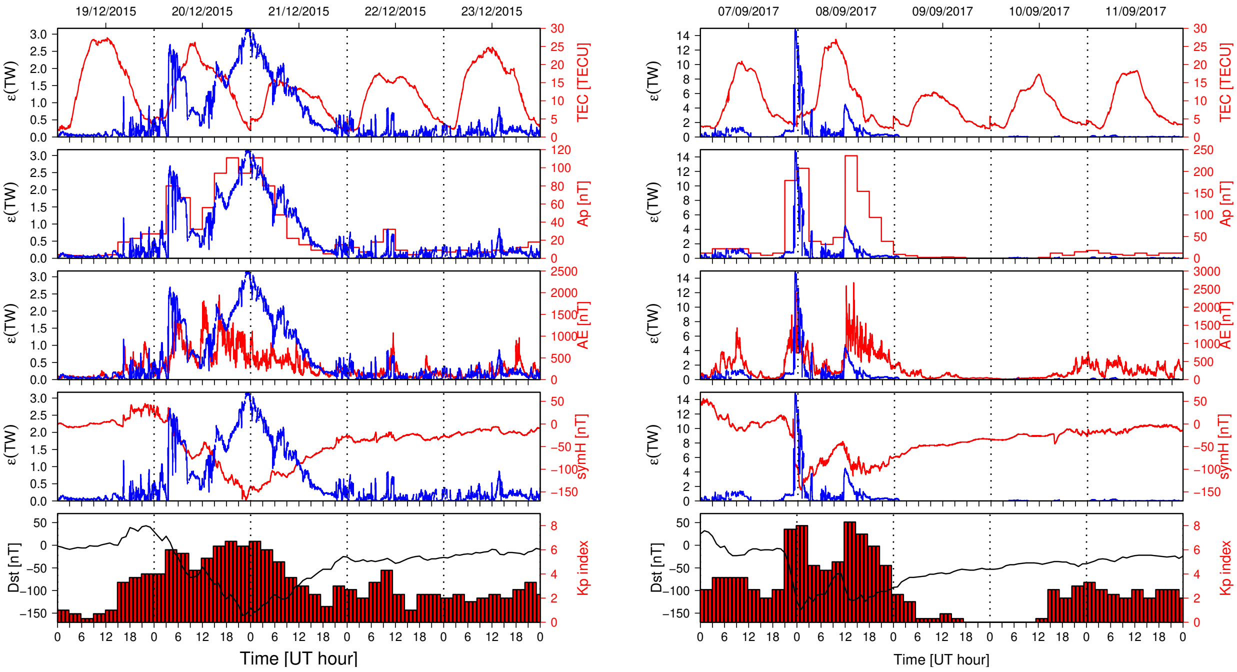

(a) Storm period of 19 - 23 December 2015.

(b) Storm period of 07 - 11 September 2017.

Figure 7.1: Comparison of the energy input by the solar wind into the magnetosphere, along with TEC and geomagnetic indices for the negative and positive storms of 19 - 23 December 2015 and 09 - 11 September 2017 for Hartebeesthoek (HRAO, 25.89° S, 27.68° E), South Africa.

For the storm period 19 - 23 December 2015 (minimum Dst index of -155 nT), the correlation coefficients between the computed energy with geomagnetic indices are 0.64 (AE), 0.89 (A_p), and -0.78 ($symH$), while for the 07 - 11 September 2017 (minimum Dst index of -124 nT), they are 0.48 , 0.56, -0.38 for AE, A_p, and $symH$, respectively. For some storms (e.g., 19 - 23 December 2015), there is thus some hope that storm-time modelling results may be improved when the solar wind energy input into magnetosphere is taken into account. It is, however, worth noting that when the energy is transferred into the magnetosphere at time t, the ionosphere will respond some time later at $t + \tau$. The challenge is the computation of the elapsed time τ which differs from storm to another since the response of the ionosphere to a specific geomagnetic storm depends on the time of onset of the storm, the storm intensity, season, solar activity, and location (Prölss, 1980; Ngwira *et al.*, 2012b). Therefore, the computation of τ should be done by first classifying the storms into different categories based on its time of onset, intensity, season, location, and solar activity period, and then apply a cross-correlation function to each category to find the maximum lag between TEC and the energy. The results of this ongoing work will probably be available in the future.

One aspect of modeling is that modelling inputs can be changed and this facilitates to explore the importance of a given parameter and understand individual mechanisms. As the meridional neutral wind model gives both magnitude and direction, it will be useful in the future to explore both components and focus on individual days instead of storm intervals. It will also be important to evaluate how the change in magnitude of the neutral wind velocity affects modelling results.

Another aspect of difficulty of modeling storms is that the UT of the SSC can have an impact on the dayside response. For example, if the SSC hits at noon LT, the response at other local times during the daytime is different since the lag between the day and SSC is variable. The effect of the SSC on dayside response in storm-time TEC modelling will be investigated in future.

Bibliography

Abe, O., Villamide, X.O., Paparini, C., Radicella, S., Nava, B. & Rodríguez-Bouza, M. (2017). Performance evaluation of GNSS-TEC estimation techniques at the grid point in middle and low latitudes during different geomagnetic conditions. *Journal of Geodesy*, **91**, 409–417.

Acharya, R., Roy, B., Sivaraman, M. & Dasgupta, A. (2011). Prediction of ionospheric total electron content using adaptive neural network with in-situ learning algorithm. *Advances in Space Research*, **47**, 115–123.

Adewale, A., Oyeyemi, E., Adeniyi, J., Adeloye, A. & Oladipo, O. (2011). Comparison of total electron content predicted using the IRI-2007 model with GPS observations over Lagos, Nigeria. *Indian Journal of Radio & Space Physics*, **40**, 21–25.

Akala, A., Seemala, G., Doherty, P., Valladares, C., Carrano, C., Espinoza, J. & Oluyo, S. (2013). Comparison of equatorial GPS-TEC observations over an African station and an American station during the minimum and ascending phases of solar cycle 24. *Annales Geophysicae*, **31**, 2085–2096.

Akasofu, S.I. (1981). Energy coupling between the solar wind and the magnetosphere. *Space Science Reviews*, **28**, 121–190.

Akasofu, S.I. (2007). *Exploring the Secrets of the Aurora, 2nd ed.*. Springer Science & Business Media, New York.

Akeret, J., Seehars, S., Amara, A., Refregier, A. & Csillaghy, A. (2013). CosmoHammer: Cosmological parameter estimation with the MCMC Hammer. *Astronomy and Computing*, **2**, 27–39.

Anderson, D. & Klobuchar, J. (1983). Modeling the total electron content observations above Ascension Island. *Journal of Geophysical Research: Space Physics*, **88**, 8020–8024.

Anderson, D., Anghel, A., Chau, J. & Veliz, O. (2004). Daytime vertical E × B drift velocities inferred from ground-based magnetometer observations at low latitudes. *Space Weather*, **2**.

Anderson, D., Anghel, A., Chau, J., Yumoto, K., Bhattacharyya, A. & Alex, S. (2006). *Daytime, low latitude, vertical E × B drift velocities, inferred from ground-based magnetometer observations in the Peruvian, Philippine and Indian longitude sectors under quiet and disturbed conditions*. ILWS Workshop, Goa, India.

Appleton, E.V. (1946). Two anomalies in the ionosphere. *Nature*, **157**, 691.

Araujo-Pradere, E. (2005). GPS-derived total electron content response for the Bastille Day magnetic storm of 2000 at a low mid-latitude station. *Geofísica Internacional*, **44**, 211–218.

Astafyeva, E., Zakharenkova, I. & Förster, M. (2015). Ionospheric response to the 2015 St. Patrick's Day storm: A global multi-instrumental overview. *Journal of Geophysical Research: Space Physics*, **120**, 9023–9037.

Bagiya, M.S., Joshi, H., Iyer, K., Aggarwal, M., Ravindran, S. & Pathan, B. (2009). TEC variations during low solar activity period (2005-2007) near the Equatorial Ionospheric Anomaly crest region in India. *Annales Geophysicae*, **27**, 1047–1057.

Balan, N., Otsuka, Y., Nishioka, M., Liu, J. & Bailey, G. (2013). Physical mechanisms of the ionospheric storms at equatorial and higher latitudes during the recovery phase of geomagnetic storms. *Journal of Geophysical Research: Space Physics*, **118**, 2660–2669.

Ballatore, P. & Maclennan, C. (1999). Significance of the high-latitude geomagnetic index AES-80: comparison with the PC index. *Earth, Planets and Space*, **51**, 425–430.

Bartels, J., Heck, N., & Johnston, H. (1939). The three-hour-range index measuring geomagnetic activity. *Terrestrial Magnetism and Atmospheric Electricity*, **44**, 411–454.

Baumjohann, W., Treumann, R.A. & Treumann, R.A. (1997). *Basic Space Plasma Physics*, vol. 57. Imperial College Press, London.

Bhattacharyya, A., Abdu, M.A. & Pancheva, D. (2011). *Aeronomy of the Earth's Atmosphere and Ionosphere*, vol. 2. Springer, New York.

Bhonsle, R., da Rosa, A. & Garriott, O. (1965). Measurements of the total electron content and the equivalent slab thickness of the midlatitude ionosphere. *Radio Science Journal of Research NBS/USNC-URSI*, **69D**.

Bilitza, D. (2001). International reference ionosphere 2000. *Radio Science*, **36**, 261–275.

Bilitza, D. (2003). International reference ionosphere 2000: examples of improvements and new features. *Advances in Space Research*, **31**, 757–767.

Bilitza, D. (2004). A correction for the IRI topside electron density model based on Alouette/ISIS topside sounder data. *Advances in Space Research*, **33**, 838–843.

Bilitza, D. (2009). Evaluation of the IRI-2007 model options for the topside electron density. *Advances in Space Research*, **44**, 701–706.

Bilitza, D. (2014). The international reference ionosphere: Rawer's IRI and its status today. *Advances in Radio Science*, **12**, 231–236.

Bilitza, D. (2017). *International Reference Ionosphere - Introduction and Open Problems*. COSPAR and URSI, Department of Physics and Astronomy, George Mason University, Fairfax, Virginia, USA.

Bilitza, D. & Reinisch, B.W. (2008). International reference ionosphere 2007: improvements and new parameters. *Advances in Space Research*, **42**, 599–609.

Bilitza, D., Rawer, K. & Pallaschke, S. (1988). Study of ionospheric models for satellite orbit determination. *Radio Science*, **23**, 223–232.

Bilitza, D., McKinnell, L.A., Reinisch, B. & Fuller-Rowell, T. (2011). The international reference ionosphere today and in the future. *Journal of Geodesy*, **85**, 909–920.

Bilitza, D., Altadill, D., Zhang, Y., Mertens, C., Truhlik, V., Richards, P., McKinnell, L.A. & Reinisch, B. (2014). The International Reference Ionosphere 2012 – a model of international collaboration. *Journal of Space Weather and Space Climate*, **4**, A07.

Bilitza, D., Altadill, D., Truhlik, V., Shubin, V., Galkin, I., Reinisch, B. & Huang, X. (2017). International reference ionosphere 2016: from ionospheric climate to real-time weather predictions. *Space Weather*, **15**, 418–429.

Björnsson, H. & Venegas, S.A. (1997). *A Manual for EOF and SVD Analysis of Climatic Data*. Center of Climate and Global Change Research, Montreal.

Blanc, M. & Richmond, A. (1980). The ionospheric disturbance dynamo. *Journal of Geophysical Research: Space Physics*, **85**, 1669–1686.

Borovsky, J.E. & Denton, M.H. (2006). Differences between CME-driven storms and CIR-driven storms. *Journal of Geophysical Research: Space Physics*, **111**, A07S08.

Borre, K., Akos, D.M., Bertelsen, N., Rinder, P. & Jensen, S.H. (2007). *A software-defined GPS and Galileo receiver: a single-frequency approach*. Springer Science & Business Media, New York.

Borries, C., Jakowski, N. & Wilken, V. (2009). Storm induced large scale TIDs observed in GPS derived TEC. *Annales Geophysicae*, **27**, 1605–1612.

Borries, C., Mahrous, A.M., Ellahouny, N.M. & Badeke, R. (2016). Multiple ionospheric perturbations during the Saint Patrick's Day storm 2015 in the European-African sector. *Journal of Geophysical Research: Space Physics*, **121**.

Boyd, J.D., Kennelly, E.P. & Pistek, P. (1992). *Estimation of EOF Expansion Coefficients from Incomplete Data*. Technical note 29, Naval Oceanographic and Atmospheric Research Laboratory, Mississippi.

Bremner, S. (2009). *Analysing Transient Effects in the Ionosphere Using Narrowband VLF Data*. Master's thesis, University of KwaZulu-Natal, Westville.

Bretthorst, G.L. (1988). *Bayesian Spectrum Analysis and Parameter Estimation*. Springer-Verlag, Berlin.

Buonsanto, M., Salah, J., Miller, K., Oliver, W., Burnside, R. & Richards, P. (1989). Observations of neutral circulation at mid-latitudes during the Equinox Transition Study. *Journal of Geophysical Research: Space Physics*, **94**, 16987–16997.

Buonsanto, M.J. (1999). Ionospheric storms - a review. *Space Science Reviews*, **88**, 563–601.

Burešová, D. & Laštovička, J. (2007). Pre-storm enhancements of foF2 above Europe. *Advances in Space Research*, **39**, 1298–1303.

Bust, G., Crowley, G., Garner, T., Gaussiran, T., Meggs, R.W., Mitchell, C.N., Spencer, P.S., Yin, P. & Zapfe, B. (2007). Four-dimensional GPS imaging of space weather storms. *Space Weather*, **5**, S02003.

Campbell, W.H. (1996). Geomagnetic storms, the dst ring-current myth and lognormal distributions. *Journal of Atmospheric and Terrestrial Physics*, **58**, 1171–1187.

Cander, L.R. (1998). Artificial neural network applications in ionospheric studies. *Annals of Geophysics*, **41**.

Cander, L.R. (2015). Forecasting foF2 and MUF (3000) F2 ionospheric characteristics – A challenging space weather frontier. *Advances in Space Research*, **56**, 1973–1981.

Carrano, C. & Groves, K. (2009). Ionospheric data processing and analysis. In *Workshop on Satellite Navigation Science and Technology for Africa, The Abdus Salam ICTP, Trieste, Italy, 23 March - 09 April 2009*, `https://www2.bc.edu/charles-carrano/carrano-trieste-2009.pelf`.

Chartier, A.T., Mitchell, C.N. & Jackson, D.R. (2012). A 12 year comparison of MIDAS and IRI 2007 ionospheric Total Electron Content. *Advances in Space Research*, **49**, 1348–1355.

Chartier, A.T., Kinrade, J., Mitchell, C.N., Rose, J.A., Jackson, D.R., Cilliers, P., Habarulema, J.B., Katamzi, Z., McKinnell, L.A., Matamba, T. *et al.* (2014). Ionospheric imaging in Africa. *Radio Science*, **49**, 19–27.

Chatterjee, S. & Hadi, A.S. (2013). *Regression Analysis by Example, 4th ed.*. John Wiley & Sons, Hoboken, New Jersey.

Chauhan, V., Singh, O. & Singh, B. (2011). Diurnal and seasonal variation of GPS-TEC during a low solar activity period as observed at a low latitude station agra. *Indian Journal of Radio & Space Physics*, **40**, 26–36.

Chen, F.F. (1984). *Introduction to Plasma Physics and Controlled Fusion, volume 1: Plasma Physics*. Plenum Press, New York.

Chen, Y., Liu, L. & Wan, W. (2011). Does the F10.7 index correctly describe solar EUV flux during the deep solar minimum of 2007–2009? *Journal of Geophysical Research: Space Physics*, **116**, A04304.

Chen, Z., Zhang, S.R., Coster, A.J. & Fang, G. (2015). EOF analysis and modeling of GPS TEC climatology over north America. *Journal of Geophysical Research: Space Physics*, **120**, 3118–3129.

Christensen, N., Meyer, R., Knox, L. & Luey, B. (2001). Bayesian methods for cosmological parameter estimation from Cosmic Microwave Background measurements. *Classical and Quantum Gravity*, **18**, 2677.

Christensen, N., Meyer, R. & Libson, A. (2003). A Metropolis-Hastings routine for estimating parameters from compact binary inspiral events with laser interferometric gravitational radiation data. *Classical and Quantum Gravity*, **21**, 317.

Ciraolo, L., Azpilicueta, F., Brunini, C., Meza, A. & Radicella, S. (2007). Calibration errors on experimental slant total electron content (TEC) determined with GPS. *Journal of Geodesy*, **81**, 111–120.

Codrescu, M., Fuller-Rowell, T., Munteanu, V., Minter, C. & Millward, G. (2008). Validation of the coupled thermosphere ionosphere plasmasphere electrodynamics model: CTIPe-Mass Spectrometer Incoherent scatter temperature comparison. *Space Weather*, **6**.

Coïsson, P., Radicella, S., Leitinger, R. & Nava, B. (2006). Topside electron density in IRI and NeQuick: Features and limitations. *Advances in Space Research*, **37**, 937–942.

Crawford, F.S. (1968). *Waves*. Mc Graw-Hill, New York.

Dabbakuti, J.K. & Ratnam, D.V. (2017). Modeling and analysis of GPS-TEC low latitude climatology during the 24th solar cycle using empirical orthogonal functions. *Advances in Space Research*, **60**, 1751–1764.

Dabbakuti, J.K., Devanaboyina, V.R. & Kanchumarthi, S.R. (2016). Analysis of local ionospheric variability based on SVD and MDS at low-latitude GNSS stations. *Earth, Planets and Space*, **68**, 94.

Danilov, A. & Lastovicka, J. (2001). Effects of geomagnetic storms on the ionosphere and atmosphere. *International Journal of Geomagnetism and Aeronomy*, **2**, 209–224.

Darrouzet, F., de Keyser, J. & Pierrard, V. (2009). *The Earth's Plasmasphere: A Cluster and IMAGE Perspective*. Springer Science & Business Media, Brussels, Belgium.

Davies, K. (1990). *Ionospheric Radio*. Peter Peregrinus, London, United Kingdom.

Davis, T.N. & Sugiura, M. (1966). Auroral electrojet activity index AE and its universal time variations. *Journal of Geophysical Research*, **71**, 785–801.

De Michelis, P., Tozzi, R. & Consolini, G. (2010). Principal components' features of mid-latitude geomagnetic daily variation. *Annales Geophysicae*, **28**, 2213–2226.

Dear, R.M. & Mitchell, C.N. (2006). GPS interfrequency biases and total electron content errors in ionospheric imaging over Europe. *Radio Science*, **41**, RS6007.

Denton, M.H., Borovsky, J.E., Skoug, R., Thomsen, M., Lavraud, B., Henderson, M., McPherron, R., Zhang, J.C. & Liemohn, M. (2006). Geomagnetic storms driven by ICME- and CIR-dominated solar wind. *Journal of Geophysical Research: Space Physics*, **111**, A07S07.

Doherty, P., Coster, A.J. & Murtagh, W. (2004). Space weather effects of October–November 2003. *GPS Solutions*, **8**, 267–271.

Doran, M. & Müller, C.M. (2004). Analyse this! A cosmological constraint package for CMBEASY. *Journal of Cosmology and Astroparticle Physics*, **2004**, 003.

Drob, D., Emmert, J., Crowley, G., Picone, J., Shepherd, G., Skinner, W., Hays, P., Niciejewski, R., Larsen, M., She, C. *et al.* (2008). An empirical model of the Earth's horizontal wind fields: HWM07. *Journal of Geophysical Research: Space Physics*, **113**.

Drob, D.P., Emmert, J.T., Meriwether, J.W., Makela, J.J., Doornbos, E., Conde, M., Hernandez, G., Noto, J., Zawdie, K.A., McDonald, S.E. *et al.* (2015). An update to the Horizontal Wind Model (HWM): the quiet time thermosphere. *Earth and Space Science*, **2**, 301–319.

Dunkley, J., Bucher, M., Ferreira, P.G., Moodley, K. & Skordis, C. (2005). Fast and reliable Markov Chain Monte Carlo technique for cosmological parameter estimation. *Monthly Notices of the Royal Astronomical Society*, **356**, 925–936.

Emmert, J., Fejer, B.G., Shepherd, G. & Solheim, B. (2002). Altitude dependence of middle and low-latitude daytime thermospheric disturbance winds measured by WINDII. *Journal of Geophysical Research: Space Physics*, **107**.

Emmert, J., Drob, D., Shepherd, G., Hernandez, G., Jarvis, M.J., Meriwether, J., Niciejewski, R., Sipler, D. & Tepley, C. (2008). DWM07 global empirical model of upper thermospheric storm-induced disturbance winds. *Journal of Geophysical Research: Space Physics*, **113**.

England, S., Maus, S., Immel, T. & Mende, S. (2006). Longitudinal variation of the E-region electric fields caused by atmospheric tides. *Geophysical Research Letters*, **33**.

Ercha, A., Zhang, D.H., Xiao, Z., Hao, Y.Q., Ridley, A.J. & Moldwin, M. (2011). Modeling ionospheric foF2 by using empirical orthogonal function analysis. *Annales Geophysicae*, **29**, 1501–1515.

Ercha, A., Zhang, D., Ridley, A.J., Xiao, Z. & Hao, Y. (2012). A global model: empirical orthogonal function analysis of total electron content 1999 – 2009 data. *Journal of Geophysical Research: Space Physics*, **117**, A03328.

Ercha, A., Huang, W., Yu, S., Liu, S., Shi, L., Gong, J., Chen, Y. & Shen, H. (2015). A regional ionospheric TEC mapping technique over China and adjacent areas on the basis of data assimilation. *Journal of Geophysical Research: Space Physics*, **120**, 5049–5061.

Erdogan, E., Schmidt, M., Seitz, F. & Durmaz, M. (2017). Near real-time estimation of ionosphere vertical total electron content from GNSS satellites using B-splines in a Kalman filter. *Annales Geophysicae*, **35**, 263–277.

Fagundes, P.R., Abalde, J., Bittencourt, J., Sahai, Y., Francisco, R., Pillat, V. & Lima, W. (2009). F layer postsunset height rise due to electric field prereversal enhancement: 2. Traveling planetary wave ionospheric disturbances and their role on the generation of equatorial spread F. *Journal of Geophysical Research: Space Physics*, **114**.

Farley, D., Bonelli, E., Fejer, B.G. & Larsen, M. (1986). The prereversal enhancement of the zonal electric field in the equatorial ionosphere. *Journal of Geophysical Research: Space Physics*, **91**, 13723–13728.

Farrell, J. & Barth, M. (1999). *The Global Positioning System & Inertial Navigation*. McGraw-Hill, New York.

Fausett, L. (1994). *Fundamentals of Neural Networks: Architectures, Algorithms, and Applications*. Prentice-Hall, Upper Saddle River, New Jersey.

Fedrizz, M., Fuller-Rowell, T., Maruyama, N., Codrescu, M. & Khalsa, H. (2008). Sources of f-region height changes during geomagnetic storms at mid latitudes. *Geophysical monograph*, **181**, 247–258.

Fejer, B.G., Farley, D., Woodman, R. & Calderon, C. (1979). Dependence of equatorial F region vertical drifts on season and solar cycle. *Journal of Geophysical Research: Space Physics*, **84**, 5792–5796.

Fejer, B.G., Jensen, J., Kikuchi, T., Abdu, M. & Chau, J. (2007). Equatorial ionospheric electric fields during the November 2004 magnetic storm. *Journal of Geophysical Research: Space Physics*, **112**.

Feng, J., Wang, Z., Jiang, W., Zhao, Z. & Zhang, B. (2016). A new regional total electron content empirical model in northeast China. *Advances in Space Research*, **58**, 1155–1167.

Fesen, C., Crowley, G. & Roble, R. (1989). Ionospheric effects at low latitudes during the March 22, 1979, geomagnetic storm. *Journal of Geophysical Research: Space Physics*, **94**, 5405–5417.

Fisher, D.J., Makela, J.J., Meriwether, J.W., Buriti, R.A., Benkhaldoun, Z., Kaab, M. & Lagheryeb, A. (2015). Climatologies of nighttime thermospheric winds and temperatures from Fabry-Perot interferometer measurements: from solar minimum to solar maximum. *Journal of Geophysical Research: Space Physics*, **120**, 6679–6693.

Forbes, J.M. (1989). Evidence for the equatorward penetration of electric fields, winds, and compositional effects in the Asian/Pacific sector during the September 17–24, 1984, ETS interval. *Journal of Geophysical Research: Space Physics*, **94**, 16999–17007.

French, G.T. (1996). *Understanding the GPS: An Introduction to the Global Positioning System: What it is and How it Works*. GeoResearch, Bethesda.

Fuller-Rowell, T., Codrescu, M., Moffett, R. & Quegan, S. (1994). Response of the thermosphere and ionosphere to geomagnetic storms. *Journal of Geophysical Research: Space Physics*, **99**, 3893–3914.

Fuller-Rowell, T., Codrescu, M., Araujo-Pradere, E. & Kutiev, I. (1998). Progress in developing a storm-time ionospheric correction model. *Advances in Space Research*, **22**, 821–827.

Fuller-Rowell, T., Codrescu, M. & Wilkinson, P. (2000). Quantitative modeling of the ionospheric response to geomagnetic activity. *Annales Geophysicae*, **18**, 766–781.

Fuller-Rowell, T., Araujo-Pradere, E., Minter, C., Codrescu, M., Spencer, P., Robertson, D. & Jacobson, A.R. (2006). US-TEC: A new data assimilation product from the Space

Environment Center characterizing the ionospheric total electron content using real-time GPS data. *Radio Science*, **41**, 1–8.

Fuller-Rowell, T.J. & Rees, D. (1980). A three-dimensional time-dependent global model of the thermosphere. *Journal of the Atmospheric Sciences*, **37**, 2545–2567.

Gao, Y. & Liu, Z. (2002). Precise ionosphere modeling using regional GPS network data. *Journal of Global Positioning Systems*, **1**, 18–24.

Gershenson, C. (2003). Artificial neural networks for beginners. arXiv preprint cs/0308031, University of Sussex, Falmer.

Giday, N.M. & Katamzi-Joseph, Z.T. (2018). Performance of MIDAS over East African longitude sector: case study during 4–14 March 2012 quiet to disturbed geomagnetic conditions. *Space Weather*, **16**, 126–137.

Giday, N.M., Katamzi, Z.T. & McKinnell, L.A. (2016). Ionospheric tomography over South Africa: comparison of MIDAS and ionosondes measurements. *Advances in Space Research*, **57**, 245–256.

Gleason, S. & Gebre-Egziabher, D. (2009). *GNSS Applications and Methods*. Artech House, Boston, MA.

Gonzalez, W., Joselyn, J.A., Kamide, Y., Kroehl, H.W., Rostoker, G., Tsurutani, B. & Vasyliunas, V. (1994). What is a geomagnetic storm? *Journal of Geophysical Research: Space Physics*, **99**, 5771–5792.

Goodfellow, I., Bengio, Y., Courville, A. & Bengio, Y. (2016). *Deep learning*. MIT press, `http://www.deeplearningbook.org`.

Gosling, J.T. (1993). The solar flare myth. *Journal of Geophysical Research: Space Physics*, **98**, 18937–18949, doi: `10.1029/93JA01896`.

Griffiths, D.J. (1999). *Introduction to Electrodynamics*. Prentice Hall, Upper Saddle River, New Jersey.

Gurney, K. (1997). *An Introduction to Neural Networks*. UCL Press, London.

Habarulema, J. & McKinnell, L.A. (2012). Investigating the performance of neural network backpropagation algorithms for TEC estimations using South African GPS data. *Annales Geophysicae*, **30**, 857–866.

Habarulema, J.B. & Ssessanga, N. (2017). Adapting a climatology model to improve estimation of ionosphere parameters and subsequent validation with radio occultation and ionosonde data. *Space Weather*, **15**, 84–98.

Habarulema, J.B., McKinnell, L.A. & Cilliers, P.J. (2007). Prediction of global positioning system total electron content using neural networks over South Africa. *Journal of Atmospheric and Solar-Terrestrial Physics*, **69**, 1842–1850.

Habarulema, J.B., McKinnell, L.A., Cilliers, P.J. & Opperman, B.D. (2009a). Application of neural networks to South African GPS TEC modelling. *Advances in Space Research*, **43**, 1711–1720.

Habarulema, J.B., McKinnell, L.A. & Opperman, B.D. (2009b). Towards a GPS-based TEC prediction model for Southern Africa with feed forward networks. *Advances in Space Research*, **44**, 82–92.

Habarulema, J.B., McKinnell, L.A. & Opperman, B.D. (2010). TEC measurements and modelling over Southern Africa during magnetic storms; a comparative analysis. *Journal of Atmospheric and Solar-Terrestrial Physics*, **72**, 509–520.

Habarulema, J.B., McKinnell, L.A. & Opperman, B.D. (2011). Regional GPS TEC modeling; attempted spatial and temporal extrapolation of TEC using neural networks. *Journal of Geophysical Research: Space Physics*, **116**, A04314.

Habarulema, J.B., McKinnell, L.A., Burešová, D., Zhang, Y., Seemala, G., Ngwira, C., Chum, J. & Opperman, B. (2013). A comparative study of TEC response for the African equatorial and mid-latitudes during storm conditions. *Journal of Atmospheric and Solar-Terrestrial Physics*, **102**, 105–114.

Habarulema, J.B., Katamzi, Z.T. & Yizengaw, E. (2015). First observations of poleward large-scale traveling ionospheric disturbances over the African sector during geomagnetic storm conditions. *Journal of Geophysical Research: Space Physics*, **120**, 6914–6929.

Habarulema, J.B., Katamzi, Z.T., Yizengaw, E., Yamazaki, Y. & Seemala, G. (2016). Simultaneous storm time equatorward and poleward large-scale TIDs on a global scale. *Geophysical Research Letters*, **43**, 6678–6686.

Habarulema, J.B., Yizengaw, E., Katamzi-Joseph, Z.T., Moldwin, M.B. & Buchert, S. (2018). Storm time global observations of large-scale TIDs from ground-based and in situ satellite measurements. *Journal of Geophysical Research: Space Physics*, **123**, 711–724.

Hagan, M.T., Demuth, H.B. & Beale, M. (1996). *Neural Network Design*. PWS Publishing Company, Boston, USA.

Hajj, G.A., Wilson, B., Wang, C., Pi, X. & Rosen, I. (2004). Data assimilation of ground GPS total electron content into a physics-based ionospheric model by use of the Kalman filter. *Radio Science*, **39**, RS1S05.

Hajra, R., Chakraborty, S.K., Tsurutani, B.T., DasGupta, A., Echer, E., Brum, C.G., Gonzalez, W.D. & Sobral, J.H.A. (2016). An empirical model of ionospheric total electron content (TEC) near the crest of the equatorial ionization anomaly (EIA). *Journal of Space Weather and Space Climate*, **6**, A29.

Hannachi, A. (2004). *A Primer for EOF Analysis of Climate Data*. Departement of Meteorology, University of Reading, Reading, United Kingdom.

Hannachi, A., Jolliffe, I. & Stephenson, D. (2007). Empirical orthogonal functions and related techniques in atmospheric science: a review. *International Journal of Climatology*, **27**, 1119–1152.

Hastings, W.K. (1970). Monte Carlo sampling methods using Markov chains and their applications. *Biometrika*, **57**, 97–109.

Haykin, S. (1994). *Neural Networks. A Comprehensive Foundation*. Macmillan College Publishing Company, New York.

Hedin, A.E., Spencer, N. & Killeen, T. (1988). Empirical global model of upper thermosphere winds based on Atmosphere and Dynamics Explorer satellite data. *Journal of Geophysical Research: Space Physics*, **93**, 9959–9978.

Hedin, A.E., Biondi, M., Burnside, R., Hernandez, G., Johnson, R., Killeen, T., Mazaudier, C., Meriwether, J., Salah, J.E., Smith, R. *et al.* (1991). Revised global model of thermosphere winds using satellite and ground-based observations. *Journal of Geophysical Research*, **96**, 7657–7688.

Hedin, A.E., Fleming, E., Manson, A., Schmidlin, F., Avery, S., Clark, R., Franke, S., Fraser, G., Tsuda, T., Vial, F. *et al.* (1996). Empirical wind model for the upper, middle and lower atmosphere. *Journal of Atmospheric and Terrestrial Physics*, **58**, 1421–1447.

Hernandez-Pajares, M., Juan, J. & Sanz, J. (1997). Neural network modeling of the ionospheric electron content at global scale using GPS data. *Radio Science*, **32**, 1081–1089.

Hines, C. (1959). An interpretation of certain ionospheric motions in terms of atmospheric waves. *Journal of Geophysical Research*, **64**, 2210–2211.

Ho, C., Wilson, B., Mannucci, A., Lindqwister, U. & Yuan, D. (1997). A comparative study of ionospheric total electron content measurements using global ionospheric maps of GPS, TOPEX radar, and the Bent model. *Radio Science*, **32**, 1499–1512.

Hofmann-Wellenhof, B., Lichtenegger, H. & Collins, J. (1992). *GPS: Theory and Practice*. Springer-Verlag, Vienna.

Holland, S.M. (2016). *Principal Components Analysis (PCA)*. University of Georgia, Athens.

Huang, Y.N. & Cheng, K. (1995). Solar cycle variation of the total electron content around equatorial anomaly crest region in east Asia. *Journal of Atmospheric and Terrestrial Physics*, **57**, 1503–1511.

Huang, Z. & Yuan, H. (2014). Ionospheric single-station tec short-term forecast using rbf neural network. *Radio Science*, **49**, 283–292.

Huba, J., Joyce, G. & Fedder, J. (2000). Sami2 is Another Model of the Ionosphere (SAMI2): a new low-latitude ionosphere model. *Journal of Geophysical Research: Space Physics*, **105**, 23035–23053.

Huttunen, K.E.J., Koskinen, H.E. & Schwenn, R. (2002). Variability of magnetospheric storms driven by different solar wind perturbations. *Journal of Geophysical Research: Space Physics*, **107**.

Jakowski, N., Mayer, C., Hoque, M. & Wilken, V. (2011). Total electron content models and their use in ionosphere monitoring. *Radio Science*, **46**.

Jang, J.S.R., Sun, C.T. & Mizutani, E. (1997). *Neuro-Fuzzy and Soft Computing; A computational approach to learning and machine intelligence*. Prentice-Hall, Upper Saddle River, NJ.

Jayawardena, P., Talini, S., Chartier, A.T., Spencer, P. & Mitchell, C.N. (2016). Imaging the topside ionosphere and plasmasphere with ionospheric tomography using COSMIC GPS TEC. *Journal of Geophysical Research: Space Physics*, **121**, 817–831.

Jewell, J., Levin, S. & Anderson, C. (2004). Application of Monte Carlo algorithms to the Bayesian analysis of the Cosmic Microwave Background. *The Astrophysical Journal*, **609**, 1–14.

Kaab, M., Benkhaldoun, Z., Fisher, D.J., Harding, B., Bounhir, A., Makela, J.J., Laghriyeb, A., Malki, K., Daassou, A. & Lazrek, M. (2017). Climatology of thermospheric neutral winds over oukaïmeden observatory in morocco. **35**, 161.

Kakinami, Y., Chen, C., Liu, J., Oyama, K., Yang, W., Abe, S. *et al.* (2009). Empirical models of total electron content based on functional fitting over Taiwan during geomagnetic quiet condition. **27**, 3321–3333.

Kaplan, E. & Hegarty, C. (2006). *Understanding GPS: Principles and Applications, 2nd ed.*. Artech House, Norwood, MA.

Karavaev, A.V. (2010). *Waves in plasmas generated by a rotating magnetic field and implications to radiation belts*. Ph.D. thesis, University of Maryland, College Park, MD.

Katamzi, Z.T. & Habarulema, J.B. (2013). Traveling ionospheric disturbances observed at South African midlatitudes during the 29–31 October 2003 geomagnetically disturbed period. *Advances in Space Research*, **53**, 48–62.

Kelley, M., Fejer, B.G. & Gonzales, C. (1979). An explanation for anomalous equatorial ionospheric electric fields associated with a northward turning of the interplanetary magnetic field. *Geophysical Research Letters*, **6**, 301–304.

Kelley, M.C. (2009). *The Earth's ionosphere: plasma physics and electrodynamics*, vol. 96. Academic press.

Kenpankho, P., Watthanasangmechai, K., Supnithi, P., Tsugawa, T. & Maruyama, T. (2011). Comparison of GPS TEC measurements with IRI TEC prediction at the equatorial latitude station, Chumphon, Thailand. *Earth, Planets and Space*, **63**, 365–370.

Kinrade, J. (2013). *Ionospheric Imaging and Scintillation Monitoring in the Antarctic and Arctic*. Ph.D. thesis, University of Bath, Bath, United Kingdom.

Kintner, P.M., Coster, A.J., Fuller-Rowell, T., Mannucci, A.J., Mendillo, M. & Heelis, R. (2008). *Midlatitude Ionospheric Dynamics and Disturbances*. Wiley Online Library.

Knox, L., Christensen, N. & Skordis, C. (2001). The age of the universe and the cosmological constant determined from Cosmic Microwave Background anisotropy measurements. *The Astrophysical Journal Letters*, **563**, L95.

Koskinen, H.E. & Tanskanen, E.I. (2002). Magnetospheric energy budget and the epsilon parameter. *Journal of Geophysical Research: Space Physics*, **107**, SMP 42–1 – SMP 42–16.

Kriesel, D. (2005). *A Brief Introduction to Neural Networks*. `www.dkriesel.com`.

Kumar, S., Tan, E.L., Razul, S.G., See, C.M.S. & Siingh, D. (2014). Validation of the IRI-2012 model with GPS-based ground observation over a low-latitude Singapore station. *Earth, Planets and Space*, **66**, 17.

Kumar, S., Tan, E.L. & Murti, D.S. (2015). Impacts of solar activity on performance of the IRI-2012 model predictions from low to mid latitudes. *Earth, Planets and Space*, **67**, 1–17.

Langley, R. (2002). Mapping the low-latitude ionosphere with GPS. *GPS World*, **13**, 41–47.

Le, H., Yang, N., Liu, L., Chen, Y. & Zhang, H. (2016). The latitudinal structure of nighttime ionospheric TEC and its empirical orthogonal functions model over North American sector. *Journal of Geophysical Research: Space Physics*, 963–977.

Leandro, R. & Santos, M. (2007). A neural network approach for regional vertical total electron content modelling. *Studia Geophysica et Geodaetica*, **51**, 279–292.

Lee, W., Kil, H., Kwak, Y.S., Wu, Q., Cho, S. & Park, J. (2011). The winter anomaly in the middle-latitude f region during the solar minimum period observed by the constellation observing system for meteorology, ionosphere, and climate. *Journal of Geophysical Research: Space Physics*, **116**.

Lewis, A. & Bridle, S. (2002). Cosmological parameters from CMB and other data: a Monte Carlo approach. *Physical Review D*, **66**, 103511.

Liddle, A. (2009). Statistical methods for cosmological parameter selection and estimation. *Annual Review of Nuclear and Particle Science*, **59**, 95–114.

Lin, C., Liu, J., Fang, T.W., Chang, P., Tsai, H., Chen, C. & Hsiao, C. (2007). Motions of the equatorial ionization anomaly crests imaged by FORMOSAT-3/COSMIC. *Geophysical Research Letters*, **34**.

Lin, C.H., Richmond, A., Bailey, G., Liu, J.Y., Lu, G. & Heelis, R. (2009). Neutral wind effect in producing a storm time ionospheric additional layer in the equatorial ionization anomaly region. *Journal of Geophysical Research: Space Physics*, **114**.

Lin, J., Yue, X., Zeng, Z., Lou, Y., Shen, X., Wu, Y., Schreiner, W.S. & Kuo, Y.H. (2014). Empirical orthogonal function analysis and modeling of the ionospheric peak height during the years 2002–2011. *Journal of Geophysical Research: Space Physics*, **119**, 3915–3929.

Liu, C., Zhang, M.L., Wan, W., Liu, L. & Ning, B. (2008). Modeling M (3000) F2 based on empirical orthogonal function analysis method. *Radio Science*, **43**, 1003.

Liu, G., Huang, W., Gong, J. & Shen, H. (2013). Seasonal variability of GPS-VTEC and model during low solar activity period (2006–2007) near the equatorial ionization anomaly crest location in Chinese zone. *Advances in Space Research*, **51**, 366–376.

Liu, L. & Chen, Y. (2009). Statistical analysis of solar activity variations of total electron content derived at Jet Propulsion Laboratory from GPS observations. *Journal of Geophysical Research: Space Physics*, **114**, A10311.

Liu, L., Wan, W., Ning, B., Pirog, O. & Kurkin, V. (2006). Solar activity variations of the ionospheric peak electron density. *Journal of Geophysical Research: Space Physics*, **111**, A08304.

Llewellyn, S.K. & Bent, R.B. (1973). Documentation and description of the bent ionospheric model. Tech. rep., Atlantic Science Corporation, Indialantic, Florida.

Loewe, C. & Prölss, G. (1997). Classification and mean behavior of magnetic storms. *Journal of Geophysical Research: Space Physics*, **102**, 14209–14213.

Lu, G., Richmond, A., Roble, R. & Emery, B. (2001). Coexistence of ionospheric positive and negative storm phases under northern winter conditions: a case study. *Journal of Geophysical Research: Space Physics*, **106**, 24493–24504.

Lu, G., Goncharenko, L., Richmond, A., Roble, R. & Aponte, N. (2008). A dayside ionospheric positive storm phase driven by neutral winds. *Journal of Geophysical Research: Space Physics*, **113**, A08304.

Makela, J.J., González, S.A., MacPherson, B., Pi, X., Kelley, M.C. & Sultan, P.J. (2000). Intercomparisons of total electron content measurements using the Arecibo incoherent scatter radar and GPS. *Geophysical research letters*, **27**, 2841–2844.

Mankin, E. (2014). Principal components analysis: a how-to manual for r.

Mannucci, A., Wilson, B., Yuan, D., Ho, C., Lindqwister, U. & Runge, T. (1998). A global mapping technique for GPS-derived ionospheric total electron content measurements. *Radio Science*, **33**, 565–582.

Mannucci, A.J., Wilson, B.D. & Edwards, C.D. (1993). A new method for monitoring the Earth's ionospheric total electron content using the GPS global network. In *Proceedings of the 6th International Technical Meeting of the Satellite Division of The Institute of Navigation (ION GPS 1993)*, 1323–1332, Salt Lake City, UT.

Manoj, C., Maus, S., Lühr, H. & Alken, P. (2008). Penetration characteristics of the interplanetary electric field to the daytime equatorial ionosphere. *Journal of Geophysical Research: Space Physics*, **113**.

Mao, T., Wan, W.X. & Liu, L.B. (2005). An EOF based empirical model of TEC over Wuhan. *Chinese Journal of Geophysics*, **48**, 827–834.

Mao, T., Wan, W., Yue, X., Sun, L., Zhao, B. & Guo, J. (2008). An empirical orthogonal function model of total electron content over China. *Radio Science*, **43**, RS2009.

Maruyama, T. (2007). Regional reference total electron content model over Japan based on neural network mapping techniques. *Annales Geophysicae*, **25**, 2609–2614.

Matamba, T.M. & Habarulema, J.B. (2018). Ionospheric responses to CME-and CIR-driven geomagnetic storms along 30°E – 40°E over the African sector from 2001 to 2015. *Space Weather*, **16**, 538–556.

Matamba, T.M., Habarulema, J.B. & McKinnell, L.A. (2015). Statistical analysis of the ionospheric response during geomagnetic storm conditions over South Africa using ionosonde and GPS data. *Space Weather*, **13**, 536–547.

Matamba, T.M., Habarulema, J.B. & Burešová, D. (2016). Midlatitude ionospheric changes to four great geomagnetic storms of solar cycle 23 in Southern and Northern hemispheres. *Space Weather*, **14**, 1155–1171.

Materassi, M. & Mitchell, C.N. (2005). Imaging of the equatorial ionosphere. *Annals of Geophysics*, **48**, 477–482.

McKinnell, L.A. & Poole, A.W. (2004). Predicting the ionospheric F layer using neural networks. *Journal of Geophysical Research: Space Physics*, **109**, A08308.

McKinnell, L.A., Opperman, B. & Cilliers, P.J. (2007). GPS TEC and ionosonde TEC over Grahamstown, South Africa: First comparisons. *Advances in Space Research*, **39**, 816–820.

McNamara, L. (1985). The use of total electron content measurements to validate empirical models of the ionosphere. *Advances in space research*, **5**, 81–90.

McNamara, L.F. (1991). *The Ionosphere: Communications, Surveillance, and Direction Finding*. Krieger, Malabar, Florida.

Meggs, R.W., Mitchell, C.N. & Howells, V. (2005). Simultaneous observations of the main trough using GPS imaging and the EISCAT radar. *Annales Geophysicae*, **23**, 753–757.

Mendillo, M. (2006). Storms in the ionosphere: Patterns and processes for total electron content. *Reviews of Geophysics*, **44**.

Mengistu, E., Damtie, B., Moldwin, M. & Nigussie, M. (2018). Comparison of GPS-TEC measurements with NeQuick2 and IRI model predictions in the low latitude east african region during varying solar activity period (1998 and 2008–2015). *Advances in Space Research*, **61**, 1456–1475, doi: `10.1016/j.asr.2018.01.009`.

Metropolis, N., Rosenbluth, A.W., Rosenbluth, M.N., Teller, A.H. & Teller, E. (1953). Equation of state calculations by fast computing machines. *The Journal of Chemical Physics*, **21**, 1087–1092.

Meyer-Vernet, N. (2007). *Basics of the Solar Wind*. Cambridge University Press, Cambridge.

Misra, P. & Enge, P. (2006). *Global Positioning System: Signals, Measurements and Performance, 2nd ed.*. Ganga-Jamuna Press, Lincoln, Massachusetts.

Mitchell, C. & Cannon, P. (2002). Multi-Instrument Data Analysis System (MIDAS) Imaging of the Ionosphere. Tech. rep., University of Bath, United Kingdom, report for the United States Air Force European Office of Aerospace Research and Development.

Mitchell, C.N. & Spencer, P.S. (2003). A three-dimensional time-dependent algorithm for ionospheric imaging using GPS. *Annals of Geophysics*, **46**, 687–696.

Moldwin, M. (2008). *An Introduction to Space Weather*. Cambridge University Press, New York.

Muella, M.T., de Paula, E.R., Mitchell, C.N., Kintner, P.M., Paes, R.R. & Batista, I.S. (2011). Tomographic imaging of the equatorial and low-latitude ionosphere over central-eastern Brazil. *Earth,Planets and Space*, **63**, 129–138.

Mukhtarov, P., Andonov, B. & Pancheva, D. (2013a). Global empirical model of TEC response to geomagnetic activity. *Journal of Geophysical Research: Space Physics*, **118**, 6666–6685.

Mukhtarov, P., Pancheva, D., Andonov, B. & Pashova, L. (2013b). Global TEC maps based on GNSS data: 1. empirical background TEC model. *Journal of Geophysical Research: Space Physics*, **118**, 4594–4608.

Muslim, B., Haralambous, H., Oikonomou, C. & Anggarani, S. (2015). Evaluation of a global model of ionospheric slab thickness for foF2 estimation during geomagnetic storm. *Annals of Geophysics*, **58**, A0551.

Namgaladze, A., Förster, M. & Yurik, R.Y. (2000). Analysis of the positive ionospheric response to a moderate geomagnetic storm using a global numerical model. *Annales Geophysicae*, **18**, 461–477.

Negreti, S., Paula, E.R.d., Candido, C.M.N. *et al.* (2017). Total electron content responses to HILDCAAs and geomagnetic storms over South America. *Annales Geophysicae*, **35**, 1309–1326, doi: `10.5194/angeo-35-1309-2017`.

Ngwira, C.M., McKinnell, L.A., Cilliers, P.J. & Coster, A.J. (2012a). Ionospheric observations during the geomagnetic storm events on 24–27 july 2004: Long-duration positive storm effects. *Journal of Geophysical Research: Space Physics*, **117**, A00L02.

Ngwira, C.M., McKinnell, L.A., Cilliers, P.J. & Yizengaw, E. (2012b). An investigation of ionospheric disturbances over South Africa during the magnetic storm on 15 may 2005. *Advances in Space Research*, **49**, 327–335.

Okoh, D., Owolabi, O., Ekechukwu, C., Folarin, O., Arhiwo, G., Agbo, J., Bolaji, S. & Rabiu, B. (2016). A regional GNSS-VTEC model over Nigeria using neural networks: A novel approach. *Geodesy and Geodynamics*, **7**, 19–31.

Olwendo, O., Baki, P., Mito, C. & Doherty, P. (2012). Characterization of ionospheric GPS Total Electron Content (GPS TEC) in low latitude zone over the Kenyan region during a very low solar activity phase. *Journal of Atmospheric and Solar-Terrestrial Physics*, **84**, 52–61.

Oron, S., Dujanga, F. & Ssenyonga, T. (2013). Ionospheric tec variations during the ascending solar activity phase at an equatorial station, uganda. *Indian Journal of Radio & Space Physics*, **42**, 7–17.

Oyeyemi, E.O., McKinnell, L.A. & Poole, A. (2006). Near-real time foF2 predictions using neural networks. *Journal of Atmospheric and Solar-Terrestrial Physics*, **68**, 1807–1818.

Page, D.E. (1973). *Correlated Interplanetary and Magnetospheric Observations*, vol. 42. D. Reidel Publishing Company, Boston, USA.

Panda, S., Gedam, S. & Rajaram, G. (2015). Study of ionospheric TEC from GPS observations and comparisons with IRI and SPIM model predictions in the low latitude anomaly Indian subcontinental region. *Advances in Space Research*, **55**, 1948–1964.

Pawitan, Y. (2001). *In All Likelihood: Statistical Modelling and Inference Using Likelihood*. Oxford University Press, Oxford.

Perreault, P. & Akasofu, S.I. (1978). A study of geomagnetic storms. *Geophysical Journal of the Royal Astronomical Society*, **54**, 547–573.

Perrone, L. & De Franceschi, G. (1998). Solar, ionospheric and geomagnetic indices. *Annali Di Geofisica*, **41**, 843–855.

Picone, J., Hedin, A., Drob, D.P. & Aikin, A. (2002). NRLMSISE-00 empirical model of the atmosphere: Statistical comparisons and scientific issues. *Journal of Geophysical Research: Space Physics*, **107**, SIA 15–1 – SIA 15–16.

Pignalberi, A., Pezzopane, M., Rizzi, R. & Galkin, I. (2017). Effective solar indices for ionospheric modeling: a review and a proposal for a real-time regional IRI. *Surveys in Geophysics*, **39**, 125–167.

Poole, A.W. & McKinnell, L.A. (2000). On the predictability of foF2 using neural networks. *Radio Science*, **35**, 225–234.

Prölss, G. (1980). Magnetic storm associated perturbations of the upper atmosphere: recent results obtained by satellite-borne gas analyzers. *Reviews of Geophysics*, **18**, 183–202.

Radicella, S. & Leitinger, R. (2001). The evolution of the DGR approach to model electron density profiles. *Advances in Space Research*, **27**, 35–40.

Radicella, S.M. (2009). The NeQuick model genesis, uses and evolution. *Annals of Geophysics*, **52**, 417–422.

Ram, S.T., Rao, P.R., Niranjan, K., Prasad, D., Sridharan, R., Devasia, C. & Ravindran, S. (2006). The role of post-sunset vertical drifts at the equator in predicting the onset of VHF scintillations during high and low sunspot activity years. *Annales Geophysicae*, **24**, 1609–1616.

Rama Rao, P.R., Niranjan, K., Prasad, D., Krishna, S.G. & Uma, G. (2006). On the validity of the ionospheric pierce point IPP altitude of 350 km in the Indian equatorial and low-latitude sector. **24**, 2159–2168.

Ratnam, D.V., Sarma, A., Srinivas, V.S. & Sreelatha, P. (2011). Performance evaluation of selected ionospheric delay models during geomagnetic storm conditions in low-latitude region. *Radio Science*, **46**, RS0D08.

Ratnam, D.V., Dinesh, B.V., Tejaswi, B., Kumar, D.P., Ritesh, T., Brahmanadam, P. & Vindhya, G. (2012). TEC prediction model using neural networks over a low latitude GPS station. *International Journal of Soft Computing and Engineering (IJDCE)*, **2**, 517–521.

Rawer, K., Bilitza, D. & Ramakrishnan, S. (1978). Goals and status of the International Reference Ionosphere. *Reviews of Geophysics*, **16**, 177–181.

Richards, P., Fennelly, J. & Torr, D. (1994a). EUVAC: A solar EUV flux model for aeronomic calculations. *Journal of Geophysical Research: Space Physics*, **99**, 8981–8992.

Richards, P., Torr, D., Reinisch, B., Gamache, R. & Wilkinson, P. (1994b). F 2 peak electron density at Millstone Hill and Hobart: comparison of theory and measurement at solar maximum. *Journal of Geophysical Research: Space Physics*, **99**, 15005–15016.

Richmond, A., Ridley, E. & Roble, R. (1992). A thermosphere/ionosphere general circulation model with coupled electrodynamics. *Geophysical Research Letters*, **19**, 601–604.

Ridley, A., Deng, Y. & Toth, G. (2006). The global ionosphere–thermosphere model. *Journal of Atmospheric and Solar-Terrestrial Physics*, **68**, 839–864.

Rishbeth, H. & Garriott, O.K. (1969). *Introduction to Ionospheric Physics*. Academic Press, New York, USA.

Rose, J.A., Watson, R.J., Allain, D.J. & Mitchell, C.N. (2014). Ionospheric corrections for GPS time transfer. *Radio Science*, **49**, 196–206.

Rostoker, G. (1972). Geomagnetic indices. *Reviews of Geophysics*, **10**, 935–950.

Rubino-Martin, J.A., Rebolo, R., Carreira, P., Cleary, K., Davies, R.D., Davis, R.J., Dickinson, C., Grainge, K., Gutierrez, C.M., Hobson, M.P. *et al.* (2003). First results from the Very Small Array–IV. Cosmological parameter estimation. *Monthly Notices of the Royal Astronomical Society*, **341**, 1084–1092.

Saba, M.F., Gonzalez, W. & Clúa de Gonzalez, A. (1997). Relationships between the AE, ap and Dst indices near solar minimum (1974) and at solar maximum (1979). *Annales Geophysicae*, **15**, 1265–1270.

Scherliess, L. & Fejer, B.G. (1997). Storm time dependence of equatorial disturbance dynamo zonal electric fields. *Journal of Geophysical Research: Space Physics*, **102**, 24037–24046.

Scherliess, L. & Fejer, B.G. (1999). Radar and satellite global equatorial F region vertical drift model. *Journal of Geophysical Research: Space Physics*, **104**, 6829–6842.

Schmidt, M., Dettmering, D., Mößmer, M., Wang, Y. & Zhang, J. (2011). Comparison of spherical harmonic and B spline models for the vertical total electron content. *Radio Science*, **46**, 1–8.

Schonfeld, S., White, S., Henney, C., Arge, C. & McAteer, R. (2015). Coronal sources of the solar f10. 7 radio flux. *The Astrophysical Journal*, **808**, 29.

Seemala, G. & Valladares, C. (2011). Statistics of total electron content depletions observed over the South American continent for the year 2008. *Radio Science*, **46**.

Serway, R.A. & Jewett, J.W. (2004). *Physics for Scientists and Engineers, 6th ed.*. Thomson Brooks/Cole, Belmont, CA.

Serway, R.A. & Jewett, J.W. (2010). *Physics for scientists and engineers with modern physics*. Cengage learning, Belmont, CA.

Shlens, J. (2003). *A Tutorial on Principal Component Analysis*. arXiv preprint arXiv:1404.1100, University of California, San Diego, CA.

Singh, R. & Sripathi, S. (2017). Ionospheric response to 22–23 june 2015 storm as investigated using ground-based ionosondes and GPS receivers over india. *Journal of Geophysical Research: Space Physics*, **122**.

Smith, L.I. *et al.* (2002). *A Tutorial on Principal Components Analysis*. Cornell University, Ithaca, NY.

Spencer, P.S. & Mitchell, C.N. (2007). Imaging of fast moving electron-density structures in the polar cap. *Annals of Geophysics*, **50**, 427–434.

Srivastava, N. & Venkatakrishnan, P. (2004). Solar and interplanetary sources of major geomagnetic storms during 1996–2002. *Journal of Geophysical Research: Space Physics*, **109**, A10103.

Stolle, C., Liu, H., Truhlík, V., Lühr, H. & Richards, P. (2011). Solar flux variation of the electron temperature morning overshoot in the equatorial F region. *Journal of Geophysical Research: Space Physics*, **116**, doi: `10.1029/2010JA016235`.

Suhov, Y. & Kelbert, M. (2005). *Probability and Statistics by Example, Volume I. Basic Probability and Statistics*. Cambridge University Press, Cambridge.

Sur, D., Ray, S. & Paul, A. (2015). Role of neutral wind in the performance of artificial neural-network based TEC models at diverse longitudes in the low latitudes. *Journal of Geophysical Research: Space Physics*, **120**, 2316–2332, doi: `10.1002/2014JA020594`.

Sur, D., Haldar, S., Ray, S. & Paul, A. (2017). Response of data-driven artificial neural network-based tec models to neutral wind for different locations, seasons, and solar activity levels from the indian longitude sector. *Journal of Geophysical Research: Space Physics*, **122**, 7713–7733, doi: `10.1002/2016JA023678`.

Tapping, K. (2013). The 10.7 cm solar radio flux (F10. 7). *Space Weather*, **11**, 394–406.

Tesema, F., Mesquita, R., Meriwether, J., Damtie, B., Nigussie, M., Makela, J., Fisher, D., Harding, B., Yizengaw, E. & Sanders, S. (2017). New results on equatorial thermospheric winds and temperatures from Ethiopia, Africa. *Annales Geophysicae*, **35**, 333–344.

Titheridge, J. (1972). Determination of ionospheric electron content from the Faraday rotation of geostationary satellite signals. *Planetary and Space Science*, **20**, 353–369.

Titheridge, J. (1995a). The calculation of neutral winds from ionospheric data. *Journal of Atmospheric and Terrestrial Physics*, **57**, 1015–1036.

Titheridge, J. (1995b). Winds in the ionosphere–a review. *Journal of Atmospheric and Terrestrial Physics*, **57**, 1681–1714.

Tshisaphungo, M., Habarulema, J.B. & McKinnell, L.A. (2018). Modeling ionospheric foF2 response during geomagnetic storms using neural network and linear regression techniques. *Advances in Space Research*, **61**, 2891–2903.

Tsurutani, B., Mannucci, A., Iijima, B., Abdu, M.A., Sobral, J.H.A., Gonzalez, W., Guarnieri, F., Tsuda, T., Saito, A., Yumoto, K. *et al.* (2004). Global dayside ionospheric uplift and enhancement associated with interplanetary electric fields. *Journal of Geophysical Research: Space Physics*, **109**, A08302.

Tsurutani, B., Saito, A., Verkhoglyadova, O., Mannucci, A., Abdu, M., Araki, T., Gonzalez, W., Iijima, B., Lakhina, G., McCreadie, H. *et al.* (2006a). *The Dayside Ionospheric "Superfountain" (DIS), plasma transport and other consequences*. ILWS Workshop, Goa, India, February 19-24, 2006.

Tsurutani, B., Verkhoglyadova, O., Mannucci, A., Saito, A., Araki, T., Yumoto, K., Tsuda, T., Abdu, M., Sobral, J., Gonzalez, W. *et al.* (2008). Prompt penetration electric fields (PPEFs) and their ionospheric effects during the great magnetic storm of 30–31 october 2003. *Journal of Geophysical Research: Space Physics*, **113**.

Tsurutani, B.T. (2001). The interplanetary causes of magnetic storms, substorms and geomagnetic quiet. In *Space storms and space weather hazards*, 103–130.

Tsurutani, B.T. & Gonzalez, W.D. (1997). *The interplanetary causes of magnetic storms: A review*, vol. 98, 77–89. American Geophysical Union.

Tsurutani, B.T., McPherron, R.L., Gonzalez, W.D., Lu, G., Gopalswamy, N. & Guarnieri, F.L. (2006b). Magnetic storms caused by corotating solar wind streams. *Recurrent magnetic storms: corotating solar wind streams*, **167**, 1–17.

Tulunay, E., Senalp, E.T., Cander, L.R., Tulunay, Y.K., Bilge, A.H., Mizrahi, E., Kouris, S.S. & Jakowski, N. (2004). Development of algorithms and software for forecasting, nowcasting and variability of TEC. *Annals of Geophysics*, **47**, 1201–1214.

Tulunay, E., Senalp, E.T., Radicella, S.M. & Tulunay, Y. (2006). Forecasting total electron content maps by neural network technique. *Radio science*, **41**, RS4016.

Uwamahoro, J.C. & Habarulema, J.B. (2015). Modelling total electron content during geomagnetic storm conditions using empirical orthogonal functions and neural networks. *Journal of Geophysical Research: Space Physics*, **120**, 11000 –11012, doi: `10.1002/2015JA021961`.

Uwamahoro, J.C., Giday, N.M., Habarulema, J.B., Katamzi-Joseph, Z.T. & Seemala, G.K. (2018a). Reconstruction of storm-time total electron content using ionospheric tomography and artificial neural networks: A comparative study over the African region. *Radio Science*, **53**, 1328–1345, doi: `10.1029/2017RS006499`.

Uwamahoro, J.C., Habarulema, J.B. & Okouma, P.M. (2018b). Storm time total electron content modeling over African low-latitude and midlatitude regions. *Journal of Geophysical Research: Space Physics*, **123**, 7889–7905, doi: `10.1029/2018JA025455`.

Uwamahoro, J.C., Habarulema, J.B. & Burešová, D. (2019). Highlights about the performances of storm-time TEC modelling techniques for low/equatorial and mid-latitude locations. *Advances in Space Research*, https://doi.org/10.1016/j.asr.2019.01.027.

Van Diggelen, F.S.T. (2009). *A-GPS: Assisted GPS, GNSS, and SBAS*. Artech House, Boston, MA.

Venegas, S.A. (2001). *Statistical methods for signal detection in climate*. Danish Center for Earth System Science Report, Niels Bohr Institute for Astronomy, Physics and Geophysics, University of Copenhagen, Denmark.

Vijaya Lekshmi, D., Balan, N., Tulasi Ram, S. & Liu, J. (2011). Statistics of geomagnetic storms and ionospheric storms at low and mid latitudes in two solar cycles. *Journal of Geophysical Research: Space Physics*, **116**.

Visconti, G. (2001). *Fundamentals of Physics and Chemistry of the Atmosphere*. Springer-Verlag, Berlin, Germany.

Volland, H. (1995). *Handbook of Atmospheric Electrodynamics*, vol. 2. CRC Press, Bonn.

Walton, E. & Bowhill, S. (1979). Seasonal variations in the low latitude dynamo current system near sunspot maximum. *Journal of Atmospheric and Terrestrial Physics*, **41**, 937–949.

Watthanasangmechai, K., Supnithi, P., Lerkvaranyu, S., Tsugawa, T., Nagatsuma, T. & Maruyama, T. (2012). TEC prediction with neural network for equatorial latitude station in Thailand. *Earth, Planets and Space*, **64**, 473–483.

Weare, B.C. & Nasstrom, J.S. (1982). Examples of extended empirical orthogonal function analyses. *Monthly Weather Review*, **110**, 481–485.

Wells, D., Beck, N., Kleusberg, A., Krakiwsky, E.J., Lachapelle, G., Langley, R.B., Schwarz, K.p., Tranquilla, J.M., Vanicek, P. & Delikaraoglou, D. (1987). *Guide to GPS positioning*. Canadian GPS Associates.

White, S. (1970). *Space Physics*. Gordon and Breach, Science Publishers, New York, USA.

Willmott, C.J. & Matsuura, K. (2005). Advantages of the mean absolute error (MAE) over the root mean square error (RMSE) in assessing average model performance. *Climate research*, **30**, 79–82.

Xu, W.Y. & Kamide, Y. (2004). Decomposition of daily geomagnetic variations by using method of natural orthogonal component. *Journal of Geophysical Research: Space Physics*, **109**, A05218.

Yan, X. (2009). *Linear Regression Analysis: Theory and Computing*. World Scientific Publishing Co. , Singapore, New Jersey, USA.

Yin, P., Mitchell, C., Spencer, P. & Foster, J. (2004). Ionospheric electron concentration imaging using GPS over the USA during the storm of July 2000. *Geophysical Research Letters*, **31**, L12806.

Yin, P., Zheng, Y.N., Mitchell, C.N. & Li, B. (2017). A multi-resolution inversion for imaging the ionosphere. *Journal of Geophysical Research: Space Physics*, **122**, 6799–6811.

Yizengaw, E., Zesta, E., Moldwin, M., Damtie, B., Mebrahtu, A., Valladares, C. & Pfaff, R. (2012). Longitudinal differences of ionospheric vertical density distribution and equatorial electrodynamics. *Journal of Geophysical Research: Space Physics*, **117**.

Yu, Y., Wan, W., Xiong, B., Ren, Z., Zhao, B., Zhang, Y., Ning, B. & Liu, L. (2015). Modeling Chinese ionospheric layer parameters based on EOF analysis. *Space Weather*, **13**, 339–355.

Yuan, Z., Ning, B., Liu, L., Wan, W. & Zhao, B. (2003). A new method for determining the meridional wind velocity during an ionospheric storm. *Geophysical research letters*, **30**.

Yue, X., Schreiner, W.S., Hunt, D.C., Rocken, C. & Kuo, Y.H. (2011). Quantitative evaluation of the low Earth orbit satellite based slant total electron content determination. *Space Weather*, **9**.

Zhang, M.L., Liu, C., Wan, W., Liu, L. & Ning, B. (2009). A global model of the ionospheric F2 peak height based on EOF analysis. *Annales Geophysicae*, **27**, 3203–3212.

Zhang, M.L., Liu, C., Wan, W., Liu, L. & Ning, B. (2010). Evaluation of global modeling of M (3000) F2 and hmF2 based on alternative empirical orthogonal function expansions. *Advances in Space Research*, **46**, 1024–1031.

Zhang, Y., Paxton, L., Morrison, D., Wolven, B., Kil, H., Meng, C.I., Mende, S. & Immel, T. (2004). O/N2 changes during 1–4 october 2002 storms: IMAGE SI-13 and TIMED/GUVI observations. *Journal of Geophysical Research: Space Physics*, **109**, A10308.

Zolesi, B. & Cander, L.R. (2014). *Ionospheric Prediction and Forecasting*. Springer, New York, USA.